How does plankton distribution and activity influence the variability of carbon dioxide uptake in the North Atlantic?

A thesis submitted to the School of Environmental Sciences of the University of East Anglia in partial fulfilment of the requirements for the degree of Doctor of Philosophy

By Clare Ostle

September 2015

Abstract

This study combines two invaluable datasets that have been collected on-board volunteer observing ships to analyse the variability of the carbon dioxide (CO_2) sink in the North Atlantic at a range of spatial and temporal scales. Phytoplankton indices collected from the continuous plankton recorder (CPR) and the concentration of CO_2 within the surface waters show that at seasonal time-scales phytoplankton play an important role in maintaining the carbon drawdown within the northeast Atlantic, while sea surface temperature (SST) drives the seasonal signal in CO_2 flux in the subtropics. The North Atlantic remained a significant sink of CO_2 between 2002 and 2013, despite strong inter-annual variability in CO_2 flux that was correlated to changes in the North Atlantic Oscillation and the influence that this had on SST.

Discrete dissolved inorganic carbon, total alkalinity and dissolved oxygen samples were collected during 4 voyages between April 2012 and February 2013. Using these measurements this study successfully developed and implemented a simple and inexpensive technique to estimate net community production in the surface ocean, with the potential to extend coverage of such measurements over wider regions at low cost.

Two key observations were made in the northeast Atlantic. Firstly, the increase in SST was significantly correlated with the increase in phytoplankton colour index measured by the CPR between 1960 and 2012, despite other micro and nano-phytoplankton counts decreasing over this time frame. This suggests that as the surface ocean warms and stratification is enhanced, pico-phytoplankton (which contribute to the colour index but not the phytoplankton counts) may be better equipped to dominate the system, compared to larger species that are more nutrient dependent. Secondly, the CO_2 uptake capacity has decreased compared to the 1990s. Combined, these two results will likely have a significant impact on carbon flux, export efficiency and ecosystem dynamics.

Acknowledgements

First and foremost I would like to thank my primary supervisor, Carol Robinson, who has made me feel inspired and encouraged in so many ways. She has sustained my enthusiasm and happiness throughout our many supervisory sessions, chats, cake-breaks and ice creams. I would like to thank Martin Johnson for stepping in and adding a whole further dimension to my thought process, and maintaining the fun. My thanks also to Ute Schuster and Arie Louwerse for their unwavering commitment to the measurements, and their support and training which provided me with opportunities that I will never forget. I am also very grateful to Martin Edwards and Andrew Watson for their helpful comments and suggestions.

Significant ($p<0.05$) thanks to Peter who introduced me to the magical world of Matlab and discovery, supported by Ollie and Sunke. You all showed tremendous patience and willingness to help, which kept me playing and learning. I would like to acknowledge and thank all involved in the incredible amount of work and organisation that goes in to creating such valuable datasets as the CPR survey and SOCAT. All of the lab work involved in this thesis would not have been possible without the expertise of Gareth, Stephen, Rob, Steve, Andy, and Dorothee. Furthermore, this lab work would not have happened without the willingness and generosity of the captains and crew from the *MV Benguela Stream*.

I have loved my time at UEA, largely because of the wonderful people around me: my fabulous housies, past and present; Cat for taking me under your wing and those flatty times, Katrin, Nat and Fanny for our unforgettable house 32 experiences and adventures; my lobster room companions Liam, Sam R., Sam A., Sandra, James, Ben, Matt, Tom, Davi and Andrew (those chats and yoga sessions kept me going towards the end); my sporting teammates/opponents who kept me sane and laughing - Davi, Osgur, Jon, Becky, Dave, Karl, Kelly, Wayne, Jenny, and the rest of the football and badders crew; and all of my other lovelies who were always up for a hug/chat/tea/walk - Emma, Elena, Elli, Vanessa, Bastien, and Markilan.

Massive thanks to my amazing friends from afar, old and new, who've braved the East Anglia trains, planes and roads to come and visit and are always my rocks: Tony, Esther, Rachael, Laura, Jennie, Hayley, Vanessa, and Clare.

And finally, thank you to Mum, Dad, and the best family in the world. I feel so loved and supported.

Publications

Work contributing to, or done alongside, this thesis has been published in:

Clare Ostle, Martin Johnson, Peter Lanschützer, Ute Schuster, Susan Hartman, Tom Hull, and Carol Robinson (2015) Net community production in the North Atlantic Ocean derived from Volunteer Observing Ship data, *Global Biogeochemical Cycles*, 29, doi:10.1002/2014GB004868.

Susan Hartman, Zong-Pei Jiang, Daniela Turk, Richard S. Lampitt, Helene Frigstad, **Clare Ostle**, and Ute Schuster (2015), Biogeochemical variations at the Porcupine Abyssal Plain Sustained Observatory (PAP-SO) in the northeast Atlantic Ocean, from weekly to inter-annual time scales, *Biogeosciences*, 12, doi:10.5194/bg-12-845-2015.

Stephanie L. Hinder, Mike B. Gravenor, Martin Edwards, **Clare Ostle**, Owen G. Bodger, Patricia L. M. Lee, Antony W. Walne, and Graeme C. Hays (2014) Multi-decadal range changes vs. thermal adaptation for north east Atlantic oceanic copepods in the face of climate change, *Global Change Biology*, 20, doi:10.1111/gcb.12387.

Contents

List of tables

List of figures

Chapter 1

Introduction

The ocean plays a fundamentally important role in the global cycling of carbon, taking up 26% of anthropogenically produced carbon dioxide (CO_2) (House *et al.*, 2002; Le Quéré *et al.*, 2010). The processes involved in the oceanic uptake of CO_2 are therefore critical in slowing the rate of increase of CO_2 in the atmosphere and of subsequent climate change. The temperate and subtropical North Atlantic (between 14° N and 50° N) is an important sink region for CO_2, and is estimated to have a net air-sea flux of CO_2 of -0.22 Pg C y^{-1}, representing 13% of the global contemporary carbon sink and storing $\sim$ 23% of the global anthropogenic carbon inventory (Gruber *et al.*, 2009; Takahashi, 2009; Schuster *et al.*, 2009b, 2013). Studies have suggested that the uptake of CO_2 in the North Atlantic is changing (Schuster and Watson, 2007; Schuster *et al.*, 2009b). However, as of yet, it is unclear how much of this change is due to changing circulation patterns or to changes in plankton activity (Hays *et al.*, 2005), particularly on seasonal, interannual and decadal time scales. This thesis aims to address this uncertainty by investigating the interactions between the variability of sea surface partial pressure of carbon dioxide (pCO_2), and the air-sea flux of CO_2, in relation to the abundance

and distribution of different phytoplankton taxonomic groups in the North Atlantic Ocean.

Each data chapter (3 to 6) aims to address topics included within the overarching aim of this thesis, and are self-contained with short introductions included. Chapter 3 introduces the importance of phytoplankton and their role in carbon drawdown in the North Atlantic and investigates their spatio-temporal variability over the last ∼50 years. Chapter 4 introduces and investigates net community production in the North Atlantic. Chapter 5 presents carbonate and biological data in the North Atlantic in order to investigate the seasonal carbon cycle. And finally chapter 6 investigates the spatio-temporal variability of CO_2 and phytoplankton abundance in the North Atlantic.

This chapter introduces the importance of the topic by giving background information on anthropogenic emissions and their impact on ocean and climate warming, and the contribution carbon dioxide (CO_2) has on this warming effect. The marine carbonate system and the dissolution of CO_2 within seawater is then detailed, along with an explanation of the influences on CO_2 concentration in surface waters. To show how estimates of carbon cycling within the oceans are derived, some of the key findings from long-term datasets of carbon and productivity estimates are introduced. The chapter then outlines the current knowledge of the variability of both CO_2 and phytoplankton community structure and abundance within the North Atlantic. Finally the overall aims, and objectives of the thesis are stated, and the thesis structure is outlined.

1.1 Background

1.1.1 Ocean warming and CO_2

Understanding the variability in the carbon cycle and the influences involved has become increasingly important with rising emissions and evidence of anthropogenic impacts on our environment (IPCC, 2013; Myhre *et al.*, 2013). The continued emission of greenhouse gases into the atmosphere through fossil fuel burning, cement production and land use change has increased the surface temperature of the

globe. This increase in surface temperature combined over the world's land and oceans from 1880 to 2012 is 0.85°C (Hartmann *et al.*, 2013).

The radiative energy entering the Earth's system is not in balance, with more energy entering the atmosphere than exiting it (Rhein *et al.*, 2013). Figure 1.1 shows that the upper oceans (upper 700 m) shows the largest change in energy compared to the atmosphere, deep ocean (below 700 m), ice, and land. This is mostly due to the high heat capacity and low albedo of the ocean, which leads to ocean warming. This warming is largest in the surface waters, with global mean temperatures of the surface ocean (upper 75 m) increasing by 0.11°C per decade compared to an increase of 0.015°C per decade in the deep ocean (below 700 m), between 1971 and 2010 (Rhein *et al.*, 2013).

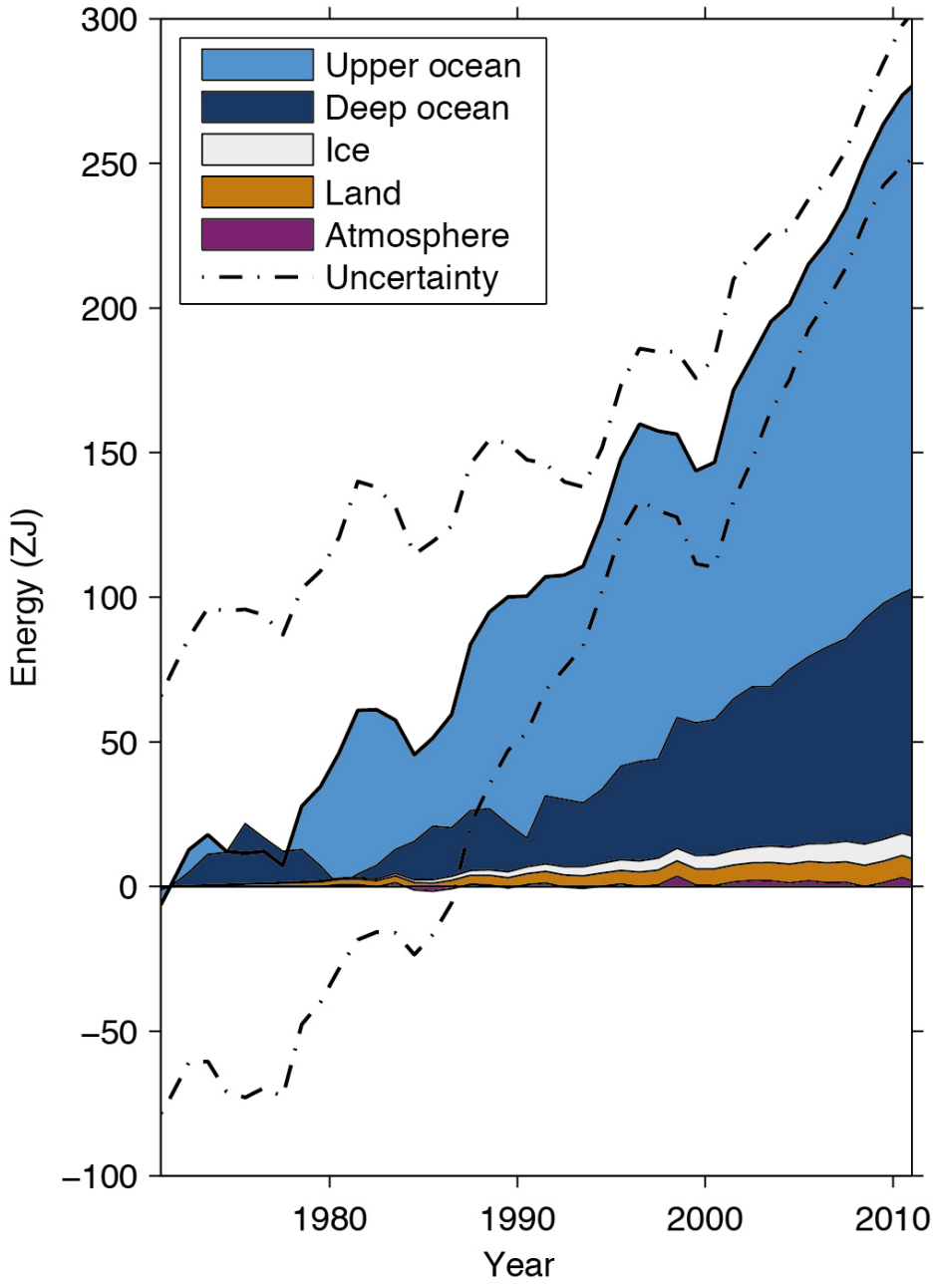

Figure 1.1: The energy accumulated in ZJ (1 ZJ = 10^{21} J) from 1971 to 2010 for different components of the Earth's climate system. Upper ocean (surface 700 m) = light blue, deep ocean (below 700 m) = dark blue, ice melt (glaciers and ice caps, Greenland and Antarctic ice sheet estimates starting from 1992, and Arctic sea ice estimate from 1979 to 2008) = light grey, land = orange, atmosphere = purple. The total uncertainty about the error from all five components at the 90% confidence interval is shown as a dot-dashed black line. Reproduced from Rhein *et al.* (2013).

Figure 1.2 presents the radiative forcings of the main agents that have influenced the climate from 1750 to 2011. The anthropogenic influence on radiative forcing during this period is much larger than the natural influence, with the anthropogenic radiative forcing over the industrial era estimated to be a total of 2.29

W m^{-2} (Myhre *et al.*, 2013). Greenhouse gases show a strong positive radiative forcing on climate, with carbon dioxide (CO_2) showing the largest contribution (figure 1.2).

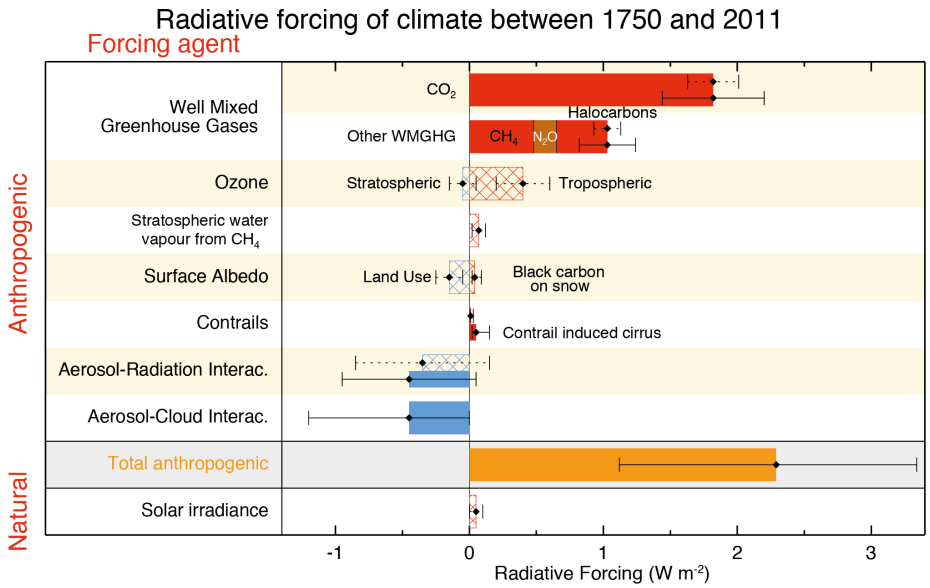

Figure 1.2: The radiative forcing of the main agents that have influenced the climate from 1750 to 2011. These forcing estimates were derived from models, model simulations combined with observations and observations. The hatched bars represent previously presented estimates of radiative forcing and the solid bars represent novel effective radiative forcing estimates. The 5 to 95% confidence range are displayed as error bars on each bar. Reproduced from Myhre *et al.* (2013).

Since the industrial revolution, measurements of CO_2 from ice-cores have shown that atmospheric CO_2 concentration has continued to rise at an unprecedented rate and that it has reached concentrations higher than those seen in the past 800,000 years (Lüthi *et al.*, 2008). Between 1959 and 2008 the proportion of CO_2 emissions that remain in the atmosphere each year have been suggested to have increased by 40% to 50% (Le Quéré *et al.*, 2009). Models suggest that this increase is due to decreased uptake by both land and ocean sinks due to a number of processes such as volcanic eruptions, climate variability and change (Le Quéré *et al.*, 2009; Raupach *et al.*, 2014). Regional variations in surface water CO_2 concentration are due to complex interactions between physical, chemical, and biological processes which drive the air-sea flux (Sarmiento and Gruber, 2006). These processes have been difficult to quantify and predict in terms of their impact on this variability (SAHFOS, 2006).

1.1.2 The marine carbonate system

The following reactions take place when carbon dioxide dissolves in seawater, with the bracketed letters (g), (aq), and (l) referring to the states; gas, aqueous solution, and liquid respectively (Dickson *et al.*, 2007). Dissolved carbon dioxide ($CO_{2(aq)}$) reacts with water to form carbonic acid ($H_2CO_{3(aq)}$), which in a two-step process, dissociates to form bicarbonate ($HCO^-_{3(aq)}$), hydrogen (H^+(aq)) and carbonate ions ($CO^{2-}_{3(aq)}$):

$$CO_{2(g)} \leftrightarrows CO_{2(aq)} \tag{1.1}$$

$$CO_{2(aq)} + H_2O_{(l)} \leftrightarrows H_2CO_{3(aq)} \tag{1.2}$$

$$H_2CO_{3(aq)} \leftrightarrows H^+_{(aq)} + HCO^-_{3(aq)} \tag{1.3}$$

$$HCO^-_{3(aq)} \leftrightarrows H^+_{(aq)} + CO^{2-}_{3(aq)} \tag{1.4}$$

Because it is difficult to distinguish analytically between $CO_{2(aq)}$ and $H_2CO_{3(aq)}$ these are often combined and referred to as $CO^*_{2(aq)}$ (Dickson *et al.*, 2007):

$$CO^*_{2(aq)} = CO_{2(aq)} + H_2CO_{3(aq)} \tag{1.5}$$

Using this term, the equilibrium constants between these different species' concentrations are written as the following, where $pCO_{2,atm}$ is the partial pressure of carbon dioxide in the air (Dickson *et al.*, 2007; Sarmiento and Gruber, 2006):

$$K_0 = \frac{[CO_2^*]}{pCO_{2,atm}} \tag{1.6}$$

$$K_1 = \frac{[HCO_3^-] \times [H^+]}{[CO_2^*]} \tag{1.7}$$

$$K_2 = \frac{[CO_3^{2-}] \times [H^+]}{[HCO_3^-]} \tag{1.8}$$

The sum of the products formed in equations 1.6 to 1.8 is the total dissolved inorganic carbon (DIC) concentration:

$$[DIC] = [CO_2^*] + [HCO_3^-] + [CO_3^{2-}] \tag{1.9}$$

The Total Alkalinity (TA) of a sample of seawater also influences the concentration of carbon and is defined as "the number of moles of hydrogen ion equivalent to the excess of proton acceptors (bases formed from weak acids with a dissociation constant K $\leq$ 10 to 4.5 at 25°C and zero ionic strength) over proton donors (acids with K $>$ 10 to 4.5) in 1 kilogram of sample" (Dickson *et al.*, 2007). Although there are different definitions within the literature (Peng *et al.*, 1987), Dickson (1981) defines TA as:

$$\begin{aligned}[TA] = [HCO_3^-] + 2 \times [CO_3^{2-}] + [B(OH)_4^-] + [OH^-] - [H^+] \\ +[HPO_4^{2-}] + 2 \times [PO_4^{3-}] + [SiO(OH)_3^-] + [NH_3] \\ +[HS^-] - [HSO_4^-] - [HF] - [H_3PO_4]\end{aligned} \tag{1.10}$$

The partial pressure of carbon dioxide in seawater ($pCO_{2,sea}$) is the product of the mole fraction of CO_2 and total pressure, while the fugacity of CO_2 (fCO_2) takes into account the non-ideal nature of the gas phase. The equilibrium constants in equations 1.6 to 1.8 can be used to estimate the $pCO_{2,sea}$ using the reactions in equations 1.2 to 1.4 (Sarmiento and Gruber, 2006):

$$pCO_{2,sea} = \frac{K_2}{K_0 \times K_1} \times \frac{[HCO_3^-]^2}{[CO_3^{2-}]} \tag{1.11}$$

This, using approximations to express bicarbonate and carbonate concentration in terms of DIC and TA is equivalent to the following (Sarmiento and Gruber, 2006):

$$pCO_{2,sea} = \frac{K_2}{K_0 \times K_1} \times \frac{2 \times [DIC] - [TA]^2}{[TA] - [DIC]} \tag{1.12}$$

Therefore the $pCO_{2,sea}$ is affected by the ratio of the equilibrium constants, and the ratio between the concentration of DIC and TA (Sarmiento and Gruber, 2006). The equilibrium constants are affected by solubility, which in seawater is controlled by salinity and temperature, while the DIC and TA are influenced by the exchange of CO_2 with the atmosphere, mixing and biological processes, such as plankton photosynthesis, respiration and calcification (this is summarised in figure 1.3).

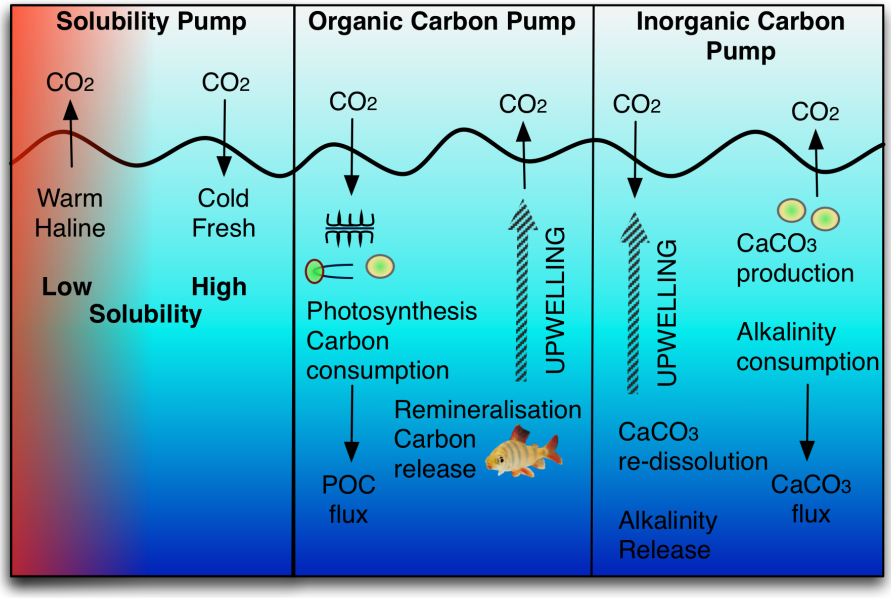

Figure 1.3: Schematic of the solubility, organic carbon, and inorganic carbon pumps.

Sea-surface temperature (SST) influences the solubility of DIC, as well as mixing events (via stratification) which can limit the amount of nutrient and CO_2 rich waters that are mixed from below the thermocline into surface waters. With continued warming predicted from climate change, the solubility of DIC will decrease, therefore reducing the carbon flux from the atmosphere into the ocean. Model studies suggest that this has a particularly strong influence in the North Atlantic (Le Quéré *et al.*, 2010). Ocean warming has also been linked to increased thermal stratification in the top 0 to 200 m surface layer by 4% (Levitus *et al.*, 2009), which can have significant implications for ventilation and nutrient upwelling. With increasing concentrations of $pCO_{2,sea}$ due to increased emissions (figure 1.4), it is likely that the buffer capacity of the oceans will change. The buffer capacity is representative of the capacity for a body of water to take up surplus CO_2 (anthropogenic) from the atmosphere, and is calculated as the fractional change in $pCO_{2,sea}$ relative to the fractional change in DIC (Zeebe and Wolf-Gladrow, 2001). This capacity is directly proportional to the ratio of DIC:TA mostly due to the regional temperature influence on DIC concentrations (Sabine *et al.*, 2004; Sarmiento and Gruber, 2006). It is referred to as the buffer capacity because the increase in CO_2 concentration in seawater is less than the CO_2 concentration that is added from the

atmosphere. This is due to the conversion of CO_2 to HCO_3^- (bicarbonate) and the scavenging properties of CO_3^{2-} (carbonate) in seawater. Increased $pCO_{2,sea}$ will cause an increase in hydrogen ion concentration (increasing acidity, see increasing pH in figure 1.4b) and a decrease in carbonate ion concentration, which combined with the increased concentration of $pCO_{2,sea}$ will likely decrease the buffer capacity (Sabine *et al.*, 2004).

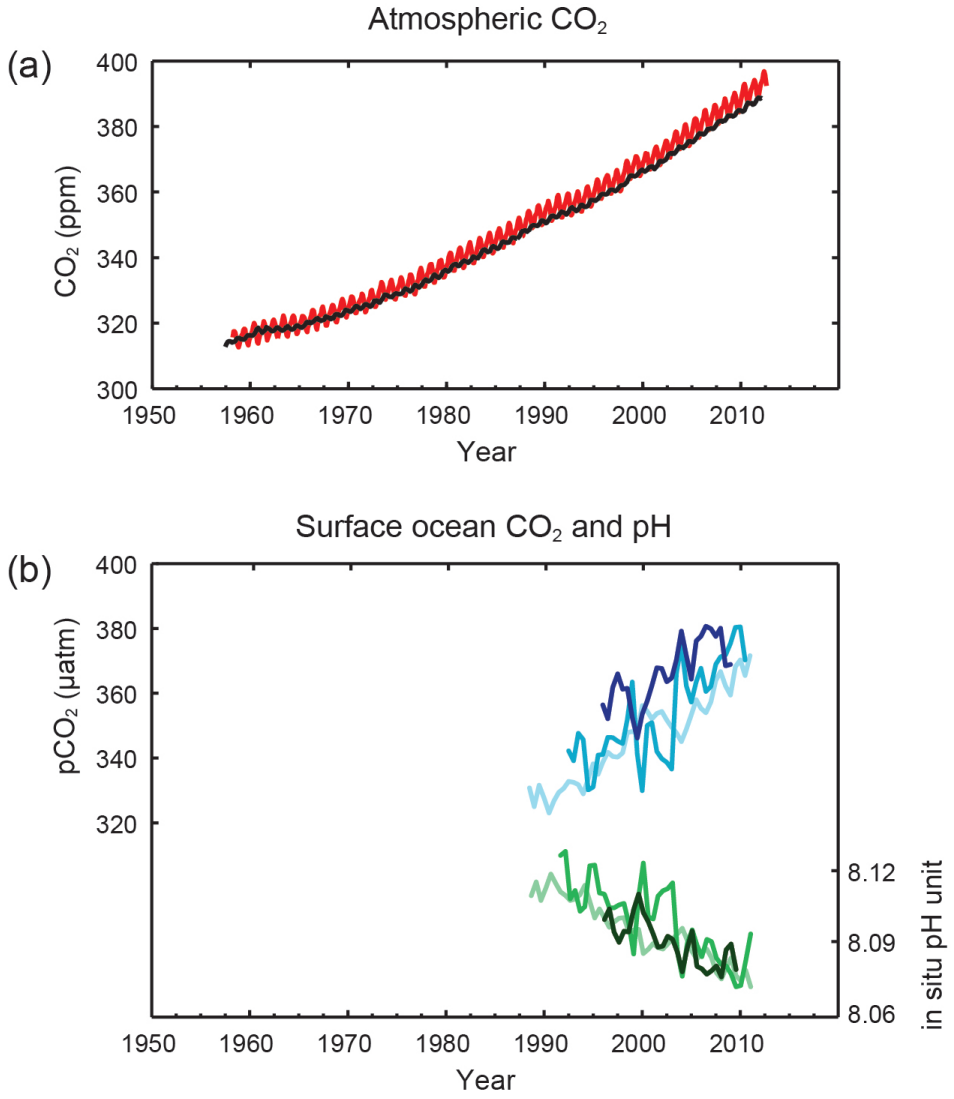

Figure 1.4: (a) The atmospheric concentration of CO_2 (ppm) from 1958 to 2011 recorded at Mauna Loa = red (located at 19.32 °N, 155.34°W) and the South Pole = black (located at 89.59°S, 24.48°W). (b) Sea surface pCO_2 (μatm) = blue curves, and *in situ* pH = green curves. These measurements are from three different time-series stations; Atlantic = Bermuda Atlantic Time Series (BATS, 32°N 74°W) = dark blue/green and European Station for Time Series in the Ocean (ESTOC, 29.2°N 15.5°W) = blue/green, Pacific = the Hawaii Ocean Time-series (HOT, 22.45°N 158.00°W) = light blue/green. Reproduced from IPCC (2013).

Phytoplankton play an important role in the uptake of CO_2 due to photosynthesis, particularly in the North Atlantic where the spring bloom is a prominent feature (Takahashi *et al.*, 1993; Follows and Dutkiewicz, 2001; Shutler *et al.*, 2013). Redfield *et al.* (1963) describes photosynthesis using the constant stoichiometric relationship between CO_2, nutrients and oxygen:

$$\begin{aligned} 106CO_2 + 16NO_3^- + HPO_4^{2-} + 122H_2O + 18H^+ \\ \leftrightarrows (CH_2O)_{106}(NH_3)_{16}(H_3PO_4) + 128O_2 \end{aligned} \tag{1.13}$$

In the surface waters this process decreases the pCO_2, DIC and nutrient concentrations which increases the gradient of CO_2 between the atmosphere and the surface waters, allowing for increased uptake of CO_2. Most of the organic matter produced in the surface waters is regenerated as a source of nitrogen and phosphorus used by phytoplankton or labile carbon used by bacteria. However some of the organic matter is exported to the deep ocean by sinking particles (export production) in the form of particulate organic carbon (POC flux in the organic carbon pump in figure 1.3). Processes which lead to increased CO_2 concentrations in the surface waters are respiration, remineralisation of organic matter by heterotrophic bacteria, and upwelling of CO_2 rich waters from the deep ocean (Sarmiento and Gruber, 2006).

The inorganic carbon pump describes the production of calcium carbonate by calcifying plankton in the surface waters and the dissolution of calcium carbonate at depth (figure 1.3, equation 1.14).

$$Ca^{2+} + 2HCO_3^- \leftrightarrows CaCO_3 + H_2O + CO_2 \tag{1.14}$$

The export of calcium carbonate ($CaCO_3$) to the deep ocean is important in the sequestration of carbon. Studies have also indicated a negative feedback between CO_2 flux and the activities of calcifying phytoplankton (Robertson *et al.*, 1993; Shutler *et al.*, 2013). This is because during calcification CO_2 is produced (equation 1.14) which can reduce the gradient of CO_2 between the atmosphere and

surface waters therefore reducing the flux. In the North Atlantic, coccolithophores, such as *Emiliania huxleyi*, form a large component of the phytoplankton blooms (Shutler *et al.*, 2013) (see figure 1.5), and are thought to be major contributors to the export of carbon in the global oceans (Broecker and Clark, 2009).

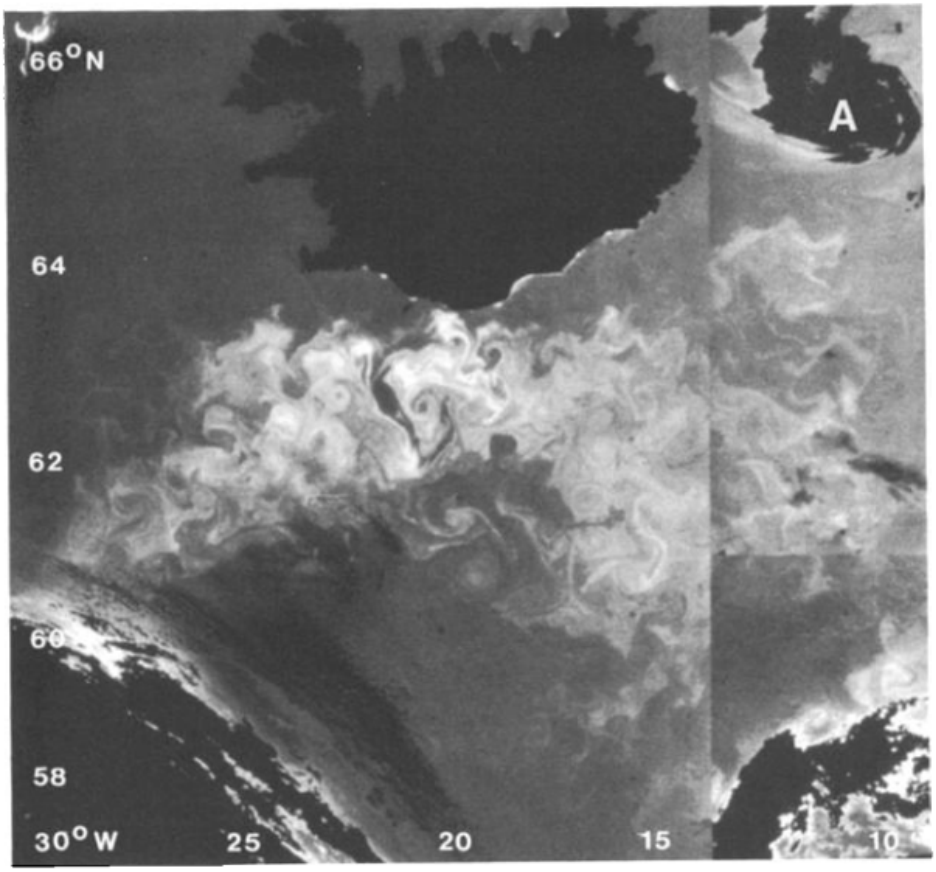

Figure 1.5: National oceanic and atmospheric administration (NOAA) advanced very high resolution radiometer (AVHRR) composite image of *Emiliania huxleyi* bloom in the north-east Atlantic, from June 18th, June 29th and July 1st 1991. Light shades are coccolith light scatter, land and clouds are black. Reproduced from Holligan *et al.* (1993).

1.1.3 Estimating the spatio-temporal variability in carbon cycling

In order to quantify and investigate the seasonal, inter-annual and decadal variability of biogeochemical cycles in the North Atlantic, long-term measurements are needed. There are a number of different methodologies used to collect such data ranging from *in situ* measurements to satellite imagery. In the North Atlantic there are three main time-series stations; Bermuda Atlantic Time Series (BATS, 32°N 74°W), European Station for Time Series in the Ocean (ESTOC, 29.2°N 15.5°W) and the Porcupine Abyssal Plain site (PAP, 49°N 16.3°W) (see figure 1.6).

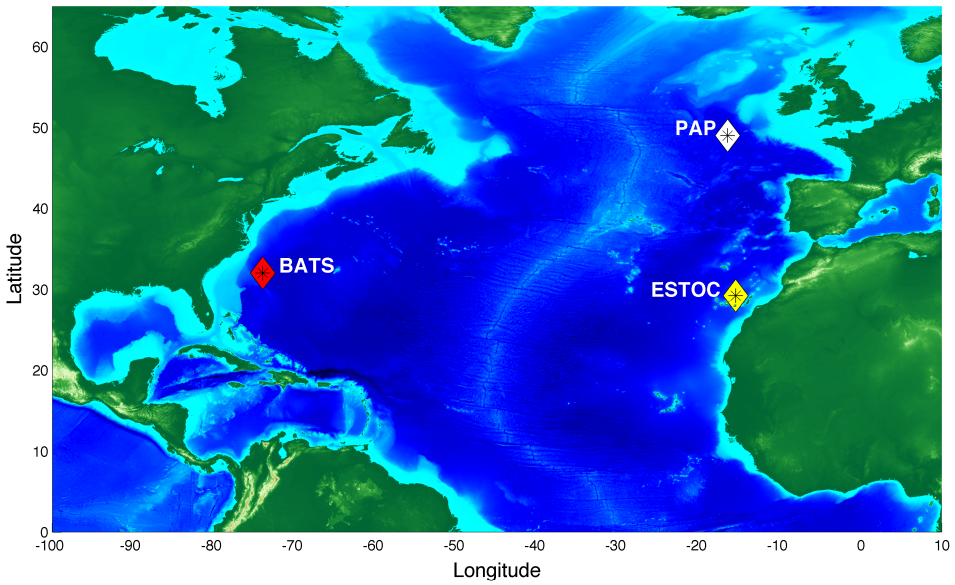

Figure 1.6: Map of the North Atlantic with BATS (red diamond), ESTOC (yellow diamond) and the PAP site (white diamond) time-series stations marked.

These stations use a range of sampling techniques designed around sampling buoys with sensors attached that are calibrated and maintained regularly. Gruber *et al.* (2002) provide an 18 year time series of carbon measurements from BATS demonstrating that the seasonal cycle in near-surface waters of inorganic carbon is driven by SST and changes in the winter-mixed layer depth, which was found to be linked to the North Atlantic Oscillation (NAO, described in section 1.2.1). A similar trend is seen in the eastern Atlantic at ESTOC, with a three-year time lag between the NAO and the inter-annual variability in the carbon sink (Santana-Casiano *et al.*, 2007; Schuster *et al.*, 2013). At the PAP site the seasonal cycle of carbon is driven by a seasonal minimum caused by biological drawdown in the spring-summer, and a maximum caused by winter mixing of carbon rich waters (Körtzinger *et al.*, 2008). Hartman *et al.* (2015) demonstrated that at this site there is variability in the intensity of the spring bloom and the timing of the deepening of the mixed layer between years, but that the net annual CO_2 flux remained a sink of $\sim$5 mmol CO_2 m^{-2} d^{-1}.

There is also a network of volunteer observing ships (VOS) that measure CO_2 within the surface waters (this methodology is described in section 2.5). The Surface Ocean Carbon ATlas (SOCAT) provides a quality controlled database of these

measurements, with the latest update including over 10 million data points from 1968 to 2011 (Bakker *et al.*, 2014). Figure 1.7 shows the number of unique months sampled within this dataset, demonstrating that currently the northern hemisphere has more data coverage and months sampled than the southern hemisphere, with the North Atlantic appearing relatively well-sampled.

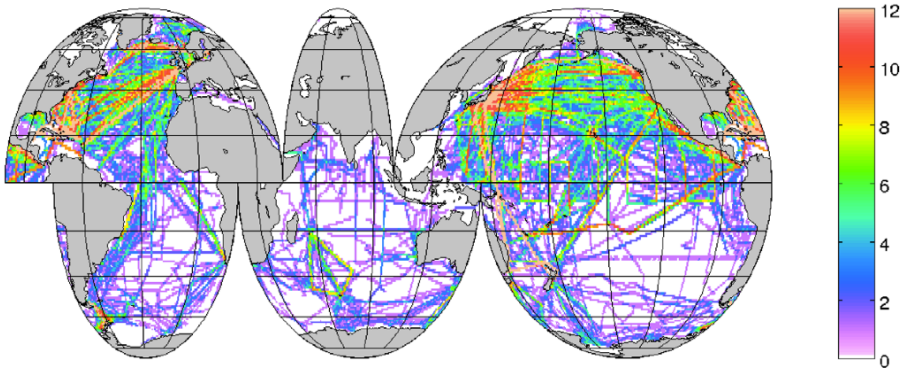

Figure 1.7: The number of unique months with fCO_2 observations in each 1°by 1°grid cell from 1970 to 2011 in SOCAT version 2. Reproduced from Bakker *et al.* (2014).

The use of VOS allows for a cost-effective efficient platform to collect *in situ* measurements. The continuous plankton recorder (CPR) is an example of a long-standing system that uses VOS networks globally (a detailed methodology is described in section 2.1). The CPR survey provides a semi-quantitative record of the plankton within the surface waters dating back to 1958. The dataset has been used to determine a number of important ecological shifts and patterns, such as the northward extension of warm-water copepod assemblages (Beaugrand *et al.*, 2002; Hinder *et al.*, 2014), which has knock-on implications for their prey and predators (including fish stocks).

Using satellite imagery it is possible to estimate the amount of chlorophyll in the sea surface from ocean colour. This can be used to estimate plankton productivity. Global net primary production (NPP) is calculated as the difference between gross primary production (GPP) (rate of carbon fixed by photosynthesis) and respiration by phytoplankton (primary producers). It can be estimated using a chlorophyll based satellite technique (e.g. Vertically Generalized Production Model (VGPM)) (Behrenfeld and Falkowski, 1997) or a carbon-based satellite

technique (e.g. carbon-based productivity model (CbPM)) (Westberry *et al.*, 2008). Net community production (NCP) indicates the balance between production of organic carbon by autotrophs (P) and production of CO_2 by heterotrophs (R) at the time and space scale of the measurement technique used (Serret *et al.*, 2009). The metabolic state of a system can be defined by NCP (=P-R); with autotrophic systems occurring when gross primary production is greater than respiration, and heterotrophic systems occurring when respiration is greater than primary production (Ducklow and Doney, 2013) (see chapter 4 for further details).

Behrenfeld *et al.* (2006) used the VGPM to estimate global NPP (figure 1.8a), and demonstrate that stratification anomalies in the permanently stratified regions of the ocean were dominating the anomalies seen in global productivity (figure 1.8b and 1.8c). The advantage of using satellite data is that it can cover large regions with relatively high spatial and temporal resolution, and as more satellites are deployed and these sensors and algorithms develop further, they will greatly enhance our understanding of large-scale oceanic processes.

Combining the range of measurement techniques available (i.e. *in situ* and satellite) provides the best estimate and resolution of biogeochemical processes that may be occurring in the oceans and allows for validation of the different techniques available.

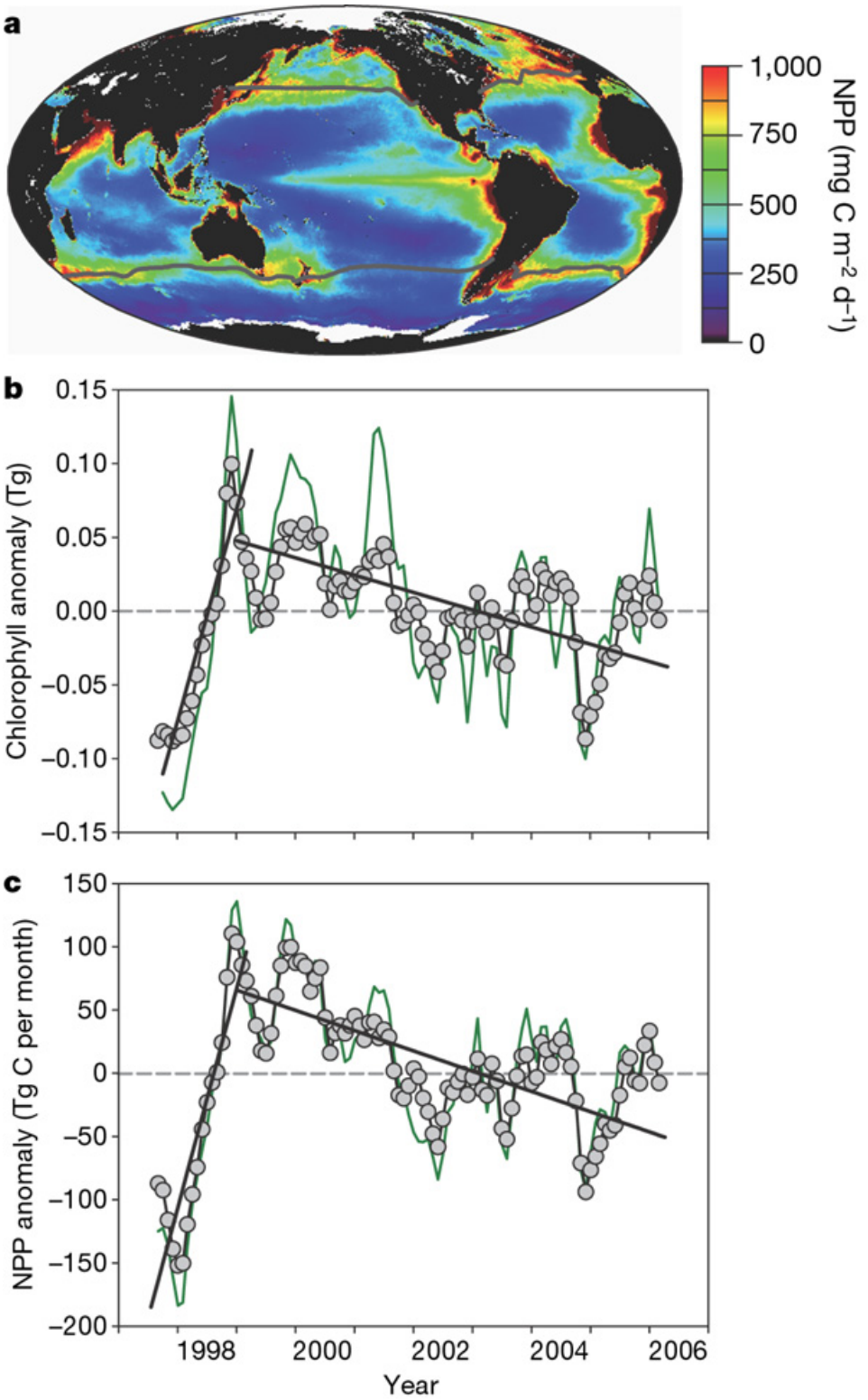

Figure 1.8: a) World map of annually averaged net primary production (NPP). b) Globally integrated water-column chlorophyll concentration anomalies (green line) with changes occurring in permanently stratified ocean regions (grey circles with black line). c) Global NPP anomalies (green line) also with changes occurring in permanently stratified ocean regions (grey circles with black line). Demonstrates that changes in the stratified regions dominate the productivity trends. Reproduced from Behrenfeld *et al.* (2006).

1.2 CO_2 in the North Atlantic

The contemporary carbon flux is a combination of both anthropogenic and natural carbon flux. Geochemical processes and the natural seasonality of temperature and vegetation primarily maintain the natural carbon flux, while the anthropogenic carbon flux is influenced by carbon emissions due to human activity. On a global scale the natural carbon flux is thought to be roughly balanced (neither a source or a sink) (Gruber, 2009) with the exception of the natural out-gassing of carbon by rivers (Wanninkhof *et al.*, 2013). The North Atlantic Ocean is an important contemporary sink of CO_2 because it is thought to be driven by $\sim$50% natural carbon flux and $\sim$50% anthropogenic carbon flux (Gruber, 2009; Schuster *et al.*, 2013). Takahashi (2009) calculated the climatological mean annual net global air-to-sea carbon flux for the reference year 2000 as -1.6 $\pm$0.9 Pg C y^{-1} (negative value representing marine uptake from the atmosphere), using the available pCO_2 measurements and an advection-based interpolation. The global ocean map produced from these calculations demonstrates that the temperate and subtropical North Atlantic (between 14° N and 50° N) is an important sink region for CO_2 (figure 1.9). For the reference year 2000, this region is estimated to have a net air-sea flux of CO_2 of -0.22 Pg C y^{-1} (Takahashi, 2009; Schuster *et al.*, 2013).

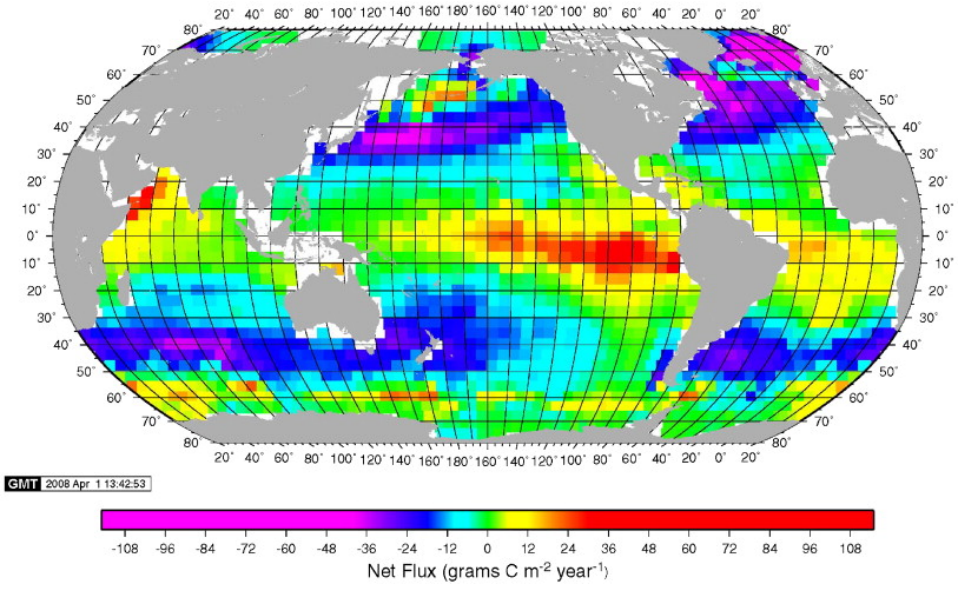

Figure 1.9: Climatological mean annual net sea-air CO_2 flux for the reference year 2000 (g C m^{-2} y^{-1}). Negative values (pink and blues) represent sink areas, positive values (yellows and red) represent source areas. Reproduced from Takahashi (2009).

The ocean sink of CO_2 can be estimated from *in situ* measurements of sea surface partial pressure of CO_2 (pCO_2) and the difference between pCO_2 and the concentration of CO_2 in the atmosphere. Although atmospheric pCO_2 is relatively homogenous, marine pCO_2 varies both spatially and temporally (Telszewski *et al.*, 2009). The CO_2 sink in the North Atlantic is maintained by the year-round northward transport of cool waters, and accentuated by phytoplankton blooms that primarily occur within the subpolar gyre during spring (Watson *et al.*, 2009). The subtropical gyre has high surface pCO_2 during the spring and summer, acting as a source of CO_2, and then developing into a net sink during the winter months as pCO_2 levels decline. This process is thought to be mainly temperature driven (Telszewski *et al.*, 2009). The subpolar gyre has been reported as a major sink of CO_2, with a high biological CO_2 drawdown linked to the spring and summer blooms, that are represented by lower levels of surface pCO_2. However, mixing that occurs in the autumn counter-acts this and is believed to bring CO_2 rich waters back to the surface increasing surface pCO_2 levels once again (Telszewski *et al.*, 2009). The contrasting seasonal cycle of pCO_2 in these two regions creates a transition zone at about 40 °N, in which the seasonal cycles cancel each other out, and the seasonal amplitude is reduced (Takahashi and Sutherland, 2002; Landschützer *et al.*, 2013). This can be seen in figure 1.10, which shows the difference between the effects on pCO_2 of seasonal thermal (pCO_2T) and non-thermal (pCO_2NT) changes (pCO_2T - pCO_2NT).

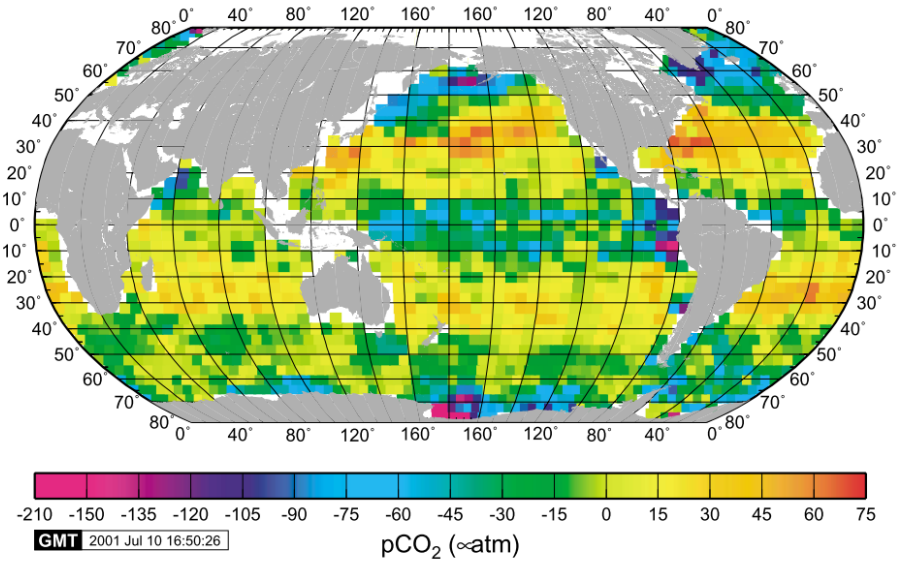

Figure 1.10: The difference between the effects on pCO_2 of seasonal thermal (pCO_2T) and non-thermal (pCO_2NT) changes (pCO_2T - pCO_2NT). Negative values (green and blues) represent where non-thermal effects exceed thermal effects, positive values (orange and red) represent where thermal effects exceed non-thermal effects. Reproduced from Takahashi and Sutherland (2002).

1.2.1 The North Atlantic Oscillation

Long-term trends in CO_2 and phytoplankton species abundance have been linked to large scale climate modes (Gruber *et al.*, 2002; Harris *et al.*, 2013). The North Atlantic Oscillation (NAO) is the dominant climate mode in the North Atlantic (Hurrell, 1995), and is therefore potentially important for CO_2 uptake. It is an oscillation of atmospheric pressure over the North Atlantic between the high pressure centered in the subtropics around the Azores and low pressure around Iceland. This phenomenon is thought to affect weather patterns, which can impact sea surface temperatures, stratification, and mixing of the upper ocean (Planque and Fromentin, 1996). The NAO index is measured as the difference between the mean winter sea-level pressure over the Azores, and the mean winter sea-level pressure over Iceland (Marshall *et al.*, 2001). Figure 1.11 shows the annual NAO index, with prolonged positive NAO periods occurring between 1900 to 1920 and 1990 to 2000, and prolonged negative periods occurring between 1870 to 1880 and 1960 to 1975.

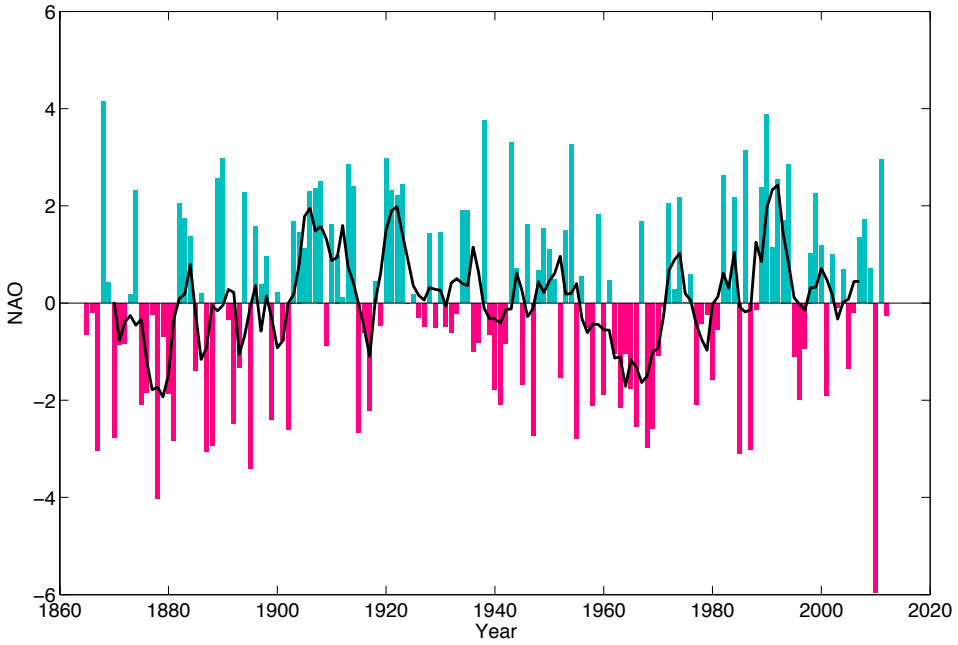

Figure 1.11: Annual NAO index from 1865 to 2012 (Hurrell, 1995). Cyan = positive NAO, pink = negative NAO, black line = 5 year moving average.

A weaker seasonal cycle in subpolar regions of the North Atlantic can be linked to a negative NAO pattern, in which westerly winds across the North Atlantic would be expected to weaken. In mid-latitude regions (temperate and subtropical) a positive NAO index would be expected to result in increased SST due to changes in circulation, while in the subpolar and tropical latitudes this would result in decreased SST (Visbeck *et al.*, 2003). This regional difference induces a tripole that can be seen in figure 1.12, which shows the de-trended linear regressions between the NAO index and SST, heat flux and wind stress curl. The NAO is therefore likely to have differing regional influences on the pCO_2. Schuster *et al.* (2009b) describe the regional tripole of SST regressed on to the NAO index as seen in figure 1.12a, and suggest that an increase in the NAO will cause an increasing sink of carbon in subpolar regions of the North Atlantic.

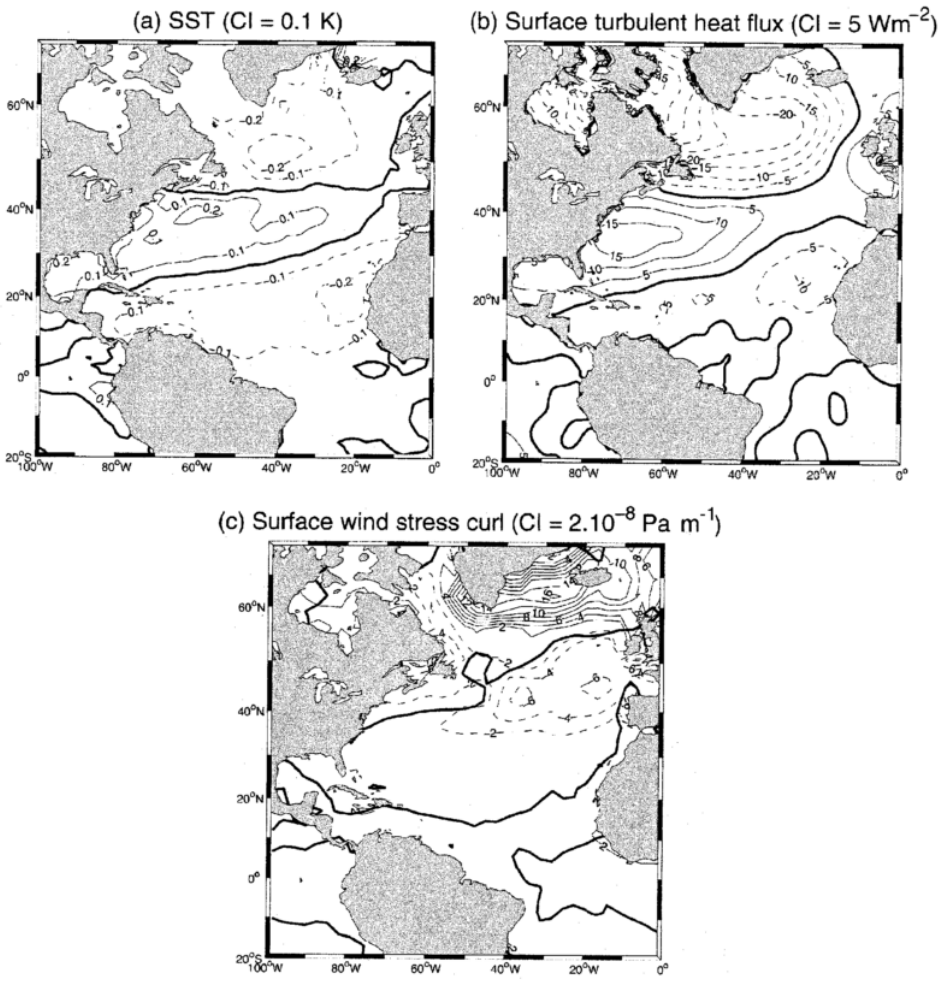

Figure 1.12: Maps of the North Atlantic showing the linear regression between the NAO index and the anomalies of a) sea surface temperature (SST, negative is shown using a dashed line) b) surface turbulent heat flux (latent and sensible, dashed is out of the ocean) and c) surface wind stress curl (dashed line for anti-cyclonic, black lines are zero wind curl). The linear trend was removed from each dataset before calculating the linear regression. Reproduced from Marshall *et al.* (2001).

1.2.2 Circulation in the North Atlantic

Circulation within the North Atlantic influences the air-sea exchange and transportation of carbon. The ocean conveyor circulation is driven by temperature and salinity, with the formation of North Atlantic deep water in the high latitude North Atlantic. The surface pCO_2 remains low in this region due to the cool temperatures. The cooling of the northward movement of the conveyor means that large quantities of anthropogenic carbon are taken up and transported into the interior ocean (Sabine *et al.*, 2004). The surface ocean currents in the North Atlantic also influence the distribution of carbon (green arrows in figure 1.13), with low latitude water masses which are warm and carbon rich being transported to higher

latitudes and cool water masses from higher latitudes being transported to low latitudes where warming reduces the gas solubility, therefore increasing the surface pCO_2.

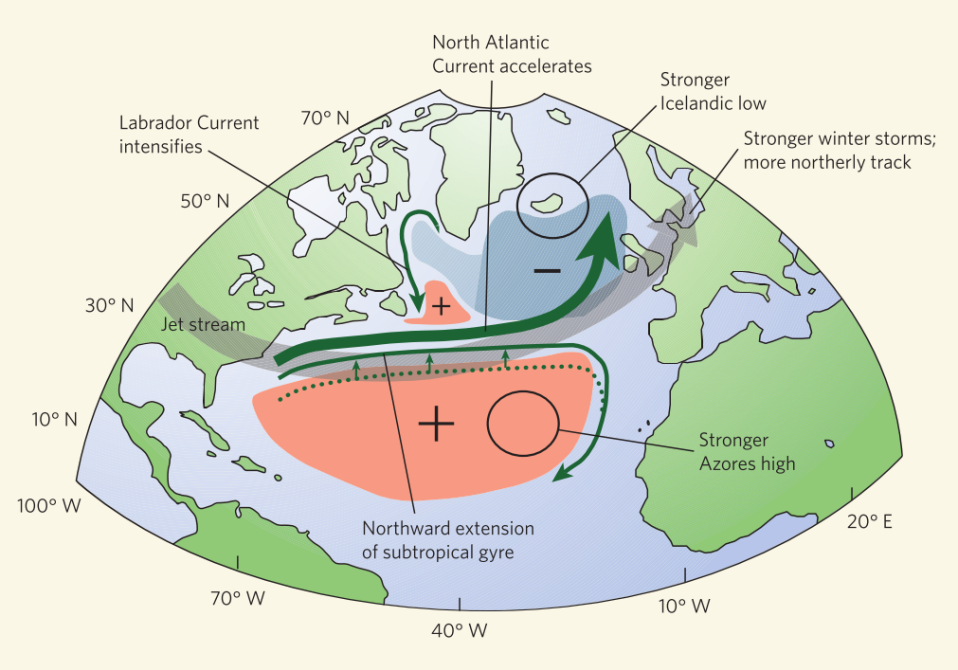

Figure 1.13: Map showing the influence of a positive NAO phase on the circulation and CO_2 sink in the North Atlantic. Green arrows represent different ocean currents. The negative sign represents an increased CO_2 sink, and the positive sign represents a decreased CO_2 sink. Reproduced from Gruber (2009), based on model results from (Thomas *et al.*, 2008).

Figure 1.13 depicts the impact of a positive phase NAO on circulation in the North Atlantic and how this is modelled to influence the CO_2 sink. The increased westerly winds cause an extension of the subtropical gyre northward, and an acceleration of the North Atlantic Current, which brings more low carbon waters from the subtropics northeastward. This increases the carbon sink in the eastern subpolar region (blue region with negative sign in figure 1.13), because the cooling of these waters increases their potential to take up CO_2. The Labrador Current intensifies during a positive NAO phase, which brings high concentrated carbon waters from the Arctic into the subpolar gyre, decreasing the CO_2 sink off the Grand Banks of Newfoundland. The subtropical gyre also has a decreased carbon sink (red region with positive sign in figure 1.13), because of warm conditions and reduced convection (Gruber, 2009).

1.2.3 CO_2 variability

An analysis of pCO_2 observations and models within the Regional Carbon Cycle Assessment and Processes (RECCAP) synthesis has demonstrated that there is disagreement about the trends of pCO_2 within the North Atlantic (Schuster *et al.*, 2013). Schuster and Watson (2007) reviewed available *in situ* pCO_2 observations from the mid-1990s and the period 2002-2005 suggesting that there is a large region of decreasing air-sea flux in the North Atlantic, particularly within the northeast. This review also demonstrated that the sink for atmospheric CO_2 in the North Atlantic shows important seasonal, and interannual variability, and that there has been an overall inter-decadal decline; with the sink reducing by $>50\%$ between the two study periods (Schuster and Watson, 2007). This decline was thought to be linked to a number of changing variables such as increased stratification, and decreased rates of wintertime mixing and ventilation. CO_2 uptake is higher in temperate and subpolar regions of the North Atlantic compared to tropical regions due to the seasonal deep mixing that occurs at higher latitudes in the North Atlantic. Watson *et al.* (2009) further demonstrated that the change in CO_2 flux had declined by $>20\%$ in 2005 compared to the mid 1990s, and that the declining sink was non-uniform with location. This decrease in CO_2 uptake is believed to be enhanced by the changing buffer capacity of the North Atlantic, as increasing levels of carbon content have been recorded in the sea surface waters on the sampling route between the UK and the Caribbean from 1995-2000s (Schuster and Watson, 2007). Numerous model studies have predicted a weakening in the Atlantic meridional overturning circulation (AMOC), which if correct, would further decrease the CO_2 uptake in the North Atlantic (Landschützer *et al.*, 2011). The reported decrease in the intensity of the subpolar gyre circulation due to freshening and warming of the northern regions, has been linked with decreasing formation of dense water (Curry *et al.*, 2003), and thus is likely to add to the decreasing uptake of CO_2 (Schuster and Watson, 2007). Watson *et al.* (2009) demonstrated that there was significant inter-annual variability in the air-sea carbon flux in the northeast Atlantic between 2002 and 2007. This has been attributed to decadal scale climate variability (McKinley *et al.*, 2011; Schuster *et al.*, 2013). Although Lefèvre (2004), Olsen

et al. (2006), Lüger *et al.* (2006), and Watson *et al.* (2009) agreed with Schuster and Watson (2007) about the declining pCO_2 sink, Ullman *et al.* (2009) argue that this region has actually shown an increased sink, and Thomas *et al.* (2008) suggest that the decreasing sink is transitory and due to natural variability rather than an anthropogenic influence. More recently Landschützer *et al.* (2014), using a neural network based approach to interpolate the available pCO_2 measurements, showed that the sink in the Atlantic Ocean has increased from 1998 to 2011. However, caution must be taken when comparing different regions and time-scales as it has been demonstrated that on longer time-scales ($>$ 25 years) the inter-annual and decadal trends are lost, and the rise in pCO_2 is in-line with increasing atmospheric CO_2 (McKinley *et al.*, 2011). These discrepancies between studies demonstrate the importance of improved understanding and continued measurements to determine the variability in the pCO_2 sink and enhance model outputs.

1.3 Phytoplankton in the North Atlantic

A key control on CO_2 is the biological carbon pump (both organic and inorganic), in which phytoplankton play a large role (described previously in section 1.1.2 and figure 1.3). Decadal changes in phytoplankton abundance have been documented in the North Atlantic, with the phytoplankton colour index (PCI) from the continuous plankton recorder (CPR) showing that north of 59°N phytoplankton are in decline, and those further south are increasing in season length and abundance (Reid *et al.*, 1998). The spreading of relatively cold waters from the Arctic is a likely cause for the phytoplankton decline in the north North Atlantic (Reid *et al.*, 1998), and the increase further south in the North Atlantic could be due to a decline in abundance of the herbivorous calanoid copepod *Calanus finmarchicus* (Beaugrand, 2009; Hinder *et al.*, 2014). Phytoplankton spring blooms in the North Atlantic are the most pronounced of any open ocean region (Ueyama and Monger, 2005). For this reason it is believed that phytoplankton, due to their photosynthetic capabilities, are the main biological drivers of surface pCO_2 and carbon flux variability in this region (Takahashi and Sutherland, 2002).

1.3.1 Phytoplankton taxonomic groups

The two most abundant phytoplankton taxonomic groups in the North Atlantic are diatoms and dinoflagellates, with the classic North Atlantic bloom consisting of a diatom bloom in the spring followed by a summer and late autumn bloom of dinoflagellates and smaller phytoplankton species, such as coccolithophores (Henson *et al.*, 2012; Hopkins *et al.*, 2015) (figure 1.14).

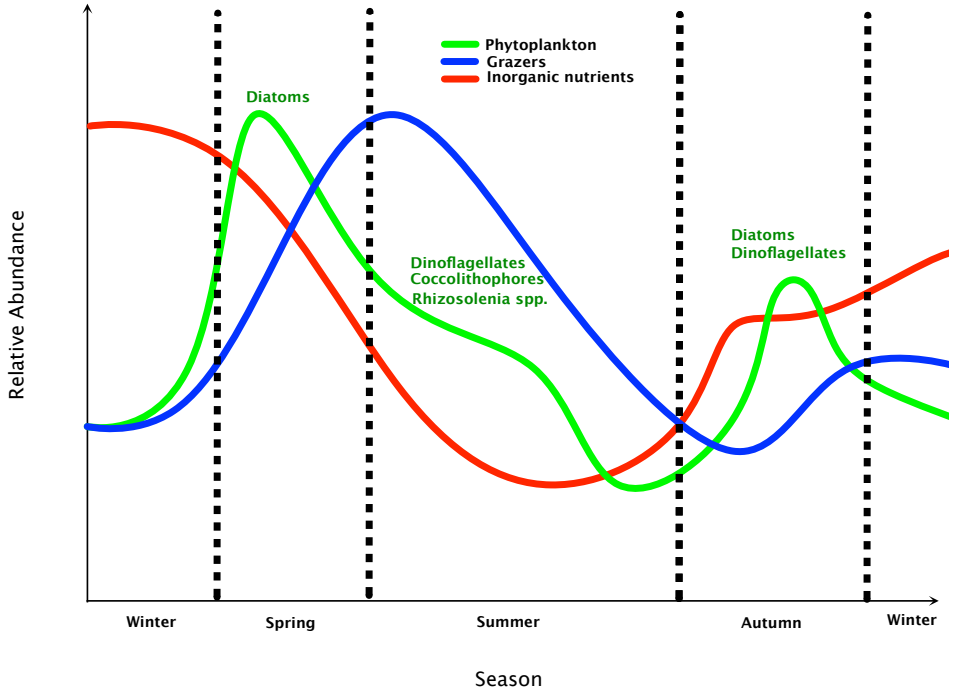

Figure 1.14: Schematic of the typical seasonal changes in the relative abundance of phytoplankton (green), grazers (blue), and inorganic nutrients (red) within the surface waters of the North Atlantic. Green text indicates the dominant phytoplankton taxonomic groups. Adapted from Kaiser *et al.* (2005).

This succession is mainly driven by the availability of light and nutrients, and the life-strategies of different taxonomic groups enabling them to bloom under differing environmental conditions. Diatoms can generally bloom before other phytoplankton because of their relatively fast growth rates in nutrient rich turbulent waters (typical of spring time, see figure 1.14) (Margalef, 1978). Dinoflagellates and other smaller phytoplankton species are able to bloom under relatively poor nutrient conditions due to a range of characteristics including; mixotrophy (both autotrophic and heterotrophic capabilities), high nutrient uptake and low growth rates relative to diatoms, and the presence of flagella (providing motility) (Henson

et al., 2012). Coccolithophores are thought to adopt a life-strategy between the two extremes of fast-growing diatoms and dinoflagellates (Margalef, 1978; Hopkins *et al.*, 2015). *Rhizosolenia* spp. are a family of diatoms that generally bloom slightly later than the spring-blooming diatoms because they can form algal mats that undergo vertical migrations to exploit nutrients at deeper depths. They do this through changes in buoyancy (Villareal *et al.*, 1993). Laboratory experiments indicate that this buoyancy regulation is controlled via rapid changes in the ion concentration within the vacuole sap of diatoms (Woods and Villareal, 2008). Kemp *et al.* (2006) suggest that the large algal mats formed at depth by *Rhizosolenia* spp. may have important implications for carbon export.

1.3.2 Seasonal variation

During late winter in the North Atlantic, sea surface pCO_2 and nutrient levels are relatively high due to strong vertical mixing bringing deep water to the surface (figure 1.14). As spring approaches and sea surface temperatures increase, this leads to stratification of the water column and higher irradiance, allowing phytoplankton to bloom (reaching chl-a concentrations of up to 10 mg m^{-3} (Shutler *et al.*, 2011)), thus decreasing both nutrient and pCO_2 levels. Towards the end of the summer months, nutrient levels become depleted, as stratification is too high to allow any influx of nutrients from below the thermocline, reducing the photosynthetic activity. During autumn a small phytoplankton bloom occurs as the thermocline breaks down and the mixed layer depth increases allowing for nutrient entrainment (Martinez *et al.*, 2011) (figure 1.14). Thus a small decrease in sea surface pCO_2 would be expected. Seasonal increases in phytoplankton in the subpolar North Atlantic predominantly occur during the spring, but in the subtropical North Atlantic regions this bloom occurs between autumn and winter (Ueyama and Monger, 2005). This seasonal variation shows strong correlation with stratification of the upper ocean surface, which is related to sea surface temperature. It is therefore expected that with increasing SST, increased stratification is likely to decrease primary productivity in regions that are already permanently stratified

(tropical regions) (Behrenfeld *et al.*, 2006). However, in regions where strong mixing can limit primary production due to light limitation (subpolar), an increase in stratification can stimulate primary production (Beaugrand, 2009).

The seasonal cycle of phytoplankton productivity can also be influenced by climate modes such as the NAO. Henson *et al.* (2012) demonstrated that at the PAP site during negative NAO phases the dinoflagellate bloom is increased to two-fold the long-term mean, while diatom abundance is decreased relative to the long-term mean. During positive NAO phases both phytoplankton groups have lower peak abundances than the long-term mean, and diatom abundance is greater than dinoflagellate abundance. This may be due to the decreased mixing during negative NAO phases because of decreased Westerly winds (Henson *et al.*, 2012). This reduces the nutrient concentration in the surface waters, allowing dinoflagellates to out-compete diatoms when the Si:N ratio decreases. Whereas during positive NAO and therefore high mixing conditions, diatoms are able to out-compete other phytoplankton groups due to their relatively quick growth rates (Henson *et al.*, 2012). This may have implications for the amount of carbon exported, as larger phytoplankton cells are thought to have a higher transport efficiency than smaller cells (Kemp *et al.*, 2006). However Henson *et al.* (2012) found that there were greater volumes of POC (up to $\sim$15 mL m^{-2} d^{-1}) within a sediment trap at 3000 m at the PAP site when dinoflagellates were more abundant than diatoms. This highlights the need for further investigation into phytoplankton dynamics within the North Atlantic and the possible implications they may have for carbon uptake and export.

1.3.3 Interannual variation

Lozier *et al.* (2011) used satellite data and *in situ* time-series data from BATS to demonstrate that in the North Atlantic subtropical gyre, although primary production is strongly linked with upper ocean stratification on a seasonal time scale there is little to no correlation on interannual time scales. The interannual variability seen in primary production in the North Atlantic is thought to be due to a number of variables including the strength of local and remote wind and buoyancy forcing,

as well as the supply of nutrients to the surface waters. Therefore strong interannual variability in the air-sea fluxes, winds, and formation of water masses over the North Atlantic (Marshall *et al.*, 2001) are likely to influence the interannual variation seen in stratification and thus the interannual variation of primary production in this region. The major mode believed to link to this interannual variability of phytoplankton production in the North Atlantic is the NAO, impacting on the local wind-driven mixing conditions (Henson *et al.*, 2009). Using CPR data Barton *et al.* (2015) found that there are significant correlations between phytoplankton assemblages and the physical environment (SST, total heat flux, wind speed, mixed layer depth, and stratification) on seasonal timescales in the North Atlantic, however these relationships were also not present when analysed on interannual and decadal timescales. Barton *et al.* (2015) suggest that this is due to the year-to-year variability in phytoplankton assemblages being greater than the variability in the physical drivers, suggesting that larger scale physical mechanisms (that are currently poorly understood) such as ocean circulation, may play an important role in longer-term phytoplankton trends.

1.3.4 Decadal variation

Henson *et al.* (2009) used time series of modelled decadal (1959-2004) variability in bloom timing and found that within the subtropical North Atlantic region there were no decadal long-term trends. However the North Atlantic subpolar region showed distinct decadal-scale periodicity. This periodicity was shown to be correlated with the NAO index. The timing of the phytoplankton bloom in the subpolar North Atlantic is influenced by the NAO because during positive NAO phases the surface mixed layer is deepened by stronger westerly winds, which delays the onset of the spring bloom by $\sim$2-3 weeks (Henson *et al.*, 2009). In the eastern North Atlantic the spring blooms during the early 2000s (positive NAO) showed higher abundance as well as range expansion further south than in the 1980s (negative NAO), and the autumn bloom occurred 1 month later in the 2000s than in the 1980s (Martinez *et al.*, 2011). This demonstrates the influence that a positive NAO phase has. In the 2000s stronger wintertime winds induced deeper mixing

which allows for more nutrient uplift, but also delays the onset of the phytoplankton blooms as stratification of the surface layer occurs later. Harris *et al.* (2013) highlight the importance of natural oscillations with respect to changes in the abundance of different plankton groups, with diatom abundance being primarily driven by the Atlantic Multidecadal Oscillation (AMO, climate mode based on de-trended North Atlantic SST (Enfield, 2001)) in the North Atlantic. This demonstrates the importance of long-term datasets as natural oscillations can complicate the influence of climate change and make it difficult to determine any long-term trends.

1.4 Conclusion

The links between variables that can influence the uptake of CO_2 in the North Atlantic such as temperature, stratification, biological responses, wind and buoyancy forcing are clearly complex. A major limitation of current biogeochemical models is that they struggle to consider the full complexity of the ecosystem, and are often lacking *in situ* data. Therefore when making conclusions from such models it is important to do so with caution (Beaugrand, 2009). It is vital that *in situ* data continue to be collected, and opportunities such as the use of volunteer observing ships are put into practice on a global scale in order to enhance the network of available datasets, and improve our understanding further.

The North Atlantic variability in the flux of CO_2 needs to be measured alongside phytoplankton indices to elucidate the contribution that changes in the climate, and the plankton, are having on the North Atlantic carbon uptake (Hays *et al.*, 2005; Schuster and Watson, 2007; Schuster *et al.*, 2009b). Alongside these changes, the different estimates of long-term trends and inter-annual variability of the North Atlantic carbon sink between studies, highlight the need for further investigation (Schuster *et al.*, 2013; Landschützer *et al.*, 2013). This thesis aims to address these uncertainties and investigate the variability in carbon uptake in the North Atlantic by combining different biochemical measurements made from volunteer observing ships with modelled output and process studies.

1.5 Aims

The aim of this thesis is to explore the relationships between phytoplankton taxonomic groups and sea-surface carbon dioxide within the North Atlantic. This thesis will also examine how plankton biological processes (such as photosynthesis, respiration, calcification) inter-link with the carbonate chemistry of the surface ocean and will use a range of statistical methods to analyse such links.

1.6 Objectives

Specific objectives within the over-arching aim of this thesis are as follows:

1. Evaluate the regional and temporal variability in phytoplankton taxonomic group abundance and distribution within the North Atlantic over the past $\sim$50 years.

2. Quantify the plankton net community production of temperate to subtropical regions within the North Atlantic.

3. Determine the total alkalinity to salinity relationship in the North Atlantic.

4. Examine seasonal carbonate measurements to investigate biogeochemical processes that may be occurring in the North Atlantic.

5. Investigate the flux of carbon dioxide in the northeast Atlantic in relation to phytoplankton distribution and abundance on seasonal, inter-annual and decadal time scales.

1.7 Thesis structure

Chapter 2 outlines the analytical methods used within the study to measure phytoplankton abundance, dissolved inorganic carbon and total alkalinity, dissolved oxygen and pCO_2.

The data chapters (3 to 6) aim to address the five objectives above. They are self-contained, so each include a short introduction and methods section to maintain readability and avoid repetition. Chapter 3 uses the latest long-term data

available for phytoplankton in the North Atlantic from the Continuous Plankton Recorder (CPR) to determine trends in phytoplankton abundance within the study region on seasonal, inter-annual and decadal time scales [objective 1]. Chapter 4 describes two methods used to calculate net community production (NCP), and therefore the metabolic state, from a volunteer observing ship (VOS) that traverses the North Atlantic between Portsmouth (UK) and the Caribbean [objective 2]. Using discrete dissolved inorganic carbon (DIC) and total alkalinity (TA) data, chapter 5 aims to define the TA/salinity relationship [objective 3]. The carbonate measurements are then compared with phytoplankton data from both satellite and the CPR dataset [objective 4]. Chapter 6 combines the two datasets of CO_2 and phytoplankton abundance to investigate how changes in abundance and distribution of phytoplankton taxonomic groups may be influencing the sea-surface pCO_2 and the air-sea flux of CO_2 [objective 5].

The final chapter (7) provides a summary of the key findings, and discusses the wider implications, limitations, and possible ways to extend the research in the future.

Chapter 2

Analytical methods

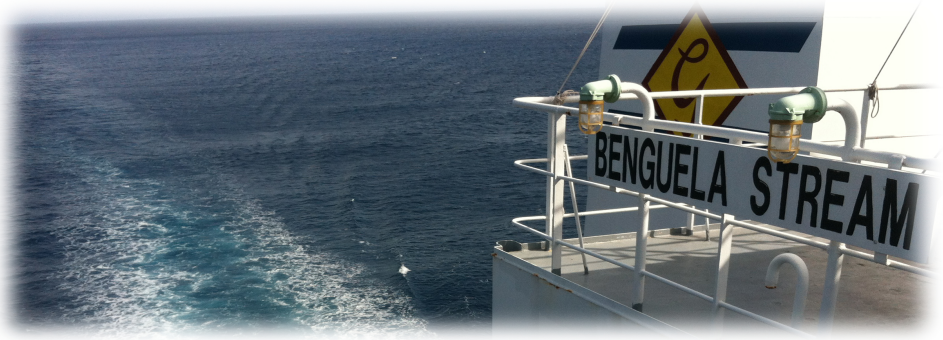

Each data chapter (3 to 6) contains a brief description of the analytical methods used in the chapter and detailed data-handling and statistical methodologies. Chapter 2 gives details of the chemical analytical methods and sampling procedures used within this study.

2.1 The Continuous Plankton Recorder

The Continuous Plankton Recorder (CPR) was first deployed in 1931 by Sir Alistair Hardy. The design is simple and robust, which has allowed the CPR methodology to remain consistent through time. The Sir Alister Hardy Foundation for Ocean Science (SAHFOS), based in Plymouth, UK, is an international charity that operates the CPR survey.

The CPR is towed within the mixed layer at a depth of ~6.5 m from the stern of volunteer ships of opportunity (VOS), and research vessels (Hays, 1994). Due to the wash created from the vessels, the water sampled incorporates the top 0 to ~20

m of surface water (Hunt, 1968). Water enters the CPR through the entrance aperture (see figure 2.1) where it passes through a silk mesh with a mesh size of 270 μm. This mesh size was chosen in order to collect the larger phytoplankton and zooplankton, without the complication of clogging from smaller plankton. However smaller plankton are maintained on the silk, particularly the colonizing species (i.e. chain forming and globular), and so are counted and included in the CPR survey (Hays, 1994). The mesh is wound on by a propeller that is turned by the flow of the seawater, at a consistent rate controlled by a drive shaft and gear system (Richardson *et al.*, 2006). The filtered plankton are sandwiched between another silk, and rolled up into a storage compartment containing formalin to preserve the samples.

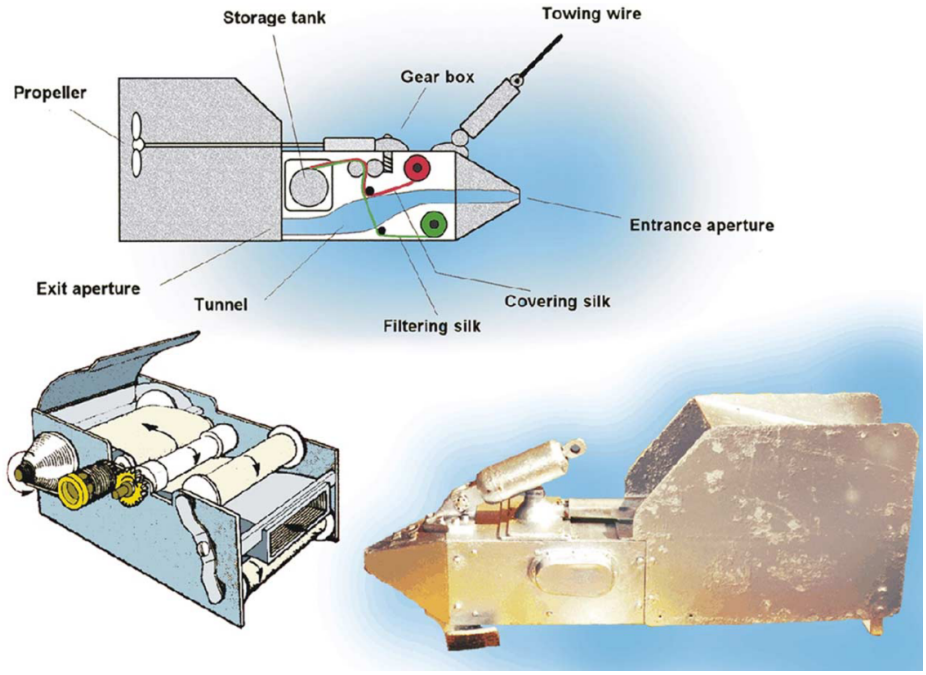

Figure 2.1: Cross-section of the CPR, the internal mechanism, and a photograph of the CPR body. Reproduced from Richardson *et al.* (2006).

On return to the laboratory the CPR silk is divided into samples representing 10 nautical miles of tow. Before carrying out the counts of plankton within a CPR sample the Phytoplankton Colour Index (PCI) is estimated using a green colour chart (level of greenness is estimated), which gives an indication of the phytoplankton abundance within the sample. This method has remained unchanged since 1946. PCI has been validated through comparisons with satellite chlorophyll estimates, and even used to bridge the time gap between different satellite missions

(Raitsos *et al.*, 2014).

The initial count from the CPR silk is based on a visual count of all zooplankton within each CPR sample that are > 2 mm, all of which are identified and counted. A 1/10,000 subset of the CPR sample is then taken and all species of plankton are identified within 20 fields of view to give an accepted value (Poisson distribution assumes plankton randomly distributed on the silk (Colebrook, 1975)), and multiplied by 10,000 to give an abundance estimate for each species identified within the CPR sample ($450\times$ magnification, using Watson Bactil microscopes). For more detailed descriptions of the CPR methodology see Warner and Hays (1994) and Richardson *et al.* (2006).

Due to the relatively large mesh-size of the CPR it is likely that the CPR under-samples many of the smaller phytoplankton species, and can only be considered a semi-quantitative measure of plankton abundance. However despite the semi-quantitative nature of the CPR, the samples are considered adequate to give a consistent estimate of the *in situ* taxa within a region, and reflects the seasonal and inter-annual patterns of the plankton well (Richardson *et al.*, 2006). When analysing CPR data it is advised to use spatial and temporal averages due to the biases associated with zooplankton behaviour such as diel vertical migration, and active avoidance (Hays, 2003), and due to the sparsity of sampling routes within certain regions (Richardson *et al.*, 2006). The CPR standard areas divide the sample routes into shelf regions and regional seas. These are roughly 10°longitude by 10°latitude in size, which is considered a trade-off size between having enough CPR samples within an area to obtain an average without compromising the spatial variability (Richardson *et al.*, 2006). The CPR dataset is the largest plankton database in the world, with international projects and routes being added and extended to gain further global coverage.

2.2 Sampling from the *MV Benguela Stream*

The *MV Benguela Stream* is one of the VOS that tows a CPR. It maintains the "B-route" (SAHFOS defined CPR route) going from 40 °W to 1 °W on a monthly basis (red track in figure 2.2). The CPR data used in this thesis were provided

by SAHFOS, and can be found at DataCite doi:10.7487/2014.44.1.10 (SAHFOS, 2014).

Discrete samples for dissolved oxygen, dissolved inorganic carbon (DIC), and total alkalinity (TA) were collected during 4 field campaigns on the *MV Benguela Stream*. This VOS operates between Portsmouth and the Caribbean Islands completing one return voyage every month (yellow track in figure 2.2). The 4 voyages during which samples were collected were April/May 2012 (BS056 - Spring), June/July 2012 (BS058 - Summer), September/October 2012 (BS062 - Autumn) and January/February 2013 (BS066 - Winter). Samples were collected on the spring and winter voyages by Peter Landschützer, and on the summer and autumn voyages by Clare Ostle.

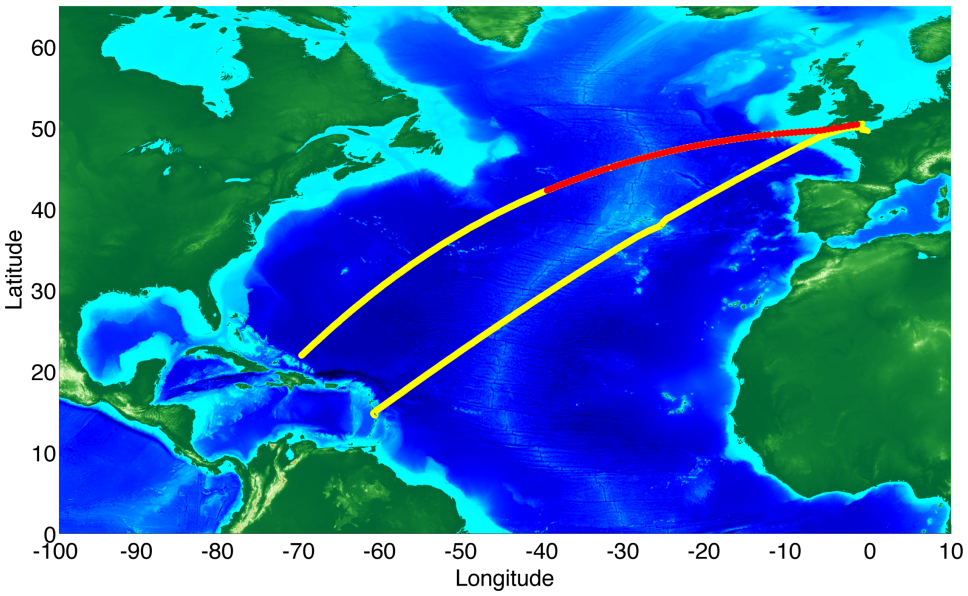

Figure 2.2: Map of the North Atlantic showing a typical *MV Benguela Stream* monthly cruise track = yellow, and the continuous plankton recorder (CPR) tow route from 40 °W (CPR B-route) = red.

Nutrient and salinity samples are collected by the crew on board the *MV Benguela Stream* every four and twelve hours respectively. These samples were analysed at the National Oceanography Centre (NOC) Southampton, using a SEAL Auto-Analyzer (Grasshoff *et al.*, 1999) and a Guildline Autosal salinometer (8400B). Silicate, phosphate and nitrate plus nitrite (NO_x) were determined following the procedures of Hansen and Koroleff (2007) (the accuracies of these measurements are given in table 2.1).

2.3 Dissolved Oxygen

An *Aanderaa* oxygen/temperature optode (model 3835) is permanently installed on the *MV Benguela Stream*. The optode works based on a principle called 'dynamic luminescent quenching'. Ambient oxygen acts as the quenching agent, and depending on the intensity and duration of red luminescence emitted after being excited by a blue-green light, the absolute oxygen concentration can be determined (Aanderaa Data Instruments, 2007). A special platinum porphyrin complex is embedded in a gas permeable foil which equilibrates with the surrounding seawater and acts as the fluorescent indicator. This foil is excited by modulated blue-green light (505 nm), and the phase of any red luminescence emitted after excitation is measured by a photodiode in the same window to give the oxygen concentration (Körtzinger *et al.*, 2005). The optode is programmed to take a reading every minute, which is logged on an onboard computer. Each month the raw data are returned to shore, where they undergo a quality control routine in which the data are corrected for salinity using calculated salinity from the conductivity probe (corrected to salinity samples collected every 12 hours) and salinity compensation equations taken from the *Aanderaa* operating manual (Aanderaa Data Instruments, 2007).

Winkler analysis (Winkler, 1888) was used to determine the concentration of oxygen in surface seawater samples and these were used to correct the optode for drift. This is an iodometric titration in which oxygen in the seawater sample quantitatively oxygenates iodide ions to form iodine. This is a multi-step oxidation, using manganese as a transfer medium (Grasshoff *et al.*, 1999).

The automated Winkler titration was undertaken using a Metrohm 765 Dosimat Titrino, and the end point is detected photometrically from the iodine colour itself (Williams and Jenkinson, 1982). Depending on sampling technique and titration method, Winkler titrations can give results that typically, within fieldwork conditions, have a precision ranging from 0.015 to 0.7% (del Giorgio and Williams, 2005). Throughout our analysis the sodium thiosulphate titrant was calibrated every 24 hours with 0.1N potassium iodate using 10 replicates that gave a SD of 0.0001. The potassium iodate was then corrected using a 0.01 N standard solution

potassium iodate (Wako Pure Chemical Industries, Ltd., Osaka, Japan). Over 8 hours (roughly the time it takes to analyse the samples from one voyage) the thiosulphate concentration was measured 3 times using the 0.01 N potassium iodate (Wako Pure Chemical Industries, Ltd., Osaka, Japan), giving a standard deviation in the thiosulphate concentration of 0.00027, which at an oxygen concentration of 280 μmol kg^{-1} at 15°C equates to a difference of 0.3659 μmol kg^{-1}. This is a maximum difference of 0.1%.

The surface seawater collected for Winkler analysis was taken directly from the ships' sea inlet using hydrostatic flow, minimising any temperature fluctuations from the surrounding environment (Cooper *et al.*, 1998). The inlet is at 3 to 5 m below the sea surface depending on cargo loading (Schuster and Watson, 2007). The seawater passes through a coarse strainer (1 mm), which was cleaned daily, before entering a T-piece with Tygon tubing attached in order to adequately control the flow into the sample bottle and check for bubbles within the tubing. Two 125 ml replicate oxygen samples were collected every two hours during the day on the return voyage. This was done by rinsing the bottle and lid with sample water and allowing the bottle to overflow $\sim$ 4 times while rotating the bottle and checking for bubbles. The sample temperature was recorded at the time of sampling, and again just before the reagents were added, in order to correct for any changes in volume due to temperature changes (Bell and Johnson, 1997). Salinity was also recorded. To fix the samples, 1 ml of $MnSO_4$ was added, followed by 1 ml of NaI+NaOH.

The manganese (II) precipitates as hydroxide:

$$Mn^{2+} + 2OH^- \rightarrow Mn(OH)_2 \tag{2.1}$$

The dissolved oxygen becomes chemically bound as the precipitate oxidises to form manganese (III) hydroxide:

$$2Mn(OH)_2 + \frac{1}{2}O_2 + H_2O \rightarrow 2Mn(OH)_3 \tag{2.2}$$

After replacing the lid and taking note if any bubbles were formed during this process, the sample was then shaken for 1 minute. After mixing the sample, the

oxygen fixes rapidly as manganese (III) hydroxide, forming a brown/whitish precipitate that sinks to the bottom of the sample bottle and remains fixed in the alkaline medium.

Due to space restrictions on board the ship the fixed sample was then stored underwater to prevent evaporation until it could be analysed within the laboratory at UEA. In order to validate this method of storage for our samples, a preliminary longevity experiment was carried out. A 20 litre water sample was decanted into 45 replicate 125 ml sample bottles. The samples were fixed, stored underwater, and analysed over a period of 36 days. Three replicate samples were analysed after 24 hours (this is within the usual time of sample storage (Knap *et al.*, 1996)) giving an average oxygen concentration of 240.28 μmol kg^{-1} with a SD of 0.15 μmol kg^{-1}. The remaining 42 replicates were analysed over the 36 day period and remained within this SD of the initial mean oxygen concentration (figure 2.3). The difference between the average oxygen concentration within the first 24hrs and over the 36 days was 0.006 μmol kg^{-1}. Oxygen concentrations were plotted against time, giving a regression of 0.00005 μmol kg^{-1} per day. This allowed us to be confident that storing the samples underwater for a period of less than 36 days would have a minimal effect on the measured oxygen concentrations to less than 0.002 μmol kg^{-1} of oxygen.

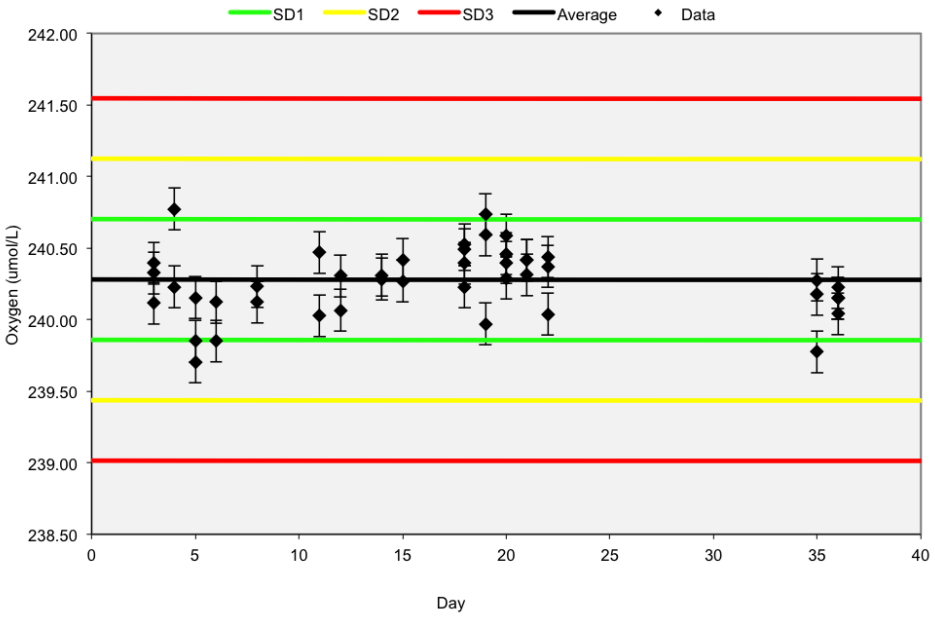

Figure 2.3: Oxygen concentration of replicate samples stored underwater against time in days (black diamonds). Black line = average oxygen concentration of 3 replicates after 24 hours, green lines = 1 standard deviation between initial replicates, yellow lines = 2 standard deviations between initial replicates, red lines = 3 standard deviations between initial replicates.

Zhang *et al.* (2002) found that this method of storage gave a $100.27\% \pm 0.3\%$ recovery of dissolved oxygen concentration over a period of 4 months and it also acts to reduce the impact of any temperature fluctuations in the surrounding environment. During our field campaigns dissolved oxygen samples for Winkler analysis were only collected on the return crossing of each voyage and analysed after returning from each voyage. Therefore the longest a sample would be stored before being analysed was 12 days.

Upon return to the laboratory the samples were analysed by adding 1 ml of 10 N sulphuric acid before titrating the sample with thiosulphate. The sulphuric acid causes the precipitated hydroxide to dissolve, freeing the manganese (III) ions. These manganese (III) ions oxidise with the previously added iodide ions from the fixing reagents to form iodine and manganese (II) ions:

$$2Mn(OH)_3 + 2I^- + 6H^+ \rightarrow 2Mn^{2+} + I_2 + 6H_2O \tag{2.3}$$

The surplus iodide ions react with the iodine to form a 3 iodine atom complex with a single negative charge:

$$I_2 + I^- \leftrightarrow I_3^- \tag{2.4}$$

This complex has a low vapour pressure (in comparison to molecular iodine) and decomposes readily if iodine is removed. The iodine is then titrated with thiosulphate, which reduces the iodine to iodide and oxidises the thiosulphate to form tetrathionate ions:

$$I_3^- + 2S_2O_3^{2-} \rightarrow 3I^- + S_4O_6^{2-} \tag{2.5}$$

1 mole of oxygen is equivalent to 4 moles of thiosulphate. However as mentioned earlier thiosulphate is not a primary standard as it deteriorates slowly. This is why it was calibrated with the potassium iodate standard. The calculated combined accuracy of measuring dissolved oxygen concentration in this study was $\pm 2.8\%$ (table 2.1).

2.4 Dissolved Inorganic Carbon and Total Alkalinity

Dissolved inorganic carbon (DIC) is defined as:

$$DIC = [CO_2^*] + [HCO_3^-] + [CO_3^{2-}] \tag{2.6}$$

Where $[CO_2^*]$ is the total concentration of all unionized carbon dioxide, which includes H_2CO_3 as well as CO_2 (Dickson *et al.*, 2007).

"The Total Alkalinity (TA) of a sample of seawater is defined as the number of moles of hydrogen ion equivalent to the excess of proton acceptors (bases formed from weak acids with a dissociation constant K $\leq$ 10 to 4.5 at 25°C and zero ionic strength) over proton donors (acids with K $>$ 10 to 4.5) in 1 kilogram of sample" (Dickson *et al.*, 2007).

DIC and TA samples were collected every 2 hours during daylight hours and immediately preserved following the standard operating procedure (SOP) outlined by Dickson *et al.* (2007). The first sample of the day was a 500 ml sample, which was used to assess the standard deviation between within bottle replicates, while

the remaining samples were 250 ml. The same sampling tubing was used for collecting DIC and TA samples as when collecting dissolved oxygen samples (see section 2.3), and the bottles were rinsed and filled in the same manner. The lids of the bottles were replaced after filling, to prevent any gas exchange while transporting them to be fixed. The samples were fixed within a minute of sampling by first removing 1% of the volume of water and then adding 50 μl of mercuric (II) chloride to the 250 ml bottles, or 100 μl of mercuric (II) chloride to the 500 ml bottles, following Dickson *et al.* (2007). The lids were then wiped and greased before being placed in the sample bottles, and held in position with rubber bands and cable ties to prevent any leakage or gas exchange before being stored in the dark. The mercuric (II) chloride acts to kill any plankton within the sample water, while preserving the carbon speciation, therefore preventing any change between organic and inorganic carbon within the sample.

The samples were analysed on return to the laboratory (within 6 months) using two VINDTA 3C (**V**ersatile **IN**strument for the **D**etermination of **T**otal inorganic carbon and titration **A**lkalinity) instruments, which combine an acid titration to determine TA and a coulometric titration to determine DIC (Mintrop, 2011).

Both the seawater sample and the cell are maintained at a relatively constant known temperature of $\sim$25°C using a thermostated circulator, and water bath. To measure TA a known volume of seawater is dispensed into a water-jacketed cell, where acid is titrated into the sample at increments of 150 μmol kg^{-1} using a motor-driven piston burette. The acid solution is made up of 0.1 M hydrochloric acid and enough sodium chloride solution (0.7 mol kg^{-1}) to give an approximate background equal to the ionic strength of seawater in order to maintain a constant activity of coefficients within the solution during the titration (Mintrop *et al.*, 2000).

A pH meter (Brinkman model Titrino, readable to 0.1mV) monitors the titration using a proton sensitive electrode within the cell, and the titration is stopped after the total amount of acid added reaches 4.2 ml. A non-linear least squares approach of plotting volume of acid added against electromotive force (EMF), is used to calculate TA from titration data past the carbonic acid end-point of $\sim$ 4.5 pH (see figure 2.4). The results are displayed both graphically and numerically within

LabVIEW (National Instruments v6.1). The end-point has to be accurate with a precision of ± 1 μmol kg^{-1} so is therefore calculated mathematically (Schuster *et al.*, 2009a; Mintrop, 2011).

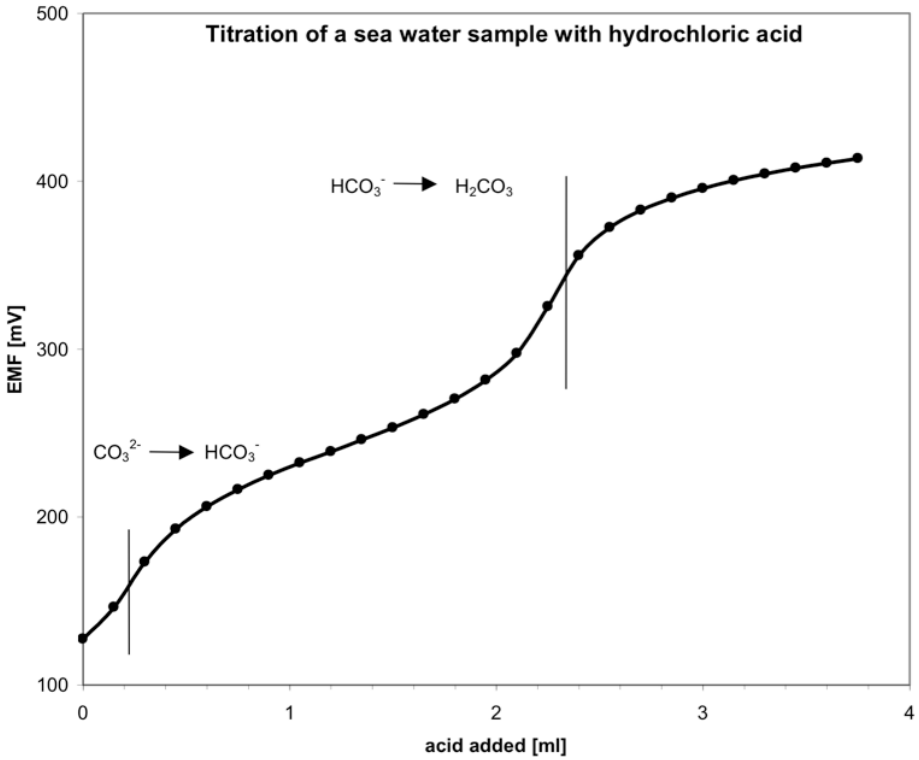

Figure 2.4: Typical titration curve from a seawater sample, showing the volume of acid added against the electromotive force (EMF). Reproduced from Mintrop (2011).

To measure DIC a known volume of seawater sample is dispensed into the stripping chamber, where it is acidified with 8.5% reagent grade phosphoric acid to convert all carbonate species to free CO_2. Pure nitrogen (N_2) gas that has run through a column of CO_2 absorbent is bubbled through a fine frit at the bottom of the stripping chamber to ensure that the sample is stripped of CO_2. The N_2 gas acts as an inert carrier gas for the evolved free CO_2. This then passes through a Peltier cooling system to condense any water vapour, and an absorbent chamber filled with magnesium perchlorate, before bubbling through the coulometer cell. Within the coulometer cell the CO_2 in the gas stream is absorbed by the cathode solution which contains a mixture of water, tetra-ethyl-ammonium bromide, ethanolamine, dimethylsulfoxide (DMSO) and thymolphthalein indicator. The side arm of the coulometer cell contains anode solution, which consists of a mixture of saturated

potassium iodide in water and DMSO (Dickson *et al.*, 2007). The reaction between the CO_2 and ethanolamine produces hydroxyethylcarbamic acid. This reaction causes a change in pH and therefore a colour change (blue to colourless) due to the thymolphthalein indicator in the solution which is measured using transmittance at ~ 610 nm. In order to maintain the transmittance of the solution at a constant value of 29% (and therefore a constant colorimetrically defined pH), hydroxide ions are generated at the platinum cathode by electrolysing water, for which the electrons required are generated at the silver anode. This generated current is related by the Faraday constant to the moles of CO_2 absorbed by the solution (Johnson *et al.*, 1993). When the DIC cpm (counts per minute) reach a set end-point threshold of below 50 cpm, the VINDTA 3C stops running and the sample results are recorded within Visual Basic (Microsoft v6.0), calculating DIC within the sample following Dickson *et al.* (2007):

$$DIC = \frac{N_s - b \times t - a}{c} \times \frac{1}{V_s \times \rho} \tag{2.7}$$

Where N_s is the coulometer reading for the sample (counts), a is the acid blank (counts, as the acid is added to the extraction cell and then stripped of CO_2 before analysis $a = 0$), b is the background level of the system (counts min^{-1}), c is the coulometer calibration factor (counts mol^{-1}, this is calculated using a calibration from Certified Reference Material (CRM)), t is the time it took to measure the sample (min), V_s is the volume of sample at the temperature of use (dm^3), and ρ is the density of the seawater sample (g cm^{-3}).

To improve the accuracy further, two minor corrections can be applied for the dilution due to the addition of mercuric chloride, and the exchange of CO_2 within the headspace of the sample. However these corrections are likely to be less than 0.5 μmol kg^{-1} (Dickson *et al.*, 2007).

CRMs were used to assess the accuracy of both of the VINDTA instruments. These are 500 ml samples of a known concentration of DIC and TA obtained from Scripps Oceanographic Institute, San Diego, USA.

The instruments were stabilized by first analysing "junk" seawater samples, and then running a CRM before running the seawater samples, and then another

CRM at the end of the day. The known CRM values are then compared with the measured CRM values for instrument calibration, and if necessary this can be used to apply an acid correction to all of the TA measurements on that instrument. The standard deviation between CRMs was also used as an indicator of accuracy. The accuracy calculated for DIC and TA was ± 2.55 μmol kg^{-1} and ± 1.46 μmol kg^{-1} respectively (table 2.1). The difference between within bottle replicate samples (500 ml) gave an indication of the precision. If replicates were > 1 μmol kg^{-1} (the uncertainty of the 3C VINDTA (Mintrop, 2011)) apart, then the analysis was halted and 500 ml "junk" seawater samples were run until the instrument consistently gave better precision. When processing the DIC and TA measurements the World Ocean Circulation Experiment (WOCE) flagging system was applied, whereby 2 represents good data, 3 likely bad data, 4 bad data, and an additional flag of 9 for missing data (this flag is not included in the WOCE flagging system). Through this process six DIC measurements were assigned a flag of 4, and one 9, and four TA measurements were assigned a 4, and eight were flagged as 9. The remaining data points were assigned a flag of 2, totalling 382 DIC measurements and 377 TA measurements collected between April 2012 and February 2013.

2.5 Underway measurements of pCO_2

Marine air and sea surface pCO_2 are measured on board the *MV Benguela Stream* using the set-up as described by Schuster and Watson (2007). The pCO_2 analyser used is a LI-COR model LI-7000 which is a differential, non-dispersive, infra-red (NDIR) gas analyser (LI-COR, 2007). The accuracy of this system is less than 1 μatm (Dickson *et al.*, 2007). The LI-COR detector measures CO_2 based on the difference in absorption of infra-red radiation through two gas sampling cells. One of the sampling cells is used as a reference cell, in which a standard gas with a known concentration of CO_2 passes through, while the other cell is the sample cell used for the sample gas. Infra-red radiation is emitted and passed through each cell path, and the resulting radiation is measured by detectors and used to calculate the absorption. The higher the absorption of infra-red, the higher the concentration of CO_2 in the gas. CO_2 dry mole fractions (xCO_2) of the gas are calculated and

recorded by the analyser using the following gas law, which is dependent on the number of moles of CO_2 in the cell (nCO_2):

$$n(CO_2) = \frac{x(CO_2) \times p \times V(cell)}{R \times T} \times \phi \tag{2.8}$$

Where ϕ is a constant that accounts for the non-ideality of the gas phase, R is the universal gas constant, and p, T and $V(cell)$ are the pressure and temperature of the gas, and volume of the sample cell respectively (Dickson *et al.*, 2007).

As this system can only measure CO_2 in the gas phase, the seawater from the underway system passes through a closed air-loop equilibrator which contains raschig rings that create a large surface area for CO_2 exchange to occur between the seawater and air (Cooper *et al.*, 1998), and the air is pumped off to the Li-COR (see figure 2.5). The gas is circulated through the equilibrator and LI-COR for about 30 minutes until equilibrium is reached. During this routine the system takes readings approximately every minute. The LI-COR system has a built-in pressure transducer to make corrections for any changes in barometric pressure (LI-COR, 2007). To calculate the partial pressure of CO_2 in the dry gas ($p(CO_2)_{dry}$) the corrected sample value of x(CO_2) (corrected using standard known concentration gases) is multiplied by the equilibrator pressure (P_{eq}) from the time of equilibration (Dickson *et al.*, 2007):

$$p(CO_2)_{dry} = x(CO_2) \times P_{eq} \tag{2.9}$$

The gas measured inside the analyser is dry whereas inside the equilibrator it is assumed to be at 100% humidity (Pierrot, 2009). Therefore a correction using water vapour pressure is applied to the CO_2 dry mole fraction calculations, given by:

$$p(CO_2)_{wet} = x(CO_2) \times [P_{eq} - VP(H_2O)] \tag{2.10}$$

In which $VP(H_2O)$ is the water vapour pressure over a seawater sample of a given salinity at the temperature of equilibration (Dickson *et al.*, 2007).

Marine air is sampled from an air inlet on the port side of the upper deck, and

is also run through the LI-COR for 30 minutes, with measurements being recorded approximately every minute (figure 2.5).

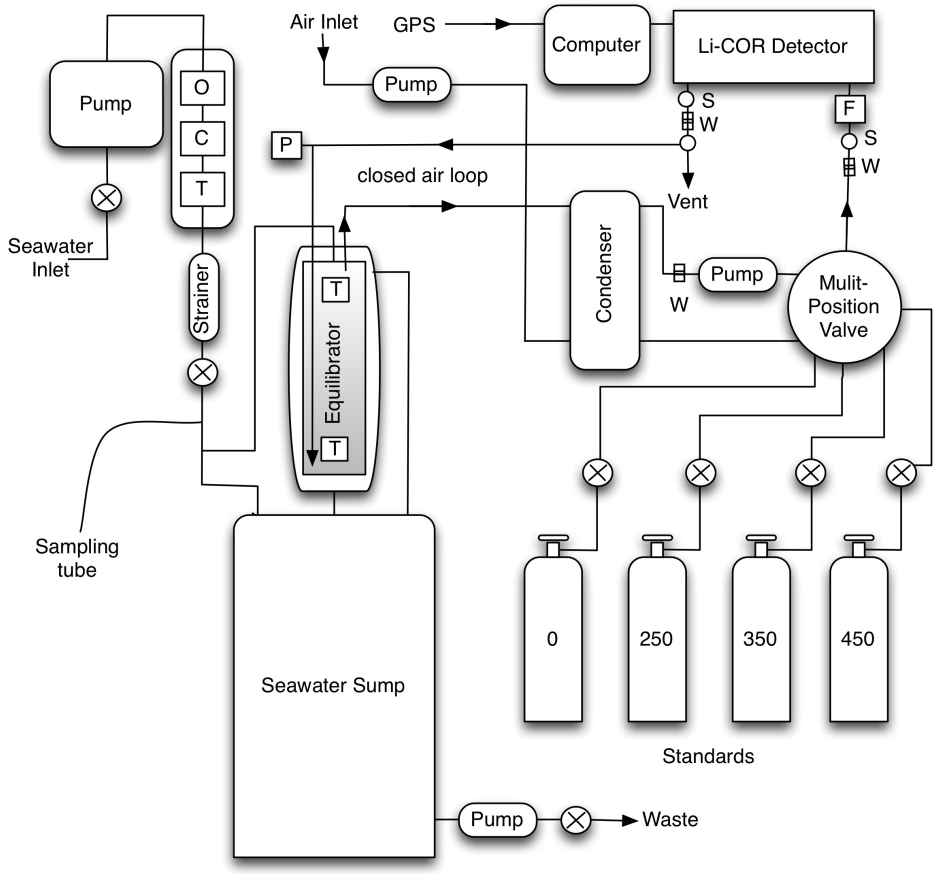

Figure 2.5: Schematic of the underway measurement system aboard the *MV Benguela Stream*, updated from Cooper *et al.* (1998) and Landschützer (2014). Sensors are labelled O for oxygen, C for conductivity, T for Temperature, and P for pressure. F stands for mass flow controller, S for solenoid valves, and W for water watchers.

The instrument is run on a looped routine whereby pCO_2 is measured from the equilibrator, air inlet, equilibrator again and then one of four secondary standard gases (at 0 μatm, 250 μatm, 350 μatm, and 450 μatm) used for calibration of the detector (figure 2.5). These standards are calibrated in the laboratory against primary gas standards supplied by the National Oceanic and Atmospheric Administration (NOAA) World Meteorological Organization (WMO) Central Calibration Laboratory (CCL). Salinity samples are collected by the ships' crew every twelve hours from the seawater inlet and are used to calibrate salinity derived from the in-line conductivity sensor. The in-situ *Aanderaa* temperature sensor is calibrated

regularly by the manufacturer, and is used to calibrate the platinum resistance thermometers located in the equilibrator on a monthly basis (figure 2.5). All raw data are recorded with position and GMT provided by a GPS module which is installed on the port-side bridge wing (figure 2.5). Once received, the raw data undergo a quality control routine and each voyage is analysed individually to check for any instrument malfunctions or contaminations. The accuracies of the measurements made on board the *MV Benguela Stream* are presented in the table below:

Table 2.1: Accuracy associated with each of the measurements made.

Measurement	Accuracy	Method to derive accuracy
O_2	$\pm 2.8\%$	Combination of RMSE of residuals (1.7%), underway sampling method (1%), and method accuracy from the iodate standard (0.1%).
DIC	± 2.55 (μmol kg^{-1})	Mean standard deviation of CRM DIC
TA	± 1.46 (μmol kg^{-1})	Mean standard deviation of CRM TA
NO_x	± 0.1(μmol kg^{-1})	SEAL AutoAnalyzer accuracy from international standards
Si	± 0.1(μmol kg^{-1})	SEAL AutoAnalyzer accuracy from international standards
PO_4	± 0.02(μmol kg^{-1})	SEAL AutoAnalyzer accuracy from international standards
Salinity	± 0.05	Calculation from conductivity, and calibration using discrete samples
Temperature	± 0.03 ($^\circ$C)	Aanderaa 3210 sensor accuracy
pCO_2	$\pm$ <1(μatm)	LI-COR suggested accuracy
Pressure	$\pm$ <0.1(mbar)	Omega model PX2760-600A5V accuracy

Chapter 3

Variability in phytoplankton distribution and abundance in the North Atlantic from 1958 to 2012

3.1 Abstract

The spatial and regional variability of phytoplankton in the North Atlantic is assessed using data from the Continuous Plankton Recorder (CPR) from 1958-2012. The main environmental drivers of this variability are wind speed and sea surface temperature (SST), which are in turn driven by climate indices. Regional variability was evident, with differing trends occurring for different phytoplankton groups. The Grand Banks of Newfoundland showed a significant increase in phytoplankton abundance throughout the time series, which was significantly correlated to an

increase in wind speed and summer wind speeds in the region. The northeast Atlantic shows an opposing trend between dinoflagellates and diatoms, with diatom abundance increasing relative to dinoflagellate abundance. This trend was found to be predominantly driven by the increasing SST in this region, which in turn had significant correlations with both the Atlantic Multidecadal Oscillation (AMO) and the North Atlantic Oscillation (NAO). There was an increase in the phytoplankton colour index (PCI) in the northeast Atlantic that also correlated with the increasing SST, this increase was not evident in any of the other phytoplankton indices. This supports the suggestion that increased stratification due to warming may allow smaller phytoplankton to increase in abundance relative to larger species due to differences in nutrient demands. This has implications for both the export of carbon, and the ecosystem dynamics within this important fisheries region. Although basin scale relationships exist, the trends between plankton abundance and climate are complex and it is more appropriate to analyse such data on a regional scale where the underlying relationships and mechanisms can be determined.

3.2 Introduction

Sea surface temperature (SST) and wind speed are known to play an important role in the distribution and abundance of phytoplankton (Beaugrand *et al.*, 2012; Hinder *et al.*, 2012; Helaouët *et al.*, 2013). The seasonal increase in SST and decrease in wind speed initiates the required stratification to allow phytoplankton to bloom and wind speed influences the mixing needed to bring nutrients required by phytoplankton into the photic zone. These climatic variables have different influences on different phytoplankton groups, depending on their physiology. For example, in temperate regions where SST has shown a marked increase, those species that are dependant on temperature for larval release or physiological development have been shown to start their seasonal cycles earlier in response to warming (Edwards and Richardson, 2004).

Dinoflagellates and diatoms are two of the most abundant phytoplankton groups and are thought to have different contributions to the export of carbon below the thermocline (Henson *et al.*, 2012). Diatoms are larger than dinoflagellates and are

hypothesized to be a major contributor to export flux (Michaels and Silver, 1988). However Henson *et al.* (2012) found that when smaller phytoplankton species dominated the plankton, the flux of carbon to 3000 m was enhanced in the northeast Atlantic. Diatoms are known to bloom during the spring, and again during the autumn (often at a smaller magnitude to the spring bloom), while dinoflagellates bloom during both the summer and autumn months.

Hinder *et al.* (2012) found that from 1960-2009 increased summer time mixing coupled with increased SST led to a decline in dinoflagellates and an increase in the abundance of diatoms relative to dinoflagellate abundance in the northeast Atlantic.

A number of studies have demonstrated that colder-water affiliated plankton species have undergone range contraction while warmer-water affiliated plankton species have shown range expansion (Hallegraeff, 2010; Helaouët *et al.*, 2013; Hinder *et al.*, 2014). There have also been suggestions of nitrogen limitation caused by a decrease in the influx of North Atlantic nutrient-rich waters in the North Sea and increased stratification (McQuatters-Gollop *et al.*, 2009). This has been linked to a decline in dinoflagellate abundance, favouring diatoms that are constrained by silica limitation. This has knock-on effects on copepod abundance and therefore the ecosystem as a whole (Alvarez-Fernandez *et al.*, 2012).

The North Atlantic Oscillation (NAO) is thought to be the predominant mode of variability in the North Atlantic and is defined by the difference in sea level pressure between the Azores and Iceland (Hurrell, 1995). The NAO is thought to impact phytoplankton distribution and abundance in regions of the North Atlantic. Henson *et al.* (2012) demonstrated that in the northeast Atlantic transition zone, positive NAO increases the wind stress allowing diatoms to dominate over dinoflagellates, and dinoflagellates dominate over diatoms during negative NAO periods.

The aim of the present study is to analyse the abundance and distribution of key phytoplankton indices in relation to SST, wind speed and a range of climatic indices. Spatio-temporal changes in four key phytoplankton indices (phytoplankton colour index (PCI), spring-bloom forming diatoms (diatoms), *Rhizosolenia* (diatom species often associated with later blooming-time), and dinoflagellates in the

North Atlantic were assessed using CPR data. Interpolation of this data was used to geo-spatially visualise the dataset and assess the seasonal, inter-annual and decadal changes with climatic variables. Regional variability was investigated and linked with key environmental drivers of phytoplankton abundance.

3.3 Methods

3.3.1 Study area and period

The study area lies within the North Atlantic Ocean between 60.5°W and 10°E and 29.5°N and 65.5°N. Data were collected between 1958 and 2012.

3.3.2 Data

All data sets were gridded on to a 3-dimensional (3D) grid by taking the monthly mean for each $1 \times 1°$grid cell, so that the datasets could be easily compared and interpolated.

3.3.2.1 Continuous Plankton Recorder data

The Continuous Plankton Recorder (CPR) is designed to be towed behind volunteer ships of opportunity (VOS). The survey uses taxonomic identification to record plankton species' abundance and has been in operation since 1948 with changes in the identification process occurring in 1958 (see methods chapter section 2.1 for more detailed CPR methodology). Our long term analyses of the CPR data therefore runs from 1958 to 2012.

The phytoplankton data from the CPR survey were divided into 4 key phytoplankton indices, namely phytoplankton colour index (PCI), spring-bloom forming diatoms (diatoms), *Rhizosolenia* (diatom genus often associated with a later blooming-time), and dinoflagellates. Kemp *et al.* (2006) suggest that *Rhizosolenia* should be treated as a separate "functional" group to diatoms due to their later blooming time, and buoyancy control. Rare species bias was removed from the dataset by only including species that occur above 1% frequency of occurrence (Edwards and Richardson, 2004). Table 3.1 lists the species that were included

in these indices. The phytoplankton indices were all log transformed using $\log_{10}(x+1)$ in order to homogenise the variance (Alvarez-Fernandez *et al.*, 2012). Each phytoplankton index was gridded onto a $1 \times 1^{\circ}$grid by taking the monthly mean for each grid cell, and removing any grid cell where the CPR sample number was < 3 (Helaouët *et al.*, 2013), resulting in a 3D grid consisting of 660 months $\times$ 180 latitude $\times$ 360 longitude.

Table 3.1: List of species in each phytoplankton index.

Diatoms	***Rhizosolenia***	**Dinoflagellates**
Paralia sulcata	*Rhizosolenia imbricata*	*Prorocentrum* spp. (*'Exuviaella'* type)
Thalassiosira spp.	*Rhizosolenia styliformis*	*Ceratium tripos*
Pseudo-nitzschia delicatissima complex	*Rhizosolenia hebetata semispina*	*Ceratium macroceros*
Pseudo-nitzschia seriata complex	*Proboscia alata*	*Cladopyxis* spp.
Chaetoceros (Hyalochaete) spp.		*Gonyaulax* spp.
Chaetoceros (Phaeoceros) spp.		*Ceratium fusus*
Thalassiothrix longissima		*Ceratium furca*
Thalassionema nitzschioides		*Ceratium lineatum*
Leptocylindrus mediterraneus		*Ceratium horridum*
Bacteriastrum spp.		*Ceratium hexacanthum*
Cylindrotheca closterium		*Oxytoxum* spp.
		Scrippsiella spp.
		Protoperidinium spp.

3.3.2.2 Climate variables

Mean monthly SST and wind speed data from 1960 to 2012 were obtained from the International Comprehensive Ocean-Atmosphere Data Set (ICOADS, 1°enhanced data) (Woodruff, 1987).

Monthly, annual and winter (DJFM) NAO indices were obtained from the Climate Data Guide: Hurrell North Atlantic Oscillation (NAO) Index (station-based) (Hurrell, 1995).

Monthly Eastern Atlantic Pattern (EAP) indices were obtained from the NOAA Climate Prediction Center, Northern Hemisphere Teleconnection Patterns (Wallace and Gutzler, 1981). Monthly and annual Atlantic Multidecadal Oscillation (AMO) indices were obtained from the NOAA Earth System Research Lab, Climate Timeseries (Enfield, 2001).

Monthly and annual Northern Hemisphere Temperature anomalies (NHT) were obtained from the Carbon Dioxide Information Analysis Center (CDIAC) (Jones *et al.*, 2012).

The enhanced data from ICOADS were only available starting from 1960, so any analyses involving climatic variables or indices were from 1960 to 2012.

3.3.3 Objective mapping

Due to the sampling nature of the CPR, which relies on shipping routes, there are irregular gaps within the dataset that have to be accounted for in order to analyse the data spatially and compare it with climate data. There are a number of different methods to interpolate the data, of which kriging, objective mapping, inverse-distance weighting, and a spring metaphor nearest neighbour method have all been trialled and are outlined in appendix A.1. Objective mapping was chosen as the interpolation technique to be used within this study as it had the least amount of variance within the decadal maps. Objective mapping is similar to kriging but it assumes that the mean drift (trend) is known and uses a covariance matrix where larger weights are assigned to points that are nearby and co-vary positively with the estimated values (Glover *et al.*, 2005). The method can be described by the following equation:

$$b = w \times E^{-1} \times r \tag{3.1}$$

Where b is the mapped property, w is the data weights, E is the covariance matrix and r is the residuals (weighted mean).

3.3.4 Decadal maps

Decadal spatio-temporal maps were produced in order to visualize the CPR dataset following the method outlined in Edwards (2000). Monthly CPR data were separated into 5 year periods, and 12 monthly averaged maps were produced for each five year period using one of the interpolation techniques. 12 monthly decadal maps were produced by taking the same month from two of the five year periods within the decade, and applying the interpolation technique to each individual grid cell. These 12 monthly decadal maps were then combined to form one decadal map by averaging each grid cell. Figure 3.1 outlines this technique, using kriging as the interpolation technique.

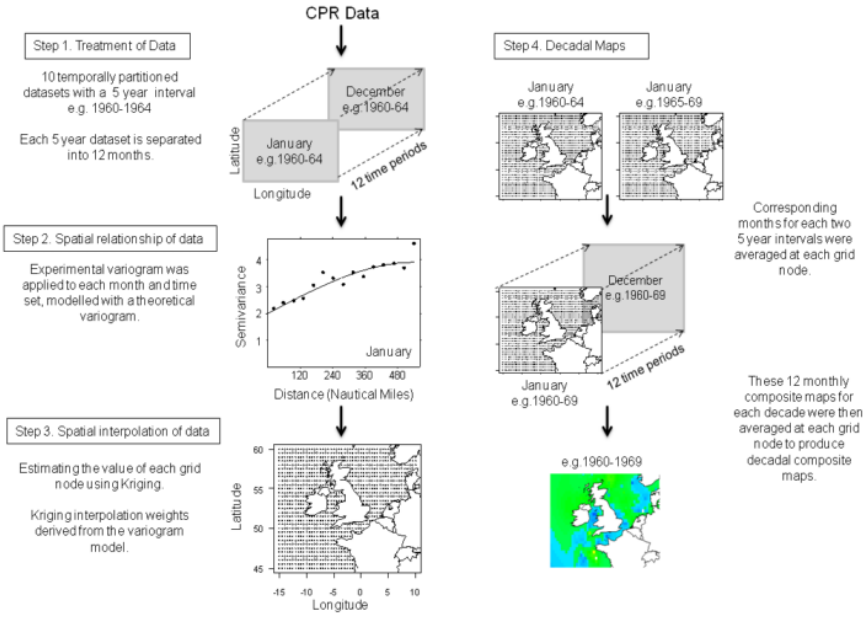

Figure 3.1: Schematic of CPR data organisation and interpolation, reproduced from Hinder *et al.* (2012) and based on Edwards (2000).

3.3.5 Linear trends and congruence

For spatial analysis of the linear trends of the phytoplankton indices with climate variables, an interpolation of the CPR data was applied to account for missing CPR values at each $1 \times 1^{\circ}$grid cell. To interpolate the data at this resolution objective mapping was used with a Gaussian distribution model with an influence radius of 2.5 and a cut off radius of 6.

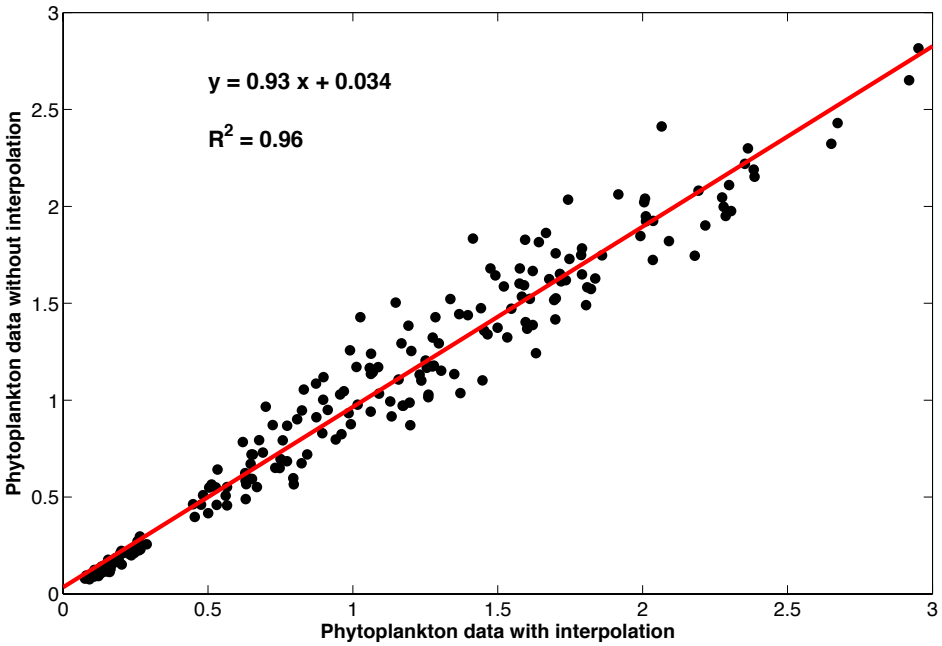

Figure 3.2: Property property plot of interpolated annual phytoplankton data against mean annual phytoplankton data for the North Atlantic from 1960 to 2012.

After applying this interpolation to the CPR data the inter-annual variability and the general linear long term trends compare well with the annual mean CPR data (figure 3.2), with an r-squared value of 0.96 (n = 212).

Yearly averages were used because the seasonal cycle can often obscure long term trends and correlations. The linear trend from 1960 to 2012 for SST, wind speed, PCI, diatom, dinoflagellate and *Rhizosolenia* abundance for each $1 \times 1^{\circ}$grid cell was calculated. Linear congruence was estimated using a technique outlined in Lovenduski *et al.* (2008), whereby the congruence (T_{Cong}) of a time series ($T1$) with another time series ($T2$) is estimated by multiplying the regression (R) coefficient between $T1$ and $T2$, by the trend in $T2$ ($T2_{Trend}$) , see equation 3.2.

$$T_{Cong} = R \times T2_{Trend} \tag{3.2}$$

The significance of the linear trend was calculated following Santer *et al.* (2000), whereby the ratio (tb) of the linear trend (T) and the standard error of the linear trend ($SE(Ne)$) (equation 3.4) was compared to a critical value of t ($tcrit$, assuming a distribution of student's t) at a 95% significance level and the effective degrees of freedom, which takes into account any autocorrelation within the time series by using the effective sample size (Ne):

$$tb > tcrit(0.95, Ne - 2) = significant \tag{3.3}$$

$$tb = \frac{T}{SE(Ne)} \tag{3.4}$$

There are numerous methods to account for autocorrelation within time series (Bartlett, 1935; Pyper and Peterman, 1998; Bretherton and Widmann, 1999; Santer *et al.*, 2000). The most common autocorrelation within time series is temporal autocorrelation, which implies that throughout time preceding observations are not independent of each other. This has implications for the significance of any trend where temporal autocorrelation exists (Pyper and Peterman, 1998). To account for temporal autocorrelation when calculating the significance of the linear trends and any correlations within the time series data the modified Chelton method was used as it has been shown to be the optimum method for altering significance due to autocorrelation within time series (Pyper and Peterman, 1998). Those samples that are not autocorrelated within the time-series are effectively independent and counted within the effective sample size (Ne) which will be less than the sample size (N). By using the effective sample size to calculate the standard error of the linear trend and the critical value of t (rather than N) this reduces the significance of the trends and therefore takes into account autocorrelation within the time series (Lovenduski *et al.*, 2008).

3.3.6 Correlation and autocorrelation

Relationships between the CPR data, climate data and climate indices were investigated using Pearson's correlation. As mentioned in section 3.3.5 the significance

of the Pearson's correlation coefficients were adjusted for temporal autocorrelation using the effective sample size (Ne) following the modified Chelton method recommended by Pyper and Peterman (1998):

$$\frac{1}{Ne} = \frac{1}{N} + \frac{2}{N}\sum_{h=1}^{N/5} autoX(h)autoY(h) \tag{3.5}$$

Where N is the sample size of the time series, h is the number of lags (which is suggested to go from 1 to $N/5$) and $autoX(h)$ is the temporal autocorrelation in the X variable at lag h, and $autoY(h)$ is the temporal autocorrelation in the Y variable at lag h. The temporal autocorrelation for each time series was calculated using the *autocorr* function in matlab, which utilises the equation outlined in Box *et al.* (1994):

$$autoX(h) = \frac{\sum_{t=h+1}^{N}(X_t - \bar{X})(X_{t-h} - \bar{X})}{\sum_{t=1}^{N}(X_t - \bar{X})^2} \tag{3.6}$$

Where X_t is X at time (t), and $\bar{X}$ is the mean of the time series X. Ne was used to calculate the significance of the Pearson's correlation coefficient (Rho) at 95% significance by first calculating the t-statistic ($tStat$):

$$tStat = Rho \times \sqrt{\frac{Ne-2}{1-Rho^2}} \tag{3.7}$$

Then using the *tcdf* function in Matlab to look up the significance (p) using Ne:

$$p = 2 \times tcdf(tStat, Ne-2) \tag{3.8}$$

3.3.7 Principal Component Analysis

Principal component analysis (PCA) is most commonly used to produce principle components from a number of variables to more efficiently describe the structure of the variance within the dataset (Glover *et al.*, 2005).

Mapping of eigenvectors and plotting the time-series principal components

produced in spatio-temporal PCA (often referred to as empirical orthogonal functions (EOF) analysis) is often used to determine possible underlying processes influencing the variability of one variable through time and space (Glover *et al.*, 2005). This method has been carried out in a number of studies looking at the spatio-temporal variability of CPR data (Beaugrand, 2003; Beaugrand *et al.*, 2012; Harris *et al.*, 2013; Edwards *et al.*, 2013). We used the same interpolation technique applied to the CPR data to map the linear trends (see section 3.3.5) to interpolate each of the phytoplankton indices and climate variables in order to map their associated eigenvectors.

3.4 Results

3.4.1 Long term trends in the North Atlantic

Figure 3.3 shows the decadal abundance of the four phytoplankton indices since the 1960's. Decadal anomaly maps were produced to visualize the change in abundance between each decade, and throughout the time period (appendix A.2). The regions with the highest abundance of phytoplankton are the southern North Sea, the northeast Atlantic approaches, and the area surrounding the Grand Banks of Newfoundland. PCI, diatoms and dinoflagellates have all increased in abundance in the Grand Banks of Newfoundland since the 1960's.

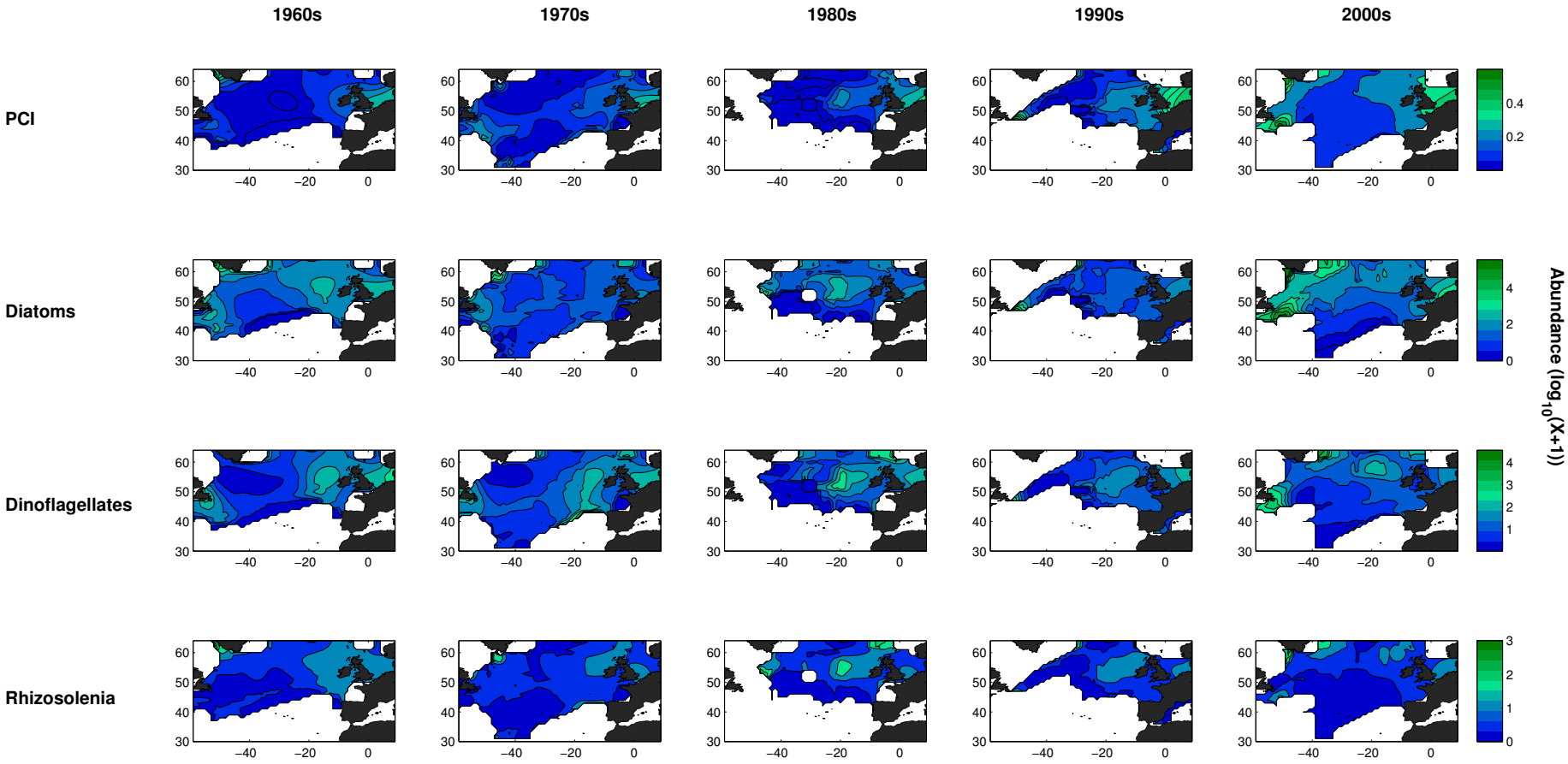

Figure 3.3: Decadal abundance of phytoplankton indices in the North Atlantic from 1960 to 2009, interpolated using objective mapping.

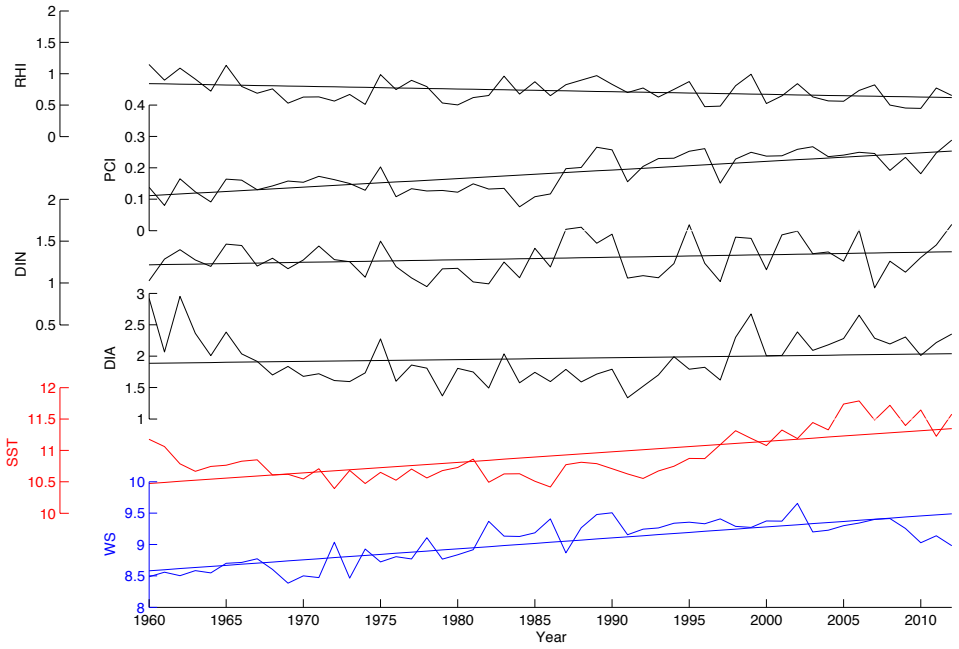

Figure 3.4: Annual phytoplankton indices (RHI (*Rhizosolenia*), PCI, DIN (dinoflagellates), DIA (diatoms)), sea surface temperature, and wind speed (WS) from 1960 to 2012 in the North Atlantic with interpolation applied to the CPR data, and line of best fit plotted.

Figure 3.4 shows that both wind speed and SST have increased and have significant positive trends of 0.02 m s^{-1} yr^{-1} and 0.02 °C yr^{-1} from 1960-2012 in the North Atlantic. PCI, diatoms and dinoflagellates show a significant positive trend of 0.003 abundance ($\log_{10}(x+1)$) yr^{-1} , while *Rhizosolenia* has a significant decreasing trend of -0.004 abundance ($\log_{10}(x+1)$) yr^{-1} . Both diatoms and dinoflagellates have decreased in abundance between 1975 and 1995. This trend can also be seen in figure 3.3 as there are lower abundances for these indices in the 1970's compared to the 1990's decadal maps.

The linear trends and congruence between each phytoplankton indices' linear trend and the linear trend of wind speed and SST from 1960 to 2012 at each grid cell are shown in figures 3.5 to 3.9 with red representing a positive trend or congruence and blue representing a negative trend.

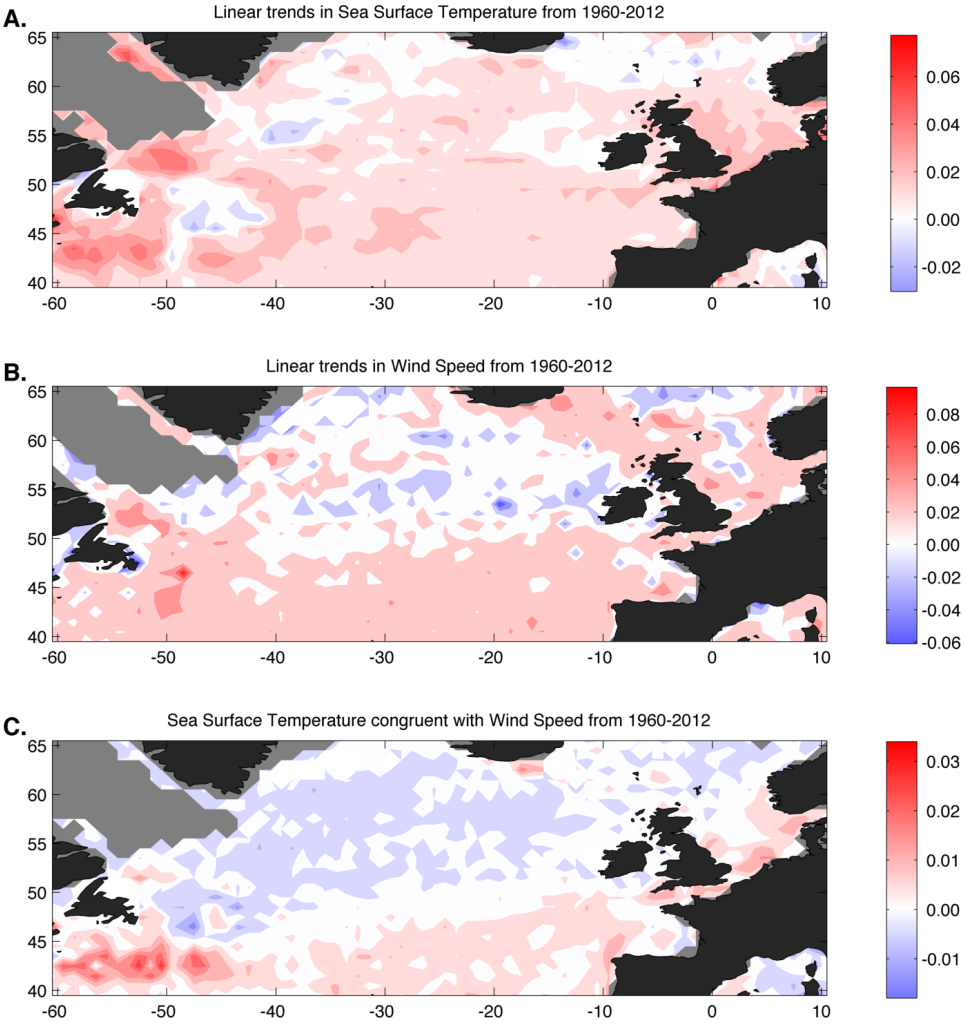

Figure 3.5: **A.** Linear trends in sea surface temperature (°C yr^{-1}) and **B.** linear trends in wind speed (ms^{-1} yr^{-1}) from 1960 to 2012 in the North Atlantic. **C.** Linear sea surface temperature trends that are congruent with wind speed. Only those trends with a significance of $> 95\%$ are shown. The areas that are shaded grey are where there were insufficient data.

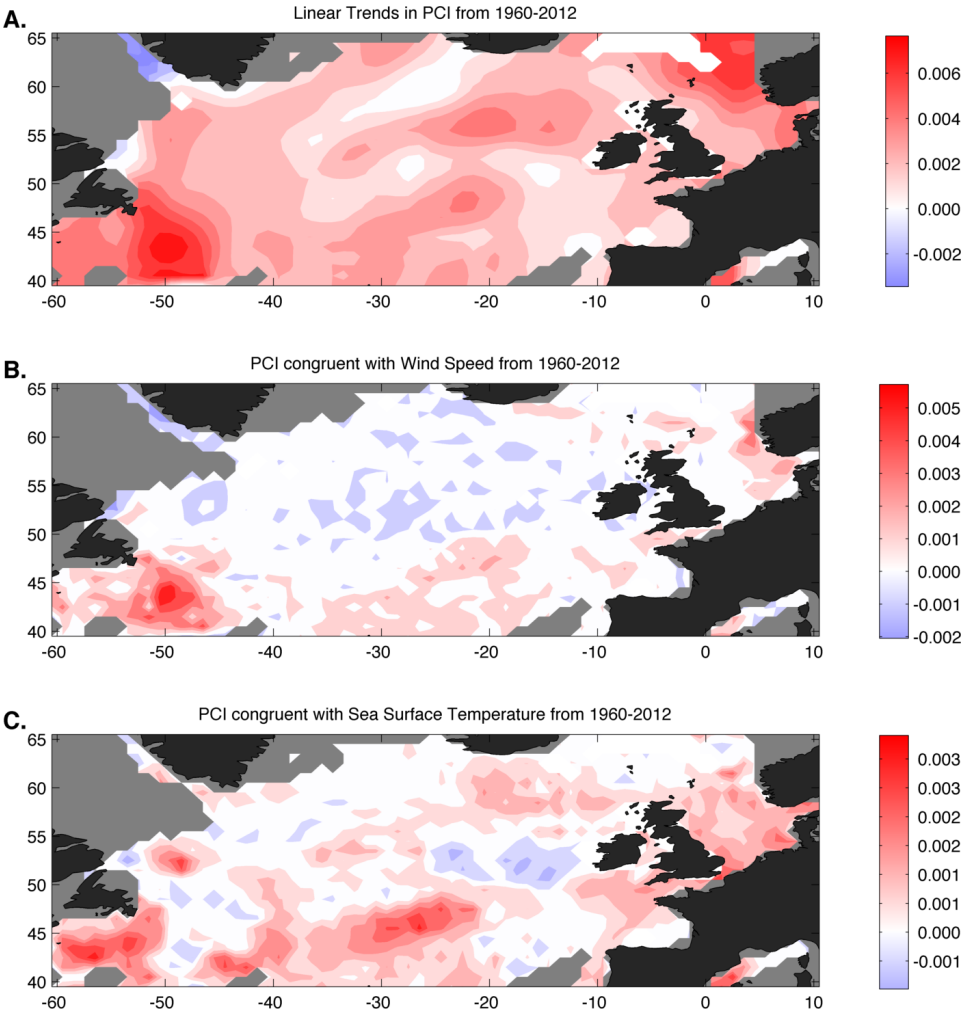

Figure 3.6: **A.**Linear trends in Phytoplankton Colour Index (PCI) from 1960 to 2012 in the North Atlantic ($\log_{10}$(x+1) yr^{-1}). **B.** Congruence of the linear trends in PCI with wind speed. **C.** Congruence of the linear trends in PCI with sea surface temperature. Only those trends with a significance of $> 95\%$ are shown. The areas that are shaded grey are where there were insufficient data.

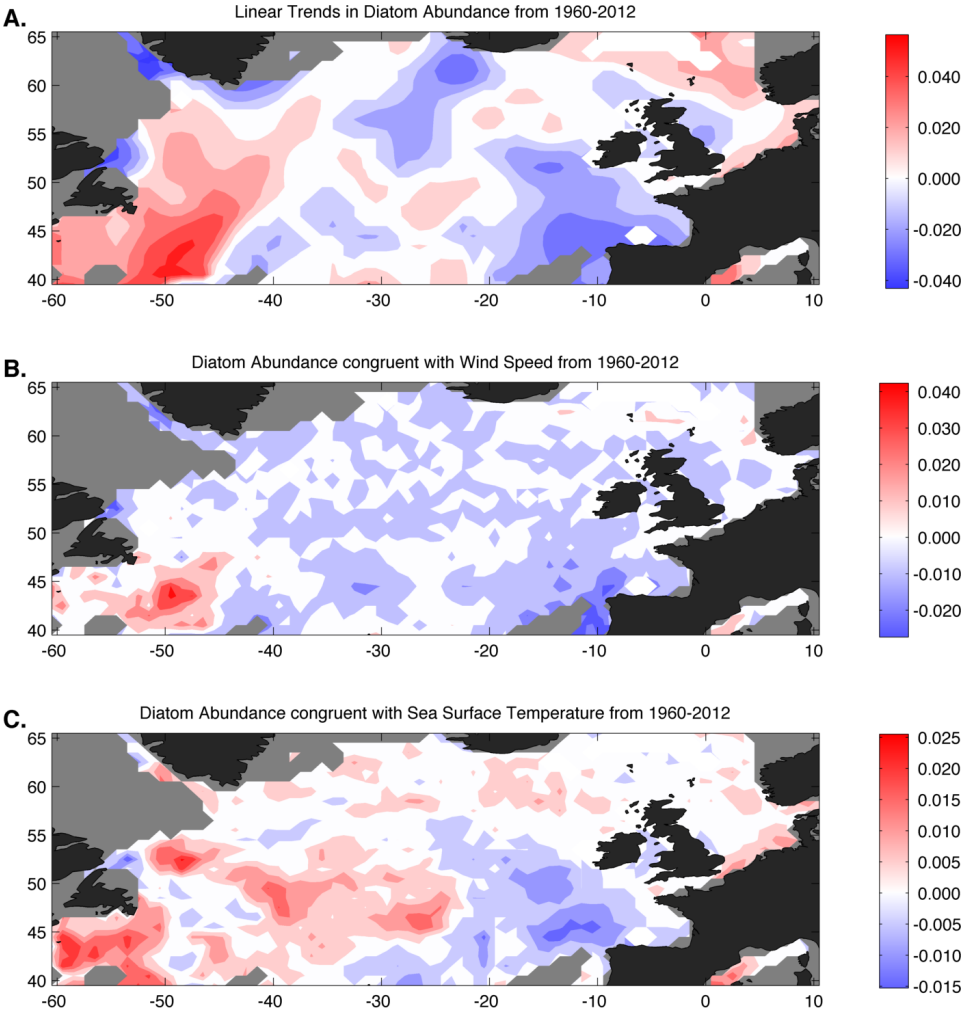

Figure 3.7: **A.** Linear trends in spring-blooming diatoms (diatom) abundance ($\log_{10}$(x+1) yr^{-1}) from 1960 to 2012 in the North Atlantic. **B.** Congruence of the linear trends in diatom abundance with wind speed. **C.** Congruence of linear trends in diatom abundance with sea surface temperature. Only those trends with a significance of $> 95\%$ are shown. The areas that are shaded grey are where there were insufficient data.

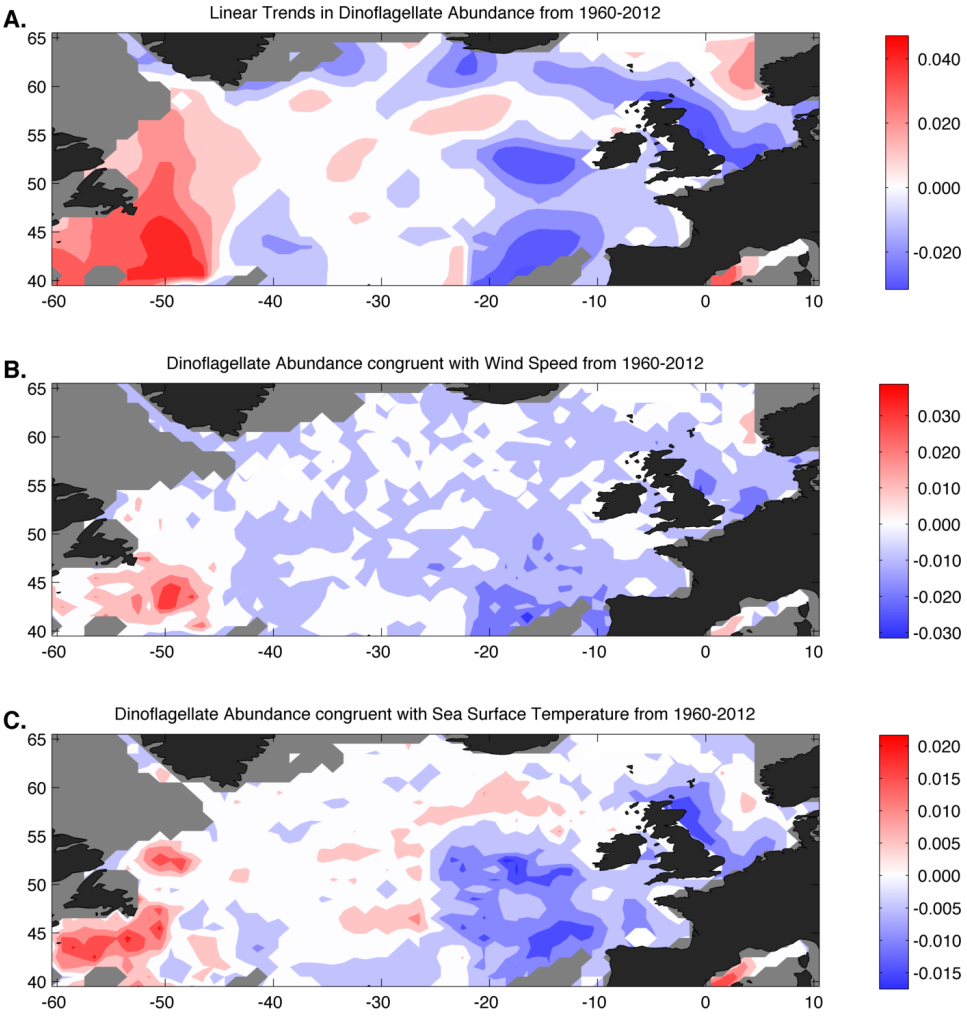

Figure 3.8: **A.** Linear trends in dinoflagellate abundance ($\log_{10}$(x+1) yr^{-1}) from 1960 to 2012 in the North Atlantic. **B.** Congruence of linear trends in dinoflagellate abundance with wind speed. **C.** Congruence of the linear trends in dinoflagellate abundance with sea surface temperature. Only those trends with a significance of $> 95\%$ are shown. The areas that are shaded grey are where there were insufficient data.

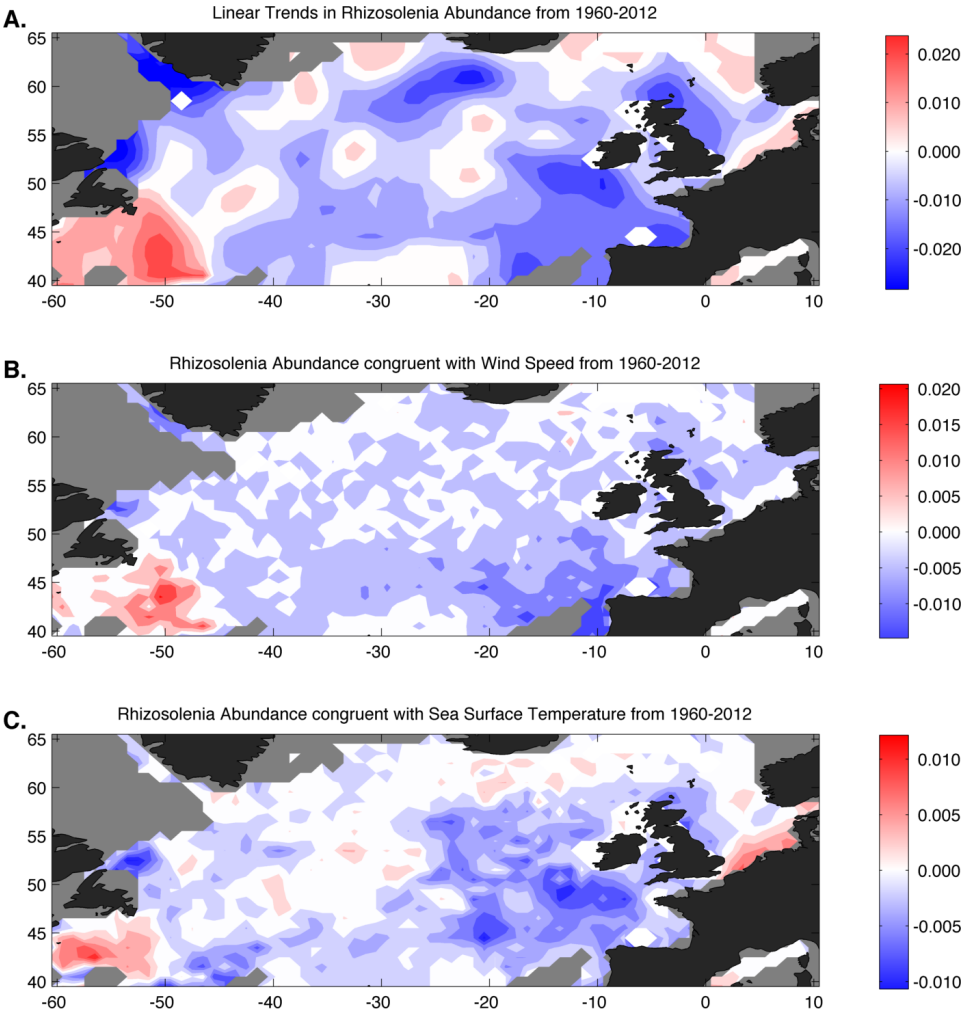

Figure 3.9: **A.** Linear trends in *Rhizosolenia* abundance ($\log_{10}$(x+1) yr^{-1}) from 1960 to 2012 in the North Atlantic. **B.** Congruence of linear trends in *Rhizosolenia* abundance with wind speed. **C.** Congruence of the linear trends in *Rhizosolenia* abundance with sea surface temperature. Only those trends with a significance of $> 95\%$ are shown. The areas that are shaded grey are where there were insufficient data.

SST and wind speed show a north-south dipole in the congruence of SST with wind speed from 1960-2012 in the North Atlantic, with SST showing positive congruence with the increasing wind speed trend from about 40 °N - 45 °N and up into the south of the North Sea, and negative congruence across the subpolar North Atlantic (figure 3.5).

Table 3.2: Percentage of congruence between each of the phytoplankton indices and the SST and wind speed linear trends within the North Atlantic from 1960 to 2012 (Given as a % of the grid cells used within the study area).

	-ve SST (%)	+ve SST (%)	-ve WS (%)	+ve WS (%)
PCI	3.9	59.1	8.2	52.3
DIA	12.4	48.0	27.2	29.8
DIN	24.2	35.3	31.0	25.8
RHI	32.9	24.0	34.4	23.5

In figure 3.6 PCI shows an increasing linear trend across most of the North Atlantic, with a small region in the Labrador Sea showing a decrease. This increasing trend in PCI was positively congruent with the increasing SST linear trend across 59% of the North Atlantic, with only 4 % showing a negative congruence, and the remaining coverage of the North Atlantic showing a non-significant congruence (table 3.2). Diatoms have a higher percentage of positive congruence with SST and wind speed than both dinoflagellates and *Rhizosolenia*, while *Rhizosolenia* have the highest percentage of negative congruence with both SST and wind speed (table 3.2).

The Grand Banks of Newfoundland show positive congruence for all four phytoplankton categories with the wind speed index and sea surface temperature, with a stronger congruence to wind speed, suggesting this is the main driver of the increasing abundance of phytoplankton in this region. Diatoms and dinoflagellates show opposing linear trends to each other in the southern North Sea, with diatoms increasing over the sampling period and dinoflagellates decreasing. This may be explained by their opposing congruence to wind speed and sea surface temperature within this region. The Bay of Biscay and south-west Atlantic approaches show a decrease in both diatom and dinoflagellate abundance which is negatively congruent with both SST and wind speed.

Further detail of the regional trend in these relationships is investigated in section 3.4.2.

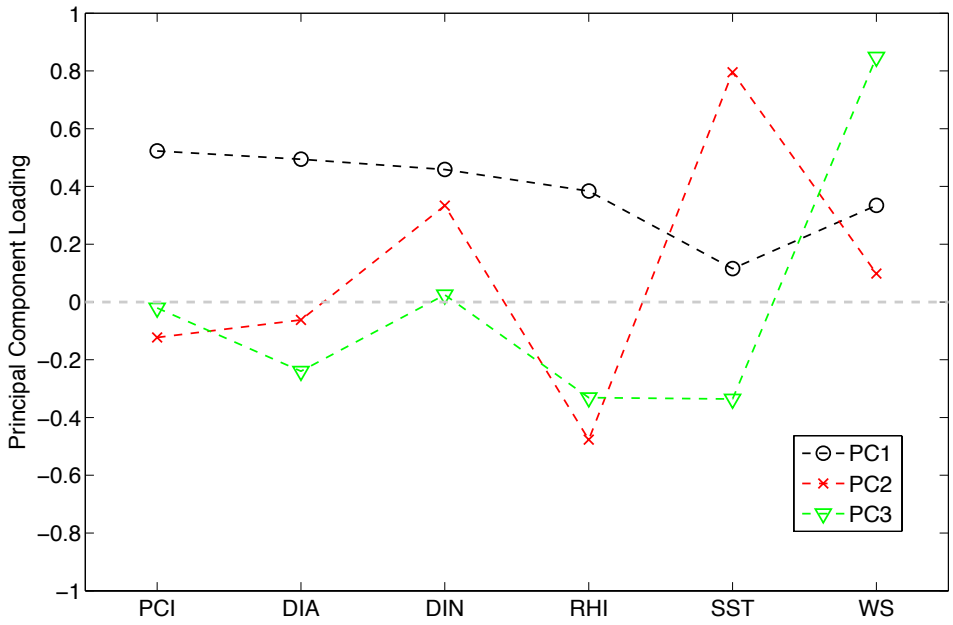

Figure 3.10: Line plot of the loadings of principal components 1, 2 and 3 for annual phytoplankton indices (PCI, diatoms (DIA), dinoflagellates (DIN), and *Rhizosolenia* (RHI)) with SST and wind speed (WS) from 1960 to 2012 in the North Atlantic.

Figure 3.10 shows the first three principal components' loadings after completing PCA on the four annual phytoplankton indices, annual SST, and annual wind speed from 1960 to 2012 in the North Atlantic (60.5°W and 10.5°E and 39.5°N and 65.5°N). The first principal component accounts for 52% of the variance within the dataset, while the sum of all three principal components accounts for 87% of the variance, which means that there is a lot in common between the variables and is descriptive of the general increasing trend seen in all of the variables across the North Atlantic (Glover *et al.*, 2005). The first principal component loadings for all four phytoplankton indices, SST, and wind speed in the North Atlantic shows that all of these variables are positively correlated, while the second principal component shows an anti-correlation between dinoflagellates and the remaining three phytoplankton indices. This pattern is also evident in principal component 3. However SST and wind speed are anti-correlated (figure 3.10).

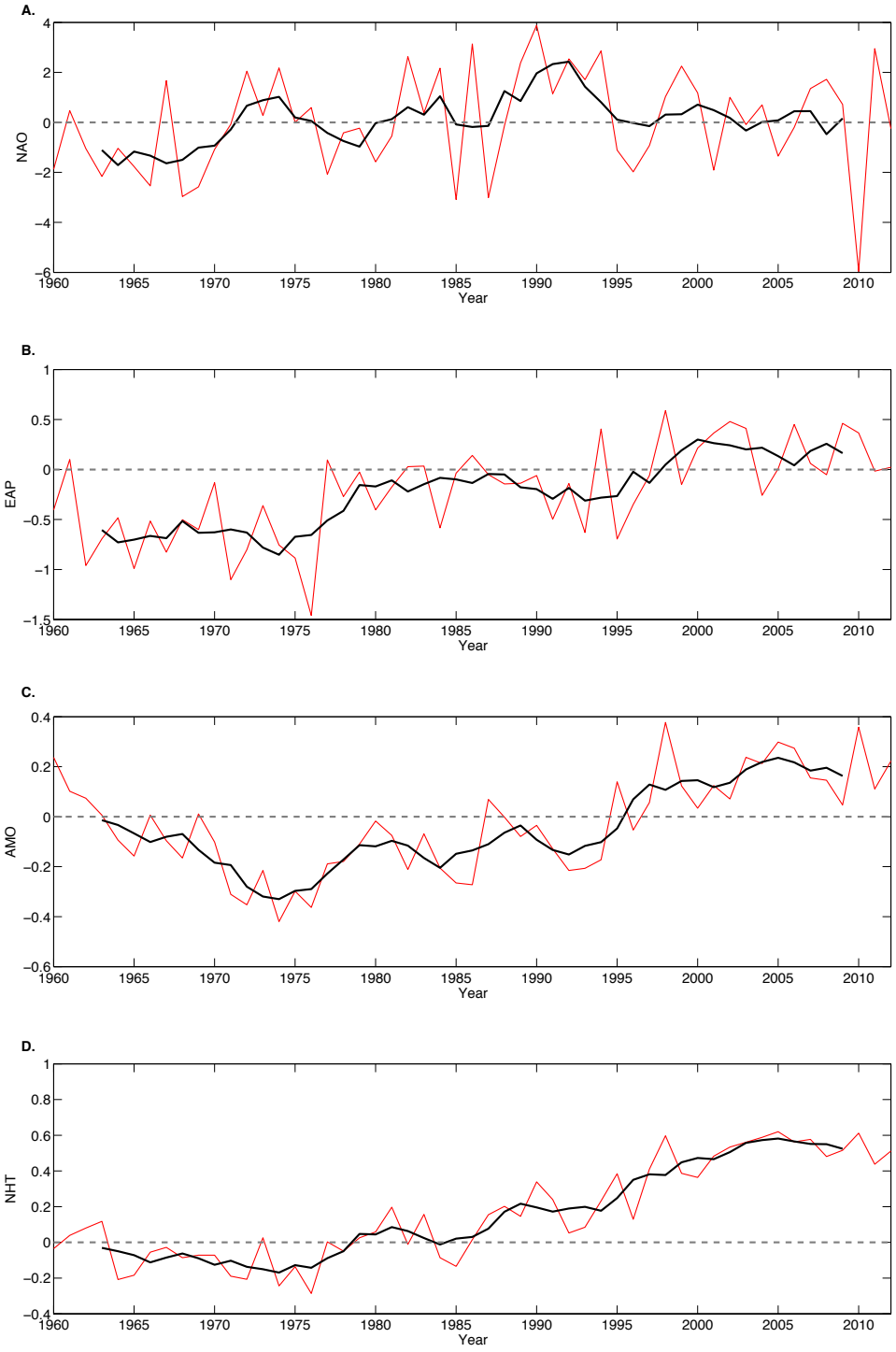

Figure 3.11: Annual North Atlantic climate indices from 1960 to 2012 plotted in red, five year running mean plotted in black. **A.** North Atlantic Ocsillation. **B.** Eastern Atlantic Pattern. **C.** Atlantic Multidecdal Oscillation. **D.** Northern Hemisphere Temperature anomaly. The grey dashed line indicates the zero line.

Trends in the amplitude of the principal components for individual variables can often be linked to climate indices that may be influencing these variables. Figure 3.11 shows four of the key climate indices (NAO, EAP, AMO, NHT) in the North Atlantic from 1960 to 2012. The NAO is known to influence wind speed and direction in the North Atlantic, which in turn influences heat transport and ocean circulation (Hurrell *et al.*, 2003). In figure 3.11**A** the NAO shows a number of oscillations since 1960, with some strong negative indices occurring in the 1980's and 2010. The Eastern Atlantic Pattern (EAP) has a similar dipole in space to the NAO with a pressure centre near to the northeast Atlantic and it is contributing to the current (2000 to 2010) warm anomaly (Cannaby and Hüsrevolu, 2009). Figure 3.11**B** shows a 20 year increasing cycle in the EAP, in which the index increases and then levels off every 20 years. Both the AMO and the NHT follow a similar increasing trend, with the latest warming phase of the AMO (1995 to 2010) being coupled with the increased warming in the Northern Hemisphere that can also be seen in the NHT signal (Edwards *et al.*, 2013)(figure 3.11**C** and **D**). After correcting for temporal autocorrelation SST was found to have a significant positive correlation with both the AMO and NHT, while wind speed was significantly positively correlated with the NAO in the North Atlantic.

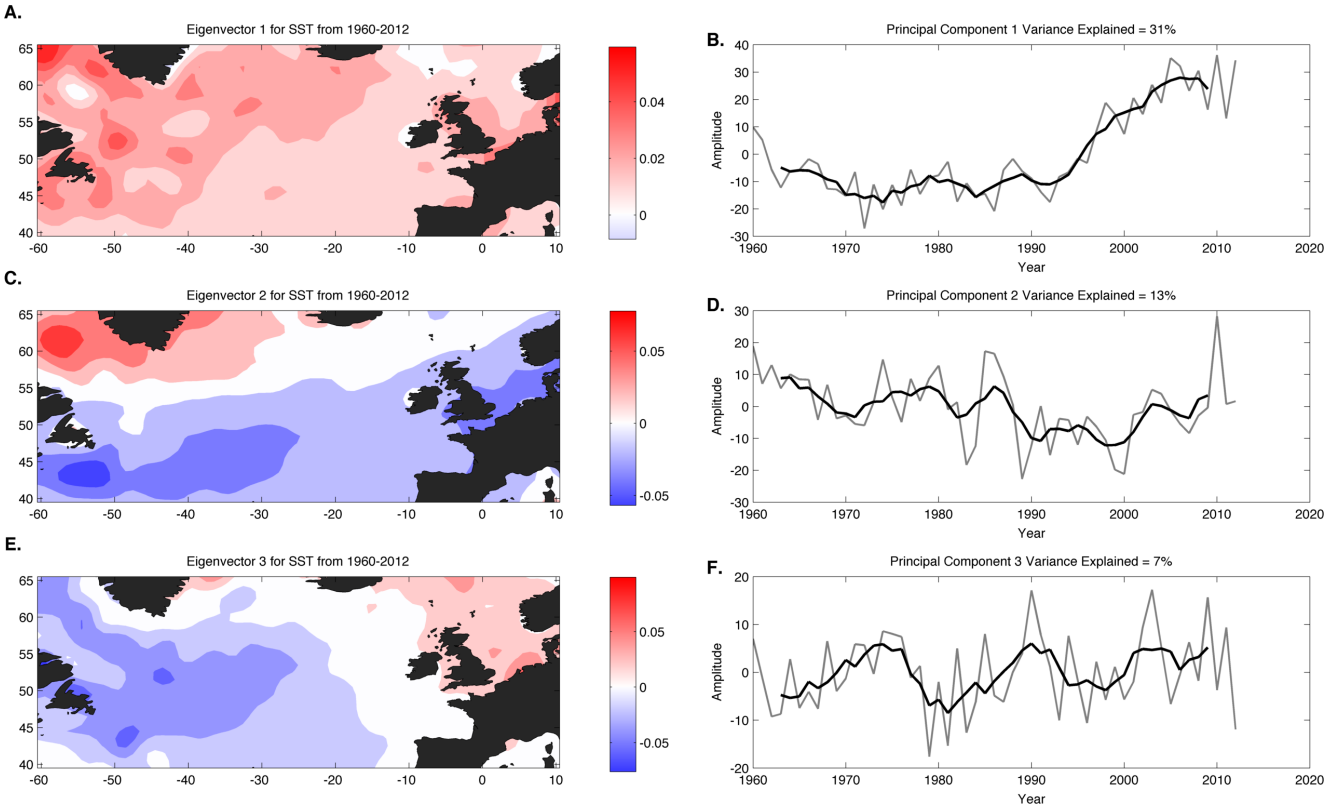

Figure 3.12: Long-term changes in annual sea surface temperature from 1960 to 2012 in the North Atlantic. **A.** Map of the eigenvectors associated with principal component 1. **B.** Line plot of principal component 1 with the percentage of the variance explained. **C. D. E.** and **F.** follow the same structure for principal components 2 and 3 respectively. The light grey line represents the annual principal components, and the black line represents the 5 year running mean. The eigenvectors show the correlations between changes in annual sea surface temperature and the corresponding principal component.

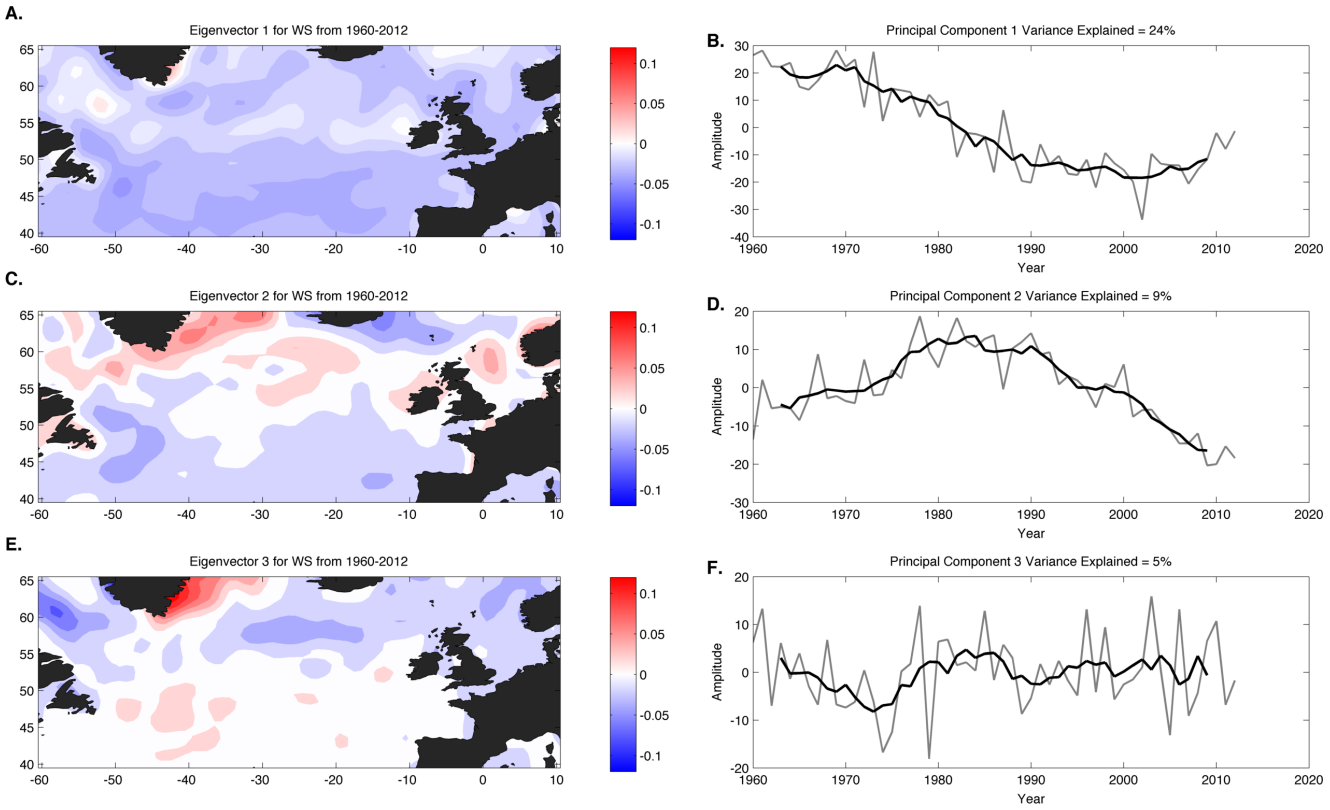

Figure 3.13: Long-term changes in annual wind speed from 1960 to 2012 in the North Atlantic.**A.** Map of the eigenvectors associated with principal component 1.**B.** Line plot of principal component 1 with the percentage of the variance explained. **C. D. E.** and **F.** follow the same structure for principal components 2 and 3 respectively. The light grey line represents the annual principal components, and the black line represents the 5 year running mean. The eigenvectors show the correlations between changes in annual wind speed and the corresponding principal component.

The first three principal components of SST (figure 3.12) and wind speed (figure 3.13) describe most of the variance in these two climate variables across the North Atlantic. When comparing these principal components with the dominant climate indices in the North Atlantic (figure 3.11), it is possible to identify the main drivers of the climate variability. Figure 3.14 shows that there are significant correlations between the first principal component of SST and the AMO, and the second principal component and the NAO. The third principal component was found to be correlated with EAP. However after correcting for temporal autocorrelation this relationship was found to be not significant. The principal components of SST agree with Schlesinger and Ramankutty (1994); Beaugrand *et al.* (2012); Harris *et al.* (2013) with the first principal component showing an oscillatory behaviour that is similar to that of the AMO and NHT indices. This trend is present across the whole North Atlantic, is centered around the Labrador basin and is more dominant in this area and the Irminger basin. There is also a strong signal in parts of the North Sea, see figure 3.12. The second principal component of SST shows a regional dipole, with the Labrador basin opposing the trend seen towards the south of the North Atlantic, which has a strong signal in the south North Sea, and near the Grand Banks of Newfoundland. The third principal component of SST again has a regional dipole, that is divided more east to west, with the strongest signals occurring in a large region to the west of the mid Atlantic ridge, and the opposing signal occurring to the east in the North Sea and Norwegian basin.

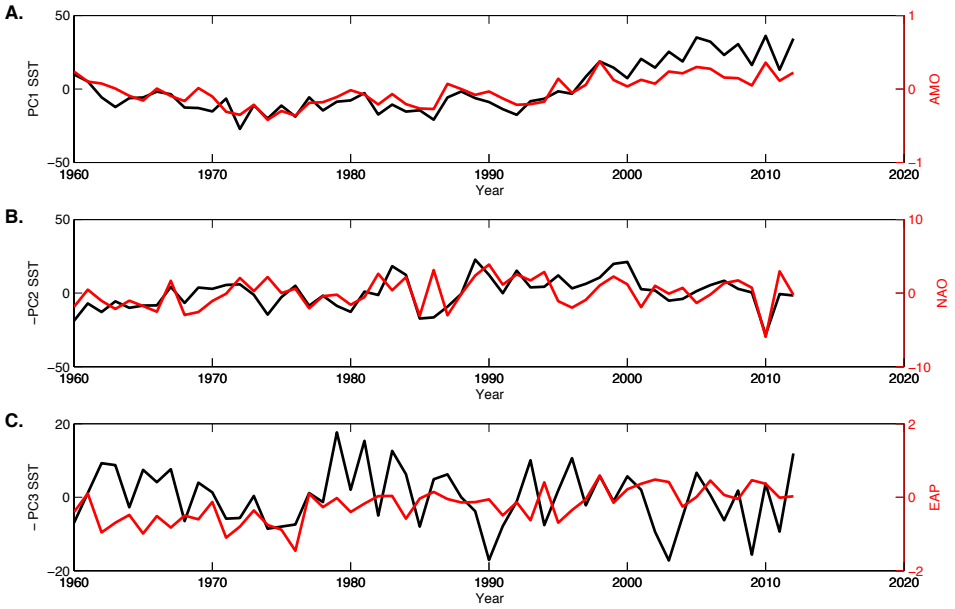

Figure 3.14: **A.** The first principal component for SST (black) and the AMO (red). **B.** The second principal component for SST inverted (black) and the NAO (red). **C.** The third principal component for SST inverted (black) and the EAP (red).

The first principal component of wind speed in figure 3.13**A**, shows a signal that is present across the whole of the North Atlantic. This is most likely the increasing wind speed trend seen in the linear trend map in figure 3.5. This principal component has an oscillatory trend that is similar to that of the NHT and AMO indices, with the third principal component showing more variability and shorter oscillatory periods. The first three principal components of wind speed best correlate with the NHT, AMO and NAO respectively (see figure 3.15), but only the NAO was found to have a significant correlation after correcting for temporal autocorrelation (Pyper and Peterman, 1998).

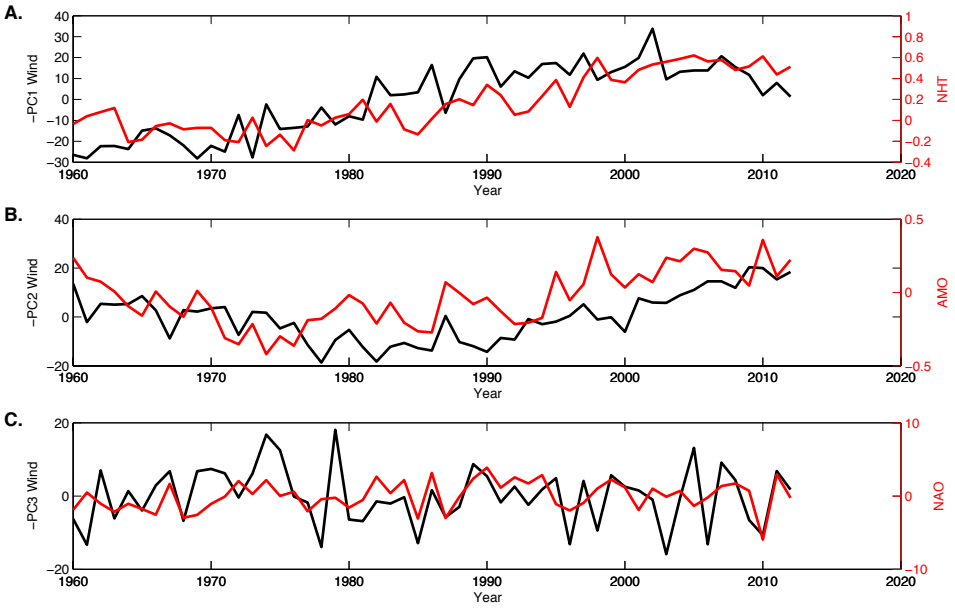

Figure 3.15: **A.** The first principal component for wind speed inverted (black) and the NHT (red). **B.** The second principal component for wind speed inverted (black) and the AMO (red). **C.** The third principal component for wind speed inverted (black) and the NAO (red).

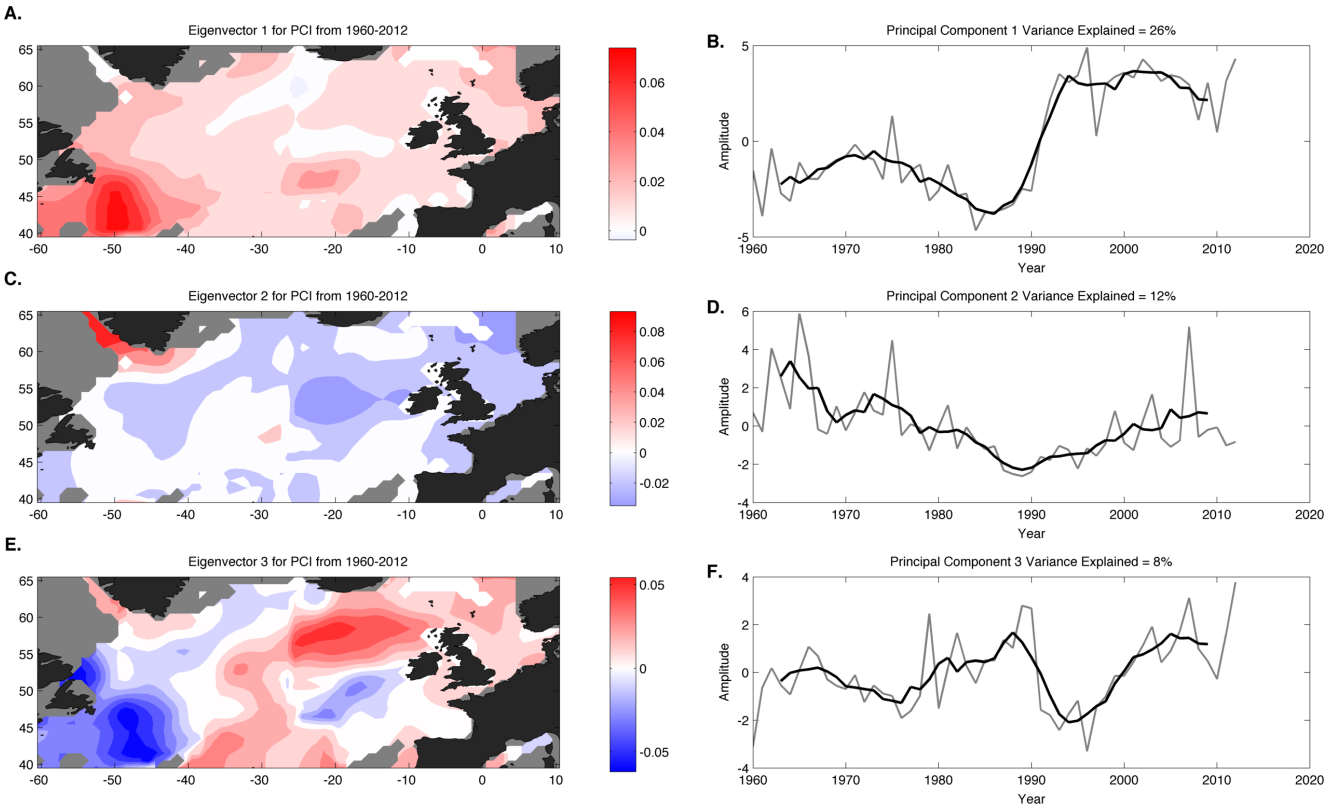

Figure 3.16: Long-term changes in annual PCI from 1960 to 2012 in the North Atlantic. **A.** Map of the eigenvectors associated with principal component 1. **B.** Line plot of principal component 1 with the percentage of the variance explained. **C. D. E.** and **F.** follow the same structure for principal components 2 and 3 respectively. The light grey line represents the annual principal components, and the black line represents the 5 year running mean. The eigenvectors show the correlations between changes in annual PCI and the corresponding principal component.

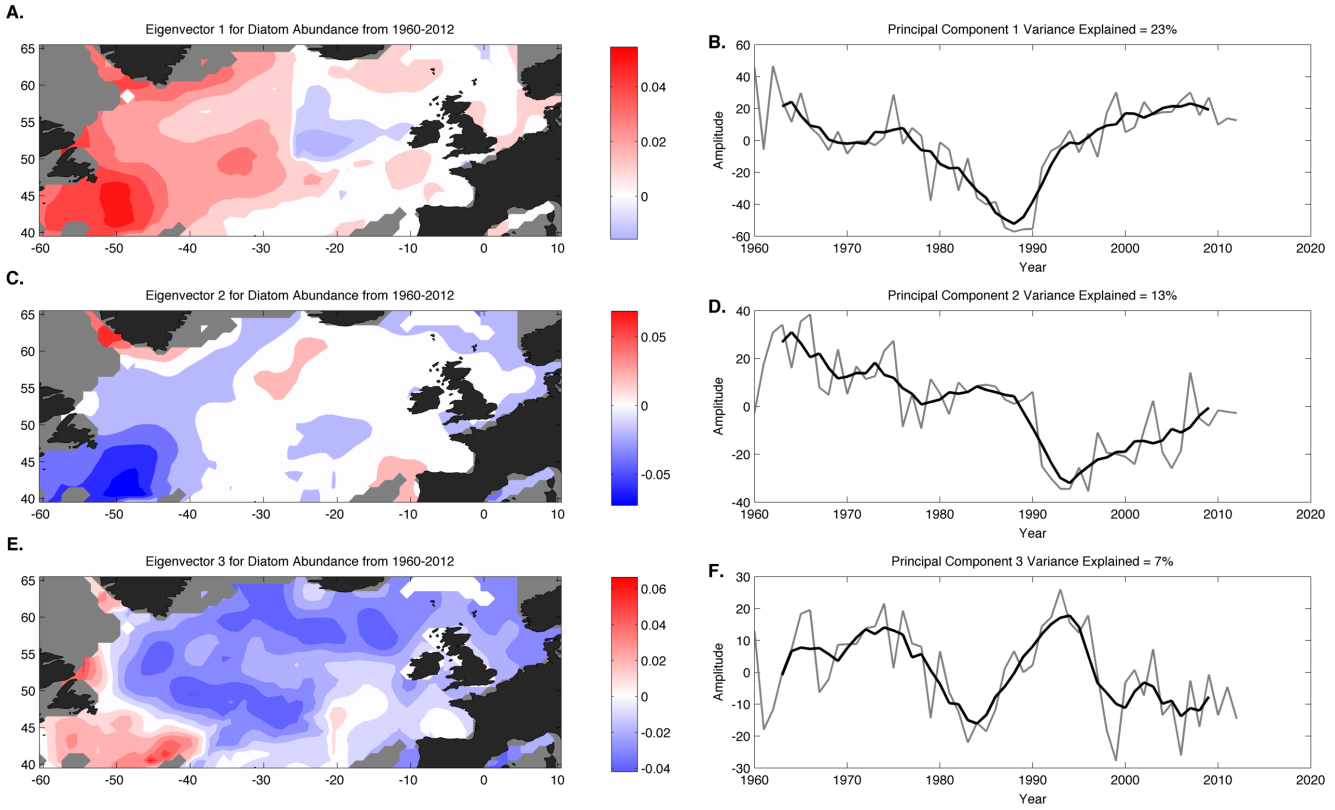

Figure 3.17: Long-term changes in annual spring-blooming diatom (diatom) abundance from 1960 to 2012 in the North Atlantic. **A.** Map of the eigenvectors associated with principal component 1. **B.** Line plot of principal component 1 with the percentage of the variance explained. **C. D. E.** and **F.** follow the same structure for principal components 2 and 3 respectively. The light grey line represents the annual principal components, and the black line represents the 5 year running mean. The eigenvectors show the correlations between changes in annual diatom abundance and the corresponding principal component.

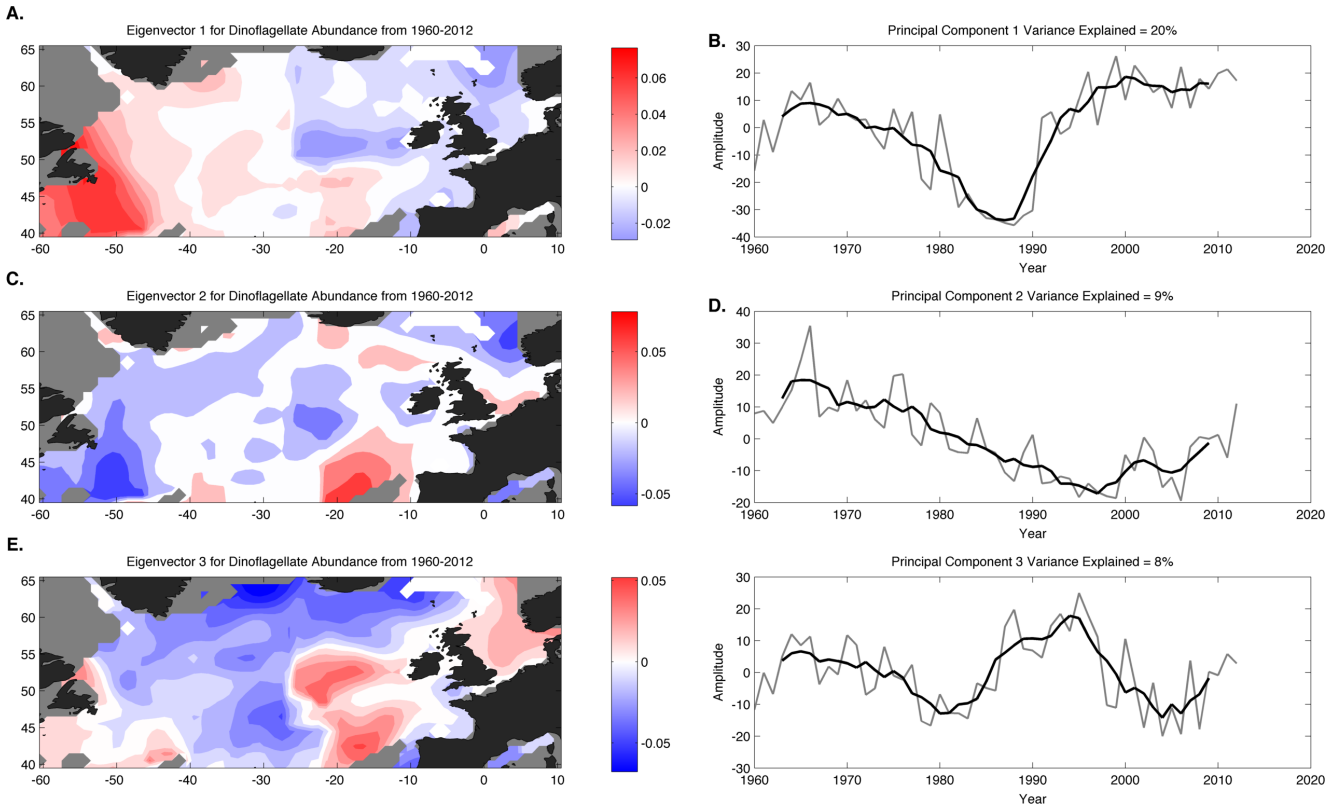

Figure 3.18: Long-term changes in annual dinoflagellate abundance from 1960 to 2012 in the North Atlantic. **A.** Map of the eigenvectors associated with principal component 1. **B.** Line plot of principal component 1 with the percentage of the variance explained. Plots **C. D. E.** and **F.** follow the same structure for principal components 2 and 3 respectively. The light grey line represents the annual principal components, and the black line represents the 5 year running mean. The eigenvectors show the correlations between changes in annual dinoflagellate abundance and the corresponding principal component.

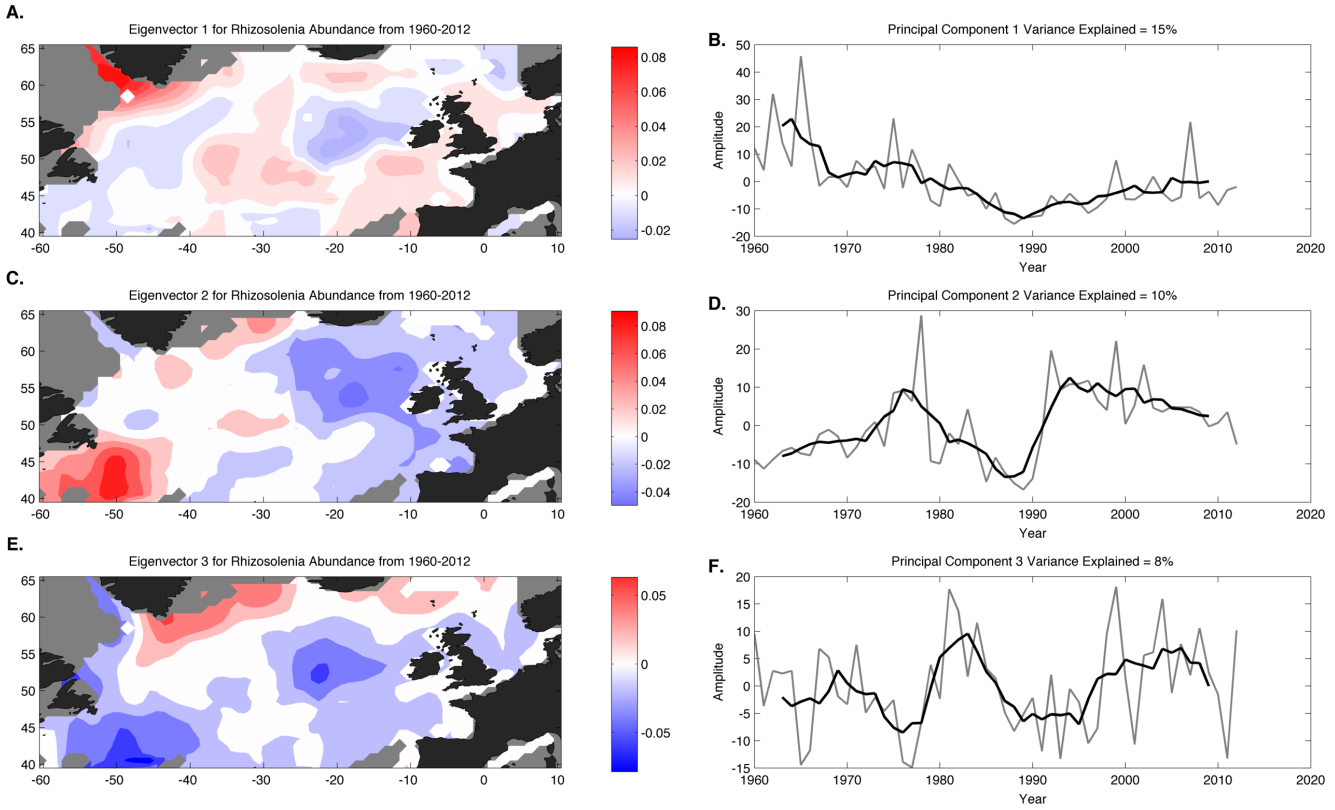

Figure 3.19: Long-term changes in annual *Rhizosolenia* abundance from 1960 to 2012 in the North Atlantic. **A.** Map of the eigenvectors associated with principal component 1. **B.** Line plot of principal component 1 with the percentage of the variance explained. **C. D. E.** and **F.** follow the same structure for principal components 2 and 3 respectively. The light grey line represents the annual principal components, and the black line represents the 5 year running mean. The eigenvectors show the correlations between changes in annual *Rhizosolenia* abundance and the corresponding principal component.

The linear trends were not removed from the data prior to running the PCA. Therefore the first principal component follows the linear trends which represents most of the variance in each of the variables. This is why figures 3.12**A** to 3.13**A**, and 3.16**A** to 3.19**A** resembles the linear trends in figures 3.5 to 3.9. It is important to note that when looking at the amplitude of the principal components and their associated eigenvector maps, that the sign of the principal components is interchangeable, and if it were to be inverted the associated eigenvectors would also be inverted.

The PCI and dinoflagellate principal components are very similar. However the associated eigenvector maps of principal component 1 show a strong east-west divide in dinoflagellate abundance and a general increasing trend across the whole of the North Atlantic for PCI (figure 3.16 and 3.18). The Grand Banks of Newfoundland is an area that shows a strong trend in the eigenvectors for all of the phytoplankton indices, with an oscillatory period of about 20 years.

Table 3.3: Pearson's correlation coefficients between phytoplankton indices principal components, SST and wind speed principal components and climate indices. Only those relationships with a significance value $> 95\%$ after accounting for temporal autocorrelation are shown (p-value < 0.05) (Pyper and Peterman, 1998).

Relationship	Correlation	Chelton p-value
DIA PC3 with AMO	-0.456	0.021
RHI PC3 with AMO	0.276	0.045
PCI PC3 with EAP	0.354	0.044
DIA PC3 with EAP	-0.468	0.007
PCI PC3 with NHT	0.399	0.039
DIA PC3 with NHT	-0.445	0.028
DIA PC3 with SST PC1	-0.451	0.034
RHI PC3 with SST PC1	0.275	0.046
DIA PC2 with SST PC2	0.400	0.046
RHI PC2 with SST PC2	-0.347	0.042
DIA PC1 with WS PC2	-0.652	0.037
DIN PC1 with WS PC2	-0.662	0.047

Table 3.3 shows the significant Pearson correlation coefficients after correcting for temporal autocorrelation (Pyper and Peterman, 1998) between each of the phytoplankton indices principal components and the climate variables principal components or the climate indices. The third principal component of PCI, diatoms

and *Rhizosolenia* follow a similar oscillatory period which was found to be significantly correlated with the EAP and the NHT for diatoms and PCI, and with the AMO for *Rhizosolenia* and diatoms. The third principal component of *Rhizosolenia* and Diatoms was found to be significantly correlated with principal component 1 of SST, and the second principal components of these two plankton indices were significantly correlated with principal component 2 of SST. The first principal components of diatoms and dinoflagellates were both found to be significantly correlated with principal component 2 of wind speed. As prinicipal component 2 of SST and wind speed and principal component 1 of SST were found to be correlated with the AMO and NAO (figures 3.14 and 3.15), this suggests that these climate indices are important drivers of the climate variability which in turn influences the plankton variability across the North Atlantic.

3.4.2 Regional long term trends in the North Atlantic

The CPR sampling method can introduce spatial bias, for example, that associated with the changing positions of sampling routes (Richardson *et al.*, 2006). Therefore in order to avoid this potential bias and assess variability on smaller spatial scales, the dataset was divided into smaller (approx. 10°by 10°) bio regions (figure 3.20).

A region designated the northeast Atlantic region was defined following the coordinates given in Hinder *et al.* (2012) (45° - 60°N; 15°W - 10°E). This region is shown in red in figure 3.20. Bio regions for further analysis were chosen based on standard CPR regions which were both adequately sampled throughout the time series and which showed a strong increase or decrease in phytoplankton abundance. Modified CPR standard areas were chosen for ease of comparison with previous CPR studies, but also because many follow continental edges and their size is optimal for the trade off between having sufficient CPR samples within the region without missing the spatial variability (Richardson *et al.*, 2006). These regions are designated numerically from east to west as regions 1 to 9, and shown in black in figure 3.20.

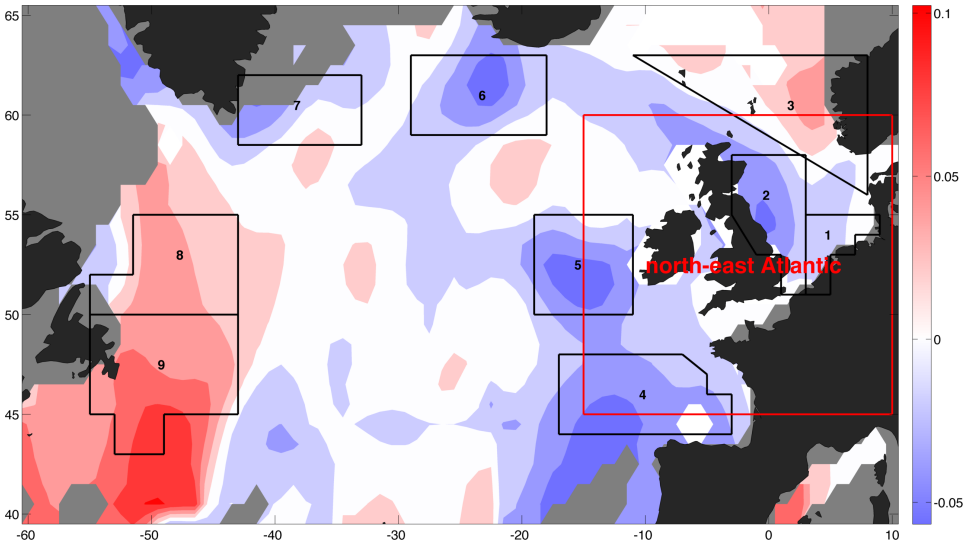

Figure 3.20: The mean linear trends in diatom and dinoflagellate abundance from 1960 to 2012 with modified CPR standard areas (bio regions) outlined and labelled as regions 1 to 9 in black, and the northeast Atlantic region labelled in red. Blue = mean decreasing trend, red = mean increasing trend.

The following figures (3.21 to 3.26) show the data from the northeast Atlantic region to assess the correspondence between the monthly sea surface temperature, wind speed and abundance of phytoplankton between 1960 and 2012.

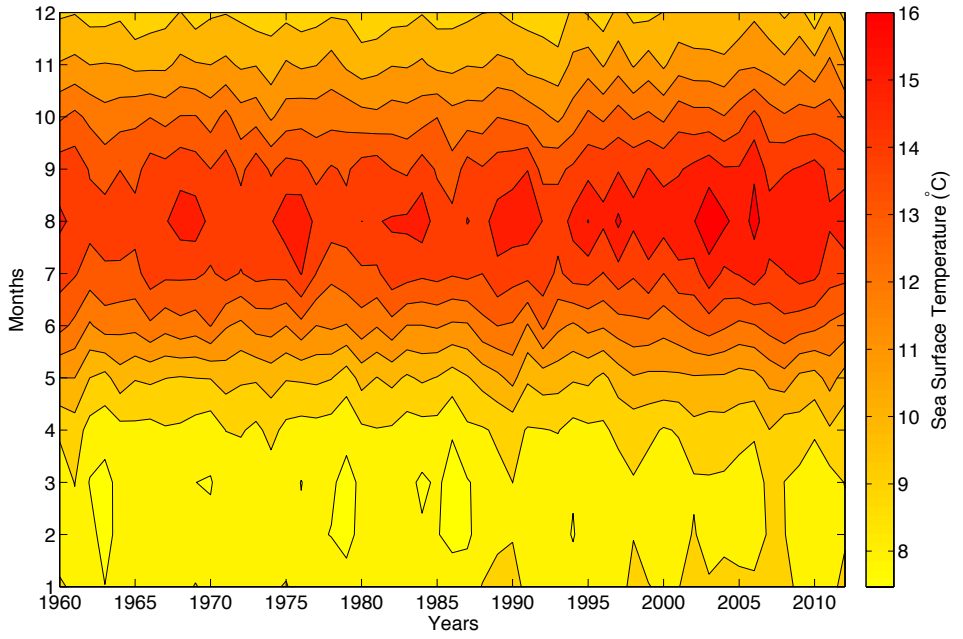

Figure 3.21: Hovmoller plot of monthly sea surface temperature from 1960-2012 in the North East Atlantic.

In the northeast Atlantic region SST and wind speed have increased in both the summer and winter months between 1960 and 2012 (figures 3.21 and 3.22).

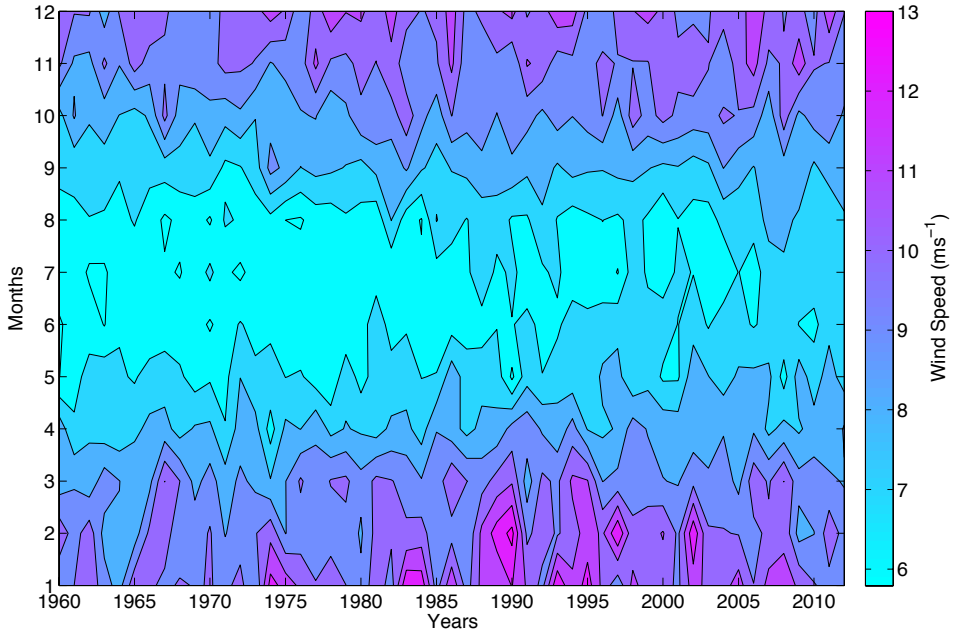

Figure 3.22: Hovmoller plot of monthly wind speed from 1960 to 2012 in the North East Atlantic.

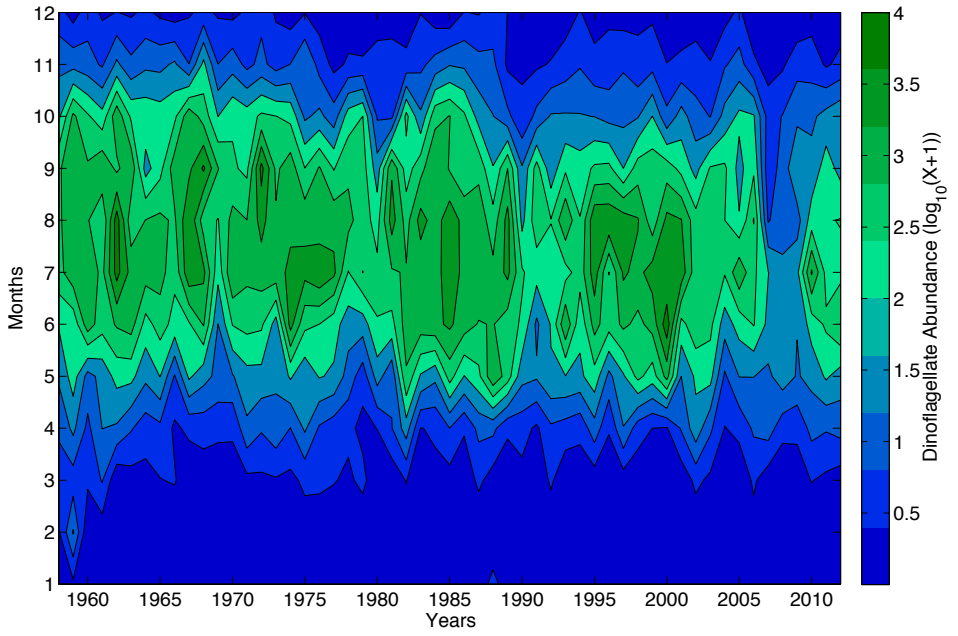

Figure 3.23: Hovmoller plot of monthly dinoflagellate abundance from 1958 to 2012 in the North East Atlantic.

In figure 3.22 during the period of low abundance of dinoflagellates (between 2006 and 2009) there is an increase in wind speed during the late summer and the autumn months (August, September and October) which corresponds to the lowest abundance in dinoflagellates (figure 3.23).

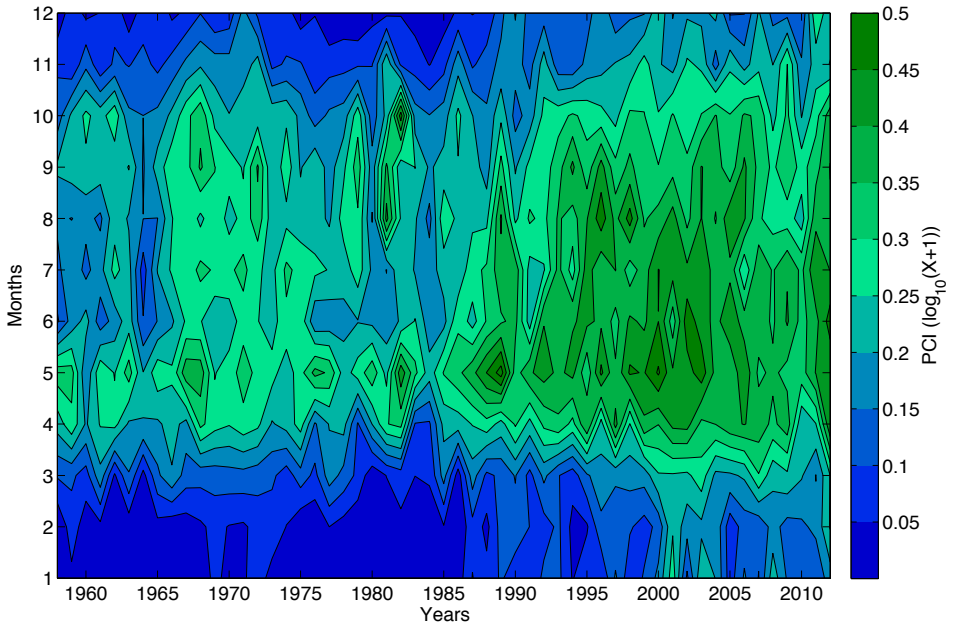

Figure 3.24: Hovmoller plot of monthly PCI from 1958 to 2012 in the North East Atlantic.

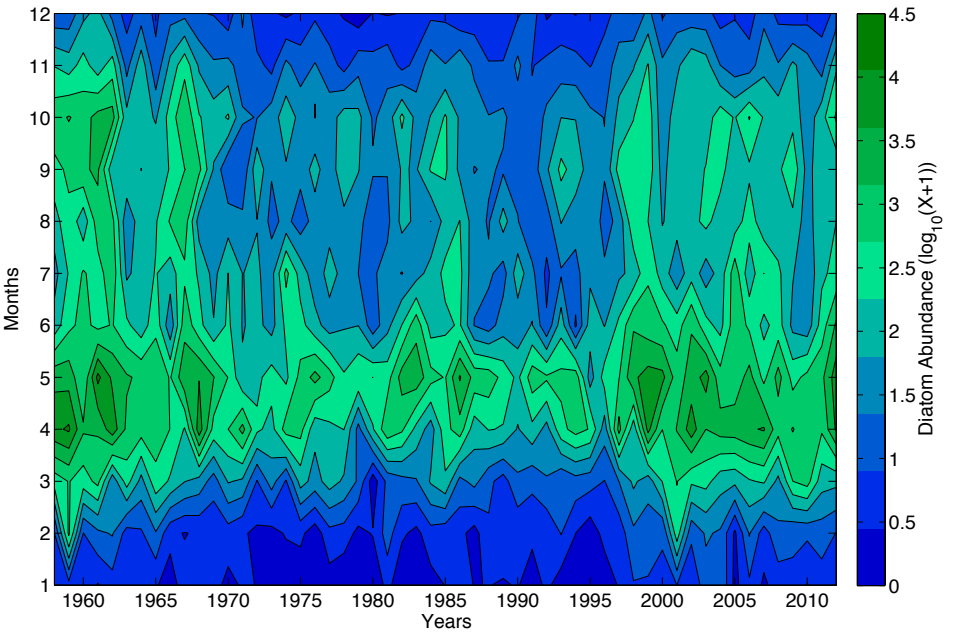

Figure 3.25: Hovmoller plot of monthly diatom abundance from 1958 to 2012 in the North East Atlantic.

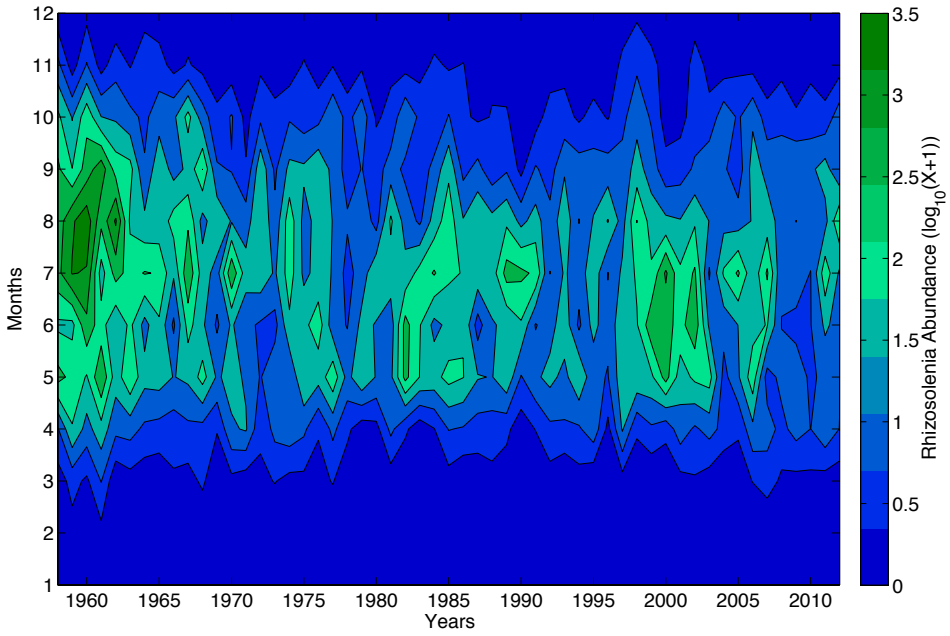

Figure 3.26: Hovmoller plot of monthly *Rhizosolenia* abundance from 1958 to 2012 in the North East Atlantic.

PCI has increased between 1958 and 2012 in the northeast Atlantic (figure 3.24). A decrease in diatom abundance can be seen during the autumn months around 2009 (figure 3.25). This decrease is more evident in the hovmoller plot of *Rhizosolenia* which are known to bloom later in the season than most diatom species, as they also show a large decrease in abundance during approximately the same period as the dinoflagellate index (between 2006 and 2010).

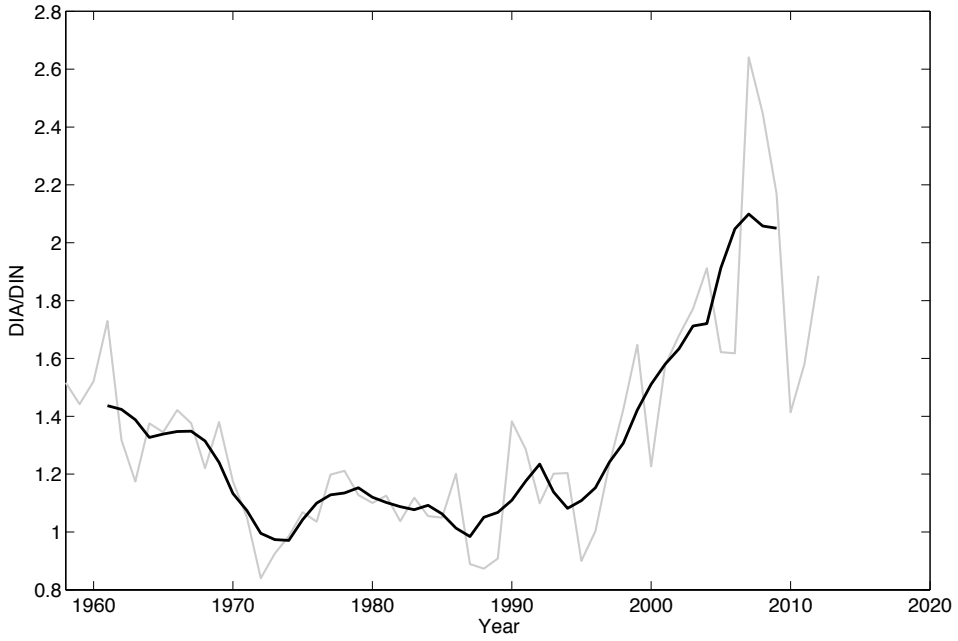

Figure 3.27: The ratio of diatom abundance ($\log_{10}(x+1)$)/dinoflagellate abundance ($\log_{10}(x+1)$) (DIA/DIN) in the northeast Atlantic region from 1958 to 2012. Light grey line represents the annual means, black line represents the 5 year running mean.

By plotting the ratio of diatom abundance to dinoflagellate abundance the decrease in dinoflagellates relative to diatoms is evident with a sharp increase in the ratio occurring between 1990 and 2009 (figure 3.27). The ratio drops in 2010, when the dinoflagellates recover their abundance, and then rises again towards the end of the time series.

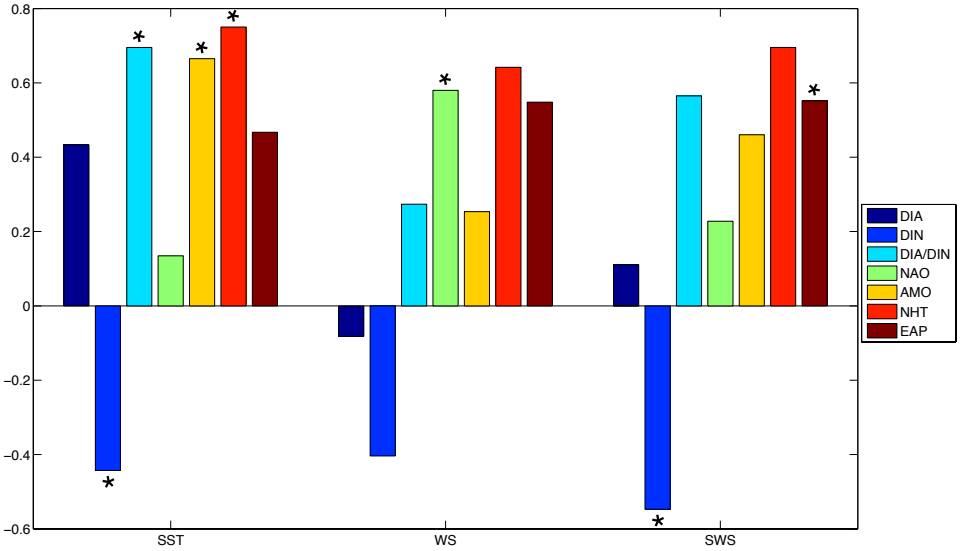

Figure 3.28: Pearson's correlation coefficients between annual SST, wind speed, summer wind speed (SWS), diatom and dinoflagellate abundance and climate indices in the northeast Atlantic from 1960 to 2012. After correcting for temporal autocorrelation, those coefficients with an asterisk were identified as significant (p-value$<$0.05) (Pyper and Peterman, 1998).

Figure 3.28 shows that dinoflagellate abundance is significantly negatively correlated with both SST and summer (June, July and August) wind speed (SWS). The ratio of diatom abundance relative to dinoflagellate abundance (DIA/DIN) is significantly positively correlated with SST, which in turn is significantly positively correlated with both the NHT and AMO in this region. Wind speed is significantly positively correlated with the NAO, but with no other indices after correcting for temporal autocorrelation. The summer wind speed however is not significantly correlated with the NAO, but was found to have a significant positive correlation with the EAP.

Using the monthly mean of the un-interpolated CPR data hovmoller plots were produced for each bio region (1 to 9), where the seasonal cycle and general linear trend (increasing or decreasing) can be observed (figure 3.29).

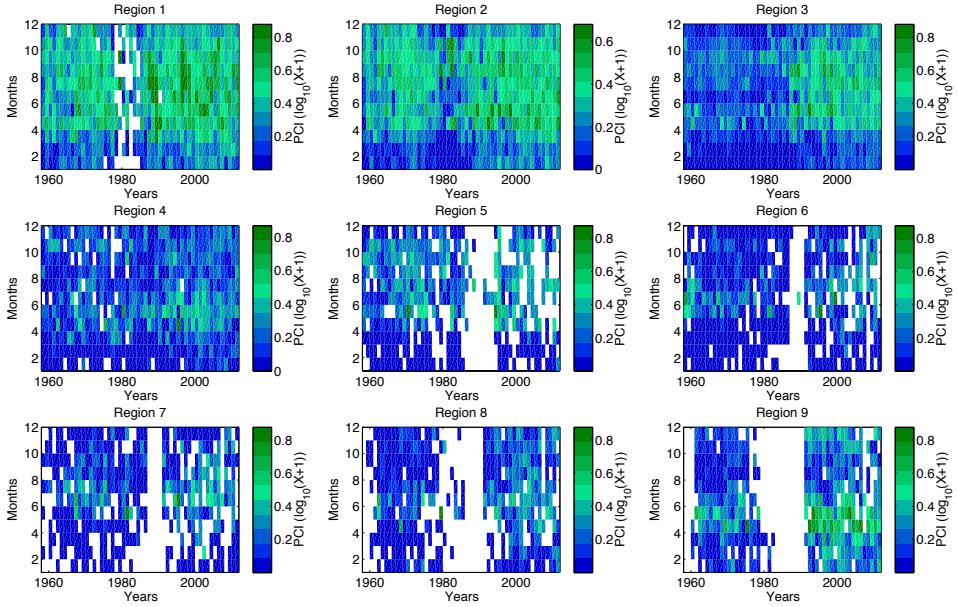

Figure 3.29: Hovmoller plot of monthly PCI from 1958 to 2012 in regions 1 to 9.

By applying the objective mapping interpolation method (section 3.3.3) used to map the linear trends and the principal component eigenvectors, the gaps within the CPR dataset were interpolated (figures 3.30 to 3.33).

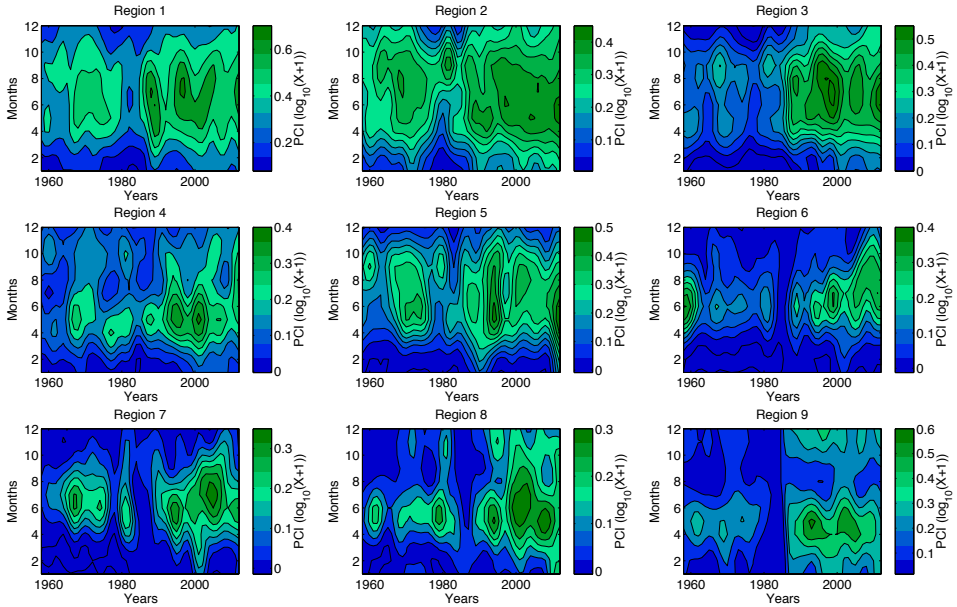

Figure 3.30: Hovmoller plot of interpolated monthly PCI from 1958 to 2012 in regions 1 to 9.

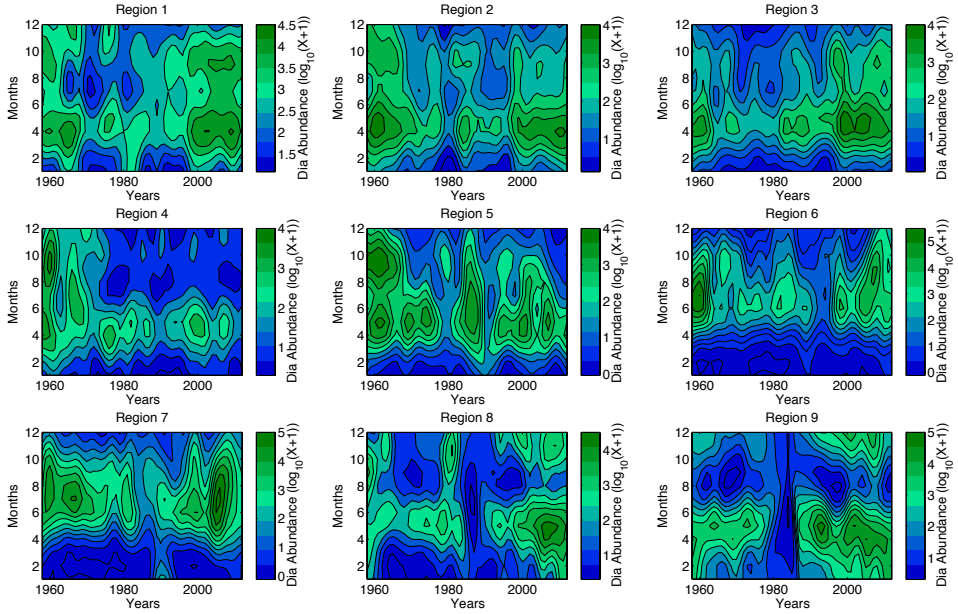

Figure 3.31: Hovmoller plot of interpolated monthly diatom abundance from 1958 to 2012 in regions 1 to 9.

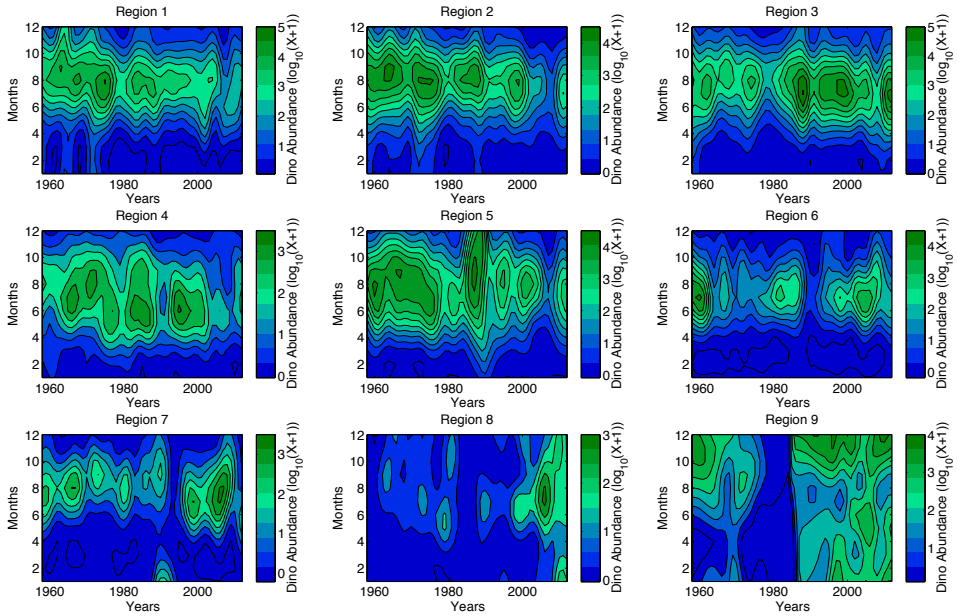

Figure 3.32: Hovmoller plot of interpolated monthly dinoflagellate abundance from 1958 to 2012 in regions 1 to 9.

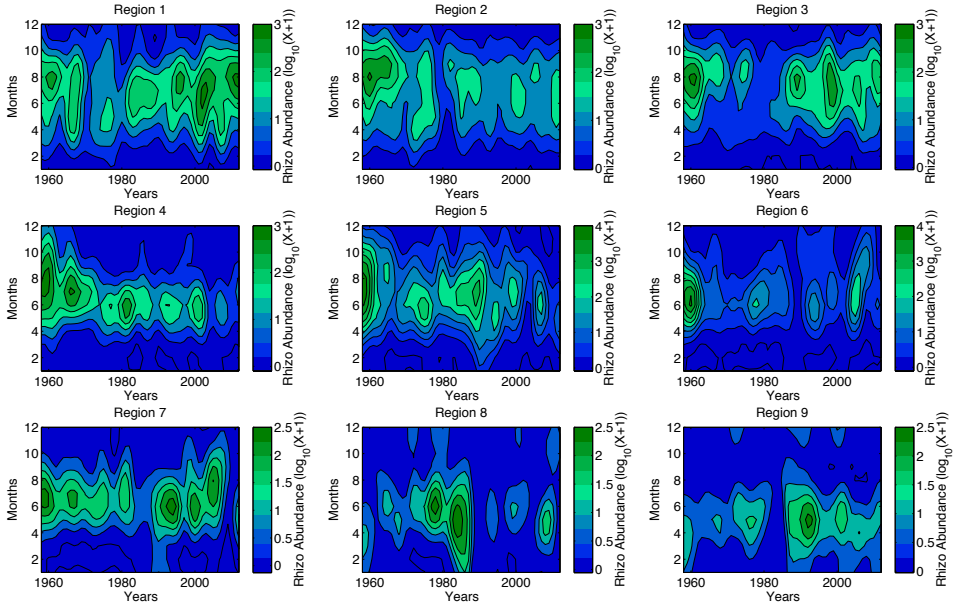

Figure 3.33: Hovmoller plot of interpolated monthly *Rhizosolenia* abundance from 1958 to 2012 in regions 1 to 9.

Hovmoller plots of sea surface temperature and wind speed were created to compare the seasonal and annual trends within each region (figures 3.34 and 3.35).

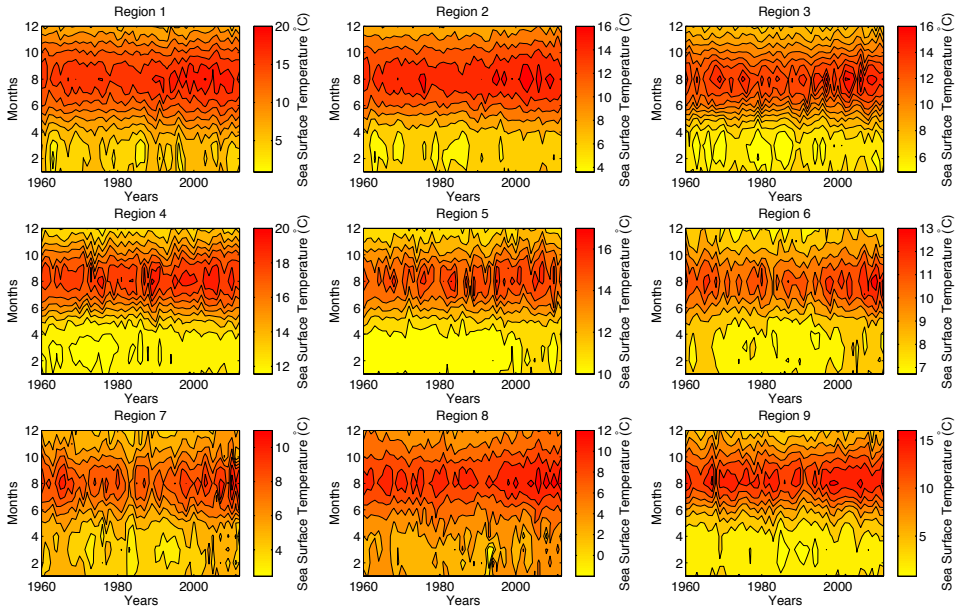

Figure 3.34: Hovmoller plot of monthly sea surface temperature from 1960 to 2012 in regions 1 to 9.

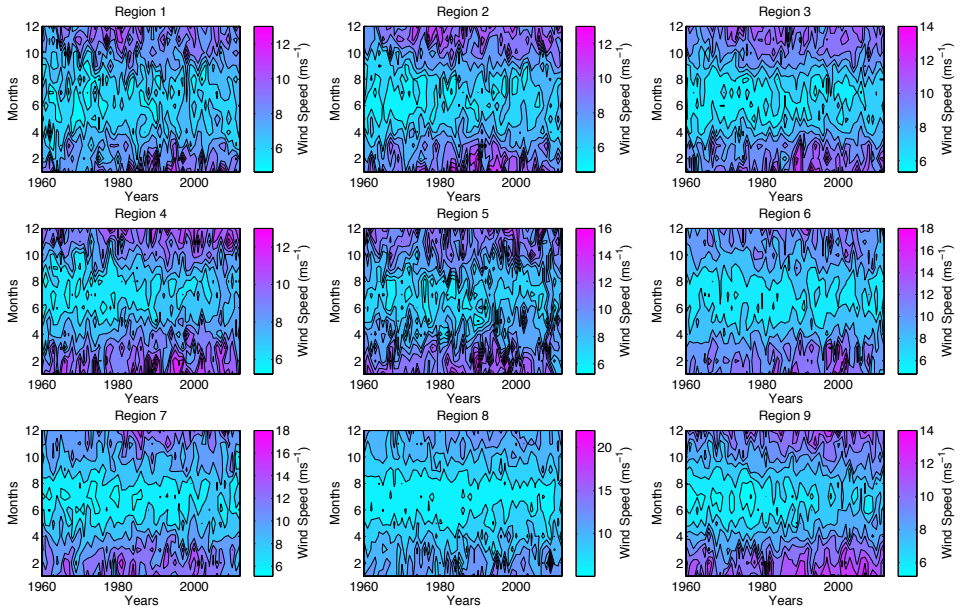

Figure 3.35: Hovmoller plot of monthly wind speed from 1960 to 2012 in regions 1 to 9.

Figures 3.30 to 3.33 demonstrate the different seasonal blooming times of each of the phytoplankton indices in each of the regions. High PCI occurs across most of the spring (months 3 to 5), summer (months 6 to 8) and autumn months (months 9 to 11) in regions 1 to 5, but in region 6 and 7 high PCI is more constrained to the summer months, and in regions 8 and 9 there is a spring/summer bloom and a separate late-autumn/winter bloom (figure 3.30). These seasonal trends are apparent in the remaining three plankton indices (figures 3.31 to 3.33), as they are incorporated into the PCI. However region 8 shows a strong increase in dinoflagellate abundance after 2000 (figure 3.32), suggesting that the PCI in the summer months within region 8 prior to this time was dominated by diatoms.

Figure 3.34 shows that the highest SST occurs in all regions in August. Region 1 has the largest range of SST from 0.9 °C to 20.2 °C. The lowest wind speeds occur around July in all 9 regions (figure 3.35). Region 8 experiences the largest range of wind speeds from 5.0 m s^{-1} to 23.3 m s^{-1}.

Figure 3.36 compares the linear trend in the un-interpolated annual abundance of each phytoplankton index with the linear trend of annual wind speed and sea surface temperature in regions 1 to 9 between 1960 and 2012, all of which were found to be significant.

The linear trends in the un-interpolated CPR data agree with the mapped linear

trends using the interpolated data (figures 3.5 to 3.9). Wind speed and SST show an increasing linear trend in all 9 regions. Regions 4 and 9 have the largest increase in wind speed, while regions 5 and 6 have the lowest increase. SST has increased most in region 1 and region 8, and has the lowest increasing trend in regions 5 and 9. PCI is also increasing in all 9 regions, with the lowest linear increase occurring in region 6, and the highest increase in region 3. All three phytoplankton indices (diatom, dinoflagellate and *Rhizosolenia* abundance) are decreasing in regions 2, 4, 5 and 6. Dinoflagellate abundance is decreasing in region 1, while both diatom and *Rhizosolenia* abundance is increasing. In region 3 dinoflagellate and diatom abundance are increasing while *Rhizosolenia* are showing a slight decrease in abundance. Diatom abundance is showing a decrease of only -0.0014 in region 7, while both dinoflagellates and *Rhizosolenia* are showing increases in abundance. Diatom and dinoflagellate abundance are increasing in region 8 and *Rhizosolenia* are decreasing by -0.0030. Region 9 shows the largest increasing trend for diatom (0.028), dinoflagellate (0.028), and *Rhizosolenia* (0.0058) abundance.

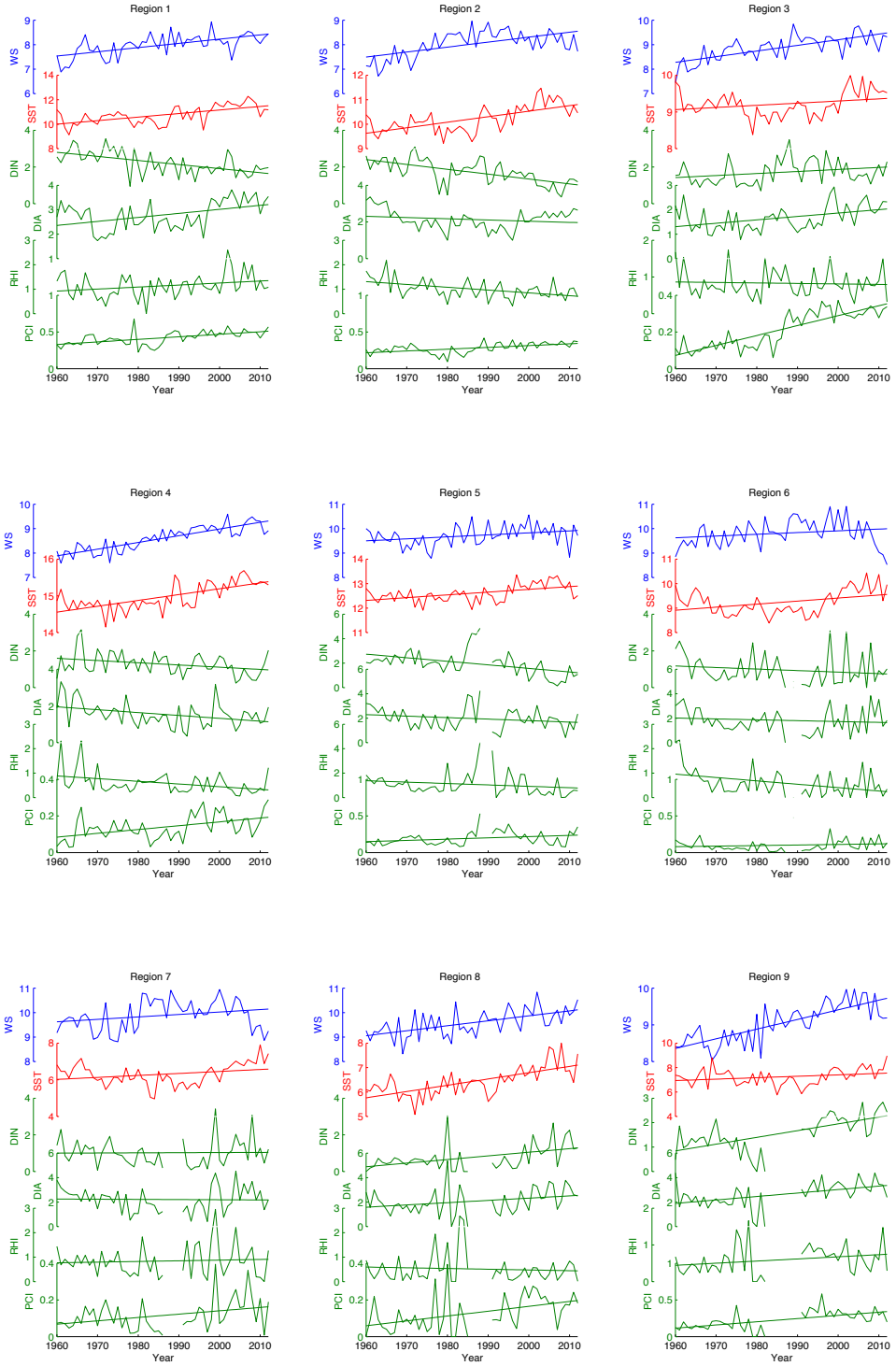

Figure 3.36: Line plots with linear trend lines of annual PCI, diatom, dinoflagellate, and *Rhizosolenia* abundance, sea surface temperature, and wind speed from 1960 to 2012 in regions 1 to 9.

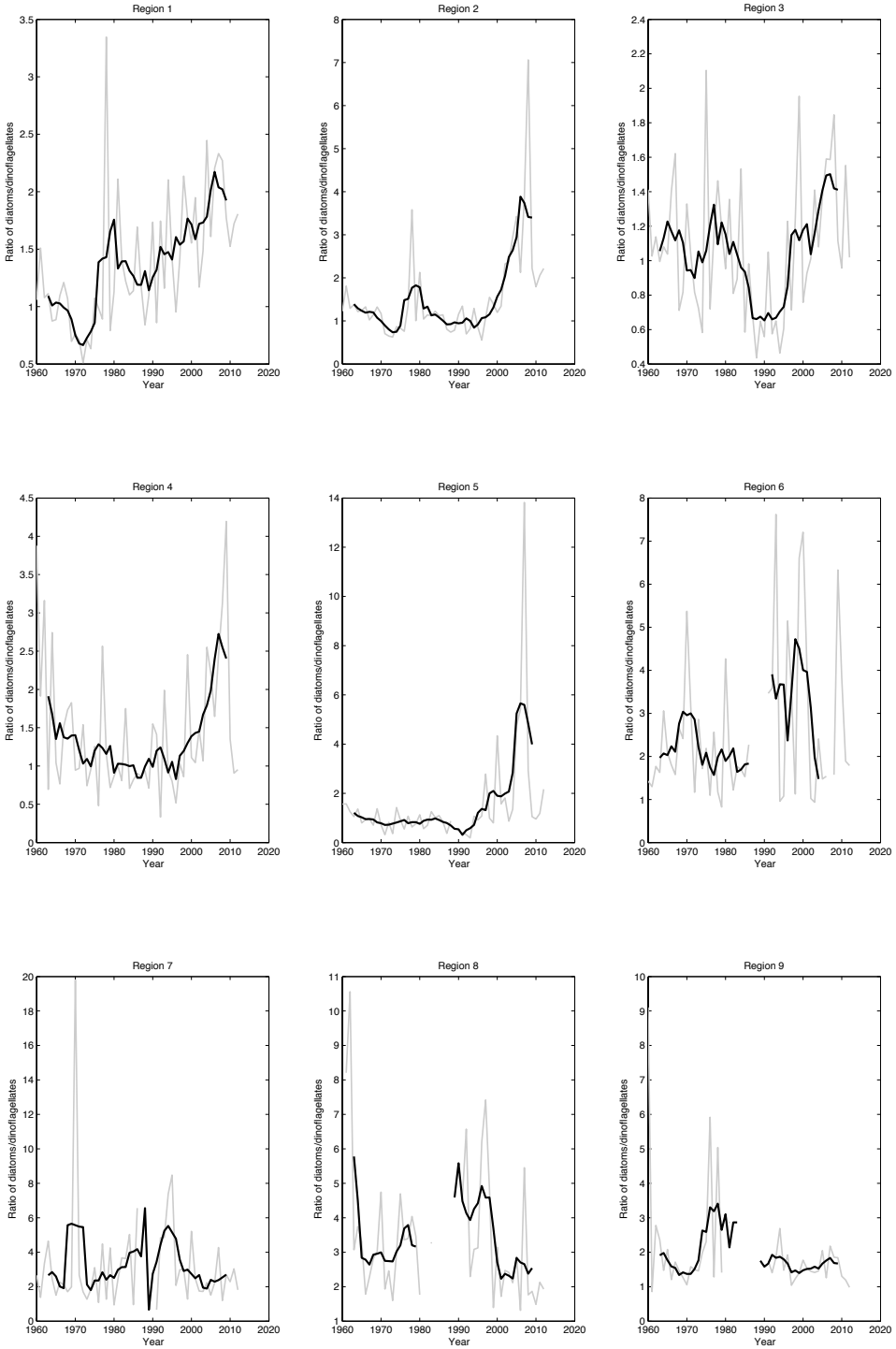

Figure 3.37: Line plots of the ratio of annual diatom abundance ($\log_{10}$ $(x + 1)$)/dinoflagellate abundance ($\log_{10}$ $(x + 1)$) in regions 1 to 9 from 1960 to 2012. Light grey line represents the annual means, black line represents the 5 year running mean.

The ratio of annual diatom to dinoflagellate abundance was plotted to assess the relationship between these two groups in each region (figure 3.37). Generally in all 9 regions diatom abundance is greater than dinoflagellate abundance. In region 1 there is a decrease in diatom abundance relative to dinoflagellate abundance

around 1970. In 1980 there is a peak in the ratio corresponding to the decrease in dinoflagellate abundance shown in figure 3.36. Region 2 shows two peaks in diatom abundance relative to dinoflagellate abundance occurring in 1978 and 2008. In region 3 there is a decrease in the ratio starting in 1985 that lasts roughly 10 years before diatom abundance starts to increase relative to the dinoflagellates. Region 4 and 5 show a peak in the ratio in 2009 and 2007 respectively. Regions 6 to 9 have some gaps in the data but diatoms consistently have a higher abundance than dinoflagellates.

Figure 3.38 shows the Pearson's correlation coefficients between annual SST, wind speed, summer wind speed and phytoplankton and climate indices in each region. Summer wind speed was added as a climate variable because the variation in mixing due to wind speeds during the summer months (June, July and August) has been linked to varying phytoplankton abundance (Hinder *et al.*, 2012). Within regions 1 to 9 the temporal autocorrelation and 95% confidence intervals were plotted for each variable to assess the amount of autocorrelation present. SST had the most autocorrelation associated with it, while diatom abundance showed the least temporal autocorrelation (see appendix A section A.3 for further details). Those correlations that were found to be significant after correcting for autorcorrelation are also listed in table format in appendix A table A.1.

The NAO is significantly positively correlated with wind speed in regions 1, 2, 3, 4 and 5, and is significantly positively correlated with SST in region 1 while being negatively correlated with SST in regions 3, 6 and 7. The AMO is significantly positively correlated with SST in regions 4, 5, 6, 7, 8 and 9. In region 1 dinoflagellate abundance is significantly negatively correlated with wind speed, while in regions 2 and 4 there is a significant negative correlation with summer wind speed, and in region 5 dinoflagellates are significantly negatively correlated with SST. Diatom abundance is significantly positively correlated with SST in region 1 and significantly positively correlated with wind speed in region 9, as is PCI with wind speed and summer wind speed in region 9. The ratio of diatom abundance to dinoflagellate abundance is significantly positively correlated with SST in regions 1 and 5, and there is also a significant positive relationship with summer

wind speed in regions 1 and 2, whereas in regions 7 and 9 this ratio is significantly negatively correlated with summer wind speed.

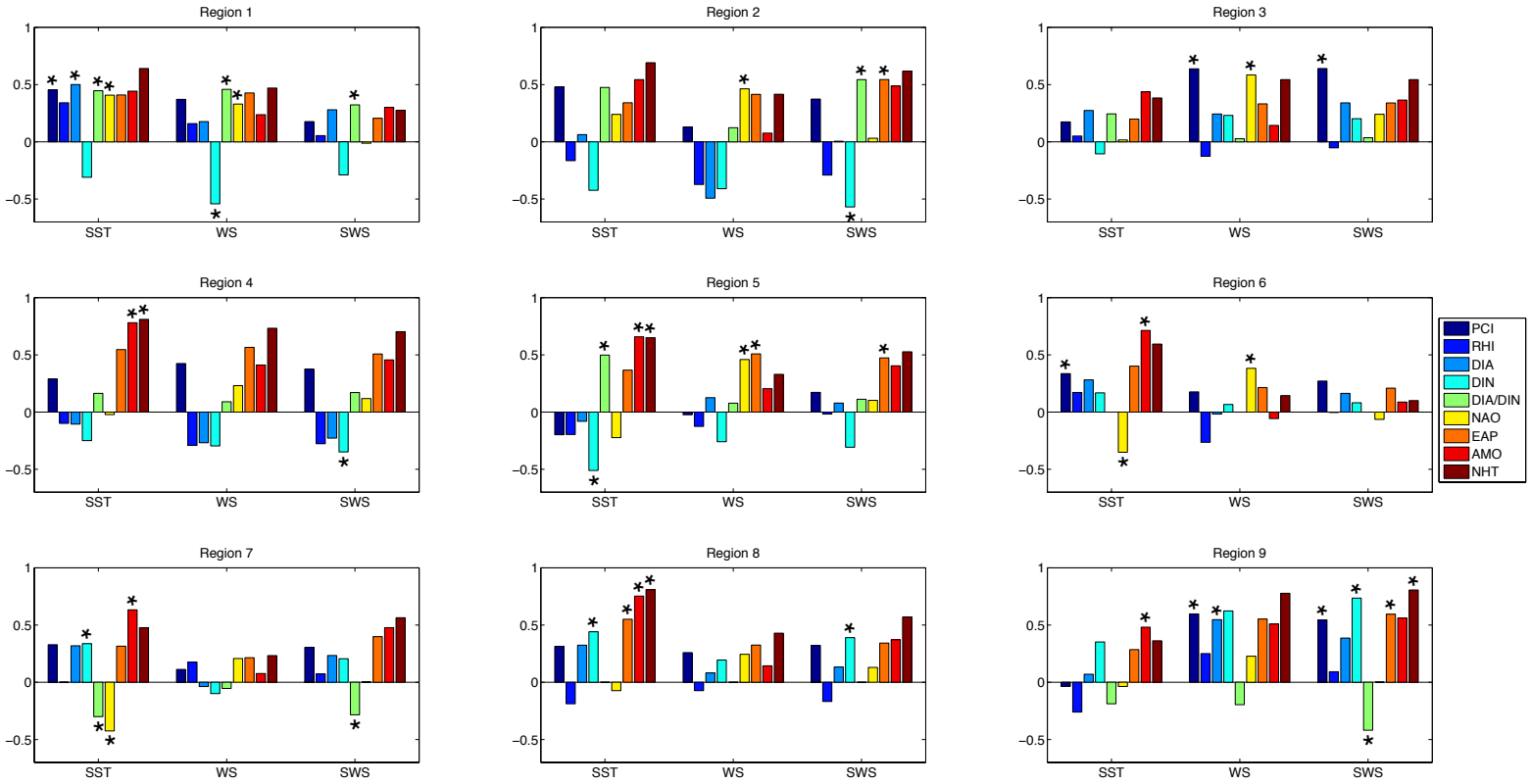

Figure 3.38: Pearson's correlation coefficients between annual SST, wind speed, summer wind speed, and phytoplankton and climate indices in regions 1 to 9 from 1960 to 2012. After correcting for temporal autocorrelation, those coefficients with an asterisk were identified as significant (p-value<0.05) (Pyper and Peterman, 1998).

PCA was applied to each region to analyse the relationships between annual phytoplankton abundance, SST and wind speed regionally (figure 3.39).

The first principal components' loadings follow the linear trends seen in figure 3.36 and many of the correlations in figure 3.38. For example, in region 1 principal component 1 (PC1) for dinoflagellate abundance is anti-correlated with all of the other variables because this was the only variable that showed a decreasing trend in this region.

Principal component 2 suggests that wind speed has a high loading in regions 1, 3, 5, 6, and 7, while SST has a high loading in regions 2, 7, 8 and 9. The highest variance explained by the first three principal components of these variables was in region 9, where 87% of the variance could be explained.

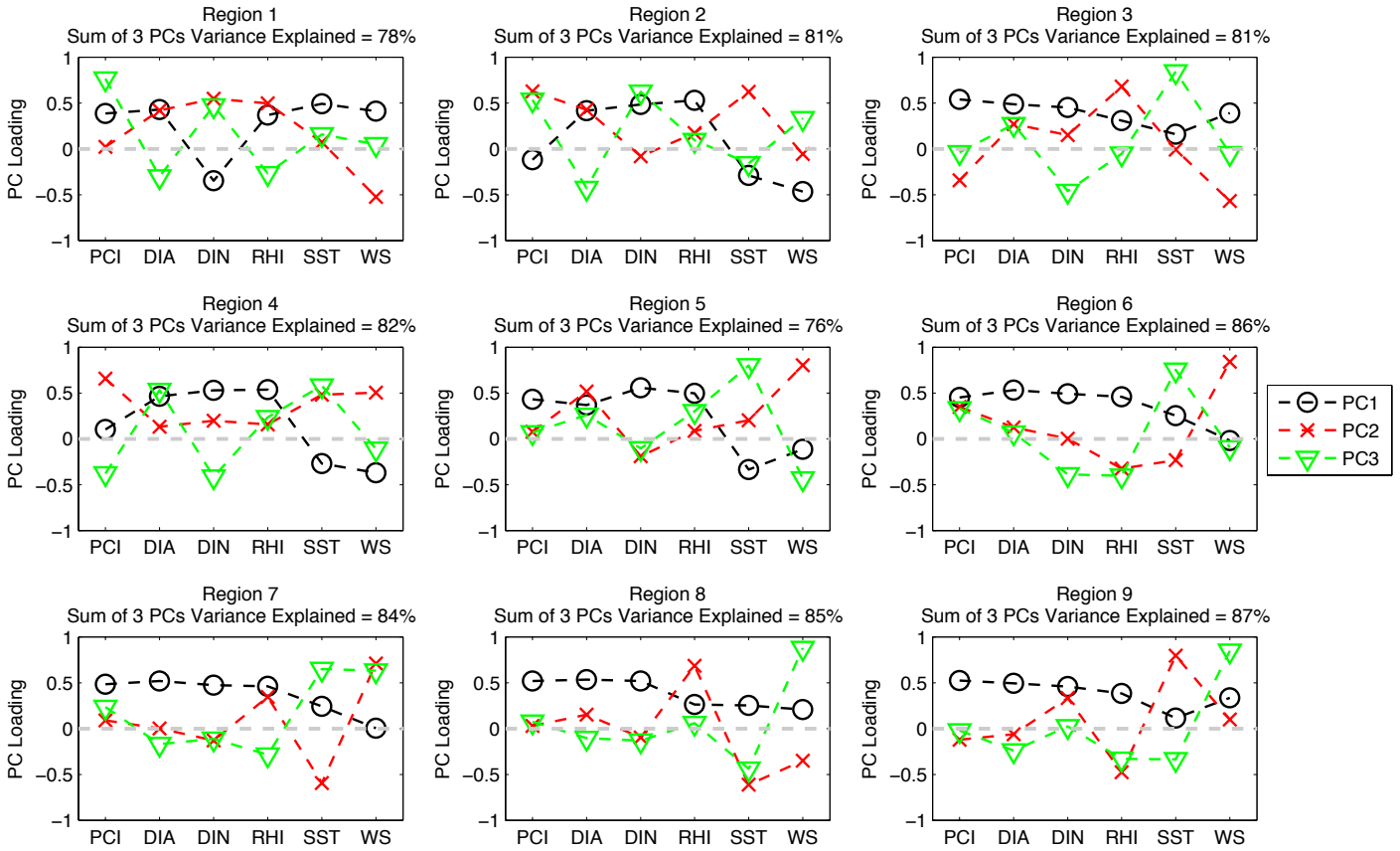

Figure 3.39: Line plot of the loadings of principal components 1, 2 and 3 when comparing different phytoplankton indices with sea surface temperature and wind speed from 1960 to 2012 in regions 1 to 9, with the variance explained by the sum of all three principal components displayed in the title.

3.5 Discussion

3.5.1 Long term trends in the North Atlantic

The region in which the CPR data have been analysed has been extended from that used in previous studies (Beaugrand *et al.*, 2012; Hinder *et al.*, 2012; Edwards *et al.*, 2013; Harris *et al.*, 2013) to include the western part of the North Atlantic by using objective mapping to interpolate the CPR data, and extended up to the year 2012.

PCI was shown to be increasing across most of the North Atlantic (figure 3.6), which agrees with the findings from both McQuatters-Gollop *et al.* (2011) and Harris *et al.* (2013). These studies suggest that temperature is the main driver of this increase, with Harris *et al.* (2013) stating that in the northeast Atlantic almost 50% of the variation in PCI was driven by warming effects. Our findings agree with these results, as across the North Atlantic 59% of the linear trends in PCI were found to be positively congruent with the increasing linear trends in SST (table 3.2).

Both SST and wind speed have increased from 1960-2012 in most regions of the North Atlantic (figure 3.5), and the trend in SST was found to be positively congruent with wind speed in the southern part of the North Atlantic and negatively congruent in the subpolar North Atlantic. This north-south dipole can be seen in the second principal component of SST (figure 3.12), and was found to be significantly correlated with the NAO (figure 3.14), suggesting that the NAO has important influences on both wind speed and SST across the North Atlantic. The influence of the NAO is strongest in regions where the second principal component of SST has more influence, such as the North Sea (figure 3.14). This agrees with Harris *et al.* (2013) who found that the NAO showed no time lag in the northeast Atlantic when compared with SST principal components, while both the NHT and AMO had a 9 year lag, which was linked to the strong influence of the NAO in the North Sea. The regional dipole seen in PC2 in figure 3.12 also agrees with Sarmiento and Gruber (2006) who describe periods of high NAO causing low SSTs in the Labrador Sea, and high SSTs in the Norwegian Sea and subtropical gyre.

The correlation of the first principal component of SST with the AMO concurs

with Harris *et al.* (2013). However they found that the second and third principal component of SST in the North Atlantic were correlated with EAP and NAO respectively. Both our study and Harris *et al.* (2013) found that the significance of the correlation with EAP was weaker than the correlations between other principal components. The likely reason for this variation in correlations is due to the weak significance of the EAP signal but also could be because Harris *et al.* (2013) de-trended the SST data and used a shorter time-series (1960 to 2009).

Edwards *et al.* (2013) found that the AMO is the underlying mechanism behind a number of biological trends in the North Atlantic, as it was found to correlate with the second principal component of SST which was linked to a cascade of dependant variables such as phytoplankton, zooplankton and fisheries stocks. Our study found the AMO to be strongly correlated with both wind speed and SST (see figures 3.14 and 3.15).

The highest significance within the phytoplankton principal component correlations was between principal component 3 for diatoms and the EAP, AMO and NHT (table 3.3), suggesting that the EAP, AMO and NHT play important roles in the abundance of this phytoplankton group within the North Atlantic. The AMO, NHT, and NAO were also significantly correlated with the principal components of wind speed and SST (figures 3.15 and 3.14). There have been tentative links made between increasing wind speeds over northern and central Europe with modelled climate scenarios, suggesting that increased warming could cause variations in teleconnections such as the AMO and NAO, therefore influencing the wind speed trends (Leckebusch and Ulbrich, 2004; Pryor *et al.*, 2005). Our results agree with Edwards *et al.* (2013) that the AMO is an important mode in the North Atlantic climate variability, and that the combination of the increasing trend in the NHT is the main driver of the rapid warming seen across the North Atlantic responsible for abrupt temperature mediated regime shifts that have been occurring. It is evident that climate indices play a significant role in the variability of both SST and wind speed in the North Atlantic, which in turn influences the variability of phytoplankton indices. This cascade is therefore likely to be regionally dependent as these climatic modes have shown regional variation (figures 3.12 and 3.13).

3.5.2 Drivers of regional variability in the North Atlantic

Figures 3.6 to 3.9 demonstrate that phytoplankton show regional variability and variation between phytoplankton groups. The likely key drivers of this variability are wind speed and SST, as they influence both the distribution and timing of blooms, and explain a large percentage of the variance in the phytoplankton data (figure 3.10).

Climate variability is in turn influenced by underlying mechanisms which are often driven by climate indices such as the NAO, NHT, EAP and AMO. As discussed previously these modes show regional variation which may also influence the regional variability in phytoplankton.

Hinder *et al.* (2012) evaluated the abundance of phytoplankton indices from 1960 - 2009 within the North East Atlantic (45° - 60°N; 15°W - 10°E), concluding that the increase in abundance of diatoms relative to dinoflagellates was due to increased SST and summertime mixing. Our results agree with Hinder *et al.* (2012) as we found that the diatom to dinoflagellate ratio was significantly correlated with SST and that dinoflagellate abundance was significantly negatively correlated with both SST and summer wind speed (figure 3.28).

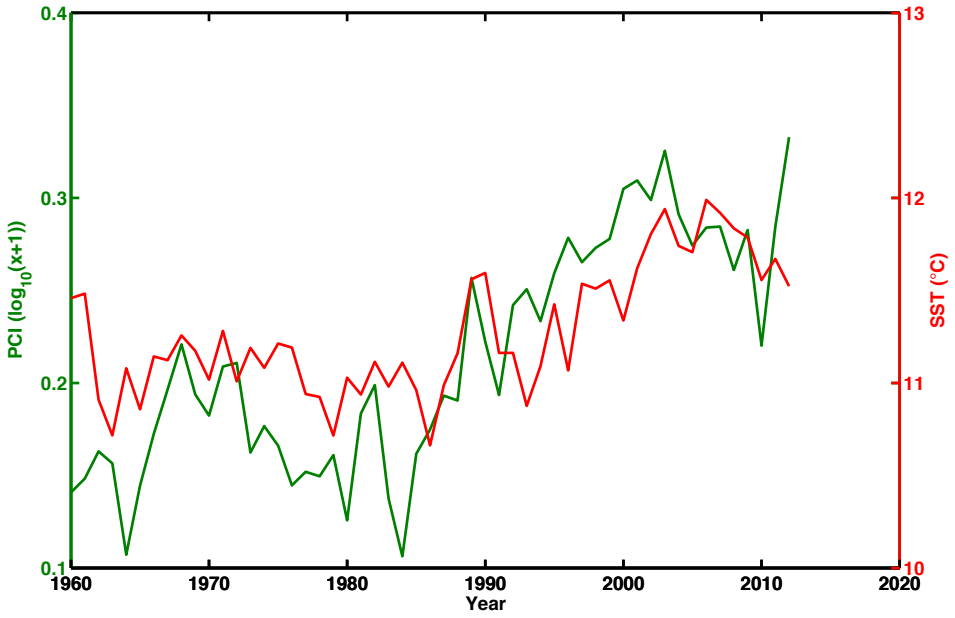

Figure 3.40: Annual phytoplankton colour index (PCI) (green), with sea surface temperature (SST) (red) from 1960-2012 in the northeast Atlantic region.

Although the PCI showed an increase from 1960-2012 in the northeast Atlantic (figures 3.24 and 3.40), there is not an evident increase in either of the other phytoplankton indices, suggesting that perhaps smaller phytoplankton species are increasingly dominating the region. There is a significant positive correlation of PCI with SST ($p<0.05$ after correcting for temporal autocorrelation, figure 3.40). This supports modelled predictions of increased stratification from global warming reducing the upward flux of nutrients, and therefore allowing smaller phytoplankton to out-compete some of the larger (more nutrient dependant) species such as diatoms (Bopp *et al.*, 2005). This may have negative implications for both the flux of carbon due to reduced export efficiencies, and the complexity of food webs which can impact on fisheries (Beaugrand *et al.*, 2010).

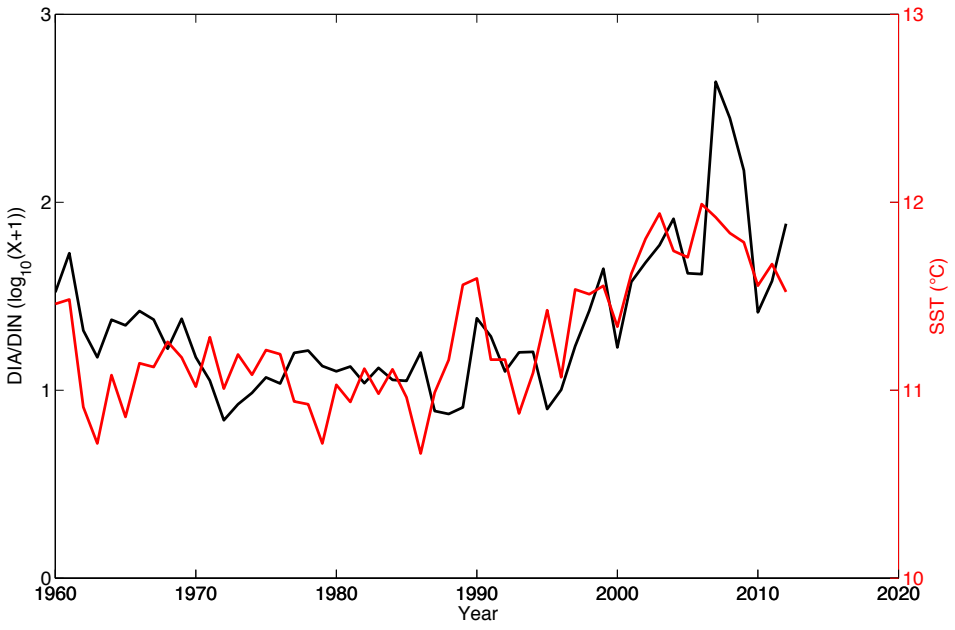

Figure 3.41: Ratio of diatom abundance and dinoflagellate abundance (black), SST (red) from 1960-2012 in the northeast Atlantic region.

Figure 3.41 demonstrates the significant positive correlation of SST with the diatom to dinoflagellate ratio (figure 3.28). As SST precedes the ratio of diatom to dinoflagellate abundance this suggests that SST is the main driver of this trend in the northeast Atlantic. It is likely that there are a number of different environmental factors linked to the increased diatom abundance relative to dinoflagellate abundance. The possible mechanisms involving SST could be that increased SST

is linked with increased stratification, which during periods that are usually associated with high turbulence, would allow diatoms to bloom and perhaps prolong their growth period allowing them to out-compete dinoflagellates (Barton *et al.*, 2015). The first principal component of SST follows the linear trend of SST in the North Atlantic, which was found to be significantly correlated with the AMO. This again agrees with Edwards *et al.* (2013) suggesting that the AMO is a key driver of phytoplankton trends in this region. The abundance of dinoflagellates increases in 2010, which can be seen clearly by a sharp drop in the ratio of diatom to dinoflagellate abundance. This peak occurs at the same time as a strong negative NAO index ($>$1 standard deviation from the mean (Henson *et al.*, 2012)). Henson *et al.* (2012) investigated the abundance of diatom and dinoflagellate abundance around the Porcupine Abyssal Plain (PAP) site, which lies within our northeast Atlantic region, and showed that during strong negative NAO indices dinoflagellates bloom more intensely and the blooms can last for double the long-term mean. This trend was suggested as being due to a decrease in westerly winds linked with negative phases of the NAO allowing dinoflagellates to outcompete diatoms in more stratified, warm and nutrient poor conditions (Henson *et al.*, 2012). Our results found that the second principal component of SST in the North Atlantic was significantly correlated with the NAO, which also showed a strong peak in the loadings in 2010 which corresponds to the strong negative NAO index (figure 3.14). Wind speed was found to be significantly correlated with the NAO in this region, and summer wind speed was significantly correlated with the EAP and significantly anti-correlated with the diatom to dinoflagellate ratio. Both the NAO and EAP have been shown to have similar characteristics, with a north-south dipole and similar centres within the North Atlantic (figure 3.12 and 3.14) (Harris *et al.*, 2013). These results suggest that the diatom to dinoflagellate ratio in the northeast Atlantic is primarily driven by the SST in this region, which in turn is significantly influenced by the AMO and NAO.

The differing linear trends (figure 3.36) and significant correlations (figure 3.38) seen in regions 1 to 9 demonstrate the regional variability and the importance of selecting regions that are small enough to investigate this variability.

Region 1 lies within the southern North Sea and was found to show a significant linear trend of increasing diatom abundance and decreasing dinoflagellate abundance (figure 3.36). These trends were found to be significantly correlated with both SST and wind speed, with SST influencing the increase in diatom abundance and wind speed driving the decrease seen in dinoflagellate abundance, and therefore both had significant impacts on the diatom to dinoflagellate ratio (figure 3.38). Both SST and wind speed have increased in this region, and were found to have a significant correlation with the NAO. The NAO is thought to be more prevalent within this region of the North Atlantic, as one of its centres is within the North Sea (Barnston and Livezey, 1987; Harris *et al.*, 2013). This suggests that this is the main driver of the climate which in turn is influencing the dominance of diatom abundance over dinoflagellates in this region.

Region 9 is on the west of the North Atlantic, close to the Grand Banks of Newfoundland. All four phytoplankton indices showed a significant increasing trend in this region after a gap in the CPR dataset in the 1980's, with dinoflagellates and diatoms increasing the most over the time period. Although SST has increased in this region, the linear trend was 0.01 ($^{\circ}$C yr^{-1}) and no significant correlations with the phytoplankton indices were found, whereas the linear trend in wind speed was 0.03 (m s^{-1} yr^{-1}) and there were significant correlations between both PCI and diatom abundance (figure 3.38). There was also a significant correlation between summer wind speeds and dinoflagellate abundance in this region. These results suggest that wind speed is the main driver of phytoplankton abundance in region 9, as wind-driven Ekman transport is an important surface flow driver in this region (Pepin *et al.*, 2013), which is likely to influence the entrainment of nutrients into the photic zone allowing a greater abundance of phytoplankton to bloom. This agrees with the conclusion made by Barton *et al.* (2015) that the physical environment within the North Atlantic drives the seasonal variability of phytoplankton.

3.6 Summary

The relationships between climate and phytoplankton are complex, often creating regional variability which is crucial to investigate in order to improve our understanding. This study demonstrates the importance of selecting regions that are at an optimum size to detect significant relationships as well as identify the differing trends between regions. Wind speed plays a crucial role in phytoplankton abundance, with the increase in wind speed in the Grand Banks of Newfoundland driving the increase in both diatom and dinoflagellate abundance since the 1980's. The influence of climate indices such as the NAO and AMO on the climate in the North Atlantic is evident, with both contributing to the changes in diatom and dinoflagellate abundance seen in the northeast Atlantic. The increase in PCI in the northeast Atlantic is driven by increasing SST, which is not represented in the other phytoplankton indices. This supports the suggestion that increased stratification due to warming may allow smaller phytoplankton to increase in abundance relative to larger species due to differences in nutrient demands. This has implications for both the export of carbon, and the ecosystem dynamics within this important fisheries region.

Chapter 4

Net community production in the North Atlantic

The work presented in the following chapter has been published in:

Net community production in the North Atlantic Ocean derived from Volunteer Observing Ship data

Clare Ostle[1,2], Martin Johnson[1,3], Peter Landschützer[1,4], Ute Schuster[1,5], Susan Hartman [6], Tom Hull[3,1], and Carol Robinson [1].

[1]Centre for Ocean and Atmospheric Sciences (COAS), School of Environmental Sciences, University of East Anglia, Norwich, UK.

[2]Sir Alister Hardy Foundation for Ocean Science (SAHFOS), Plymouth, UK.

[3]Centre for Environment Fisheries and Aquaculture Science (CEFAS), Lowestoft, UK.

[4]Institute of Biogeochemistry and Pollutant Dynamics, ETH Zürich, Zürich, Switzerland.

[5]College of Life and Environmental Sciences, University of Exeter, Exeter, UK.

[6]National Oceanography Centre, Southampton, UK.

Global Biogeochemical Cycles, 2015, 29, 80-95, doi:10.1002/2014GB004868.

The work and analysis presented in this chapter was undertaken by C. Ostle. Co-authors on this publication provided guidance and suggestions regarding the analysis and the results.

4.1 Abstract

The magnitude of marine plankton net community production (NCP) is indicative of both the biologically driven exchange of carbon dioxide between the atmosphere and the surface ocean, and the export of organic carbon from the surface ocean to the ocean interior. In this study the seasonal variability in the NCP of five biogeochemical regions in the North Atlantic was determined from measurements of surface water dissolved oxygen and dissolved inorganic carbon (DIC) sampled from a Volunteer Observing Ship (VOS). The magnitude of NCP derived from dissolved oxygen measurements (NCP_{O_2}) was consistent with previous geochemical estimates of NCP in the North Atlantic, with an average annual NCP_{O_2} of 9.5 $\pm$6.5 mmol O_2 m^{-2} d^{-1}. Annual NCP_{O_2} did not vary significantly over 35 degrees of latitude, and was not significantly different from NCP derived from DIC measurements (NCP_{DIC}). The relatively simple method described here is applicable to any VOS route on which surface water dissolved oxygen concentrations can be accurately measured, thus providing estimates of NCP at higher spatial and temporal resolution than currently achieved.

4.2 Introduction

The global cycling of oxygen and carbon is regulated by the interactions between oceanic physical and biogeochemical processes including mixing and plankton respiration and photosynthesis. The solubilities of oxygen (O_2) and carbon dioxide (CO_2) are inversely proportional to temperature, so the seasonality of the saturation concentrations of these gases correlates with seasonal temperature changes (Boyer *et al.*, 1999). The concentrations of O_2 and CO_2 are further influenced by physical processes including bubble injection (Woolf and Thorpe, 1991), and

mixing of deep, often oxygen deplete and CO_2 replete waters into the mixed layer with associated increased nutrient concentrations stimulating biological production. Heterotrophic oxidation (respiration) leads to the production of dissolved inorganic carbon (DIC) whereas autotrophy (photosynthesis) leads to a reduction of DIC (Falkowski, 1998). Improved measurements of respiration and photosynthesis and the processes that determine their variability will aid our prediction of their responses to natural and anthropogenic forcings (Najjar and Keeling, 2000; Lee, 2001).

Net Community Production (NCP; *sensu* (Williams, 1993)), indicates the balance between production of organic carbon by autotrophs (P) and production of CO_2 by heterotrophs (R) at the time and space scale of the measurement technique used (Serret *et al.*, 2009). The metabolic state of a system can be defined by NCP (=P-R); with autotrophic systems occurring when gross primary production is greater than respiration, and heterotrophic systems occurring when respiration is greater than primary production (Ducklow and Doney, 2013) (see figure 4.1).

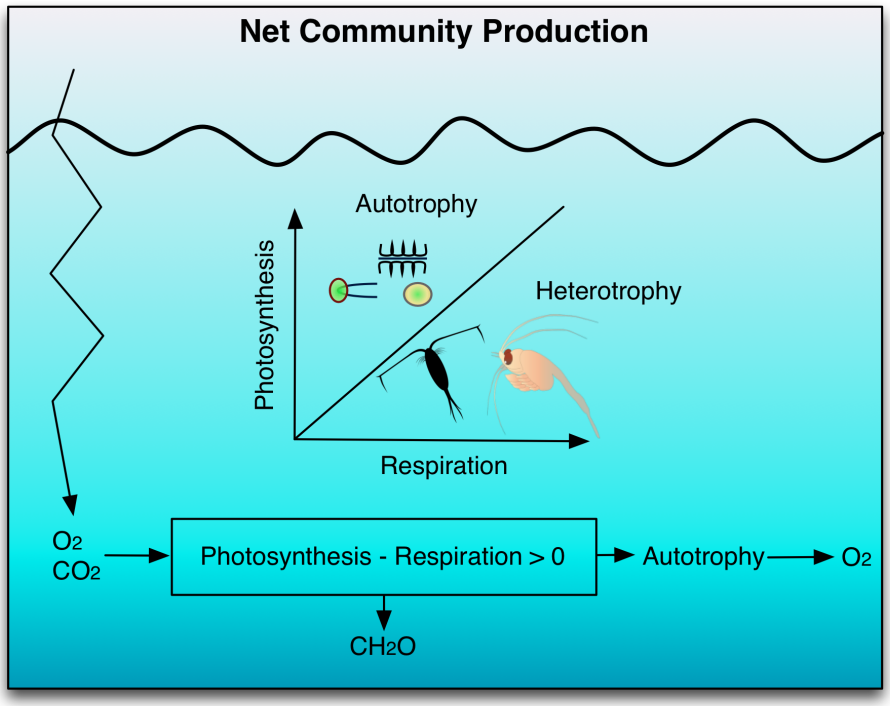

Figure 4.1: Schematic of Net Community Production (NCP), illustrating the balance between photosynthesis (autotrophy) and respiration (heterotrophy).

Our study region in the North Atlantic lies between 14° N and 50° N. It is an

important sink for atmospheric CO_2, with the net air-sea flux of CO_2 estimated at approximately -0.22 Pg C y^{-1} (negative value representing marine uptake from the atmosphere), representing 13% of the global contemporary carbon sink (Gruber *et al.*, 2009; Takahashi, 2009; Schuster *et al.*, 2013). The CO_2 sink in the North Atlantic is maintained by year-round cooling, and northward transport of waters to the Arctic. It is further accentuated by phytoplankton blooms that primarily occur within the subpolar gyre during spring (Watson *et al.*, 2009). The North Atlantic Ocean includes regions associated with high uptake of CO_2 and productivity (Schuster *et al.*, 2013), pole ward of 40° N (Takahashi and Sutherland, 2002), as well as oligotrophic regions associated with low productivity (Ducklow *et al.*, 1995), such as the North Atlantic subtropical gyre. Determining the metabolic state of such regions is of key importance to determining the temporal and spatial variability in the uptake of carbon in the North Atlantic.

The North Atlantic has been sampled through repeat transects such as the Atlantic Meridional Transect (AMT), and mooring sites such as the Bermuda Atlantic Time Series (BATS) and the European Station for Time Series in the Ocean (ESTOC) (Robinson *et al.*, 2006; Emerson and Stump, 2010; Cianca *et al.*, 2013). However there continue to be biases in the spatial and temporal coverage of data, such that oligotrophic waters are under sampled compared to shelf regions, particularly on the tropical southwestern side of the North Atlantic, and full seasonal trends are rarely recorded (del Giorgio and Williams, 2005; Serret *et al.*, 2006; Quay *et al.*, 2010). Although there are a number of techniques available to derive NCP from *in situ* data, many of the methods are expensive and time consuming and many of the processes involved, such as those that influence gas exchange, are not yet fully constrained (Lefèvre and Merlivat, 2012; Emerson and Stump, 2010). This has led to the continued debate surrounding the metabolic state of oligotrophic regions derived from *in situ* and *in vitro* measurements, with *in vitro* estimates of NCP often suggesting heterotrophy while *in situ* estimates consistently report autotrophy (Williams *et al.*, 2013). These challenges mean that there are few regions in the global ocean where the current NCP rates are known (Quay *et al.*, 2010). The aim of this study is to develop a method for estimating NCP using automated

high frequency measurements of surface water oxygen concentration collected on a Volunteer Observing Ship (VOS). We present *in situ* seasonal estimates of NCP between December 2011 and March 2013 within 5 biogeochemical regions in the North Atlantic. Our calculation of NCP involves a simple quasi-1D box model to estimate abiotic processes that may influence oxygen concentration (Emerson and Stump, 2010; Emerson, 1987) in order to determine the biologically driven oxygen change with time. These results are compared with published *in situ* estimates of NCP derived from oxygen measurements and an alternative technique for the calculation of NCP, which utilizes the seasonal change in dissolved inorganic carbon (DIC) (Bates *et al.*, 2005). This study demonstrates that well-constrained NCP estimates can be achieved through VOS campaigns, opening the way for expanded coverage of empirical NCP estimates for the global ocean.

4.3 Methods

4.3.1 Automated sampling

Using a VOS as an oceanic measuring platform is highly efficient in terms of cost, and spatial and temporal coverage. However VOS that are commercial ships, are limiting in terms of laboratory space and have no scientific personnel onboard, which means they often depend on automated sampling systems. There are a number of methods for measuring the oxygen budget, yet many of these methods are labour intensive and costly, such as the use of Ar/O_2 ratios. Although not globally applicable due to regional variability in horizontal temperature gradients that can influence the solubility of oxygen, preliminary data collected in the Western English Channel, suggest little difference between estimates of NCP derived from measurements of Ar/O_2 and those derived from optode measurements of dissolved oxygen (Gloël, 2012). Several VOS routes are equipped with optodes to continuously measure surface water dissolved oxygen, but to our knowledge, these data have not yet been used to derive estimates of NCP. The VOS (*MV Benguela Stream*) used in this study operates between Portsmouth (UK) and the Caribbean Islands completing one return voyage every 28 days.

A dual oxygen/temperature sensor (*Aanderaa* optode, model 3835), a conductivity sensor (*Aanderaa*, model 3919) and a temperature sensor (*Aanderaa*, model 3210) are permanently installed on the *MV Benguela Stream* using the set-up described by Schuster and Watson (2007). The optode measures dissolved oxygen concentration based on the principle of dynamic luminescent quenching. Ambient oxygen acts as the quenching agent, and depending on the intensity and duration of red luminescence emitted after being excited by a blue-green light, the absolute oxygen concentration can be determined (Aanderaa Data Instruments, 2007) (see Körtzinger *et al.* (2005) for further details). Data are recorded every minute onto an instrument computer. After each voyage the raw data are returned to shore where they undergo quality control.

The *in situ* temperature and conductivity sensors are calibrated annually by the manufacturer, and additionally monthly using a three-point temperature calibration and discrete seawater salinity samples. Calibration of oxygen measurements are described below. All raw data are recorded with concurrent latitude, longitude, and UTC (Coordinated Universal Time) by a GPS (Global Positioning System) integrated into the instrument.

4.3.2 Discrete sampling

Water samples were collected by scientific personnel on voyages in April/May 2012, June/July 2012, September/October 2012 and January/February 2013.

The ship's seawater intake is at 3 - 5 m below the sea surface depending on cargo loading (Schuster and Watson, 2007). The seawater passes through a coarse strainer (1 mm) before entering the instruments and a T-piece. Surface seawater for chemical analysis was collected from this T-piece at the ship's sea-chest using hydrostatic flow, minimising any temperature fluctuations from the surrounding environment (Cooper *et al.*, 1998). Tygon® tubing is connected to the T-piece in order to carefully control the flow of water into the sample bottle and check for bubbles within the tubing. Temperature (T) and conductivity of the seawater were recorded at the time of sampling. Samples were collected for dissolved oxygen,

total dissolved inorganic carbon (DIC), total alkalinity (TA), salinity, nitrate, silicate, and phosphate. Dissolved oxygen, DIC and TA samples were collected every two hours during daylight hours. Nutrient and salinity samples were collected every four and twelve hours respectively. These latter samples were analysed at the National Oceanography Centre (NOC) Southampton, using a SEAL AutoAnalyzer (Grasshoff *et al.*, 1999) and a Guildline Autosal salinometer (8400B) respectively.

4.3.3 Winkler analysis and sample storage

Dissolved oxygen samples were fixed onboard using standard procedures (Grasshoff *et al.*, 1999) and stored underwater until analysis onshore. This method of storage has been found to give 100% recovery of dissolved oxygen concentration over a period of 4 months (Zhang *et al.*, 2002). Samples were only collected on the return crossing of each voyage, therefore the longest a sample was stored before being analysed was 12 days. A preliminary 36 day longevity experiment showed that this storage procedure had a minimal effect on the measured oxygen concentration (< 0.01 mmol m^{-3}, see section 2.3 within chapter 2 for further details). Dissolved oxygen concentration was determined by Winkler titration (Williams and Jenkinson, 1982; Winkler, 1888). Depending on sampling technique and titration method, the typical precision of Winkler titrations during fieldwork is $0.015 - 0.7\%$ (del Giorgio and Williams, 2005). The sodium thiosulphate titrant was calibrated with potassium iodate (Wako Pure Chemical Industries, Ltd., Osaka, Japan) to a precision of $< 0.1\%$.

4.3.4 DIC and TA analysis

The DIC and TA samples were fixed onboard following standard methodology outlined in Dickson *et al.* (2007) and analysed once back in the laboratory using the VINDTA 3C (**V**ersatile **IN**strument for the **D**etermination of **T**otal inorganic carbon and titration **A**lkalinity), which combines the titration of acid to determine TA and a coulometric method for the measurement of DIC (Mintrop, 2011). Routine calibration using certified reference material (CRM) (provided by A.G. Dickson, Scripps Institution of Oceanography) and corrections for silicate and phosphate,

enabled a precision of 1.46 mmol m^{-3} for TA and 2.55 mmol m^{-3} for DIC, calculated from the standard deviation between CRM's (Dickson *et al.*, 2007).

4.3.5 Data processing and optode calibration

The salinity measurements derived from the conductivity probe were calibrated with measurements of salinity made with the salinometer on discrete seawater samples. The oxygen concentration derived from the optode could then be corrected to *in situ* salinity using equations provided in the *Aanderaa* operating manual (Aanderaa Data Instruments, 2007). These optode derived oxygen concentrations were calibrated with the Winkler titration data.

Winkler oxygen data were plotted against co-located 1 minute averaged optode values, and Chauvenet's criterion (Glover *et al.*, 2005) was applied to remove outliers. Only one data point was removed using this method. A standard model-1 linear regression was used to determine the calibration factors with an R^2 value of 0.94 (n = 99), see figure 4.2 (Sokal and Rohlf., 1995).

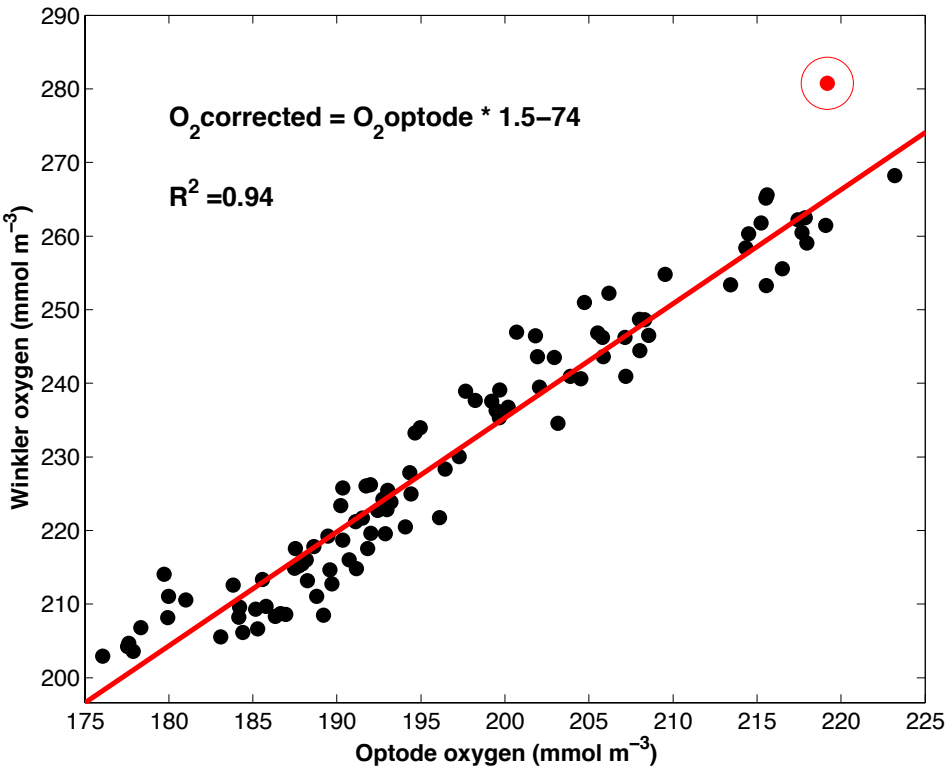

Figure 4.2: Property-property plot of Winkler derived oxygen concentration against optode derived oxygen concentration (filled black circles) showing the standard model 1 linear regression line (red line), correction equation for optode oxygen, and its R^2. A single outlier was identified (filled red circle) and excluded from the oxygen calibration.

This optode calibration (see figure 4.2) was applied to all of the optode measurements made during the study period, as it was found to be consistent, and avoids any seasonal bias that may be introduced using cruise specific regressions. The error of this calibration was calculated as the RMSE (Root-Mean-Square-Error) of the difference between the measured Winkler oxygen and the oxygen predicted by the regression (RMSE residuals = 4.3 mmol m^{-3}, percentage error of the mean = 1.7%).

During February 2012 there were sporadic temperature shifts during sections of the voyage that affected the oxygen concentration recorded by the optode. This was attributed to a technical fault and these data were removed during the quality control process.

The uncertainty of our oxygen measurements was calculated using a combination of the percentage error from the RMSE of the residuals (1.7%), an estimate of the error associated with the underway sampling method (1%), and the precision determined with the standard iodate solution (0.1%), which gives a total error of $\pm$ 2.8%.

4.3.6 Biogeochemical regions

The study area was divided into biogeochemical regions in order to assess the spatial variability in NCP in the mid-latitude North Atlantic under different biogeochemical regimes. The method used for the division of these regions is similar to that of Hooker *et al.* (2000), whereby the second derivative of *in situ* T, *in situ* density and satellite derived natural logarithm of chlorophyll-a (Chl-a) (MODIS Aqua level-3 standard chlorophyll product, http://oceandata.sci.gsfc.nasa.gov) (Sharqawy, 2010) were calculated along the ship tracks. The second derivatives for each parameter were normalised to ensure equal weighting and then averaged. Peaks in these averaged second derivatives identified the latitudinal boundaries between each biogeochemical region (see figure 4.3). This method was chosen in preference to using static ecologically defined provinces such as Longhurst (2006), because this allows the dynamics of the boundaries to shift from year to year defined by *in situ* and satellite observations.

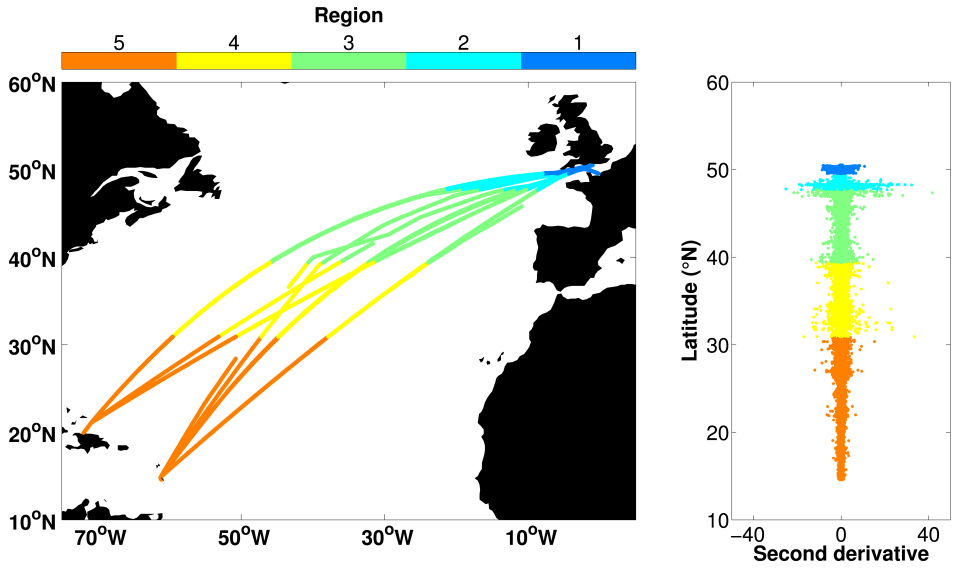

Figure 4.3: Map of the mid-latitude North Atlantic, divided into 5 biogeochemical regions, the dynamic latitudinal boundaries of which are defined by peaks in the second derivative of T, density and Chl-a. The overlapping ship tracks of 16 voyages between December 2011 and March 2013 are shown.

This method identified 4 peaks, thereby dividing the study area into 5 biogeochemical regions, labelled 1 to 5 from North to South (see figure 4.3). These dynamic biogeochemical regions were used throughout the study as they avoid calculating NCP across different water masses as the ship moved, and biases associated with the changing latitude of the ships tracks. These biogeochemical regions are in broad agreement with ecologically defined provinces within the North Atlantic (Longhurst, 2006; Hooker *et al.*, 2000), with regions 1 to 5 aligning approximately with the Longhurst (2006) biogeochemical provinces NECS (North East Atlantic Coastal Shelves), NECS/NADR (North Atlantic Drift), NADR/NASE (North Atlantic Subtropical East), NASW (North Atlantic Subtropical West) and NASW/NATR (North Atlantic Tropical) respectively.

4.3.7 Calculation of NCP_{O_2}

Net community production was derived from the change in the inventory of oxygen in the surface ocean with time (Emerson, 1987; Emerson and Stump, 2010) (NCP_{O_2}, mmol O_2 m^{-2} d^{-1}). The corrected continuous surface measurements collected between December 2011 and March 2013 were divided into biogeochemical regions (see figure 4.3) and monthly means for each region were calculated for

calibrated dissolved oxygen, temperature and salinity.

NCP_{O_2} was calculated as the biological component ($\Delta O_2 Bio$, *mmol* m^{-3}) of the total change in oxygen concentration within the mixed layer (h, m) over the period between monthly observations (Δt, days).

$$NCP_{O_2} = h\frac{\Delta O_2 Bio}{\Delta t} \tag{4.1}$$

$\Delta O_2 Bio$ was determined from the difference between the observed changes in dissolved oxygen ($\Delta O_2 Obs$, *mmol* m^{-3}) and those predicted from abiotic ($\Delta O_2 Abio$, *mmol* m^{-3}) processes (i.e. solubility, gas exchange, and changes in the mixed layer depth) on a monthly basis.

$$\Delta O_2 Bio = \Delta O_2 Obs - \Delta O_2 Abio \tag{4.2}$$

Where $\Delta O_2 Bio$, $\Delta O_2 Obs$, and $\Delta O_2 Abio$ are in units of mmol m^{-3}.

$\Delta O_2 Abio$ is calculated using the ordinary differential equation (ODE) solver 45 in Matlab (Glover *et al.*, 2005). Temperature (T, °C) and mixed layer depth (MLD) (h, m) are assumed to vary linearly over the integration period. Monthly mean MLD was calculated for each region using ECCO2 daily 0.25° MLD (Menemenlis *et al.*, 2008). Wind speed (U, m s^{-1}) was applied as a time-variable input obtained from ECMWF 6 hourly 0.75° 10 metre wind speed (Uppala *et al.*, 2005). Monthly below-thermocline oxygen concentrations ($O_2 Deep$, mmol m^{-3}) were derived from the World Ocean Atlas 2009 climatology (Garcia *et al.*, 2010) by taking the mean oxygen concentration from 0-25 m below the MLD within each region. $O_2 Deep$ remains constant within each NCP integration period. The predicted abiotic oxygen concentration change was computed as the sum of entrainment (E) and the flux of oxygen between the atmosphere and the ocean (FO_2) over the mixed layer (h) on a daily time-step within the solver (dt).

$$\Delta O_2 Abio = \int_0^{\Delta t} \frac{(E + FO_2)}{h} \times dt \tag{4.3}$$

Therefore, ΔO_2Abio is the predicted physical change in oxygen concentration over the period between monthly observations, due to E and FO_2. This method can

be described as a quasi-1D (vertical) box model applied over monthly integrations in each of the biogeochemical regions.

4.3.7.1 Entrainment

When the mixed layer deepens over time the oxygen concentration will change due to mixing between surface and deep waters. When the mixed layer shoaled we assumed that this did not cause a change in oxygen concentration. *E* is calculated as described in equation 4.4.

$$\text{if } \frac{dh}{dt} > 0; E = \frac{dh}{dt} \times (O_2Deep - O_2) \tag{4.4}$$

Where O_2 is the oxygen concentration at the beginning of each solver time-step.

4.3.7.2 O_2 Exchange with the atmosphere

FO_2 is calculated following Woolf and Thorpe (1991), where the standard thin film model of gas exchange is combined with a term to account for the transient super-saturation due to bubble injection. The transfer velocity, kO_2, and the concentration terms are expressed in terms of a concentration gradient on the water side of the interface:

$$FO_2 = kO_2 \times ((O_2Sol \times BO_2) - O_2) \tag{4.5}$$

Where O_2Sol, *mmol* m^{-3} is the oxygen solubility (or saturation) concentration (i.e. the seawater concentration that would be in equilibrium with an assumed atmospheric concentration of 0.2095 atmospheres of oxygen) calculated using the Matlab function O2sol.m (Copyright© 2010, eMarine Information Infrastructure (eMII) and Integrated Marine Observing System (IMOS). All rights reserved.). This function utilizes the equations outlined in García and Gordon (1992), which are based on values obtained from Benson and Krause (1984). O_2Sol was determined using *in situ* temperature and salinity measured at the same time, geographic location, and depth as the optode measurement. BO_2 is the functional increase in

saturation due to bubble injection (Woolf and Thorpe, 1991). More recent bubble parameterisations based on models and observations exist, but deviate from one another at high wind speeds (> 10 ms^{-1}) (Stanley *et al.*, 2009; Liang *et al.*, 2013). The NCP estimates were found to be relatively insensitive to the supersaturation bubble term, so the empirically derived model of Woolf and Thorpe (1991) was deemed most appropriate.

$$BO_2 = 1 + 0.01 \times (\frac{U}{U_o})^2 \tag{4.6}$$

Where U_o is the wind speed at which the oxygen saturation is supersaturated at 101%, this is a constant given as 9 m s^{-1} (Woolf and Thorpe, 1991). The wind speeds used for equation 4.6 were the average wind speed within each biogeochemical region for the 6 hour period preceding each solver time-step, to account for the instantaneous effect of varied wind speeds on bubbles.

Water-side transfer velocity, kO_2, was calculated using Wanninkhof *et al.* (2009) which represents the different wind speed regimes as polynomial equations; from purely diffusive flux through linear (smooth surface), quadratic (rough surface) and cubic (bubble mediated) regimes.

$$kO_2 = 0.24 \times ((3 + 0.1U + 0.064U^2 + 0.011U^3) \times (\frac{ScO_2}{660})^{-0.5}) \tag{4.7}$$

Where kO_2 is in m d^{-1}, U is the daily averaged wind speed in m s^{-1}, and ScO_2 is the temperature dependent Schmidt number of oxygen (Keeling and Stephens, 1998):

$$ScO_2 = 1638 - 81.83T + 1.483T^2 - 0.008004T^3 \tag{4.8}$$

Due to variable 6 hourly winds within the solver time-steps, square and cubic means were calculated prior to daily averaging to avoid issues with non-linearity (Wanninkhof *et al.*, 2009).

4.3.8 Calculation of NCP$_{DIC}$

Net community production can also be derived from seasonal changes in the concentration of DIC (NCP$_{DIC}$, mmol C m^{-2} d^{-1}) within the surface layer (Williams, 1993; Bates *et al.*, 2005; Mathis *et al.*, 2010). This method assumes that changes in DIC caused by processes other than NCP (e.g. air-sea CO_2 gas exchange, advection, precipitation, evaporation, formation and dissolution of calcium carbonate, riverine inputs, vertical diffusion, entrainment) can either be accounted for or are negligible (Bates *et al.*, 2005).

The influence of advection was estimated from the regional change in TA between seasons. TA is not affected significantly by photosynthesis and respiration, therefore a change in TA is likely caused by advection and/or entrainment. As there were only small changes in observed TA between seasons (mean change < 0.1 mmol m^{-3} d^{-1}), we assumed that the affect of advection on the seasonal change in DIC was negligible (Lefèvre and Merlivat, 2012).

To remove the impact of changes in local precipitation and evaporation (Bates *et al.*, 2005), DIC was normalised to a salinity of 35 (*nDIC*), resulting in a mean decrease in DIC of 69 mmol m^{-3}.

Riverine input is likely to only affect those regions that are closest to the coast, i.e. region 1; insufficient data were available to calculate NCP$_{DIC}$ in this region, and riverine input can be assumed to be negligible for the other regions.

To account for the formation and dissolution of calcium carbonate, a correction factor was used, of half the temporal change in TA, after adjusting this for the temporal change in NO_3 (Lee, 2001; Mathis *et al.*, 2010):

$$Corr = \frac{(TA^{t1} - TA^{t2})}{\Delta t} + \frac{(NO_3^{t1} - NO_3^{t2})}{\Delta t} \times 0.5 \tag{4.9}$$

Where ($TA^{t1} - TA^{t2}/\Delta t$) is the seasonal change of TA between time 1 (*t1*) and time 2 (*t2*), ($NO_3^{t1} - NO_3^{t2}/\Delta t$) is the seasonal change in NO_3 for the same time period, and Δt is the number of days between *t1* and *t2*.

NCP$_{DIC}$ was determined for each of the 5 biogeochemical regions as the change in *nDIC* over time across the mixed layer (*h*, m), corrected for the formation and dissolution of calcium carbonate:

$$NCP_{DIC} = h\frac{(nDIC^{t1} - nDIC^{t2})}{\Delta t} - Corr \tag{4.10}$$

Where $(nDIC^{t1} - nDIC^{t2}/\Delta t)$ is the seasonal change in *nDIC*. We chose the spring for *t1* and the autumn for *t2*; the autumn values were chosen rather than the summer values because there was little to no change in *nDIC* between the spring and the summer.

4.3.9 Photosynthetic Quotient

The photosynthetic quotient (PQ) was calculated as the ratio between the two independent estimations of NCP:

$$PQ = \frac{NCP_{O2}}{NCP_{DIC}} \tag{4.11}$$

4.3.10 Uncertainty

The RMSE was calculated for each of the input variables in each of the regions using a Monte Carlo approach (see table 4.1 for individual errors) (Quay *et al.*, 2010).

The RMSE was first calculated separately for errors above and below the mean NCP as variables contributed differently, and then combined using the root sum square error (RSSE) to give the variance from the mean NCP over a period of time (i.e. seasonal error, annual error). The errors are different in each region due to the varying geographical impacts of the input variables. For example region 3 had the largest error associated with it's seasonal and annual NCP_{O_2} values due to the sharp change in oxygen saturation that occurred between January and February in 2012 (see figure 4.4).

Table 4.1: Error associated with each input variable used to calculate NCP_{O2} and NCP_{DIC}

Variable	Error	Reference/Method
O_2Obs	$\pm$2.8%	Combination of RMSE of residuals (1.7%), underway sampling method (1%), and method accuracy from the iodate standard (0.1%).
O_2Deep	$\pm$4.4661(mmol m^{-3})	0.1 (ml L^{-1}) Standard error of the mean (Garcia *et al.*, 2010).
Salinity (S)	$\pm$0.05	Calculated from temperature and conductivity, calibrated using discrete salinity samples.
Temperature (T)	$\pm$0.03 (°C)	Aanderaa 3210 sensor accuracy.
MLD (h)	$\pm$30%	von Allmen *et al.* (2009).
Wind Speed (u)	$\pm$1.1(ms^{-1})	Stoffelen (1996).
kO_2	$\pm$30%	Johnson (2010b).
DIC	$\pm$2.55 (mmol m^{-3})	Mean standard deviation of CRM DIC.
TA	$\pm$1.46 (mmol m^{-3})	Mean standard deviation of CRM TA.
NO_3	$\pm$0.1(mmol m^{-3})	SEAL Auto Analyzer accuracy from international standards.

To account for the error and potential bias of excluding CO_2 exchange in our NCP_{DIC} calculation we have estimated the likely CO_2 flux between spring and autumn for each region using a neural network-based monthly climatology (from the years 1998-2011) of the ocean carbon sink (Landschützer *et al.*, 2014). We cannot assume the same fast equilibration times for carbon as we do for oxygen, hence we account for the exchange of CO_2 as a result of the disequilibrium between the atmosphere and surface ocean CO_2 partial pressures by incorporating the CO_2 flux into our uncertainty. Ocean carbon uptake was calculated per unit volume by dividing the air-sea CO_2 flux by the mean summer ECCO2 MLD (Menemenlis *et al.*, 2008) within each region. As these regions are normally sinks for CO_2 during this time of year this introduces a negative bias into our NCP_{DIC} estimates (i.e. unaccounted-for CO_2 influx to the surface ocean leads to an underestimation in biological CO_2 uptake, see table 4.2). As there are no estimates of CO_2 flux from Landschützer *et al.* (2014) for the study year, to estimate the possible effect of 2012 being an atypical year we considered the inter-annual variability (IAV) in annual CO_2 flux in the climatology (taken as 1 standard deviation) for each region (table 4.2) and included this in our error estimation. Negative error bars are thus the sum of measurement uncertainty and any net negative excursion of the uncertainty from the climatological mean CO_2 flux (i.e. representing a possible net release of CO_2 into the atmosphere over the period of NCP_{DIC} calculation). Negative uncertainty from the climatological mean only exceeds measurement uncertainty in region 5 where the percentage error from inter-annual variability is greater than the climatological CO_2 flux, see table 4.2. Positive error bars are the sum of measurement uncertainty and any net positive flux, i.e. a net sink of CO_2 from the atmosphere into the surface mixed layer over the period of NCP_{DIC} calculation.

Table 4.2: Error associated with the air sea flux of CO_2. Average CO_2 flux estimates from April to October are derived from Landschützer *et al.* (2014) and mixed layer depths are derived from Menemenlis *et al.* (2008).

Region	**CO_2 flux** ($mmol\ m^{-2}\ d^{-1}$)	**IAV CO_2 flux**[a] ($mmol\ m^{-2}\ d^{-1}$)	**MLD** (m)	**Error from Carbon Uptake** (%)	**Error from IAV** (%)
1	4.66	0.88	25.16	N/A [b]	N/A [b]
2	4.96	0.77	50.80	30.72	4.83
3	3.75	0.36	49.19	21.50	1.98
4	0.79	0.66	64.30	4.01	3.33
5	0.03	0.36	44.01	0.39	6.08

[a] Calculated as 1 standard deviation of the inter-annual variability (IAV) in CO_2 flux.

[b] Insufficient DIC and TA data were available in Spring 2012 within this region, therefore a NCP_{DIC} estimate was not calculated, hence no error estimate.

4.3.11 Assumptions and Limitations

Due to lack of DIC measurements and the different residence times of oxygen and carbon dioxide (Sarmiento and Gruber, 2006), the calculation of NCP_{DIC} is more simplistic than that of NCP_{O_2} and the uncertainties associated with the calculation are therefore less easy to estimate, see section 4.3.10. Our calculation of NCP_{DIC} does not take into account the additions of DIC through gas exchange, vertical diffusion and entrainment. These generally increase as the season progresses, which can lead to an underestimation in NCP_{DIC} (Mathis *et al.*, 2010). This was suggested by our estimations of the carbon uptake, as all five regions were found to be net sinks of CO_2 over the summer period, thus increasing the positive error on our NCP_{DIC} estimates (table 4.2).

Horizontal advection and vertical diffusion (diapycnal and isopycnal) were necessarily neglected in our calculations due to the lack of available measurements. However, as these have been shown to have a relatively small influence on oxygen concentration due to the rapid equilibration of oxygen with the atmosphere, this is unlikely to be a significant omission (Emerson *et al.*, 2008; Lefèvre and Merlivat, 2012). Entrainment was not incorporated into the NCP_{DIC} calculation as no observational depth distribution DIC data were found within 1° latitude $\times$ 1° longitude during the same month (independent of the sample year) of the sampling routes. Until more data of DIC depth distributions become available (such as in the updated GLODAP (**GL**obal **O**cean **D**ata **A**nalysis **P**roject (Key *et al.*, 2004)) dataset, whose release is imminent) such analysis will be difficult or impossible in many regions of the global ocean. Lee (2001) estimate that in the North Atlantic (between 40°N and 70°N) and the mid-Atlantic (40°N and 40°S) about 2.8% and 11.9% (respectively) of the estimate of NCP from the summer change in DIC is accounted for by diffusive carbon flux. However as there was no significant change in TA throughout the summer sampling period, this suggests that DIC had not been entrained from below the mixed layer (Lefèvre and Merlivat, 2012), and vertical diffusion and horizontal transport are likely to have only contributed in a minor way (Gruber *et al.*, 2002).

Entrainment was incorporated into the NCP_{O_2} calculations by using climatological oxygen depth distributions and a mixed layer re-analysis. The large error associated with these products (see table 4.1) significantly influences the error on our NCP_{O_2} estimates. This influence is increased when calculating NCP per unit area rather than per unit volume due to the high error associated with the multiplication across the mixed layer depth (equations 4.1 and 4.10). We estimate that the average error on our annual estimate of NCP_{O_2} (mmol m^{-2} d^{-1}) is increased by 15.75% due to the uncertainty on the entrainment terms. As we only have surface measurements, we cannot constrain potential systematic bias in the data products and climatology used, but we assume that any possible bias is incorporated in the large uncertainty associated with these products.

4.4 Results

4.4.1 Seasonal cycle of NCP_{O_2}

Monthly mean NCP_{O_2} was calculated for each month between December 2011 and March 2013 for each biogeochemical region shown in figure 4.3, from the daily time-step quasi-1D model and the calculations described above (see equations 4.1 to 4.8), and are shown in figure 4.4 together with mean monthly Chl-a data (obtained from Aqua-MODIS at a resolution of 9 km and frequency of 1 month, http://oceandata.sci.gsfc.nasa.gov), and oxygen saturation. Monthly mean NCP_{O_2} was also compared with data from the continuous plankton recorder (CPR), however no significant relationships were found (see appendix B figures B.1 and B.2 for reference).

Surface dissolved oxygen remains supersaturated for most of the sampling period. A distinct decrease in oxygen saturation occurs in February 2012 in regions 3 and 4, followed by supersaturation in March 2012. This change in saturation state occurs at the time of rapid shoaling of the mixed layer depth, which is often associated with the onset of primary production (Sverdrup, 1953). Unfortunately during this time there were sporadic electrical faults within the sampling set-up. As a result, data are missing from regions 1, 2 and 5 for these months, but the same

trend can be seen in all five regions between February and March 2013, with the saturation state becoming undersaturated in March. This suggests that a similar trend may have been present in the months where data are missing. Throughout the rest of the time series the oxygen saturation is mostly supersaturated within each region, except for times of undersaturation that occur within region 1 in May and October 2012 and in region 2 in May 2012 and January 2013. As expected, the seasonal cycle of NCP_{O2} generally follows the seasonal cycle of oxygen saturation.

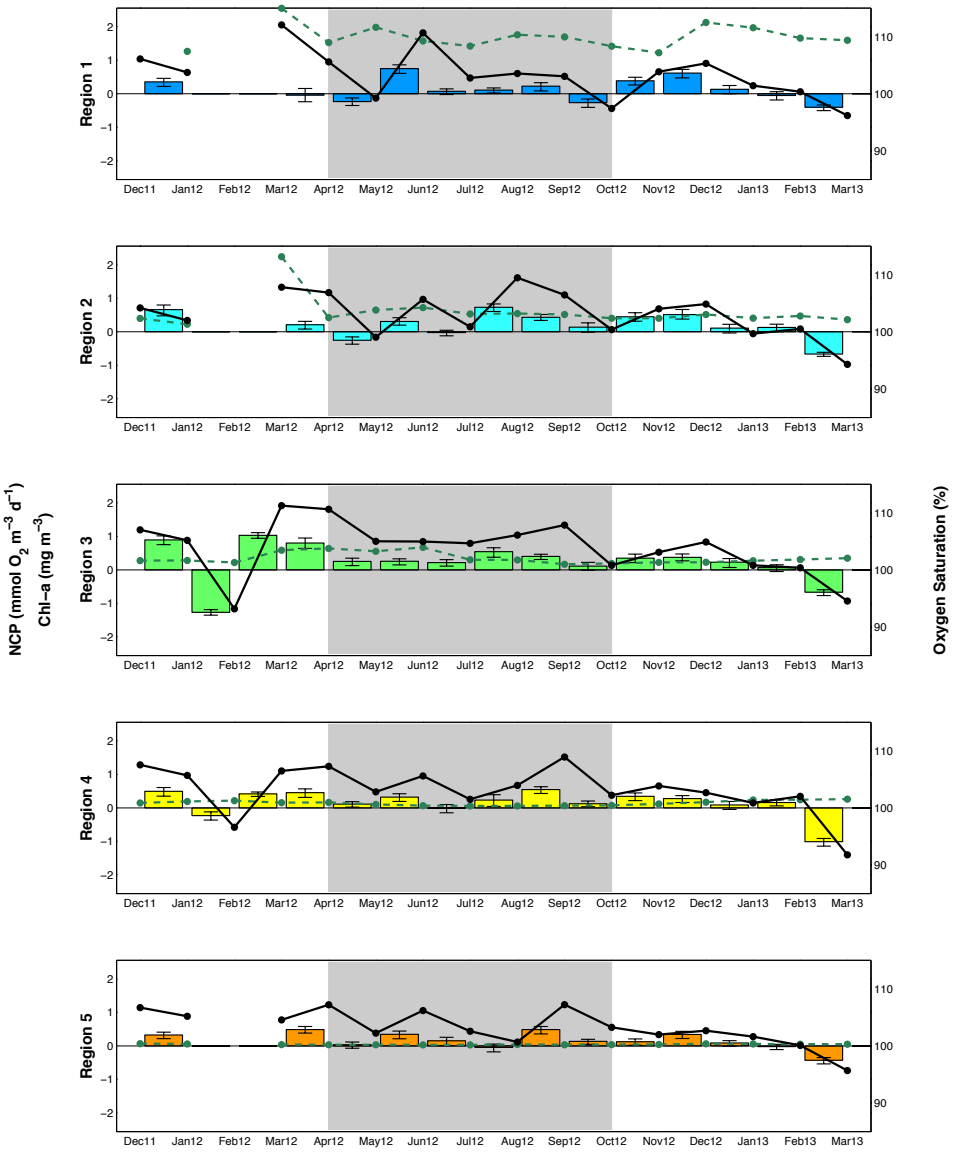

Figure 4.4: Monthly mean NCP_{O_2}, Chl-a, and oxygen saturation over time in each of 5 biogeochemical regions (see Fig. 4.3). Monthly NCP_{O_2}, was calculated using equations 4.1 to 4.8 and are shown as coloured bars with error bars indicating the uncertainty ([mmol O_2 m^{-3} d^{-1}], left axis), monthly Chl-a data are shown as green filled circles and dashed line ([mg m^{-3}], left axis) , and oxygen saturation are represented by the black closed circles and line ([%], right axis). The grey area is the period from which the summer mean NCP_{O_2} was estimated.

4.4.2 Summer mean and annual mean NCP

The summer mean NCP_{O_2} for each region was calculated as the mean NCP_{O_2} between spring and autumn 2012, and are presented in figure 4.5 together with the NCP_{DIC} (calculated between spring and autumn 2012, see section 4.3.8). There are insufficient DIC and TA data for region 1 during spring of 2012, so NCP_{DIC} for region 1 could not be calculated. The photosynthetic quotient (see equation 4.11) was calculated for each region where both NCP_{DIC} and NCP_{O_2} were available. These data are presented in table 4.3.

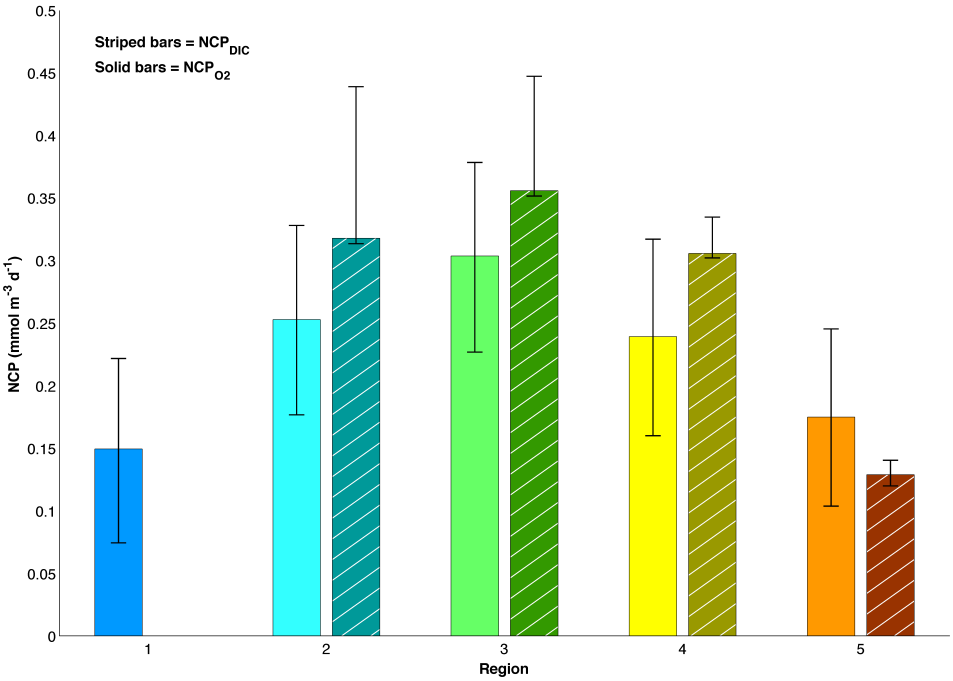

Figure 4.5: Summer mean NCP_{O_2}, and NCP_{DIC},in each of 5 biogeochemical regions (see Fig. 4.3) between spring and autumn 2012. The darker coloured striped bars represent the NCP_{DIC}, and the lighter coloured solid bars represent the NCP_{O_2}, and the error bars indicate uncertainties identified for each. Note that in region 1, insufficient data could be collected for NCP_{DIC} in spring 2012, and that there is a negative bias in the NCP_{DIC} estimates associated with CO_2 flux (see section 4.3.10).

The summer means of NCP_{O_2} and NCP_{DIC} are not significantly different in all 4 regions where both estimates were calculated (figure 4.5), and follow the same regional trend with region 3 having the highest NCP and regions 1 and 5 the lowest. As the error bars on the NCP estimates do not account for all of the assumptions of the calculations (See section 4.3.10 and 4.3.11), we can assume that the NCP estimates using the two different techniques in all 4 regions are not significantly

different.

Table 4.3: Comparison of NCP and PQ estimates

Region	**NCP**$_{DIC}$ (mmol C m^{-3} d^{-1})	**NCP**$_{O_2}$ ($_{Summer}$) (mmol O$_2$ m^{-3} d^{-1})	**PQ value**	**Annual NCP**$_{O_2}$ (mmol O$_2$ m^{-3} d^{-1})[a]	**Annual NCP**$_{O_2}$ (mmol O$_2$ m^{-2} d^{-1})[a]
1	N/[b]	0.15±0.[c]	N/[b]	0.18±0.[c]	7.1±5.[c]
2	0.32±0.[c]	0.25±0.076[c]	0.80±0.39[d]	0.26±0.094[c]	12±6.9[c]
3	0.36±0.091[c]	0.31±0.077[c]	0.85±0.35[d]	0.27±0.10[c]	9.5±9.4[c]
4	0.31±0.029[c]	0.24±0.079[c]	0.78±0.31[d]	0.22±0.10[c]	10±6.8[c]
5	0.13±0.012[c]	0.18±0.071[c]	1.4±0.62[d]	0.21±0.083[c]	8.7±3.9[c]

[a] Estimating NCP per unit area introduces increased error associated with the MLD (section 4.3.11), both units have been presented here for ease of comparison with previous studies.

[b] Insufficient DIC and TA data were available in Spring 2012 within this region, so neither NCP$_{DIC}$ nor a PQ could be calculated.

[c] Although an error for above and below the mean NCP$_{DIC}$ and NCP$_{O_2}$ was calculated, the largest of these two errors is shown here.

[d] The PQ uncertainty was calculated using the minimum and maximum values within the error distribution of both NCP$_{DIC}$ and NCP$_{O_2}$, and the largest of these two errors is shown here.

The annual NCP_{O_2} for each region was determined as the mean NCP_{O_2} of all 12 months in 2012. These data are compared with annual NCP_{O_2} estimates from similar geochemical studies in figure 4.7.

4.5 Discussion

4.5.1 Seasonality of NCP_{O2}

Our results show that autotrophy dominates our study area, including the western tropical and subtropical regions, with only 5 months between December 2011 and March 2013 showing negative NCP_{O2}. This is in line with published NCP rates derived from *in situ* measurements, such as the study of Neuer *et al.* (2007) which found that at ESTOC between 1994 and 2000 monthly NCP values were always autotrophic. However this contrasts with NCP estimates derived from *in vitro* measurements within tropical regions of the North Atlantic which are generally heterotrophic (Williams *et al.*, 2013).

Region 1 has the highest concentration of Chl-a with peaks occurring in March, May, August and December 2012. This seasonal cycle of Chl-a in region 1 is observable in the oxygen saturation and in NCP_{O2}, with NCP_{O2} peaking between May and June as well as between November and December of 2012. The monthly range in magnitude of NCP_{O2} decreases from region 1 to region 5 in line with a decrease in Chl-a concentrations. Regions 4 and 5 are oligotrophic, associated with low nutrient conditions and the dominance of smaller sized phytoplankton (Ducklow *et al.*, 1995).

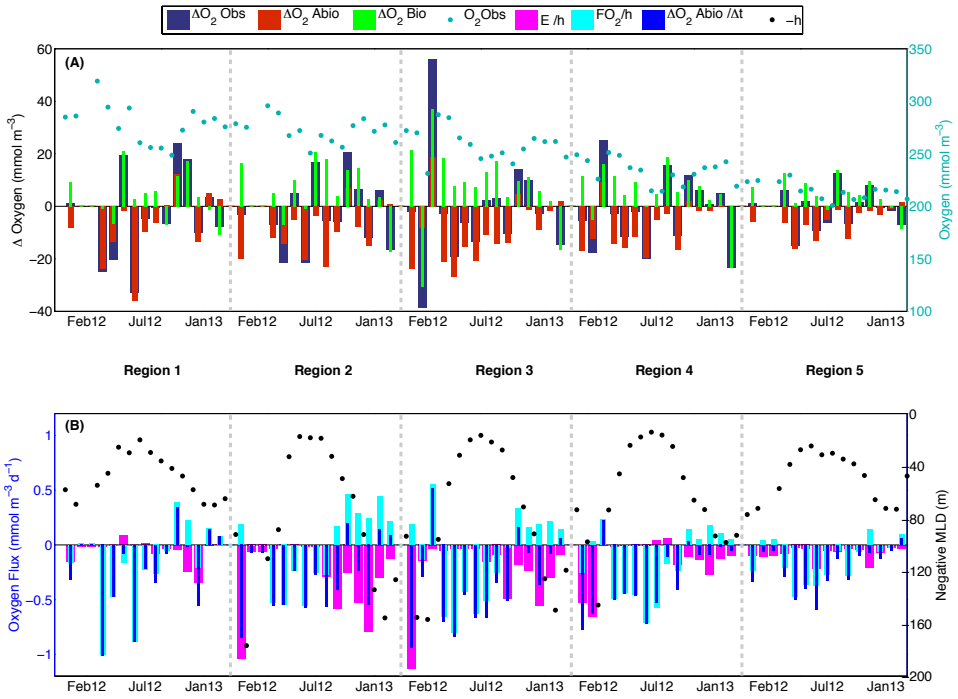

Figure 4.6: Subplot A shows the month-to-month change in the observed oxygen concentration (ΔO_2Obs, dark blue bars) along with the modelled abiotic and biotic contributions (ΔO_2Abio (red bars), and ΔO_2Bio (green bars), all in mmol m^{-3}, left axis), and the monthly oxygen concentration (O_2Obs, [mmol m^{-3}], turquoise circles, right axis) from December 2011 to March 2013 in each of the 5 biogeographical regions. Subplot B shows the oxygen flux ([mmol m^{-3} d^{-1}], left axis) associated with entrainment (E/h, pink bars), gas exchange (FO_2/h, cyan bars), and ΔO_2Abio/Δt (blue bars) between months, and the monthly negative MLD (-h, [m], black circles, right axis) from December 2011 to March 2013 in each of the 5 biogeographical regions.

Figure 4.6 shows for each of our 5 biogeochemical regions, the relative contributions of various processes involved in the calculation of NCP_{O2} (specifically, equations 4.2 and 4.3), and how this contribution varies between regions. The seasonal pattern in gas exchange is shown in figure 4.6B with sea surface outgassing of oxygen during the summer months when the mixed layer is supersaturated with oxygen, and influx of oxygen into the mixed layer when it is undersaturated with oxygen in the winter months. This change from outflux to influx of oxygen occurs after July when the wind speed starts to increase and the oxygen saturation decreases. The gas exchange term generally varies in the opposite sense to the entrainment term, as the increased deepening of the mixed layer depth during the winter months causes the decrease in oxygen concentration within the mixed layer as oxygen depleted waters are entrained, while the gas exchange causes an increased oxygen concentration as the undersaturated waters are taking up oxygen from the

atmosphere (figure 4.6B). During most of the sampling period the oxygen concentration below the thermocline is lower than that within the mixed layer. However, during May in region 1 and briefly in July in region 4, the oxygen concentration is higher below the thermocline than within the mixed layer. These subthermocline higher concentrations of oxygen are likely due to production of O_2 by phytoplankton below the mixed layer which cannot then escape to the atmosphere (Emerson *et al.*, 2008). The entrainment term has the largest influence in region 2 (see figure 4.6B) and less of an impact in regions 1 and 5 where the mixed layer depth is shallower and there is less of a change in the mixed layer depth during the sampling period. The oxygen concentration (O_2Obs) increases from region 5 to region 1 (figure 4.6A), a geographical pattern that is strongly linked to decreased solubility with increasing temperatures towards the tropics (Garcia and Keeling, 2001). The latitudinal pattern in the biological oxygen flux (ΔO_2Bio) shows highest values in region 3, decreasing towards regions 1 and 5.

4.5.2 Comparison of two independent NCP estimates

The PQs for each region are given in table 4.3 along with the regional mean annual NCP_{O_2} for 2012. The Redfield ratio of O_2:DIC (138:106) is 1.3 (Redfield *et al.*, 1963), however Laws (1991) suggest using PQ values of 1.4 and 1.1 for new and recycled production respectively. Our PQ values range from 0.78 $\pm$0.31 in region 4 to 1.4 $\pm$0.62 in region 5. Lefèvre and Merlivat (2012) measured NCP using carbon and oxygen at the PIRATA (Prediction and Research Moored Array in the Tropical Atlantic) site and also found that NCP derived from dissolved oxygen concentrations was lower than that predicted from NCP_{DIC} and a PQ of 1.4. Published PQ values range from 0.77 $\pm$0.28 to 1.26 $\pm$0.66 (Lefèvre and Merlivat, 2012; Lefèvre *et al.*, 2008; Johnson, 2010a) confirming that a constant value of 1.4 is not always applicable.

The calculation of NCP_{DIC} using the seasonal carbon mass balance approach makes several assumptions in that it does not take into account additions of DIC through gas exchange, vertical diffusion and entrainment, and the influence of riverine inputs (section 4.3.11). Although these limitations are likely to have caused

an underestimation in NCP_{DIC}, our relatively low PQ values suggest that this underestimation is small.

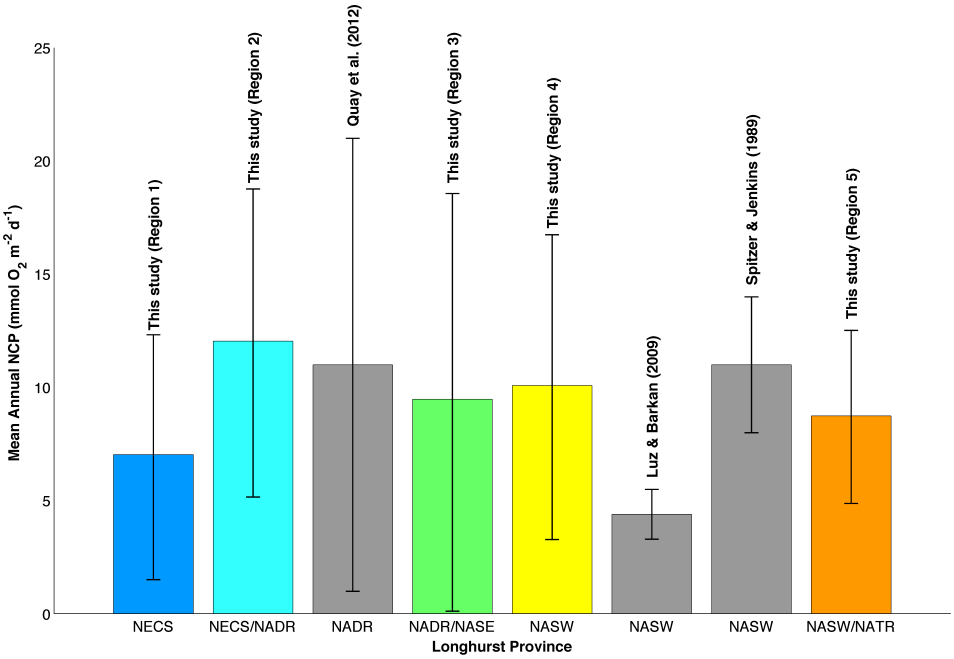

Figure 4.7: Mean annual NCP and their uncertainties in different biogeochemical regions in the mid-latitude North Atlantic. Shown are annual mean NCP_{O_2} in each of the 5 biogeochemical regions obtained in this study (coloured bars, see Fig. 4.3), along with previously published mean annual NCP estimates from the North Atlantic (grey bars) (Longhurst, 2006).

4.5.3 Annual Net Community Production

The summer mean NCP_{O2} for the months between spring and autumn is highest in region 3 and lowest in regions 1 and 5 (see figure 4.5). However, the annual mean NCP_{O2} is highest for region 2 and lowest for regions 1 and 5, (see table 4.3) highlighting the intra-annual variability in NCP_{O2} within regions. It is also important to note that our annual NCP_{O2} estimates integrate to the winter mixed layer depth which varies considerably between regions, from $<$100m in regions 1 and 5 to $\sim$150m in regions 2, 3 and 4 (figure 4.6). Körtzinger *et al.* (2008) demonstrate that at the Porcupine Abyssal Plain (PAP) site, which lies within region 2, one-third of the organic matter that is exported during the summer is returned to the mixed layer the following winter due to entrainment. This could explain why the regional variability seen in the summer mean NCP (higher NCP in regions 2, 3 and 4 than in 1 and 5 (figure 4.5)), is not seen in the annual mean NCP_{O2} (figure 4.7).

Our estimates of annual NCP_{O2} range from 7.1±5.5 to 12±6.9 (mmol O_2 m^{-2} d^{-1}), and are not significantly different from published estimates of NCP derived from geochemical oxygen budgets made in the mid-latitude North Atlantic that range from 4.4±1.1 to 11±10 (mmol O_2 m^{-2} d^{-1}) (Spitzer and Jenkins, 1989; Luz and Barkan, 2009; Quay *et al.*, 2012). Our study estimated an annual NCP of 12±6.9 (mmol O_2 m^{-2} d^{-1}) for region 2, which falls within the Longhurst (2006) provinces NECS and NADR, and 9.5±9.4 for region 3, which falls within the Longhurst (2006) provinces NADR and NASE. The geographically closest annual NCP estimate of 11 ±10 (mmol O_2 m^{-2} d^{-1}) was derived from the CARINA surface O_2 data by Quay *et al.* (2012) using Ar/O_2 ratios in the Longhurst (2006) provinces NADR/ARCT and SARC. Luz and Barkan (2009) calculated annual NCP at BATS in 2000 to 2001 using Ar/O_2 ratios, and Spitzer and Jenkins (1989) derived NCP at BATS in 1985 to 1986 from surface ocean O_2 mass balance. These estimates of 4.4 ±1.1 and 11 ±3 (mmol O_2 m^{-2} d^{-1}) respectively fall within the NASW Longhurst (2006) province. Our estimate of NCP in the NASW of 10±6.8 (mmol O_2 m^{-2} d^{-1}) is similar to that of Spitzer and Jenkins (1989), despite the suggestion of significant inter-annual variability in the air-sea oxygen flux in the North Atlantic (McKinley, 2000). Interestingly our estimates of annual NCP_{O2} in the mid-latitude North Atlantic are not significantly different from geochemical estimates of NCP in the North Pacific (Emerson *et al.*, 1997, 2008; Quay *et al.*, 2010).

The lack of latitudinal variability in our data agrees with the conclusions of Emerson (2014) and Emerson and Bushinsky (2014), who showed that the latitudinal variability in *in situ* derived NCP estimates is often less than that in model derived estimates of annual NCP. Global circulation models and satellite derived models (vertically generalised productivity model (VGPM)) (Behrenfeld and Falkowski, 1997; Najjar *et al.*, 2007), give zonally averaged estimates of annual NCP in the subtropics (equivalent to our region 5) that are about half of the annual NCP in transition regions (equivalent to our regions 3 and 4) (Emerson, 2014). Further *in situ* measurements are therefore required to determine the latitudinal and inter-annual variability in NCP and investigate the processes or assumptions that may cause *in*

situ and model estimates of NCP to differ. Emerson and Bushinsky (2014) and Körtzinger *et al.* (2005) propose a technique using atmospheric pO_2 to correct the drift of optodes installed on Argo and profiling floats. The next step is to design an automated and accurate way of correcting for optode drift on VOSs potentially by using measurements of atmospheric pO_2. This would enable accurate automated surface oxygen measurements and hence NCP on a global scale.

4.6 Summary

We present the first estimates of mean annual NCP for 5 biogeochemical regions within the mid-latitude North Atlantic, covering approximately 4,300,000 km^2. We developed a simple and cost effective method (in terms of personnel time and shipboard space requirements) which is therefore applicable for use on VOSs. The method was validated through comparison with estimates of annual NCP derived from more complex labour intensive methods such as Ar/O_2 ratios (Quay *et al.*, 2012; Luz and Barkan, 2009) and an independent method using measurements of DIC concentrations. We found no trend in the magnitude of the mean annual NCP over a 35° range in latitude. The contrast in the latitudinal variation of NCP derived from global circulation models and some satellite derived models on the one hand, and NCP derived from *in situ* measurements on the other hand, highlights the need for improved global coverage of *in situ* data and an improved mechanistic understanding of why the two approaches differ. The method developed here is ideally suited to provide the required global coverage of *in situ* NCP data.

Chapter 5

The marine carbonate system in the North Atlantic

5.1 Abstract

The container ship *MV Benguela Stream* traverses the North Atlantic between the United Kingdom (UK) and the Caribbean every month. This volunteer observing ship (VOS) is fitted with an automated pCO_2 analyser, *Aanderaa* temperature (model 3210) and conductivity (model 3919) sensors to measure surface water pCO_2, temperature and salinity and tows a Continuous Plankton Recorder (CPR) to determine the phytoplankton community composition. Discrete dissolved inorganic carbon (DIC), total alkalinity (TA) and dissolved inorganic nutrient samples were collected on-board during 4 voyages of the VOS between April 2012 and

February 2013. These data were used to analyse the spatial and seasonal variability in the surface water carbonate system in relation to the abundance and distribution of key phytoplankton groups. Dinoflagellate and coccolithophore abundance were negatively correlated with DIC north of 45 °N, while south of this, sea surface temperature (SST) was the main driver of DIC concentrations. South of 30 °N TA and salinity decrease with decreasing latitude, due to the strong influence of river discharge from the Orinoco and Amazon rivers. The study site was divided into three regions based on the ratio of DIC:TA. The C:N:P ratio in the northern most region was 75±14:13±1.7:1 and in the mid North Atlantic region was 71±32:15±0.9:1. These ratios suggest phytoplankton overconsumption of DIC with respect to N and P particularly during the autumn voyage. A decreased buffering capacity in the northeast Atlantic is suggested, using discrete measurements of DIC and pCO_2 and comparisons with literature. This is likely due to the increased uptake of anthropogenic CO_2 within this region.

TA was conservative with salinity, allowing the calculation of DIC from pCO_2 and TA derived from salinity for the entire sampling period of 11 months. Calculated DIC compared well with measured DIC with a mean difference of -1.19 μmol kg^{-1} and an R^2 value of 0.94. This calculation was therefore applied to measurements of pCO_2 and salinity that have been made along this route since 2002, which gave estimates of monthly DIC from 2002-2013 with an error of 30.3 μmol kg^{-1}.

5.2 Introduction

Across the North Atlantic there is a latitudinal gradient between the biological and upwelling driven carbon cycle in the subpolar/temperate regions and the temperature driven carbon cycle in the subtropics (Takahashi and Sutherland, 2002). During the spring and summer months north of 40 °N intense phytoplankton blooms cause a reduction in the surface pCO_2 which is then counteracted during winter months with upwelling of deep waters that are rich in carbon and nutrients (Takahashi *et al.*, 1993). The distribution of phytoplankton blooms within the northeast Atlantic is patchy, and relies on seasonally stratified nutrient rich waters (Jönsson

et al., 2011; Kitidis *et al.*, 2012). South of 40 °N is a transition zone in which the temperature effects on pCO_2 start to dominate over the biological influence and, as the region becomes more oligotrophic, the seasonal cycle is in anti-phase with that in the high latitudes, with the winter acting as a sink for pCO_2 and the summer acting as a source (Takahashi *et al.*, 1993). Determining which phytoplankton groups dominate this biological influence, and the nutrient ratios associated with these different regions is important for improved understanding of the biogeochemical variability, which in turn will be influenced by our changing environment.

Through the use of a volunteer observing ship (VOS) *MV Benguela Stream*, four field campaigns were carried out traversing the North Atlantic from the United Kingdom (UK) to the Caribbean Islands between April 2012 and February 2013. Measurements of dissolved inorganic carbon (DIC) and total alkalinity (TA) were made alongside a suite of measurements (pCO_2, temperature, salinity, nutrients) that have been collected since 2002 (Schuster and Watson, 2007). This chapter investigates the relationships between the carbonate system (pCO_2, DIC and TA), phytoplankton community composition, and nutrient availability, on basin and seasonal scales in the North Atlantic Ocean.

5.3 Methods

5.3.1 Study area

Discrete samples for analysis of DIC and TA were collected during 4 voyages of the *MV Benguela Stream*. This VOS operates between Portsmouth and the Caribbean Islands completing one return voyage every month. The 4 voyages during which samples were collected were April/May 2012 (BS56 - Spring), June/July 2012 (BS58 - Summer), September/October 2012 (BS62 - Autumn) and January/February 2013 (BS66 - Winter). Figure 5.1 shows the sampling locations, with the red closed circles representing the stations sampled while travelling from the UK to the Caribbean, and the blue representing the stations sampled during the return crossing to the UK.

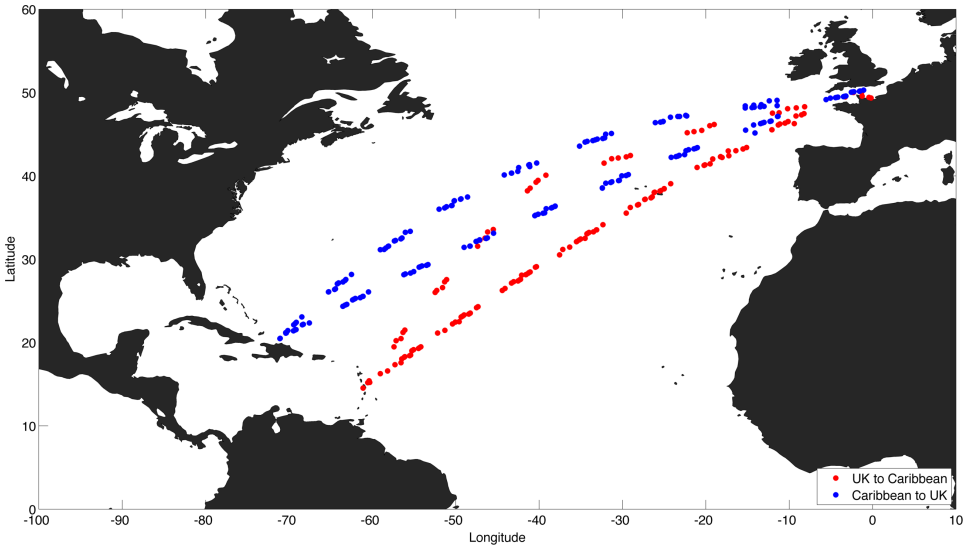

Figure 5.1: Map of the North Atlantic showing the location of each discrete sample. Red = stations sampled during the voyage from the United Kingdom (UK) to the Caribbean, Blue = stations sampled during the voyage from the Caribbean to the UK.

5.3.1.1 Regions

In order to analyse the dataset regionally, three latitudinal regions were discriminated by their ratio of DIC:TA. These regions are plotted as red boxes with SST plotted at each of the sampling locations in figure 5.2. The regions are designated region 1, 2 and 3 going from north to south.

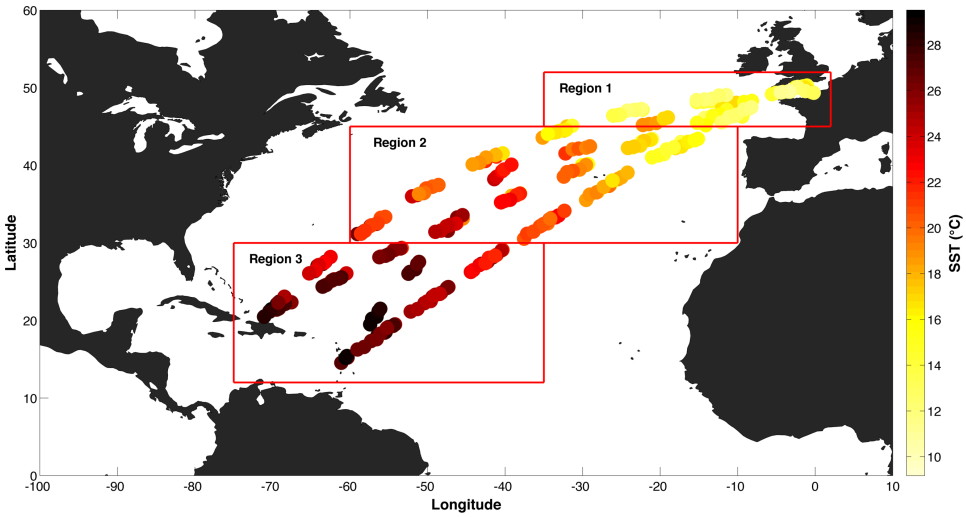

Figure 5.2: Map of the North Atlantic with SST shown at each discrete sampling position, and regions 1, 2 and 3 drawn as red boxes.

5.3.2 Discrete measurements

DIC and TA samples were collected every 2 hours during daylight hours and immediately preserved following the standard operating procedure (SOP) outlined by Dickson *et al.* (2007). Temperature, pressure and conductivity were recorded at the time of sampling. The samples were analysed on return to the laboratory (within 6 months) using two VINDTA 3C (**V**ersatile **IN**strument for the **D**etermination of **T**otal inorganic carbon and titration **A**lkalinity) instruments, which combine an acid titration to determine TA and a coulometric titration to determine DIC (Mintrop, 2011). For a detailed description of the methodology and sampling procedure see section 2.4 in the methods chapter, accuracy is given in table 5.1 below. Density was calculated using SST and calibrated salinity so that DIC, TA and nutrient data are reported in μmol kg^{-1}.

Nutrient and salinity samples were collected by the VOS crew every four and twelve hours respectively. These samples were analysed at the National Oceanography Centre (NOC) Southampton, using a SEAL AutoAnalyzer (Grasshoff *et al.*, 1999) and a Guildline Autosal salinometer (8400B). Silicate, phosphate and nitrate plus nitrite (NO_x) were determined following the procedures of Hansen and Koroleff (2007), accuracy is given in table 5.1 below.

5.3.3 Underway measurements

An automated pCO_2 analyser, a dual oxygen/temperature sensor (*Aanderaa* optode, model 3835), a conductivity sensor (*Aanderaa*, model 3919) and a temperature sensor (*Aanderaa*, model 3210) are permanently installed on the *MV Benguela Stream* using the set-up described by Schuster and Watson (2007). Data are recorded every minute alongside concurrent latitude, longitude, and UTC (Coordinated Universal Time) and stored on a computer. After each voyage the raw data are quality controlled. The *in situ* temperature and conductivity sensors are calibrated annually by the manufacturer, and additionally monthly using a three-point temperature calibration and the discrete seawater salinity samples. For a detailed description of the automated measurements set-up, calibration, and quality control see section 2.5 in the methods chapter. Accuracy is given in table 5.1.

Table 5.1: Accuracy associated with each of the measurements made.

Measurement	Accuracy	Method to derive accuracy
DIC	$\pm$2.55 (μmol kg^{-1})	Mean standard deviation of CRM DIC
TA	$\pm$1.46 (μmol kg^{-1})	Mean standard deviation of CRM TA
NO_x	$\pm$0.1(μmol kg^{-1})	SEAL AutoAnalyzer accuracy from international standards
Si	$\pm$0.1(μmol kg^{-1})	SEAL AutoAnalyzer accuracy from international standards
PO_4	$\pm$0.02(μmol kg^{-1})	SEAL AutoAnalyzer accuracy from international standards
Salinity	$\pm$0.05	Due to calculation from conductivity, and calibration using discrete samples
Temperature	$\pm$0.03 (°C)	Aanderaa 3210 sensor accuracy
pCO_2	$\pm$ <1(μatm)	LI-COR suggested accuracy
Pressure	$\pm$ <0.1(mbar)	Omega model PX2760-600A5V accuracy

5.3.4 Calculation and calibration of salinity

Salinity was calculated from the conductivity and temperature measurements, and then corrected for drift using co-located discrete salinity measurements for each voyage (figure 5.3). The accuracy was estimated from the error on the slope of the calibration lines, and is given in table 5.1.

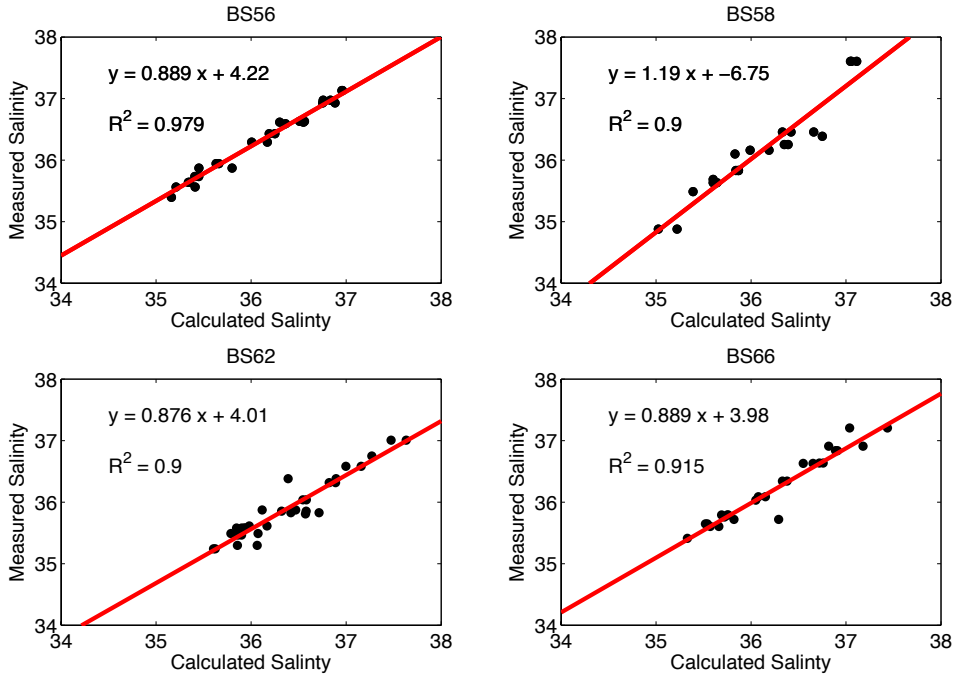

Figure 5.3: Salinity correction for each voyage (BS56, BS58, BS62, BS66), calculated using co-located discrete salinity measurements and salinity calculated from conductivity.

5.3.5 Salinity normalisation

Many studies employ the traditional salinity normalisation which designates a constant salinity to correct TA and DIC measurements for precipitation and evaporation (ie. normalise to a salinity of 35). However, this method ignores the influence on these carbonate parameters of riverine input of alkalinity, deep water upwelling, and dissolution of biogenic carbonates (Friis *et al.*, 2003).

Friis *et al.* (2003) suggest the use of a zero salinity endmember to normalise both TA and DIC as this adjusts the carbonate measurements to show no trend with salinity, whereas the traditional technique often overshoots the correction and a trend with salinity will still exist. This normalisation can be described by the following equation, where c is the intercept at zero salinity, and S is the salinity measurement.

$$nTA = (\frac{TA - c}{S}) \times (\overline{S} + c) \tag{5.1}$$

The same normalisation procedure was applied to the pCO_2, NO_x and PO_4 data in order to compare with nDIC.

5.3.6 Calculation of potential alkalinity

During organic matter cycling there is a small influence on TA concentrations that is due to the release or uptake of nutrients during remineralisation and photosynthesis respectively. The term potential alkalinity (pTA) was suggested by Brewer and Goldman (1976) as an indicator of the changes in TA that are not due to the cycling of organic matter, by summing nTA with measurements of NO_x:

$$pTA = nTA + NO_x \tag{5.2}$$

5.3.7 Intercomparison of the carbonate system

Using two measured carbonate parameters together with sea surface temperature (SST), salinity, sea level air pressure, silicate and phosphate, the remaining two carbonate parameters can be calculated (two of the following are required: DIC, TA, either fCO_2 or pCO_2, and pH). SST, salinity and sea level air pressure were measured within a minute of the sampling time, however due to the longer sampling intervals of the nutrient data, the silicate and phosphate concentrations had to be co-located to the nearest carbonate parameter sampling time. To calculate the carbonate parameters a Matlab toolbox of CO2SYS was used which is based on the program developed by Lewis *et al.* (1998) for DOS and Excel.

When using the CO2SYS toolbox there are a number of dissociation constant and formulation options that have to be selected. For this study the dissociation constants for carbonic acid (pK_1) were taken from Mehrbach *et al.* (1973) that were refitted by Dickson and Millero (1987), and the dissociation constant for HSO_4^- (K_{SO4}) (pK_2) was taken from Dickson (1990). Lueker *et al.* (2000) have estimated the root-mean-square-error (RMSE) for pK_1 as ± 0.0055 and for pK_2 as ± 0.01.

The uncertainty of calculating a carbonate parameter using CO2SYS was estimated following a Monte Carlo approach, whereby the accuracy associated with each of the input variables (see table 5.1) and the error associated with the dissociation constants (Lueker *et al.*, 2000) was randomly added/subtracted to the variable/constant within a normal distribution 10,000 times. The standard deviation of these 10,000 calculated values for each input measurement was then taken as the

uncertainty surrounding the calculated parameter, and the RMSE was calculated to provide one uncertainty value (Glover *et al.*, 2005; Quay *et al.*, 2010; Riebesell *et al.*, 2011).

5.3.8 Validation of DIC and TA

We compared our discrete measurements of DIC and TA with existing DIC and TA data. We searched for DIC and TA surface measurements from the GLODAP v1.1 (Key *et al.*, 2004) and CARINA (Velo *et al.*, 2010) databases on a spatial scale of 1 °latitude by 1 °longitude.

Figure 5.4 shows the surface measurements from GLODAP v1.1 (Key *et al.*, 2004) and the measurements of DIC and TA collected from the *MV Benguela Stream* in the North Atlantic.

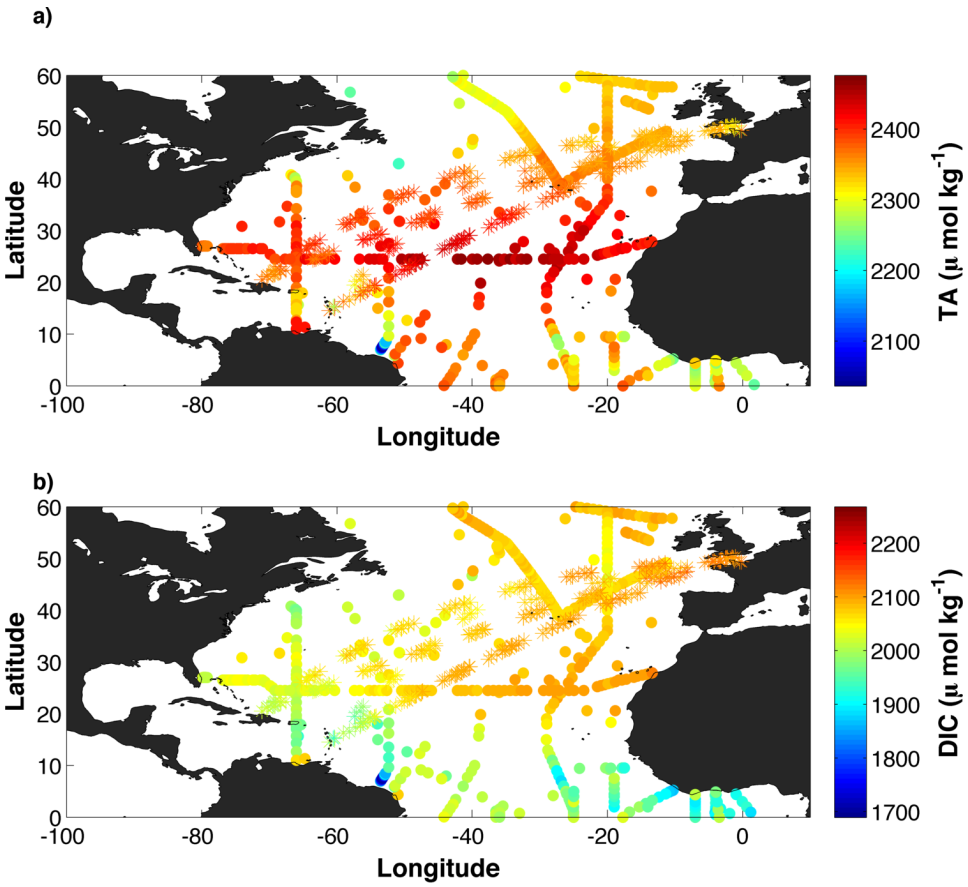

Figure 5.4: Surface measurements of a) TA and b) DIC in the North Atlantic. Circles = GLODAP v1.1 (Key *et al.*, 2004). Stars = Measurements collected from the *MV Benguela Stream* (this study).

Although GLODAP v1.1 and CARINA datasets consist of measurements that

were collected between 1972 and 1998 and between 1977 and 2006 respectively, for comparative purposes, we needed surface measurements made within the same month as the *MV Benguela Stream* data. Unfortunately not a single co-located measurement was found. Therefore a monthly 4°latitude × 5°longitude gridded climatology of DIC and TA was used to co-locate and compare with our measurements. These climatologies were obtained from the Biological and Chemical Oceanography Data Management Office (BCO-DMO) (Takahashi and Sutherland, 2013) and are based on GLODAP v1.1 (Key *et al.*, 2004), CARINA (Velo *et al.*, 2010), and LDEO databases (Takahashi *et al.*, 2009).

5.3.9 Calculation of the Revelle factor

The Revelle factor (or buffer factor) is calculated as the slope of the regression between the natural logarithm of pCO_2 and the natural logarithm of DIC ($\partial \ln(pCO_2)/\partial \ln(DIC)$) (Takahashi *et al.*, 1993). It is representative of the capacity for a body of water to take up surplus CO_2 (anthropogenic) from the atmosphere, where waters with a lower Revelle factor theoretically have a higher surplus CO_2. High latitude waters have higher Revelle factors whereas lower latitude waters have lower Revelle factors. Revelle factors are directly proportional to the ratio of DIC:TA (Sabine *et al.*, 2004).

5.3.10 Derivation of TA from salinity

Using the linear regression between TA and salinity, TA can be predicted from salinity when direct measurements of salinity but not TA have been made (Millero *et al.*, 1998). This method is particularly applicable in the open ocean where TA is mainly driven by freshwater addition and removal, which influence salinity in the same manner (Millero *et al.*, 1998; Lee *et al.*, 2006; Jiang *et al.*, 2014). TA is derived from equation 5.3 where *m* is the gradient of the linear regression between TA and salinity and *c* is the intercept:

$$TA = m \times salinity + c \tag{5.3}$$

Providing the TA:salinity relationship is robust, by measuring one of the carbonate parameters and calculating TA from salinity, the remaining carbonate parameters can be calculated using CO2SYS (Lewis *et al.*, 1998).

5.3.11 Biotic and abiotic influences on the carbonate system

Thermal (pCO_2T) and non-thermal (pCO_2NT) driving components on pCO_2 were derived following Körtzinger *et al.* (2008). This method was used by Takahashi and Sutherland (2002) and is based on the well constrained influence of temperature on pCO_2 under fixed DIC and TA conditions, where $\partial \ln pCO_2 / \partial T = 0.04231\ ^{\circ}C^{-1}$ (Takahashi *et al.*, 1993).

$$pCO_2T = \overline{pCO_2} \times e^{0.04231 \times (SST - \overline{SST})} \tag{5.4}$$

$$pCO_2NT = pCO_2 \times e^{0.04231 \times (\overline{SST} - SST)} \tag{5.5}$$

Where the over bar indicates mean parameter. pCO_2T calculated following equation 5.4 represents the pCO_2 concentration if the addition or removal of carbon by biological and air-sea exchange processes were absent. Whereas pCO_2NT calculated following equation 5.5, removes the effect of pCO_2T by correcting to the mean SST. Therefore pCO_2NT represents the pCO_2 concentration due to changes in DIC and TA, which could be influenced by biology, air-sea CO_2 exchange, advection, and mixing (Körtzinger *et al.*, 2008).

On long time scales (100,000 years) global DIC and TA are primarily driven by weathering processes. However on shorter time scales (months) after normalisation, there are three main processes that influence the ratio of nDIC and nTA. Zeebe and Wolf-Gladrow (2001) outline the relative changes in normalised DIC and TA concentration through the use of a 'Defeyes diagram' (figure 5.5), in which processes that influence the carbonate chemistry of a water parcel can be inferred by the change in the ratio between nDIC and nTA. The invasion or release of CO_2 from the atmosphere to the ocean increases or decreases the concentration of DIC

respectively, without influencing the charge balance and therefore the TA stays the same.

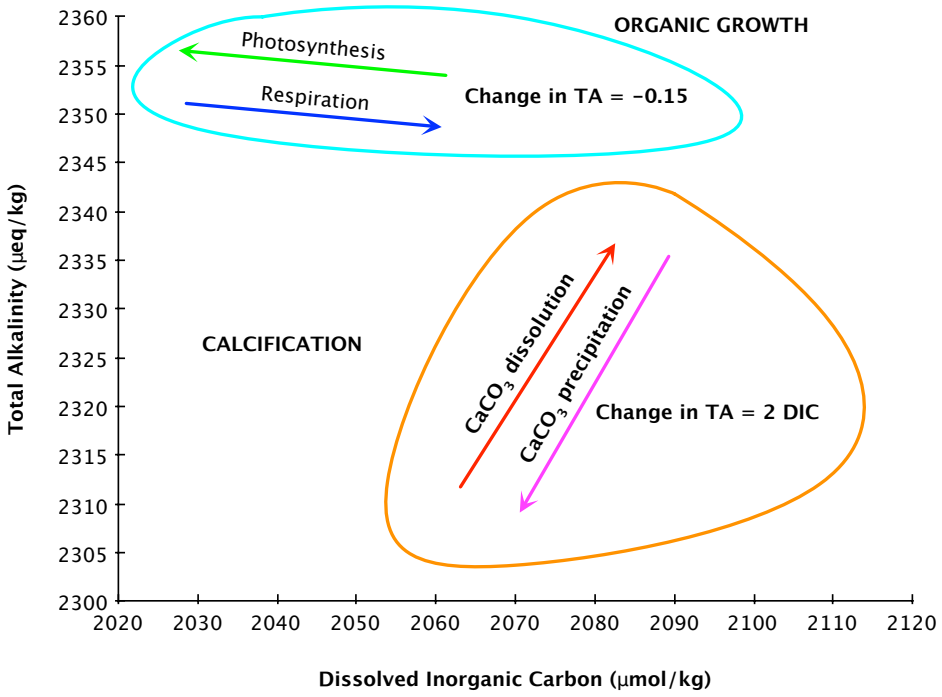

Figure 5.5: Schematic of the changes in TA and DIC that occur during respiration, photosynthesis, calcium carbonate dissolution and precipitation.

Respiration and photosynthesis have a similar trend to the air sea exchange process due to the release or uptake of CO_2, but there is a small influence on TA due to the charge that is present on nutrients. For every mole of nitrate that is assimilated by phytoplankton, TA increases by 1 mole (Wolf-Gladrow *et al.*, 2007):

$$NH_3 + 2O_2 \rightleftarrows NO_3^- + H^+ + H_2O \tag{5.6}$$

Therefore during photosynthesis for every 1 unit decrease in DIC, TA increases by 0.15 and vice versa during respiration (-16/106 = -0.15, see figure 5.5):

$$106CO_2 + 16NO_3^- + HPO_4^{2-} + 78H_2O + 18H^+ \rightleftarrows C_{106}H_{175}O_{42}N_{16}P + 150O_2 \tag{5.7}$$

The formation of calcium carbonate ($CaCO_3$) decreases DIC and TA in a ratio of 1:2 (figure 5.5), due to the loss of the positive charge which decreases TA, and the loss of bicarbonate which reduces DIC.

$$Ca^{2+} + 2HCO_3^- \longrightarrow CaCO_3 + CO_2 + H_2O \quad (5.8)$$

Although this process releases CO_2, due to the buffering capacity of seawater this only produces ∼0.03 μmol of CO_2 per μmol of $CaCO_3$ formed (Zeebe and Wolf-Gladrow, 2001).

5.3.12 Calculation of Redfield ratios

The Redfield ratio describes the stoichiometric relationship between carbon and inorganic nutrients, and is relatively constant within the open ocean when nutrient limitation is not occurring (Redfield *et al.*, 1963; Sambrotto *et al.*, 1993). For example Anderson and Sarmiento (1994) found an average (for the Atlantic and Pacific measured at depths ranging from 400m to 4000m) stochiometric ratio of 117±14:16±1:1 (C:N:P (mol:mol:mol)). Redfield used open ocean measurements of particulate and dissolved nutrients to predict the following Redfield ratio; 106:16:1 (C:N:P) (Redfield *et al.*, 1963). Deviations from the Redfield ratio indicate carbon overconsumption, nutrient limitation, and other influences such as riverine, or nutrient recycling or fixation (Jiang *et al.*, 2013).

Using the linear regression between measurements of normalised DIC and NO_x and PO_4 the C:N and C:P ratios can be determined regionally, and compared with Redfield's ratio.

5.3.13 Phytoplankton community composition

A CPR is towed behind the *MV Benguela Stream* from 40 °W on every monthly crossing between the Caribbean and the UK. For a detailed methodology of the CPR sampling see section 2.1 in the methods chapter.

The phytoplankton data from the CPR survey were divided into 6 key phytoplankton indices, namely phytoplankton colour index (PCI), spring-bloom forming diatoms (diatoms), *Rhizosolenia* (diatom genus often associated with a later blooming-time), dinoflagellates, silicoflagellates, and coccolithophores. Table 3.1 in chapter 3 lists the species that were included in these indices, with the addition

of coccolithaceae and silicoflagellatae, which have been counted in the CPR samples since 1993 (Richardson *et al.*, 2006). Rare species bias was removed from the dataset by only including species that occur above 1% frequency of occurrence (Edwards and Richardson, 2004). The phytoplankton indices were all log transformed using $\log_{10}(x+1)$ in order to homogenise the variance (Alvarez-Fernandez *et al.*, 2012).

In order to investigate phytoplankton abundance across the whole North Atlantic basin, satellite data were used as an indicator of Chl-a concentration. These data were obtained from Aqua-MODIS at a resolution of 9 km and frequency of 1 month (http://oceandata.sci.gsfc.nasa.gov).

5.3.14 Data interpolation

In order to create seasonal Hovmoller contour plots of the pCO_2 components and phytoplankton indices against longitude, objective mapping was used to interpolate between data points. The best fit to the data was found to be a Gaussian distribution, with an influence radius of 2 in the x-direction (2°longitudinal steps) and 0.5 in the y-direction (between seasons). Objective mapping can be described by the following equation:

$$b = w \times E^{-1} \times r \tag{5.9}$$

Where b is the mapped property, w is the data weight, E is the covariance matrix and r is the residual (weighted mean).

5.4 Results

5.4.1 Distributions of DIC, TA, nutrients, salinity, pCO_2 and SST

Figure 5.6 shows the relationships between DIC and TA with SST and salinity separated by latitudinal bands. DIC decreases with increasing SST (figure 5.6a) from 2138.3 μmol kg^{-1} at 9.17°C to 1934.8 μmol kg^{-1} at 29.52°C. This is to be expected as the increasing SST decreases the solubility of pCO_2. Therefore it does

not dissociate to form DIC as readily. SST increases linearly with decreasing latitude, but DIC decreases at 3 different rates with increasing SST and decreasing latitude, -7.93 μmol kg^{-1} per 1 °C between 50°N and 45°N, -4.03 μmol kg^{-1} per 1 °C between 45°N and 30°N where the decrease levels off slightly, and -13.78 μmol kg^{-1} per 1 °C between 30°N and 14°N where the rate of decrease increases again (figure 5.6a). DIC decreases with increasing salinity from high latitudes to low latitudes to about 30°N where salinity starts to decrease with decreasing DIC (figure 5.6b). TA increases with increasing SST from $\sim$ 10 to 15°C at 50°N to about 25°C at 30°N where TA starts to decrease. TA and salinity increase with decreasing latitude from 2287 μmol kg^{-1} and 33.03 salinity at 50°N to 2449.0 μmol kg^{-1} and 37.42 salinity at $\sim$ 25°N. Between 25°N and 14°N salinity decreases to 34.63 and TA decreases to 2271.6 μmol kg^{-1}. The low salinity values were reported an hour after leaving port in Le Havre. The greatest variance in the linear relationship between TA and salinity occurs at the highest latitudes (figure 5.6d).

The seasonal change in DIC, TA, salinity, NO_x, Si, and PO_4 between 70 and 0°W are shown in figure 5.7. The lowest DIC concentrations ($<$ 2020 μmol kg^{-1}) occur throughout the sampling seasons westward of 65°W, with low concentrations reaching eastward ($\sim$ 60°W) throughout the autumn and summer (figure 5.7a).

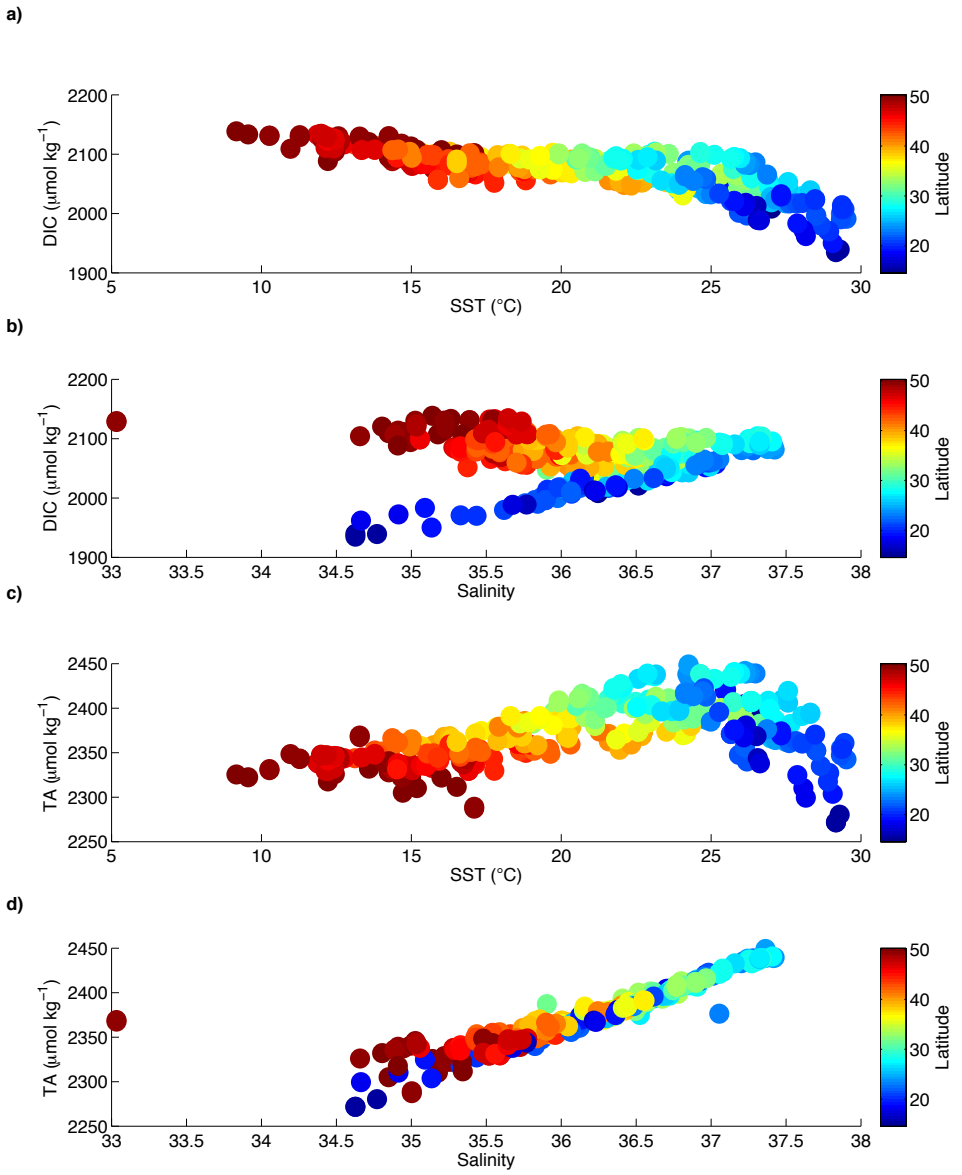

Figure 5.6: a) DIC against SST, **b)** DIC against salinity, **c)** TA against SST, **d)** TA against salinity. The colour bar for each plot corresponds to the latitude °N of the sample.

High DIC concentrations (> 2100 μmol kg^{-1}) occur between 0°W and 30°W during the winter months. Unsurprisingly, the concentrations of NO_x show a similar seasonal/latitudinal pattern to DIC (figure 5.7c), with low NO_x concentrations (< 1 μmol kg^{-1}) occurring in the summer across the whole transect and throughout all of the seasons west of 30°W. The highest concentration of NO_x (> 6 μmol kg^{-1}) occurs at 10°W in the winter (Jan/Feb). The TA and salinity have a similar distribution in the spring and winter months (figure 5.7b, d). However this similarity breaks down in the summer and autumn months as the salinity increases in the autumn months (Sep/Oct) between 10°W and 35°W while the TA decreases. The

Si and PO_4 have similar distributions to NO_x with low concentrations (~ 0.5 μmol kg^{-1} and ~ 0.05 μmol kg^{-1} respectively) occurring in the summer and higher concentrations occurring in the English Channel between 0°W and 5°W (figure 5.7e, f). At 70 °W both Si and PO_4 have a peak in concentration during the summer sampling period (Jun/Jul).

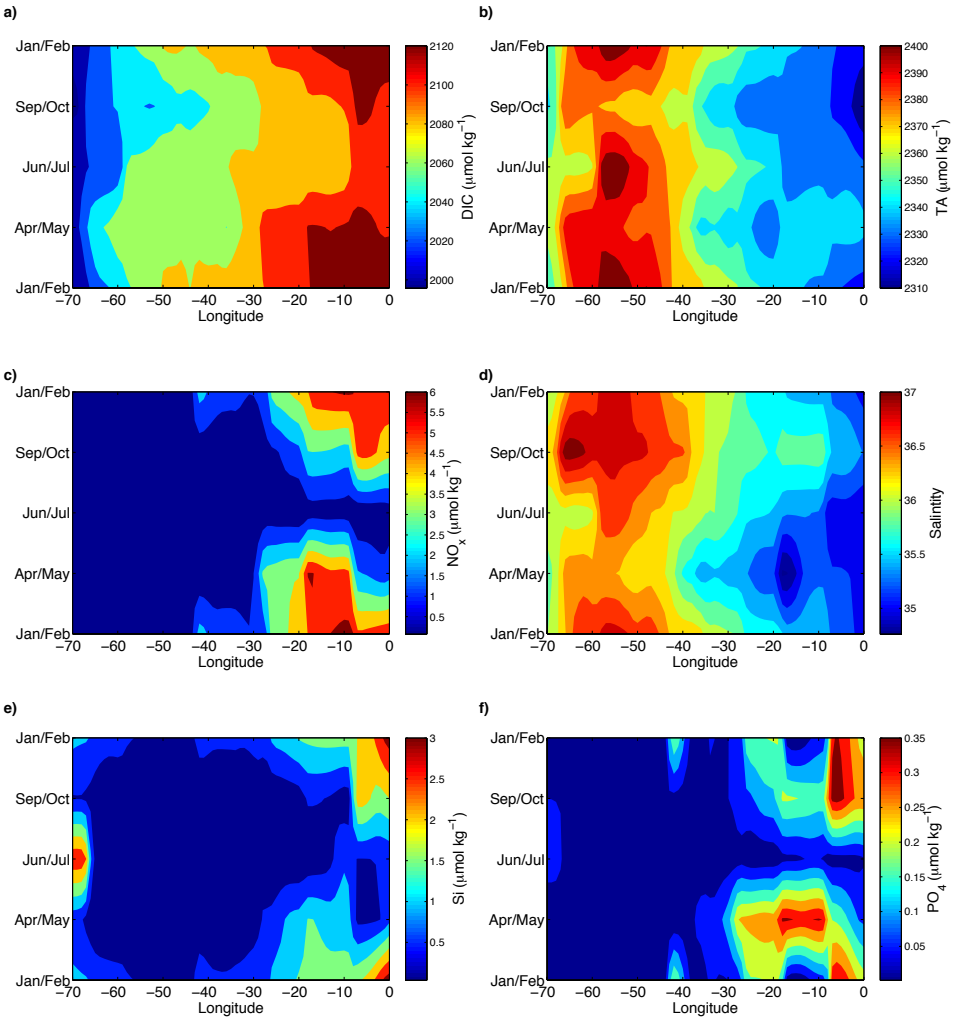

Figure 5.7: Hovmoller of **a)** DIC, **b)** TA, **c)** NO_x, **d)** salinity, **e)** Si, and **f)** PO_4 for each sampling period from 70°W to 0°W along the Caribbean to UK transect.

The monthly nutrient concentrations with monthly normalised DIC in each of the three regions defined in figure 5.2 are shown in figure 5.8. Due to sampling logistics, there are fewer nDIC data than nutrient data. In region 1 (figure 5.8a) the monthly trend in nDIC is similar to the monthly trend in inorganic nutrients. Note the different y axes scales, with decreasing concentrations of nDIC and inorganic nutrients from region 1 to region 3 and the changes in the N:P and N:Si ratios.

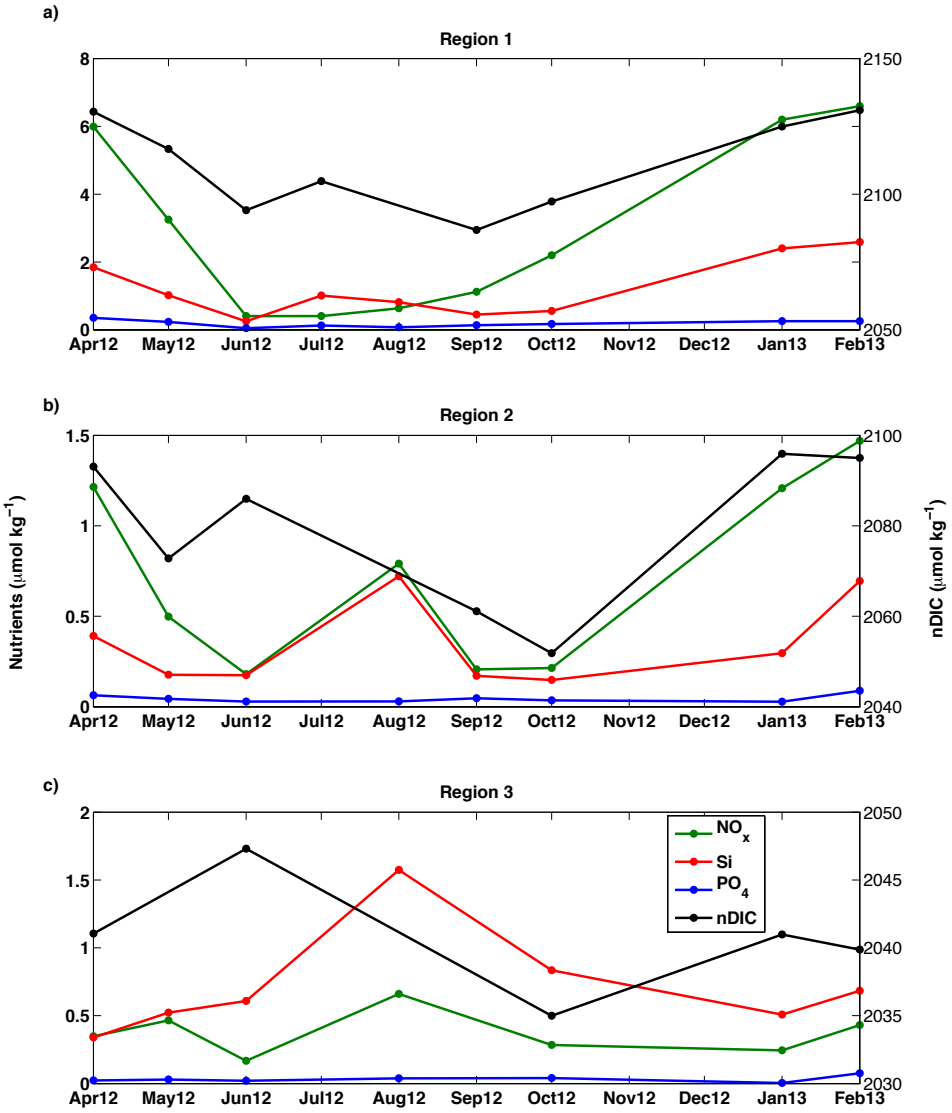

Figure 5.8: Monthly NO_3 (green), Si (red), PO_4 (blue) on the left y-axis in μmol kg^{-1}, and monthly nDIC (black) on the right y-axis in μmol kg^{-1}, from April 2012 to February 2013 for regions **a)** 1, **b)** 2, and **c)** 3. Note the different y axes scales.

pTA and nTA calculated from each TA measurement are plotted against salinity in figure 5.9 to evaluate the influence of NO_x on nTA. pTA data are plotted as open circles, with the colour indicating latitude (°N). At higher latitudes (coloured green), where concentrations of NO_x are highest, there is a greater offset between the open circles of pTA data and the closed circles of nTA data than at lower latitudes (coloured blue and purple) where NO_x concentrations are lowest and the open circles of pTA data coincide with the closed circles of nTA data.

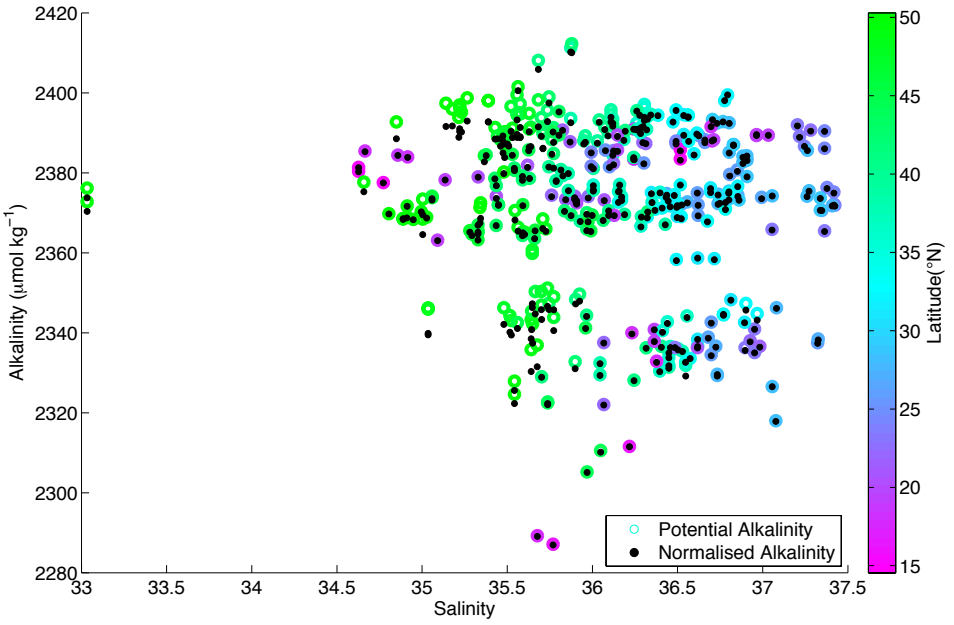

Figure 5.9: Potential Alkalinity (coloured open circles) and normalised alkalinity (black closed circles) against salinity. Colour corresponds to latitude (°N).

5.4.2 Salinity normalisation

Figure 5.10 shows the normalisation of DIC and TA in regions 1 to 3 using equation 5.1, with the regression equation of the normalised data shown on each subplot. These plots demonstrate that the variability in DIC and TA related to the variability in salinity has been removed using this correction , as the slopes of the regression lines between the normalised data and salinity are close to zero. In regions 1 and 2 (figures 5.10 a and c) there is more scatter in the DIC data than in region 3 (figure 5.10e), and the normalisation procedure for TA in region 1 (figure 5.10b) makes little difference as the normalised TA data almost completely overlays the original TA data.

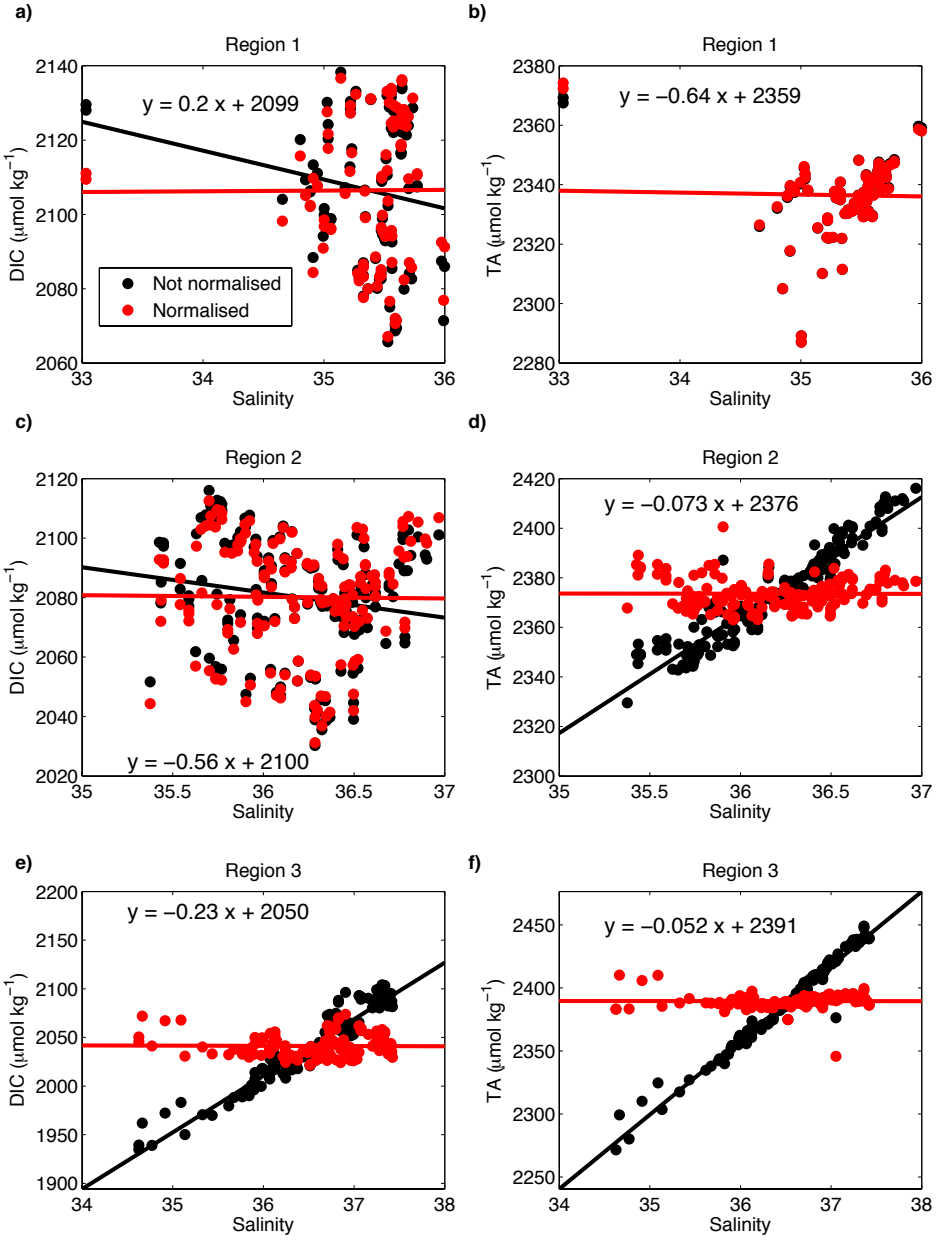

Figure 5.10: Normalisation of DIC and TA using equation 5.1 in regions 1 to 3. Red circles = normalised data, with red regression line. Black circles = original data, with black regression line. Regression equation of the normalised data is shown on each subplot.

5.4.3 Intercomparison of carbonate system

DIC, TA and pCO_2 were calculated using CO2SYS (see figures 5.11 to 5.13). Unfortunately the underway pCO_2 system had some technical problems during parts of the sampling campaign where DIC and TA were measured, particularly during the June/July voyage, which is why there are fewer calculated data than measured data and no calculated data during the summer months.

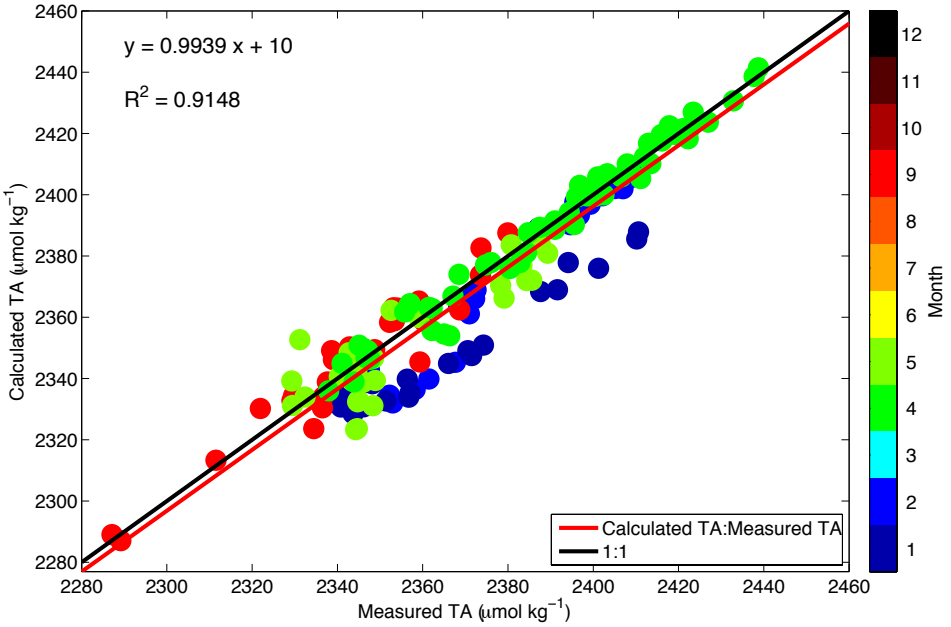

Figure 5.11: TA calculated from measured DIC and pCO_2 using CO2SYS (Lewis *et al.*, 1998) against measured TA. Red line shows the linear relationship between the co-located samples, black line shows the optimal 1:1 relationship.

The mean difference between calculated TA and measured TA was 3.58 μmol kg^{-1}, with a RMSE of 9.64 μmol kg^{-1} and a Pearson's correlation coefficient of 0.96 (figure 5.11). Some of the TA data collected in January fall below the optimal 1:1 regression. This is because the measured TA is lower than the calculated TA, whereas in figure 5.12 some of the DIC data in January are above the 1:1 regression line. The mean difference between calculated DIC and measured DIC was -3.01 μmol kg^{-1}, with a RMSE of 8.07 μmol kg^{-1} and a Pearson's correlation coefficient of 0.98 (figure 5.12).

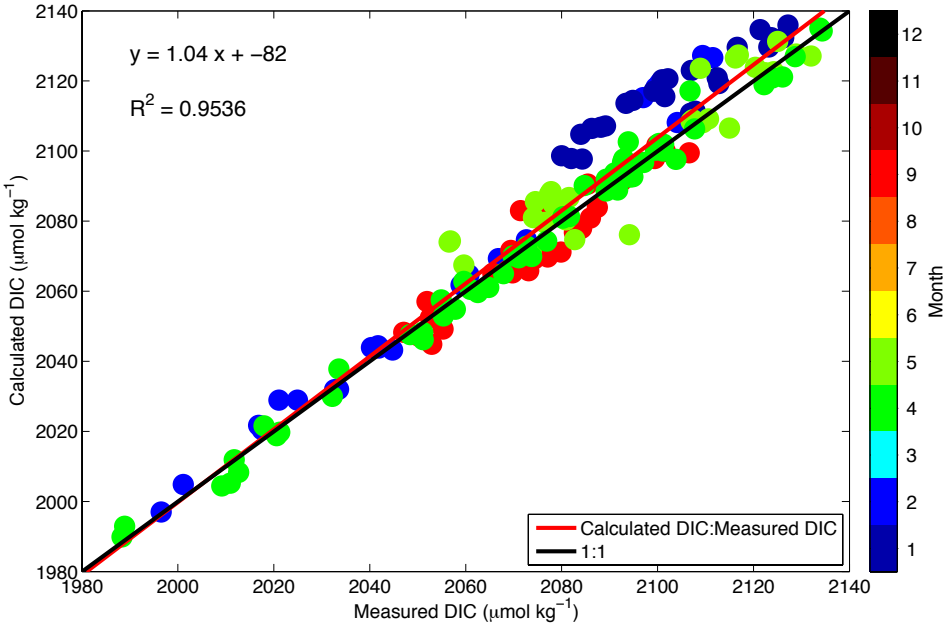

Figure 5.12: DIC calculated from measured TA and pCO_2 using CO2SYS (Lewis *et al.*, 1998) against measured DIC. Red line shows the linear relationship between the co-located samples, black line shows the optimal 1:1 relationship.

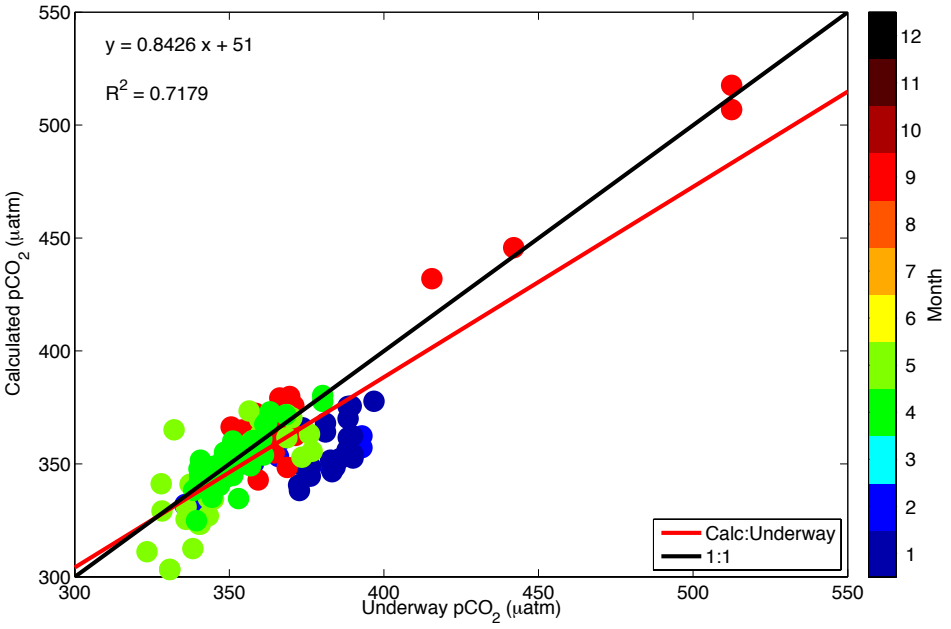

Figure 5.13: pCO_2 calculated from measured DIC and TA using CO2SYS (Lewis *et al.*, 1998) against measured pCO_2. Red line shows the linear relationship between the co-located samples, black line shows the optimal 1:1 relationship.

Figure 5.13 shows the comparison between calculated pCO_2 using the TA and DIC measurements and co-located pCO_2 measurements. The data points fall close to the optimal 1:1 regression line in the spring and autumn months (coloured green and red), even when there were high values of pCO_2 recorded during the autumn.

However during the winter months (coloured blue) some of the measurements fall below the optimal 1:1 regression, as the calculated pCO_2 is lower than the measured pCO_2 during these months. The mean difference between these data points was 5.41 μatm, with a RMSE of 14.61 μatm and a Pearson's correlation coefficient of 0.85.

The Monte Carlo approach outlined in section 5.3.7 showed that all of the errors associated with using CO2SYS to calculate each of the carbonate parameters were greater than our measurement uncertainties on the associated carbonate parameter, demonstrating that our data measurements are internally consistent (table 5.2).

Table 5.2: RMSE from calculating parameter with CO2SYS, measurement uncertainty, and RMSE of the regression between measured and the CO2SYS calculated parameter.

	RMSE CO2SYS	**Uncertainty**	**RMSE Regression**
TA (μmol kg^{-1})	5.72	$\pm$ 1.46	9.64
DIC (μmol kg^{-1})	4.14	$\pm$ 2.55	8.07
pCO_2 (μatm)	8.35	$\pm$ 1	14.61

5.4.4 Validation of DIC and TA

Figures 5.14 and 5.15 show the comparison between our measurements and the nearest measurement within the monthly 4 °$\times$ 5 °search radius of the Takahashi and Sutherland (2013) monthly climatology. Our DIC measurements correspond with the climatological data, as the slope of the regression is close to the optimal regression slope of 1 (Figure 4.13). The mean difference between the DIC measurements and the climatological DIC was 3.48 μmol kg^{-1}, with a root-mean-square-error (RMSE) of 14.95 μmol kg^{-1} and a Pearson's correlation coefficient of 0.92. This relationship does not vary between the different sampling months.

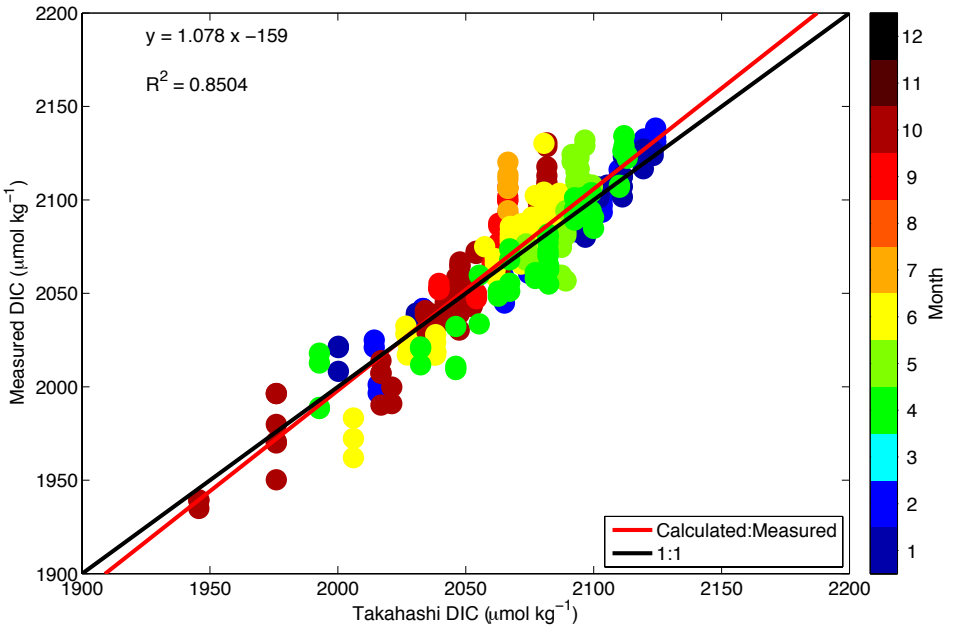

Figure 5.14: Measured DIC against co-located DIC from Takahashi and Sutherland (2013) climatology. Red line shows the linear relationship between the co-located samples, black line shows the optimal 1:1 relationship.

When comparing the TA measurements with the TA climatological data the measurements are slightly lower than the climatological values, with the mean difference being - 4.94 μmol kg^{-1} with a RMSE of 14.58 μmol kg^{-1} and a Pearson's correlation coefficient of 0.91 (figure 5.15). There is no relationship between sampling months, but there is more variation around the slope between the TA data (figure 5.15) than the DIC data (figure 5.14).

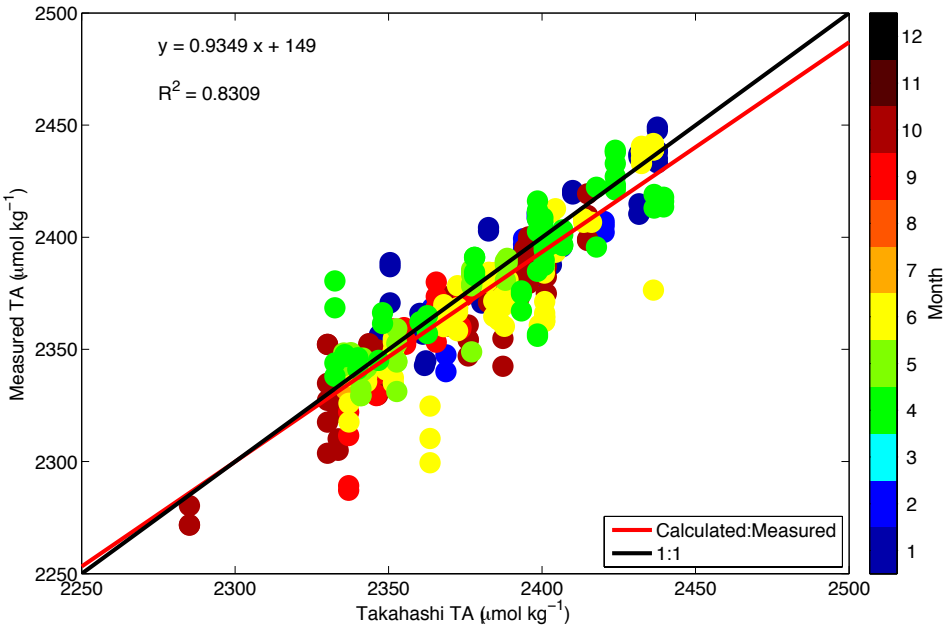

Figure 5.15: Measured TA against co-located TA from Takahashi and Sutherland (2013) climatology. Red line shows the linear relationship between the co-located samples, black line shows the optimal 1:1 relationship.

5.4.5 Revelle factors

pCO_2 ($npCO_2$) was normalised following Friis *et al.* (2003). The Revelle factors for each region ($\pm$ 1 standard deviation (SD) of the slope) are presented in figure 5.16. The Revelle factor in region 1 was highest at 15 $\pm$ 0.8, surface waters in region 2 had a Revelle factor of 11 $\pm$ 0.9, and surface waters in region 3 had the lowest Revelle factor of 7 $\pm$ 0.8. Region 2 (figure 5.16b) shows the most scatter in the data, particularly in the winter (Jan/Feb) and spring (Apr/May) months. In regions 1 and 2 (figures 5.16a and b) the autumn (Sep/Oct) months have lower values than the winter (Jan/Feb) months.

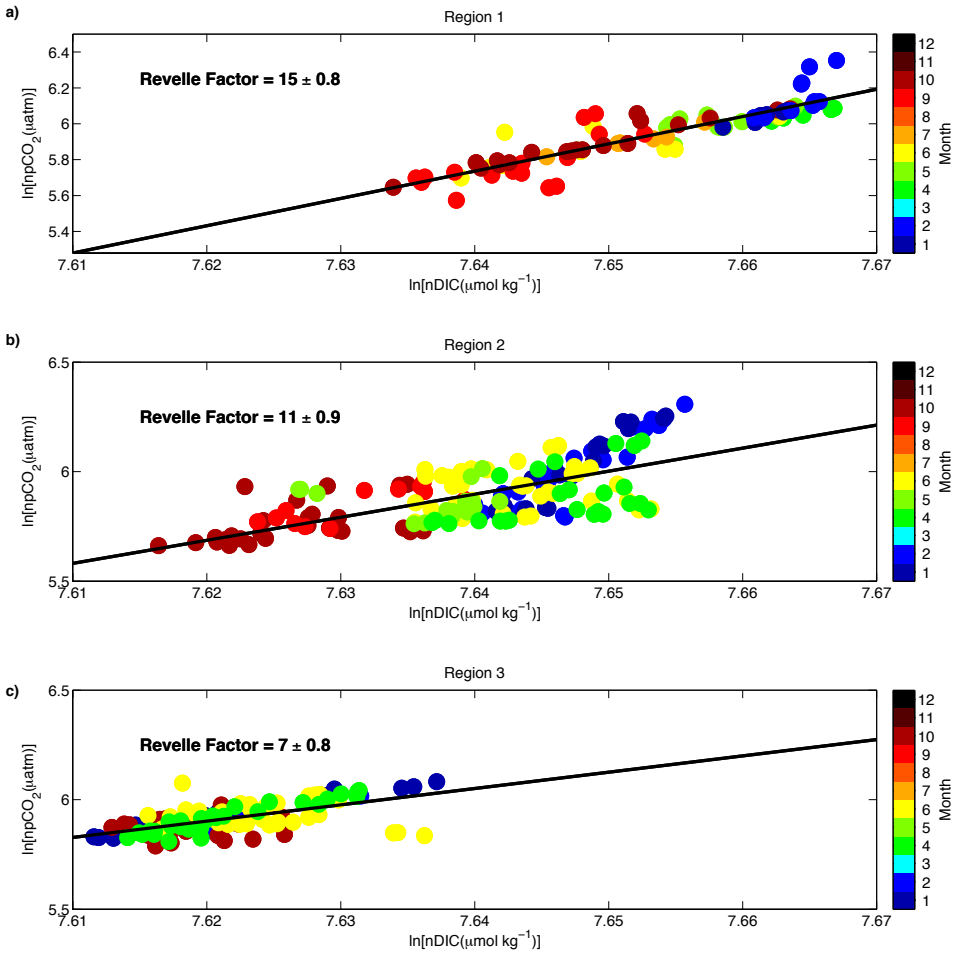

Figure 5.16: ln[npCO$_2$ (μatm)] against ln[nDIC (μmol kg^{-1})] with coloured circles corresponding to the month of sampling, and the black line showing the regression for regions **a)** 1, **b)** 2, and **c)** 3. The Revelle factor is calculated as the slope of the line $\pm$ 1 SD (standard deviation).

5.4.6 Derivation of TA from salinity

Figure 5.17 shows the relationship between TA and salinity for all data (n=389) between the UK and the Caribbean. Chauvenet's criterion was applied to the dataset to check for outliers (Glover *et al.*, 2005), of which two were identified (outlined with red circles in figure 5.17). In regions 1 and 3 there is more scatter around the regression line at low TA and salinity concentrations in the summer and autumn months (figure 5.17). This could be due to the influence of riverine input as region 2 (which is in the open ocean) doesn't show these lower values or variance. However as these measurements were not identified as outliers they were included in the derivation of the regression equation. Therefore the remaining 387 measurements were used to calculate the regression line between TA and salinity, which gave the

equation (± 1 SD):

$$TAcalc = 51(\pm 0.7) \times Salinity + 516(\pm 26) \tag{5.10}$$

The error associated with TAcalc was calculated following a Monte Carlo method, which gave a RMSE of ±36.33 μmol kg^{-1}.

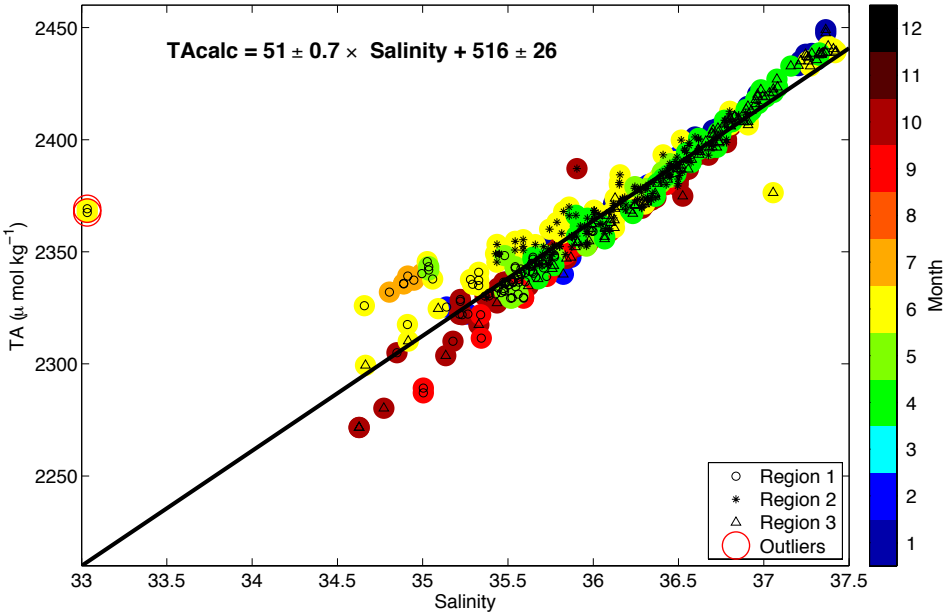

Figure 5.17: TA(μmol kg^{-1}) against salinity with coloured circles corresponding to the month of sampling, and the black line showing the regression using data that were not identified as outliers. The symbols within the coloured circles correspond to the region, circle = region 1, star = region 2, and triangle = region 3. The red open circles are measurements that were identified as outliers using Chauvenet's criterion.

DIC was then calculated using CO2SYS, from TA derived from salinity (figure 5.17) and measured pCO_2. This calculated DIC compares well with measured DIC with an R^2 value of 0.94 (figure 5.18). The mean difference between the calculated DIC and the measured DIC was -4.60 μmol kg^{-1}, with a RMSE of 9.29 μmol kg^{-1} and a Pearson's correlation coefficient of 0.97. No outliers were identified following Chauvenet's criterion (Glover *et al.*, 2005). The RMSE of calculating DIC from the TA:Salinity relationship (±36.33 μmol kg^{-1}) and pCO_2 (±1 μatm) using CO2SYS was ± 30.30 μmol kg^{-1}, following the Monte Carlo method outlined in section 5.3.7. This error is relatively large due to the large error associated with calculating TA, and the error propagation within the Monte Carlo method.

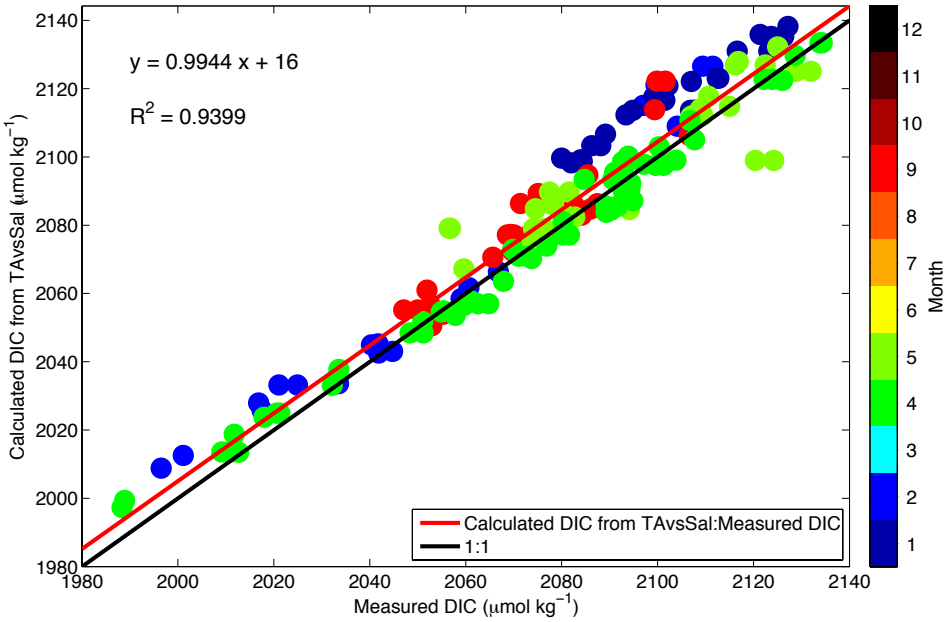

Figure 5.18: Calculated DIC from CO2SYS (Lewis *et al.*, 1998) using co-located pCO_2 and the TA:Salinity relationship against measured DIC. Red line shows the linear relationship between measured and calculated DIC, black line shows the optimal 1:1 relationship.

5.4.7 Biotic and abiotic influences on the carbonate system

pCO_2 was calculated using CO2SYS for the outward and return voyages separately (see figure 5.1), and hovmoller plots were created of the pCO_2 thermal, and non-thermal seasonal cycles using objective mapping. Figure 5.19 shows an opposing seasonal cycle of pCO_2 between 0°W to 25 °W and 25°W to 60 °W measured during the outward crossings (UK to Caribbean). The seasonal maximum in pCO_2 occurs west of 30°W during the summer and autumn months, while east of 7°W there are very high concentrations of pCO_2 during August to February (figure 5.19a). At 25 °W the thermal component begins to dominate the pCO_2 going westward, while the non-thermal components dominate going eastward with a transition zone occurring between them (at 30 to 35 °W) where the concentrations are similar ($\sim$375 μatm, figure 5.19b and c).

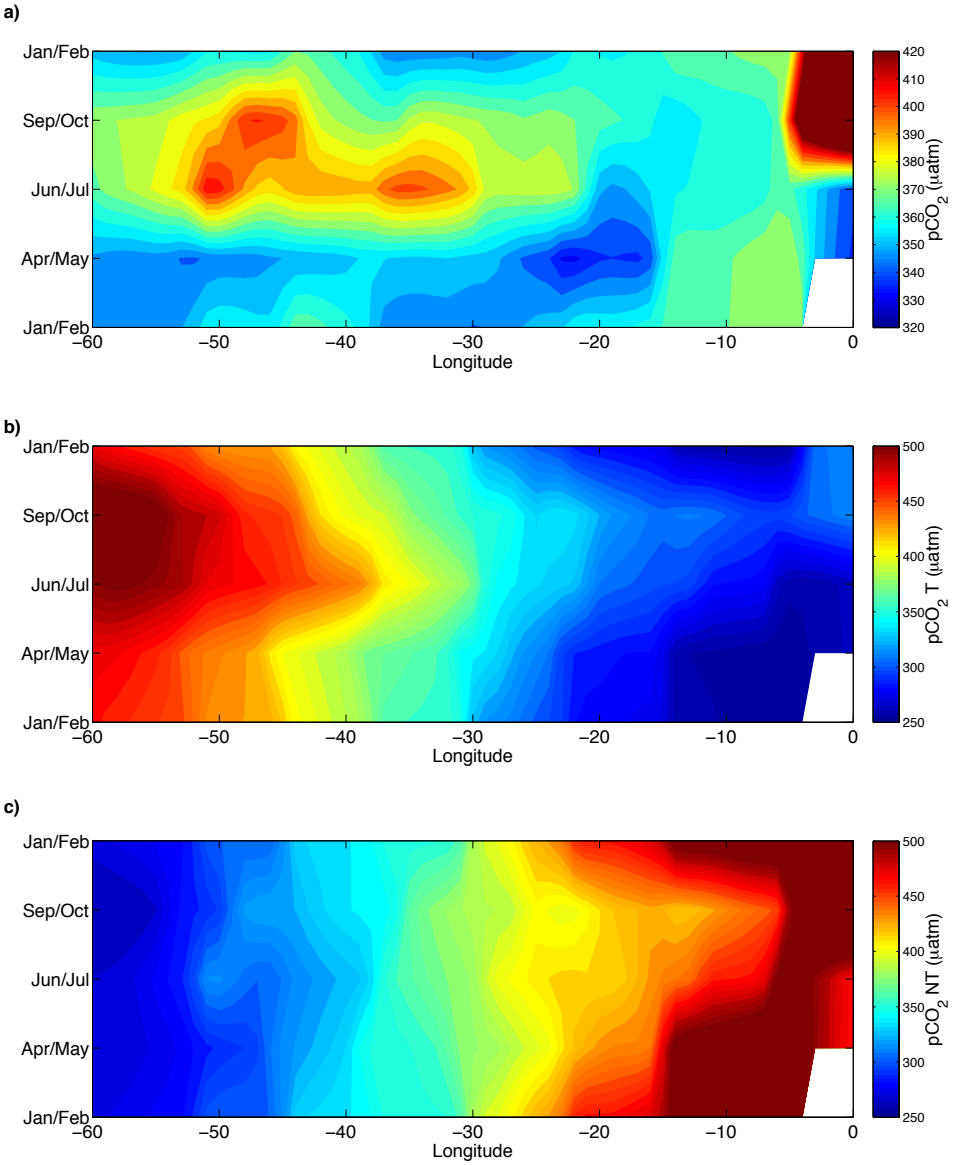

Figure 5.19: Hovmoller of **a)** pCO_2, **b)** thermal pCO_2 (pCO_2T), and **c)** non-thermal pCO_2 (pCO_2NT) between Jan/Feb 2012 and Jan/Feb 2013 from 60°W to 0°W along the UK to Caribbean transect.

Figure 5.20 shows the data collected during the return voyages plotted between 70°W and 0°W (note the port of departure in the Caribbean islands is 10°further westward than the port of arrival (figure 5.1)).

The opposing seasonal cycle of pCO_2 between 0°W to 25 °W and 25°W to 40 °W is also evident on the return crossing, with seasonal maxima (> 380 μatm) occurring west of 30°W during the summer and then in the autumn west of 60 °W, and low pCO_2 (< 360 μ atm) occurring during the summer between 10°W and 25 °W and in the spring between 0°W and 10 °W (figure 5.20a). As seen in figure

5.19a there is a peak in pCO_2 during the autumn between 0°W and 10 °W (figure 5.20a). The strong thermal and biological influence on pCO_2 can be seen in figures 5.20b and 5.20c as the seasonal cycle of DIC matches the seasonal cycle in non-thermal pCO_2NT and is in anti-phase with the seasonal cycle of thermal pCO_2T (figure 5.7a).

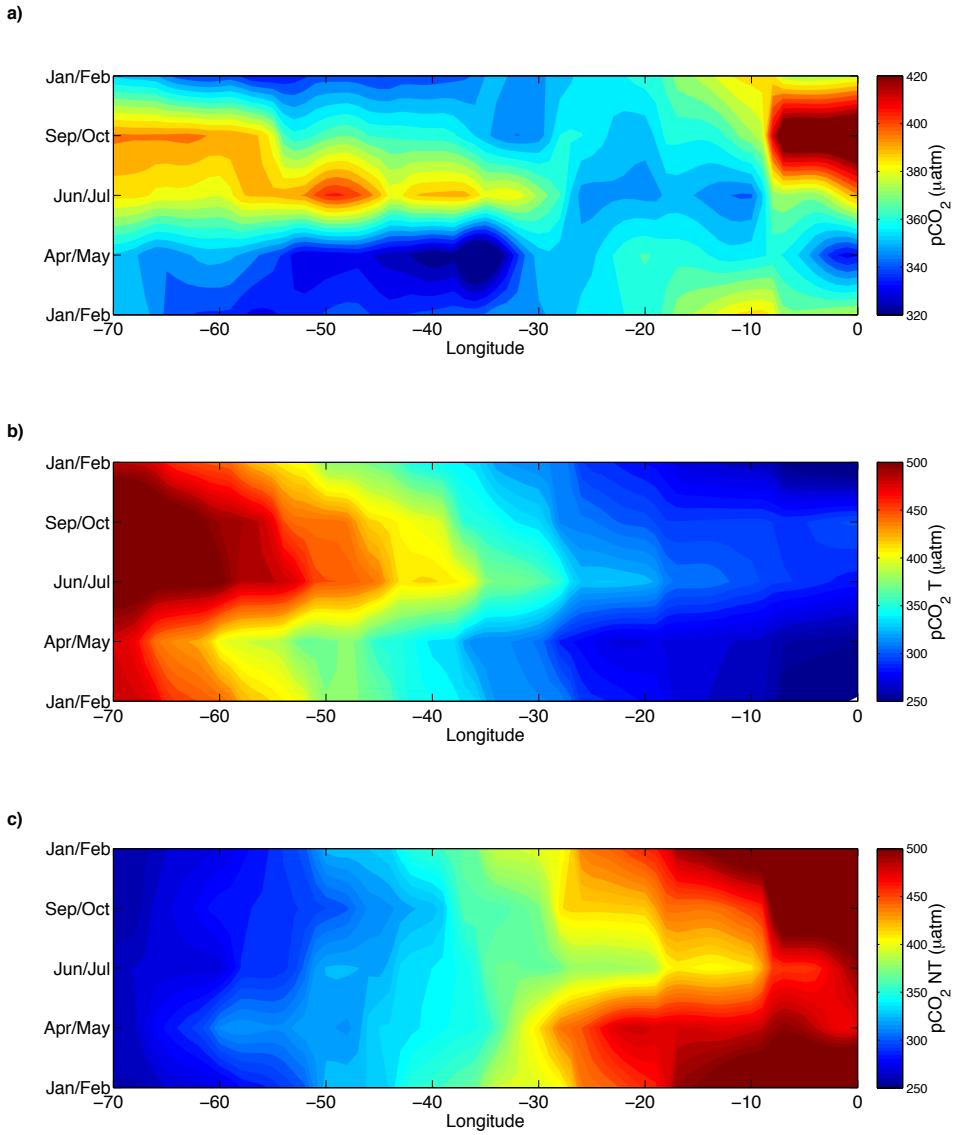

Figure 5.20: Hovmoller of **a)** pCO_2, **b)** thermal pCO_2 (pCO_2T), and **c)** non-thermal pCO_2 (pCO_2NT) between Jan/Feb 2012 and Jan/Feb 2013 from 70°W to 0°W along the Caribbean to UK transect.

Figure 5.21a shows the nTA against nDIC data in region 1 (see figure 5.2 for regions) which are coloured according to the month they were measured. Figure 5.21b uses the ratios described within methods section 5.3.11 and the values within 5.21a to create a Defeyes diagram. Lowest nTA and nDIC concentrations (2290

μmol kg^{-1}and 2070 μmol kg^{-1} respectively) occur during September and October.

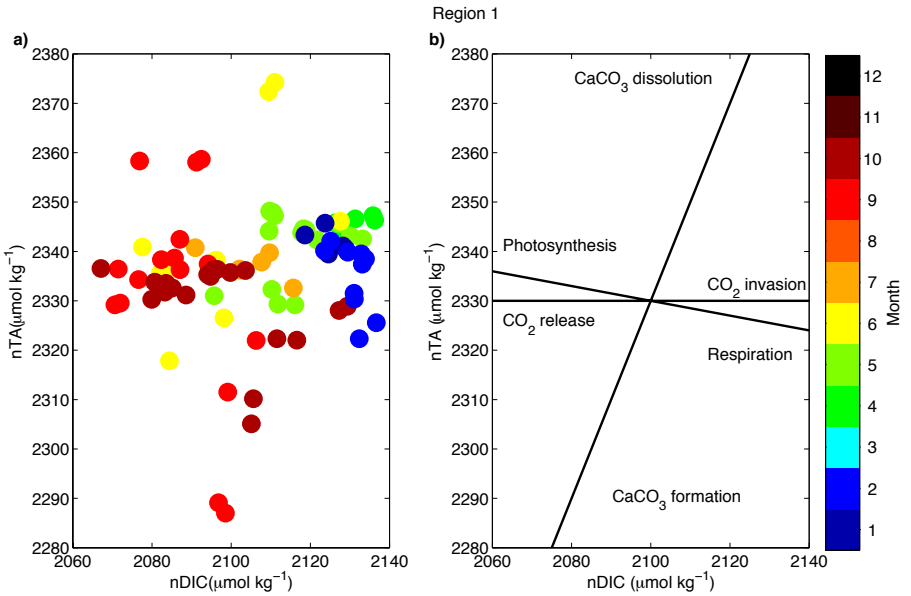

Figure 5.21: Region 1 **a)** nTA against nDIC plotted as coloured circles corresponding to the month of sampling, and **b)** processes that influence the nTA:nDIC ratio.

Data from region 2 (figure 5.22) also show lowest nTA and nDIC concentrations (2365 μmol kg^{-1} and 2030 μmol kg^{-1} respectively) during October. Highest concentrations (nTA = 2385 μmol kg^{-1} and DIC = 2110 μmol kg^{-1}) occur during June and February respectively.

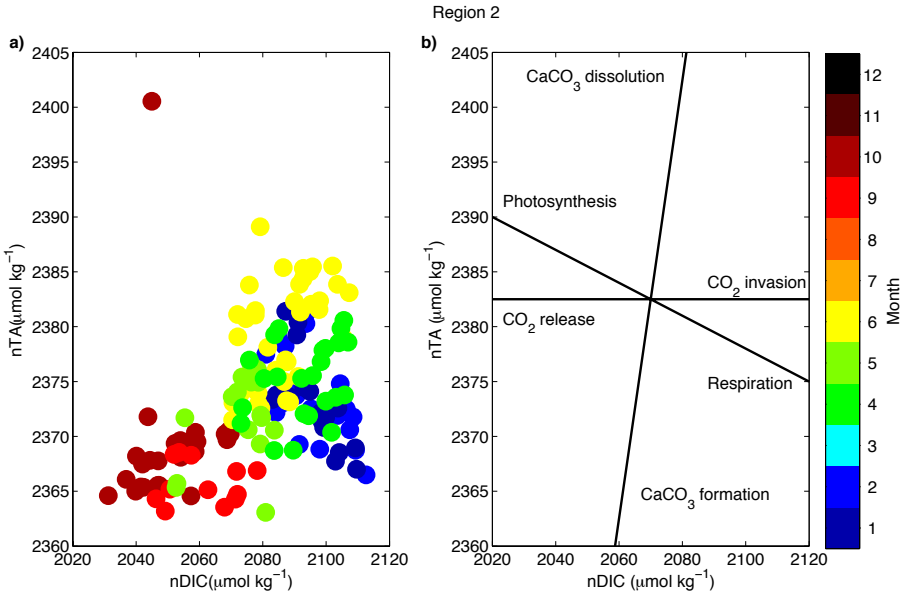

Figure 5.22: Region 2 **a)** nTA against nDIC plotted as coloured circles corresponding to the month of sampling, and **b)** processes that influence the nTA:nDIC ratio.

In region 3, the highest and lowest concentrations of nTA occur during June

and the highest and lowest concentrations of nDIC occur during January (figure 5.23).

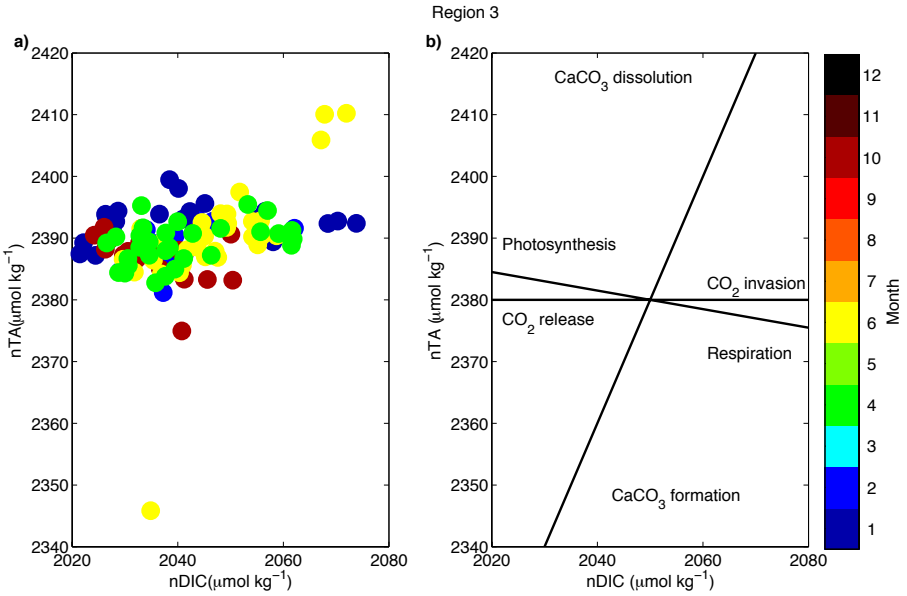

Figure 5.23: Region 3 **a)** nTA against nDIC plotted as coloured circles corresponding to the month of sampling, and **b)** processes that influence the nTA:nDIC ratio.

5.4.8 Redfield ratios

Figure 5.24 shows the nDIC against normalised NO_x (nNO_x) following Friis *et al.* (2003) for regions 1, 2 and 3. The C:N ratio of surface waters in region 1 was 6:1 $\pm$ 0.5 with lower nDIC occurring in the autumn months and higher nDIC and nNO_x occurring in February and April (Figure 5.24a). The C:N ratio of surface waters in Region 2 was 11:1 $\pm$ 1.5 with low values of nDIC and nNO_x occurring in the summer and autumn months, and the highest nNO_x occurring in the winter (Figure 5.24b). The C:N ratio of surface waters in region 3 was -21:1 $\pm$ 7.8. Note the different x and y scales between the subplots, and the different concentrations between regions, with region 3 presenting the lowest nutrient concentrations and region 1 presenting the highest nutrient concentrations.

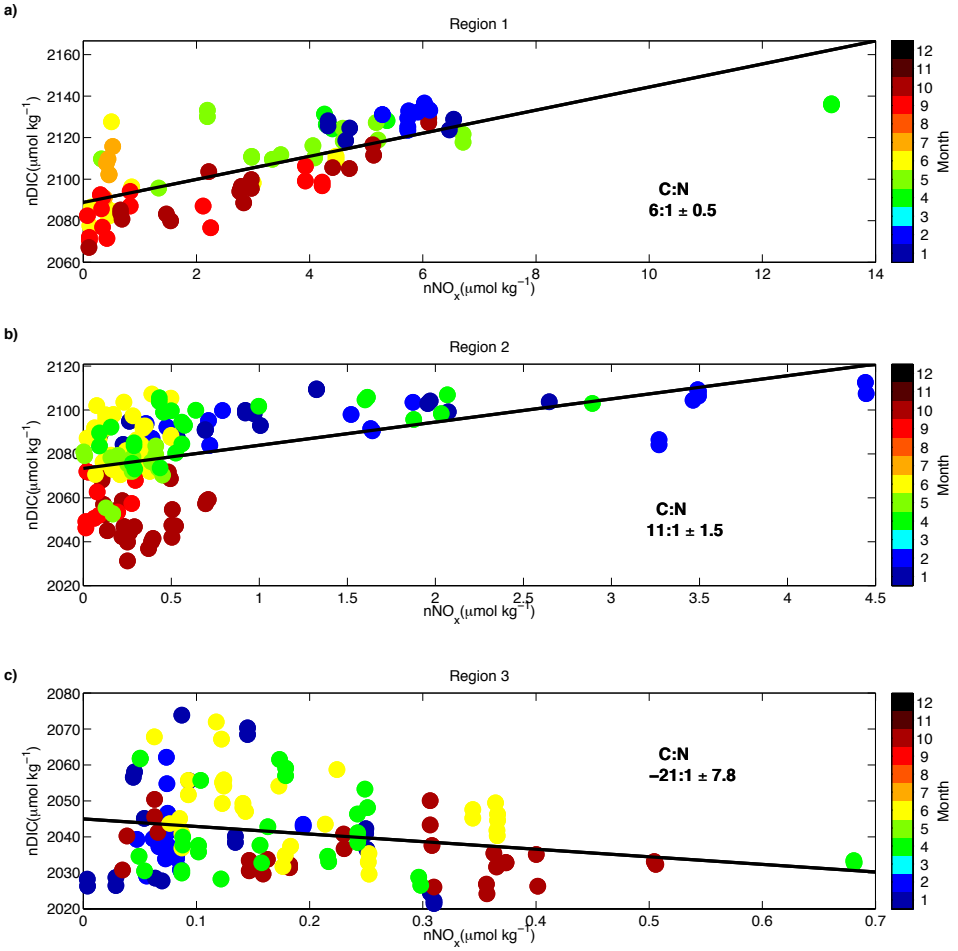

Figure 5.24: nDIC (μmol kg^{-1}) against nNO$_x$ (μmol kg^{-1}) with coloured circles corresponding to the month of sampling, and the black line showing the regression for regions **a)** 1, **b)** 2, and **c)** 3. Note the different x and y axes scales .

The ratio of C:P in regions 1, 2 and 3 was 75:1 $\pm$ 14, 71:1 $\pm$ 32, and -89:1 $\pm$ 55 respectively (figure 5.25). In region 2 during the autumn the concentrations of nDIC and nPO$_4$ were at their lowest (2030 μmol kg^{-1} and 0.02 μmol kg^{-1} respectively), with high concentrations of nPO$_4$ (0.3 μmol kg^{-1}) occurring in the winter (figure 5.25b). Region 3 had the largest error ($\pm$ 55) and the lowest concentrations of nPO$_4$ during the winter, however most of these values are below the limits of detection ($<$0.02 μmol kg^{-1}, see table 5.1).

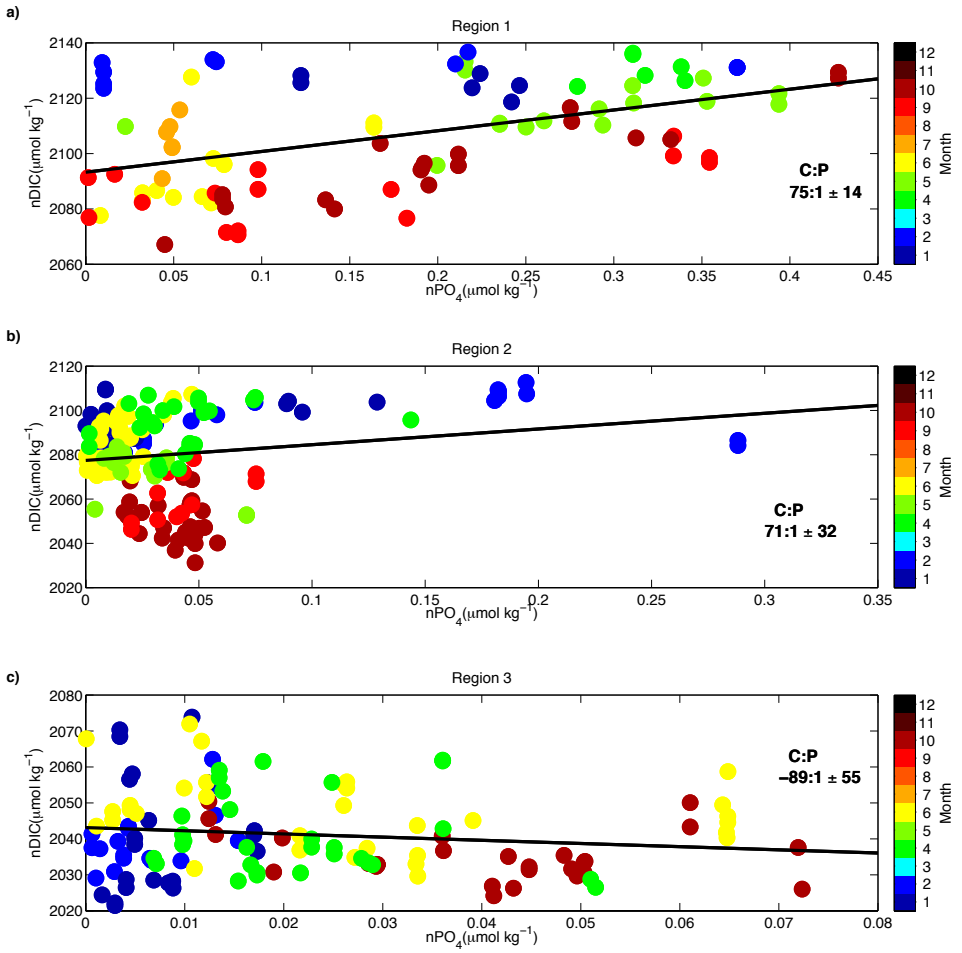

Figure 5.25: nDIC (μmol kg^{-1}) against nPO$_4$ (μmol kg^{-1}) with coloured circles corresponding to the month of sampling, and the black line showing the regression for regions **a)** 1, **b)** 2, and **c)** 3. Note different x and y axes scales between panels .

The ratio of N:P in regions 1, 2 and 3 were 13:1 $\pm$ 1.7, 15:1 $\pm$ 0.9, and 3:1 $\pm$ 0.5 respectively (figure 5.26). In region 1 the lowest concentrations of nPO$_4$ (<0.1 μmol kg^{-1})) and nNO$_x$ (<2 μmol kg^{-1})) occurred during the summer (figure 5.26a), surface waters in Region 2 generally had lower concentrations of nPO$_4$ than those in region 1 (0-0.2 μmol kg^{-1} versus 0-0.4 μmol kg^{-1}), while higher concentrations of nNO$_x$ occurred during winter (figure 5.26b). Region 3 had the lowest concentrations of both nPO$_4$ and nNO$_x$, and the lowest concentrations occurred during the winter.

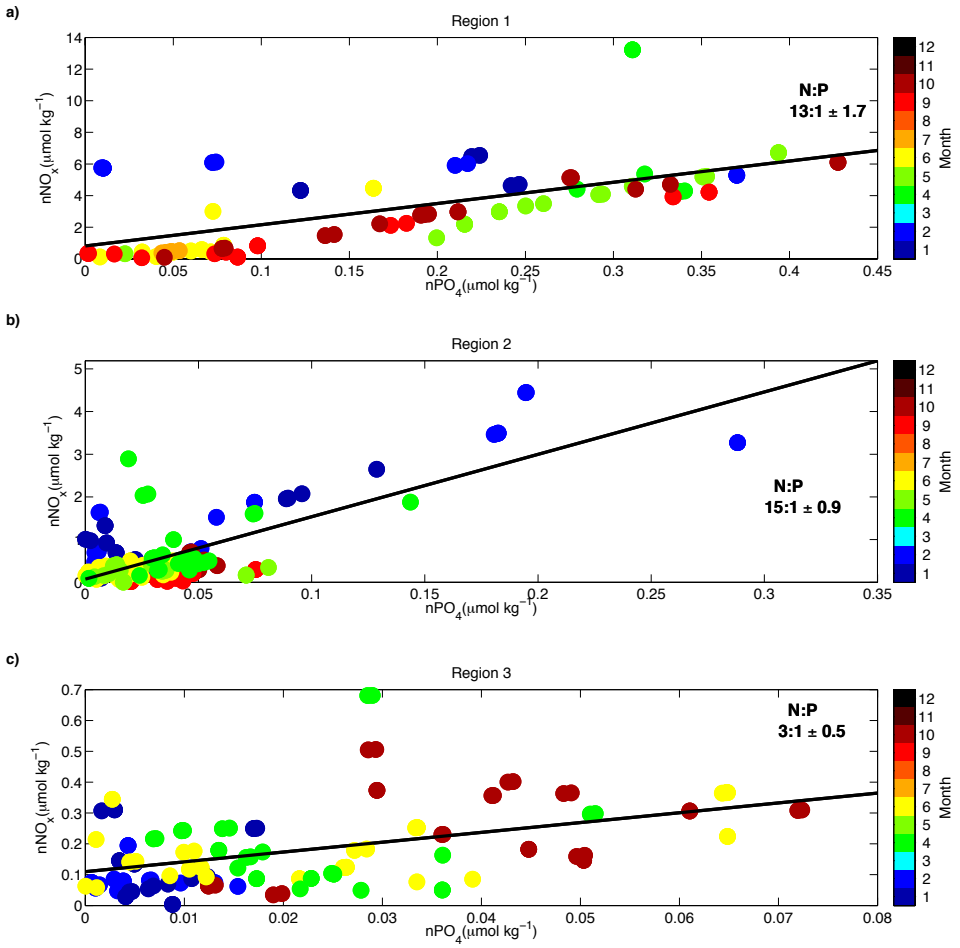

Figure 5.26: nNO_x (μmol kg^{-1}) against nPO_4 (μmol kg^{-1}) with coloured circles corresponding to the month of sampling, and the black line showing the regression for regions **a)** 1, **b)** 2, and **c)** 3. Note different x and y axes scales.

5.4.9 Phytoplankton community composition

Figure 5.27 shows the seasonal cycle of plankton abundance for each of the phytoplankton indices, from 40 °W to 0 °. Periods of increased PCI occur throughout the spring, summer and autumn months, with the highest concentrations occurring at 5°W and 10°W (figure 5.27a). Diatom abundance is highest during the spring, with some diatoms occurring in the summer and autumn months west of 10°W (figure 5.27b). Dinoflagellates show a clear seasonal cycle with the largest blooms occurring in the summer months at 10°W and 20°W (figure 5.27c). *Rhizosolenia* bloom later than most diatom species, and this can be seen by the peaks in abundance in summer (figure 5.27d) as opposed to spring (figure 5.27b) at 10°W and 5°W. Silicoflagellate abundance peaks in spring at 18°W and 24°W, with a secondary peak in the autumn months at 20 and 30°W (figure 5.27e). Coccolithophore abundance

reaches a maximum in summer at about 18°W, with further blooms in the autumn months between 10°W and 30°W (figure 5.27f).

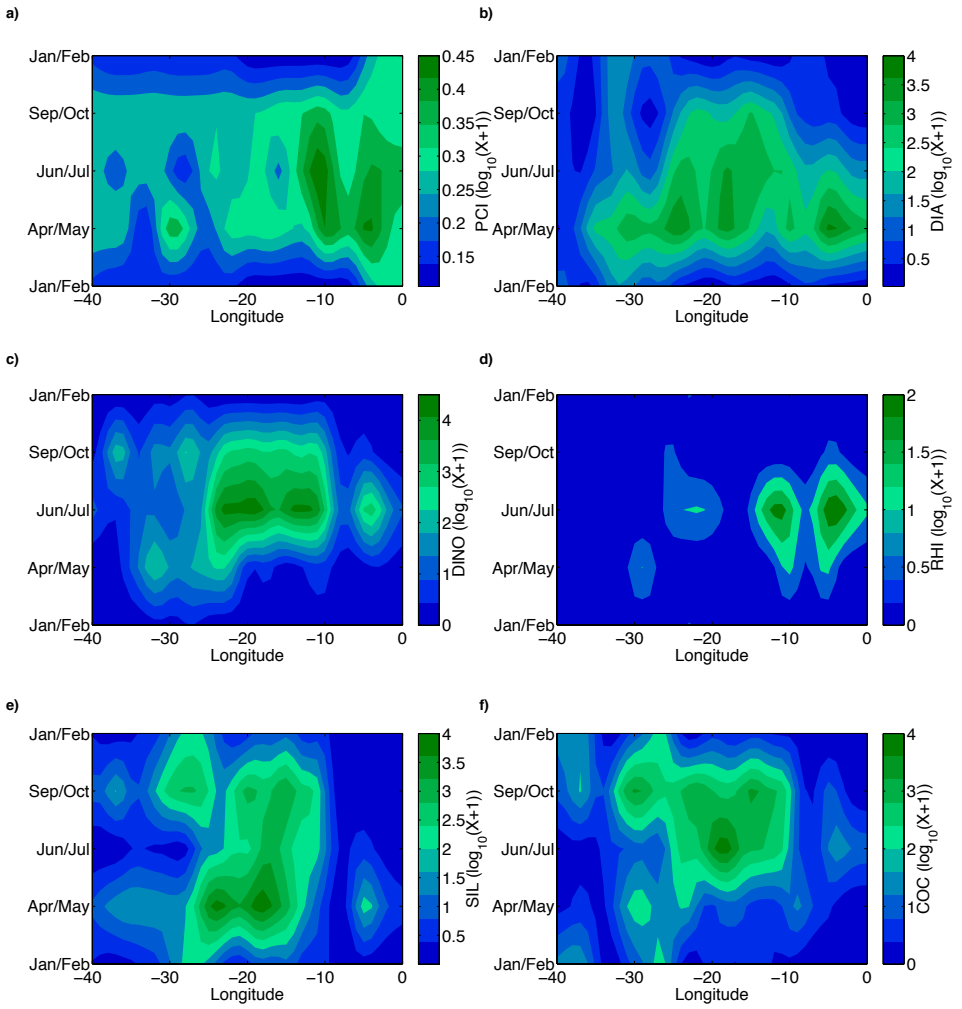

Figure 5.27: Hovmoller of **a)** PCI, **b)** diatom (DIA), **c)** dinoflagellate (DINO), **d)** *Rhizosolenia* (RHI), **e)** silicoflagellate (SIL), and **f)** coccolithophore (COC) abundance for each sampling period from 40°W to 0°W along the Caribbean to UK transect.

The monthly abundance of the CPR phytoplankton indices ($\log_{10}$(x+1)) and Chl-a estimates (mg m^{-3}) from satellite imagery in regions 1, 2 and 3 are shown in figure 5.28. Since the CPR is only towed from 40 °W back to the UK there were no CPR samples in region 3. The highest abundance of phytoplankton is in region 1, with diatoms blooming in April, and dinoflagellates blooming during the summer, peaking in August (figure 5.28a). Coccolithophores show a double peak in abundance in June/July and again with a higher peak in September. This corresponds with the $CaCO_3$ formation that was suggested in September in figure 5.21a. Region 2 has similar seasonal cycles of phytoplankton abundance to

region 1. However dinoflagellates show a double peak in abundance in June and August, and coccolithophores bloom slightly earlier in May/June and then again in September (figure 5.28b). Unfortunately there were no CPR samples collected within region 3, but the satellite concentrations of Chl-a were low (< 0.1 mg m^{-3}) with no seasonal cycle evident, suggesting that this region has low phytoplankton abundance (figure 5.28c).

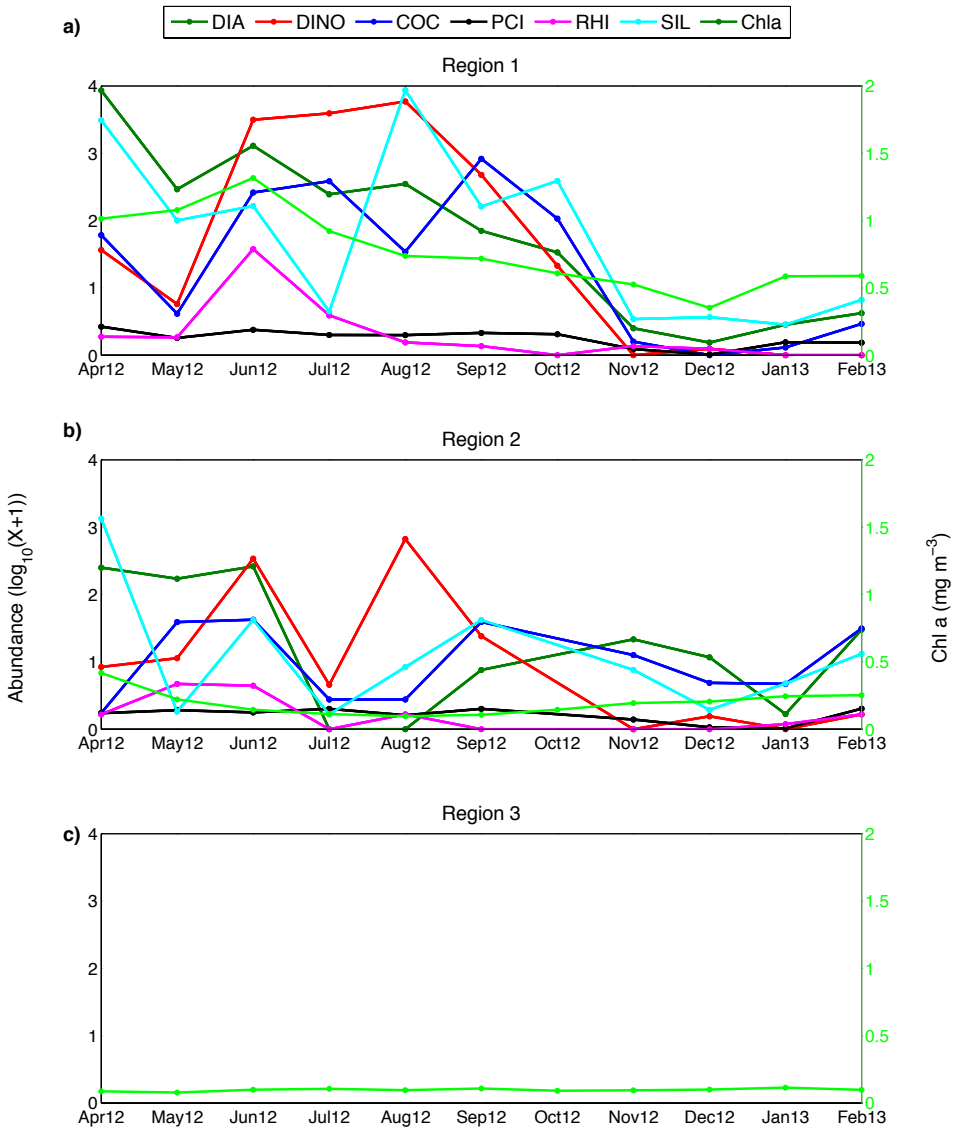

Figure 5.28: Left y-axis is monthly abundance of diatoms (DIA = dark green), dinoflagellates (DINO) = red), *Rhizosolenia* (RHI = purple), silicoflagellates (SIL = cyan), and coccolithophores (COC = dark blue) ($\log_{10}$(x+1)) and the right y-axis is Chl-a estimate (mg m^{-3} = light green) from April 2012 to February 2013 in regions **a)** 1, **b)** 2, and **c)** 3.

In region 1 nDIC was negatively correlated with all phytoplankton indices. However the only significant (p-value < 0.05) correlations were with dinoflagellate and coccolithophore abundance (see table 5.3).

Table 5.3: Correlation coefficients (r-value) and their significance (p-value) between each of the phytoplankton indices and the monthly nDIC within regions 1 (R1) and 2 (R2). Values that are significant had a p-value of < 0.05 and are marked with an asterisk (*).

	R1 r-value	R1 p-value	R2 r-value	R2 p-value
PCI	-0.38	0.35	-0.50	0.32
DIA	-0.14	0.74	0.01	0.99
DINO	*-0.72	*0.04	-0.43	0.40
RHI	-0.40	0.32	-0.05	0.93
SIL	-0.19	0.65	0.17	0.75
COC	*-0.79	*0.02	-0.58	0.23

5.5 Discussion

5.5.1 Abiotic influences on carbonate chemistry

DIC decreases with latitude in the North Atlantic (figure 5.6a). The high DIC concentrations in the northernmost latitudes are associated with the well mixed English Channel and coastal inputs of DIC (Kitidis *et al.*, 2012; Pingree and Griffiths, 1978). Towards the mid latitudes within the subtropical gyre DIC concentrations are associated with the relatively low mixing that occurs within this region and the residence time of carbon (Sarmiento and Gruber, 2006). Below 30°N DIC concentrations decrease with increasing SST, decreasing salinity and decreasing TA (figure 5.6). This decrease in TA and salinity is unlikely to be caused by precipitation as Williams and Follows (2011) calculated that this region has net annual evaporation, and the decreasing trend is seen throughout all seasons. The Amazon and Orinoco are the nearest rivers to the south of the Caribbean Islands, with the Amazon being the largest single riverine TA source to the Atlantic (Carter *et al.*, 2014) and having the world's largest volume of river water discharge (Dai and Trenberth, 2002). The influence of the discharge of the Orinoco and Amazon rivers can be seen as a low DIC and salinity signal which during peak North Equatorial Countercurrent (NECC) flow can reach from 50°W to 25°W (da Cunha and Buitenhuis, 2013; Cooley *et al.*, 2007). This river discharge is likely to be the cause of the change in the linear relationship with latitude seen in DIC, salinity and TA (figure 5.6) as at 30°N both TA and salinity reach their maximum values and then decrease rapidly going southward. This riverine influence on TA and DIC can be seen near the northeast of Brazil (figure 5.29) in mean gridded GLODAP v1.1 surface values

of DIC and TA (Key *et al.*, 2004).

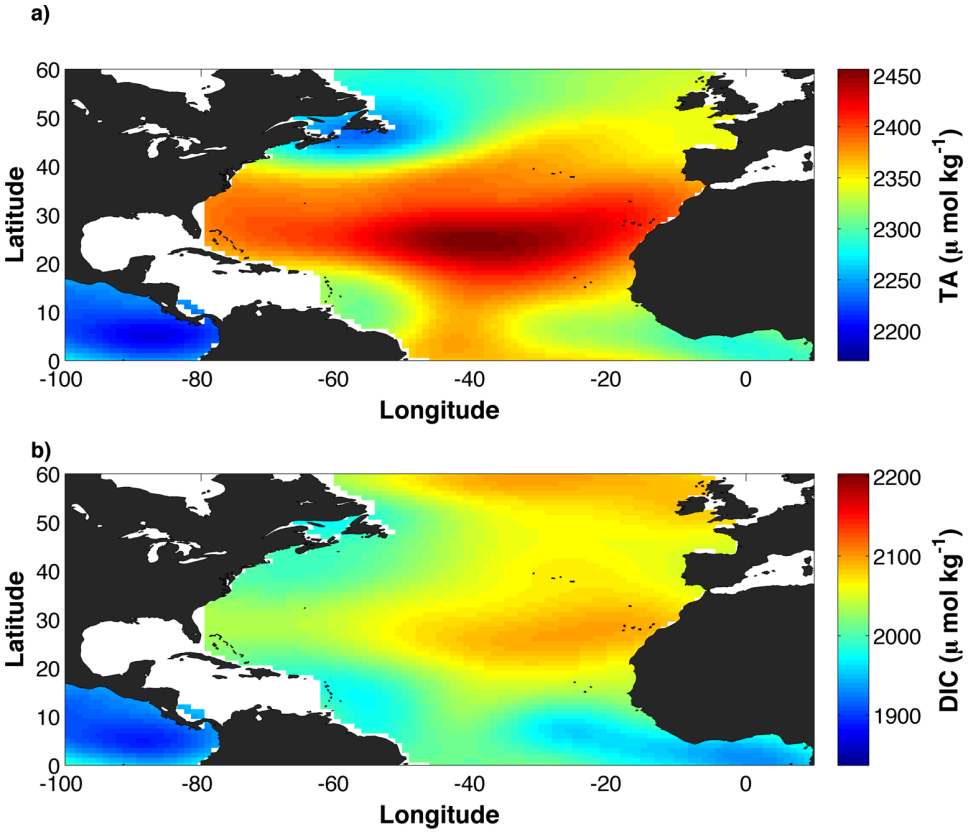

Figure 5.29: Mean gridded surface values of a) TA and b) DIC in the North Atlantic from GLODAP v1.1 (Key *et al.*, 2004).

The high values of pCO_2 in autumn and winter between 0°W and 10°W (figures 5.19a and 5.20a) correspond to high values of DIC and low values of TA and salinity (figure 5.7a,b and d), which indicates input of freshwater. These data were collected from the well mixed English Channel which receives waters from the Rivers Seine, Thames, Tamar, Loire and Gironde (Kitidis *et al.*, 2012) (see figure 5.30). Nutrient (PO_4 and NO_x) concentrations were also high (>0.3 μmol kg^{-1} and >5 μmol kg^{-1} respectively) during this period, which are typical of riverine input. Kitidis *et al.* (2012) suggest that the carbonate system in the English Channel may be influenced by riverine input as station L4 showed characteristics of riverine input in-comparison to station E1 (which is further from the coast than L4, see figure 5.30).

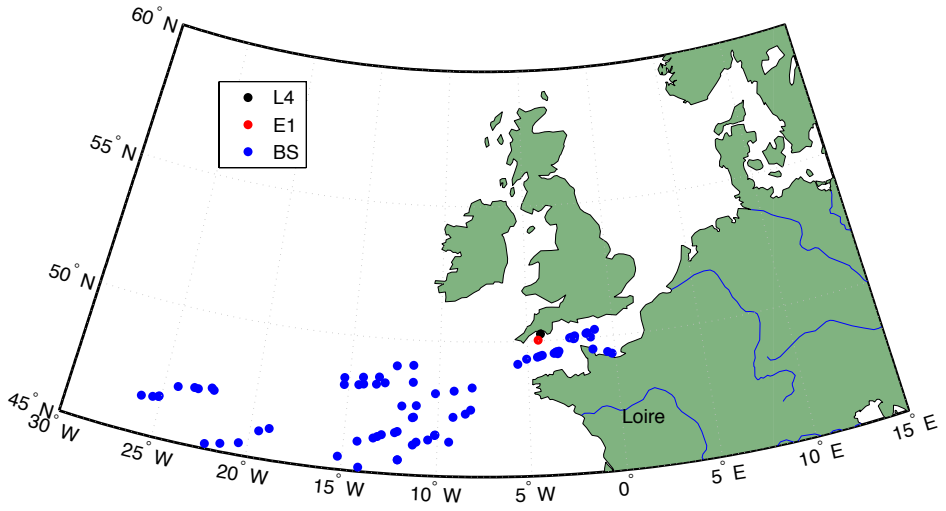

Figure 5.30: Map of station L4 (black circle) and E1 (red circle) and the location of samples from region 1 in this study (BS = blue circles), with major rivers plotted as blue lines, and the river Loire labelled.

The carbonate system has been regionally defined in Takahashi *et al.* (1993) which suggests Revelle factors of about 14 for polar waters (DIC:TA $\sim$ 0.94), 10 for the global ocean and 8 for tropical waters (DIC:TA $\sim$ 0.83) based on the ratio of DIC:TA. Figure 5.31 shows the DIC:TA ratio against latitude for each of the samples collected in each of the regions within this chapter.

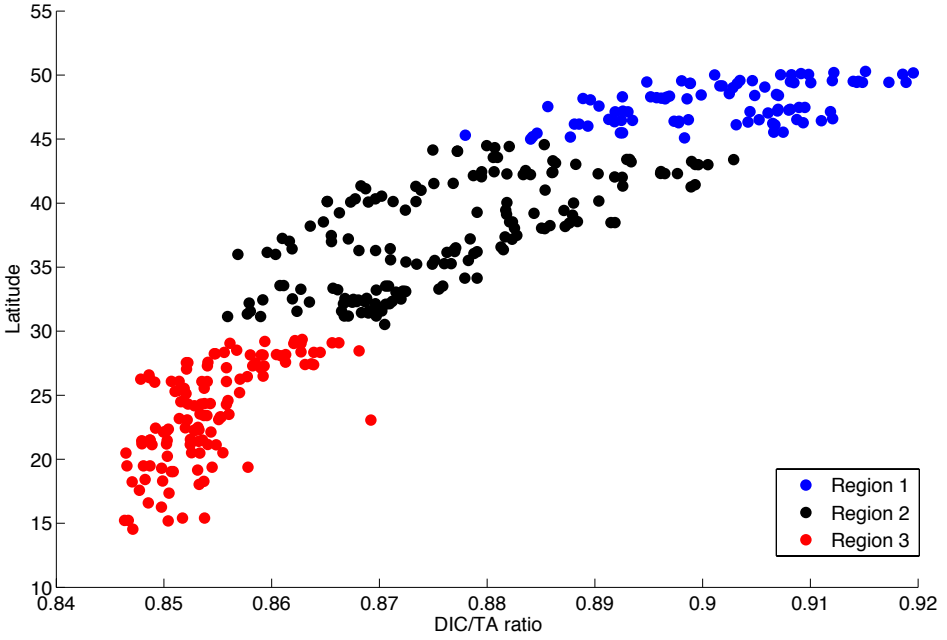

Figure 5.31: The ratio of DIC:TA against latitude plotted as coloured circles, region 1 = blue, region 2 = black, region 3 = red.

Sabine *et al.* (2004) suggest that as the oceans take up more CO_2 from the

atmosphere the decreasing pH and carbonate ion concentration will increase the Revelle factor, therefore decreasing the ocean's capacity to buffer increasing atmospheric CO_2.

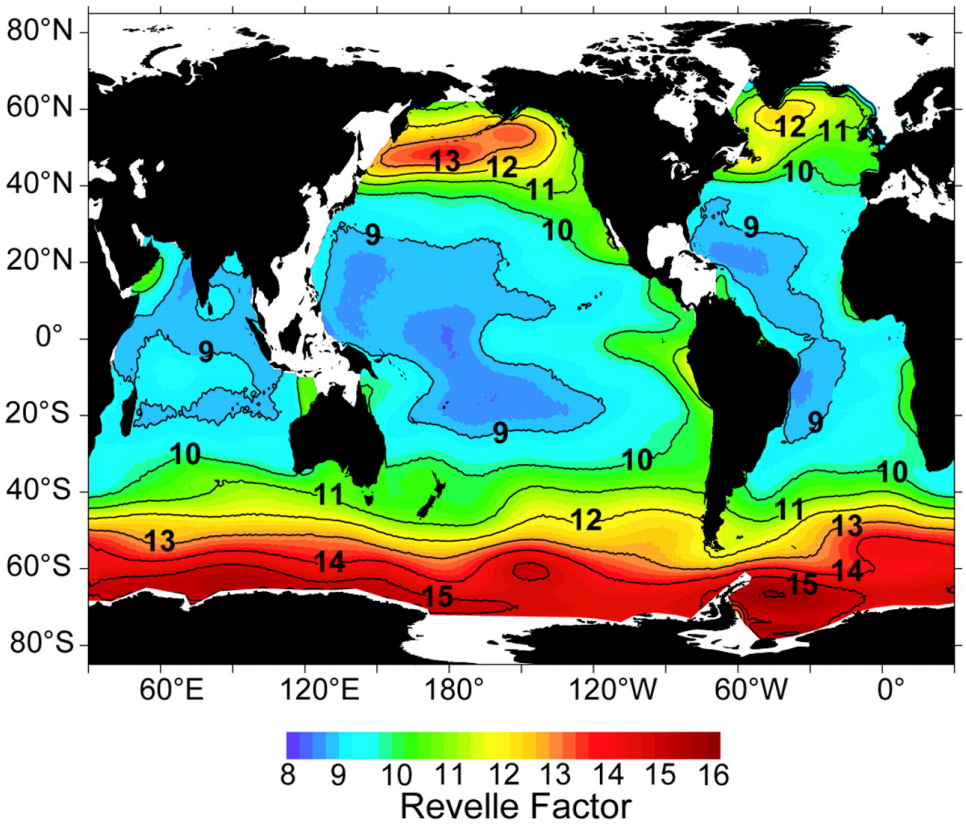

Figure 5.32: Global oceans map of the Revelle factor distribution for the year 1994. Reproduced from Sabine *et al.* (2004).

The ocean's distribution of Revelle factors for 1994 is shown in figure 5.32, from Sabine *et al.* (2004). Takahashi *et al.* (1993) report a Revelle factor of 10.97 for the north-eastern North Atlantic (44°to 49°N and 15 °to 25 °W) which is between region 1 and region 2. Regions 1 and 2 had a Revelle factor of 15±0.8 and 11±0.9 respectively (figure 5.16), both are higher than those presented in Takahashi *et al.* (1993) and Sabine *et al.* (2004) for the year 1993 and 1994, particularly in region 1. This suggests that the buffering capacity of regions 1 and 2 has decreased in the last 20 years, which is likely due to the increased uptake of CO_2 within these regions (Landschützer *et al.*, 2014), and therefore changes in speciation of the carbonate system (Riebesell *et al.*, 2009). The Revelle factor of region 3 was 7±0.8 which is similar to those suggested by Takahashi *et al.* (1993) and Sabine *et al.* (2004) for the tropics, of ∼8 (see figure 5.32). This demonstrates and

confirms previous findings on the differing regional influences due to both biological and temperature driven influences on the carbonate system, and the decreasing buffering capacity in large regions of the world's oceans.

Using the relationship between TA and salinity measured across the North Atlantic (figure 5.17), DIC can be calculated where salinity and pCO_2 have been measured. Calculated DIC compared well with measured DIC (figure 5.18). The regression obtained from our TA and salinity data was not dissimilar to other published studies within our study region (figure 5.33). Kitidis *et al.* (2012) defined the regression within the western English Channel as TA = 45.6 $\pm$ 3.3 $\times$ salinity + 733 $\pm$ 117, while Nondal *et al.* (2009) recorded the linear regression for Atlantic water as TA = 49.35 $\times$ salinity + 582. Regressions were also fitted for mean oceanic values of TA and salinity. These were obtained from Jiang *et al.* (2014) (salinity = 35, TA = 2300 μmol kg^{-1}, and salinity = 36.31 $\pm$0.35, TA = 2377 $\pm$ 22 μmol kg^{-1} for the mean open ocean and the Atlantic respectively, figure 5.33). This confirms that alkalinity is mostly conservative with salinity and this relationship can therefore be used to calculate DIC or pH in conjunction with measured pCO_2 along the sampling route used in this study.

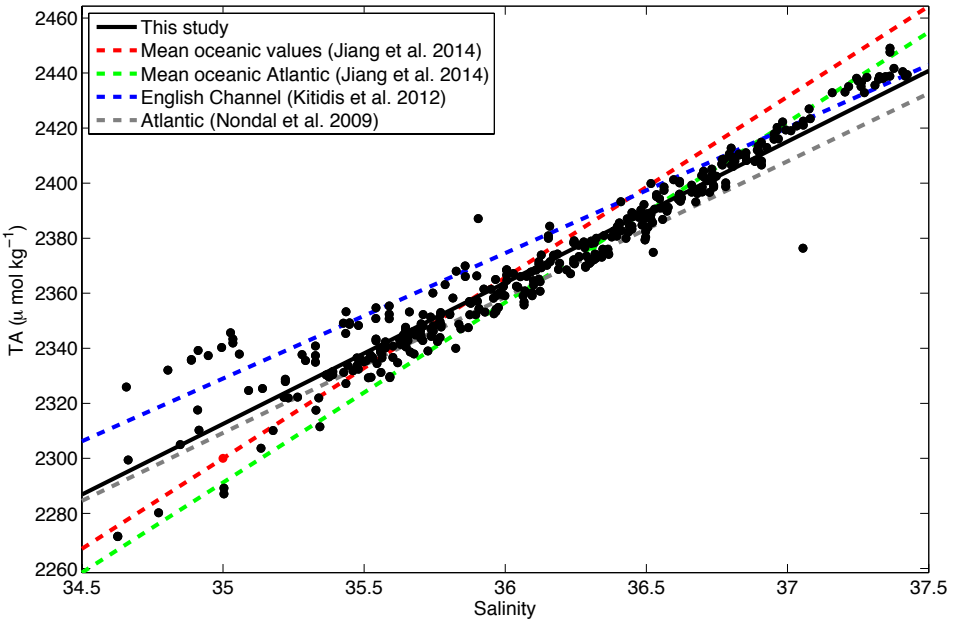

Figure 5.33: TA against salinity used to calculate the linear regression within this study (solid black line and circles). The dashed lines represent published TA:salinity relationships (Jiang *et al.*, 2014; Kitidis *et al.*, 2012; Nondal *et al.*, 2009).

Figure 5.34 demonstrates that DIC can be derived from this relationship, together with measured salinity and underway pCO_2 from the *MV Benguela Stream* between 2002 and 2013, within regions 1, 2, and 3. There is a clear seasonal cycle of DIC in region 1, which becomes less pronounced closer to the tropics (from region 1 to 3, figure 5.34). These data compare well with nutrient concentrations in regions 1 and 2 from 2002 to 2013 (see figure C.1 within appendix C for reference).

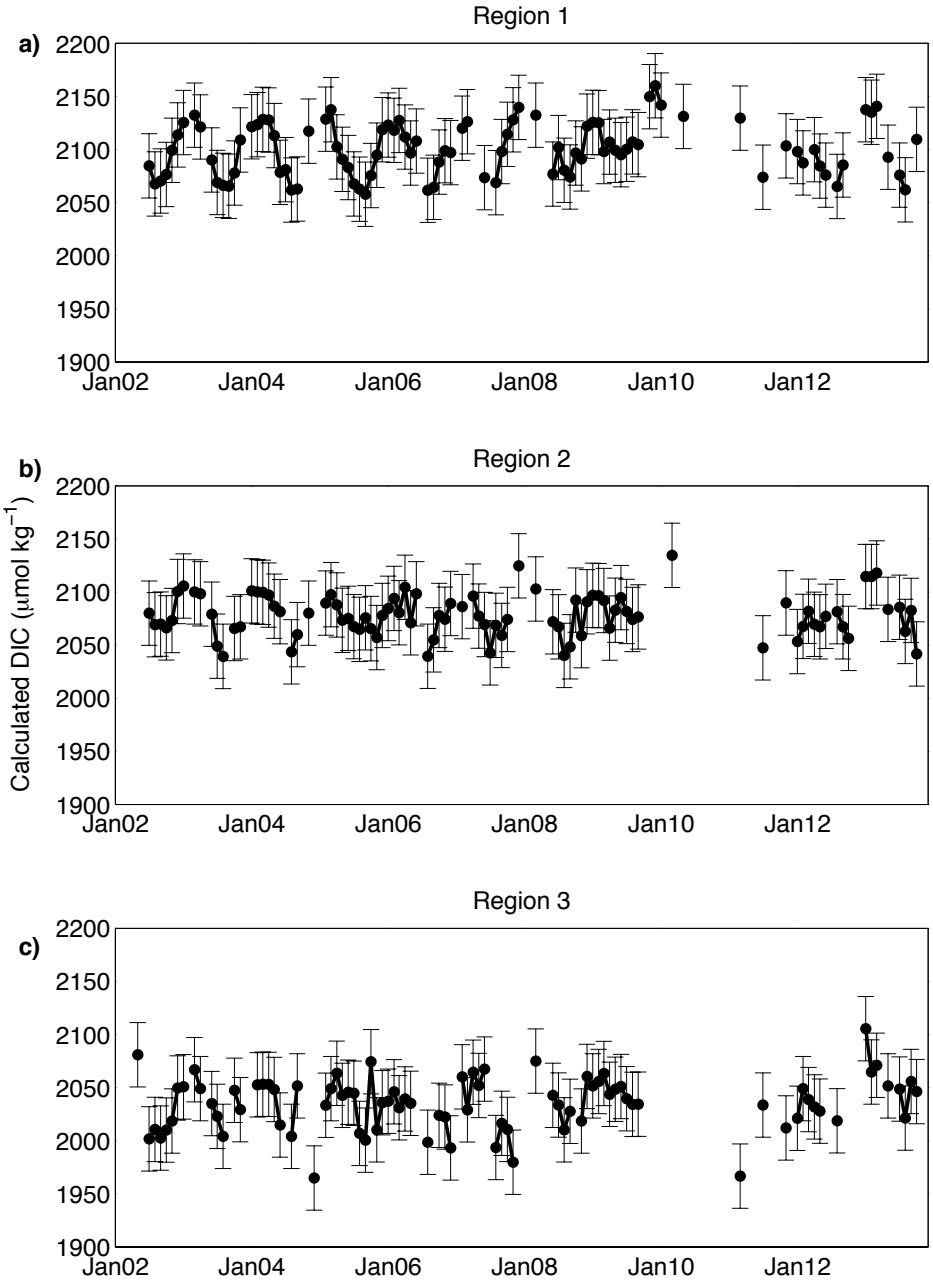

Figure 5.34: Calculated DIC with error bars of 30.3 μmol kg^{-1} (calculated from the RMSE of the DIC calculation, see section 5.4.6.), from 2002 to 2013 in regions **a)** 1, **b)** 2, and **c)** 3.

Calculated DIC was compared with pCO_2 measurements from the *MV Benguela Stream* and satellite estimates of PIC (Particulate Inorganic Carbon) (Gordon *et al.*, 2001; Balch, 2005) and POC (Particulate Organic Carbon) (Stramski *et al.*, 2007). Coccolithophore abundance from the CPR was also compared with satellite PIC to investigate relationships between satellite carbonate parameters and measurements. These results were regionally dependent, see appendix C figures C.2 to C.5 for results.

5.5.2 Biotic influences on carbonate chemistry

The low concentration of pCO_2 during the spring between 0°W and 5°W corresponds to a peak in diatom abundance (figures 5.20a and 5.27b), while the low pCO_2 at 10°W and 20 °W during the summer corresponds to the two summer peaks in dinoflagellate abundance (figure 5.7). The low concentrations of nutrients in the spring and summer also correspond to increased diatom abundance, particularly Si which is required by diatoms to produce silicate frustules (Martin-jézéquel *et al.*, 2000) (figure 5.7c e and f).

The significant trends between phytoplankton abundance and nDIC were only present in region 1 (figure 5.2), suggesting that the carbonate system is driven primarily by biology in this region, whereas the other regions are primarily driven by abiotic influences. This is consistent with the findings of Takahashi *et al.* (1993) who demonstrated that the carbon cycle is driven by biology during the productive months in the subpolar/temperate regions of the North Atlantic, and that within lower latitudes the carbon cycle is primarily driven by temperature. The high Si concentrations relative to NO_x in region 3 (figure 5.8c) suggest that diatoms are not able to compete at such low NO_x concentrations and are therefore not taking up the excess Si (Sarthou *et al.*, 2005).

Diatoms and dinoflagellates are the dominant phytoplankton groups in the northeast Atlantic, and are thought to be important in the export of carbon. Henson *et al.* (2012) demonstrated that at the Porcupine Abyssal Plain (PAP (49°N 16.5°W)) site, during a dinoflagellate bloom more particulate organic carbon (POC) was

recorded in a sediment trap at 3000 m than during a diatom bloom. This was in contrast to what is often expected of the transfer efficiency of different phytoplankton groups, which suggests that because diatoms are relatively large and have heavily silicated cells the transfer efficiency and therefore sequestration should be higher during a diatom bloom than a dinoflagellate bloom. However Rynearson *et al.* (2013) demonstrate that the dominant group at the surface can have little influence on the amount of carbon sequestered. Although all six of the phytoplankton indices were negatively correlated with nDIC concentration, only dinoflagellate and coccolithophore abundance were found to be significant ($p < 0.05$, see table 5.3). Figure 5.35 shows the monthly mean dinoflagellate and coccolithophore abundance in region 1. The seasonal cycle of nDIC appears to be related to the bloom timing of these groups, as dinoflagellates bloomed in the summer and early autumn, while coccolithophores peaked during September when nDIC concentrations were at their lowest. The lack of DIC measurements in March 2012 mean that there is no way of determining the correspondence of nDIC with peak diatom abundance, but it appears that the nDIC reached similar concentrations in February 2013 to that of April 2012 (5.28a and 5.8a). The correspondence of peak dinoflagellate abundance with low nDIC is in agreement with Henson *et al.* (2012) who suggested that at the PAP site, which is on the border of region 1 and 2 (figure 5.1), the POC export is greater during a dinoflagellate bloom than when diatoms are blooming. The correspondence between nDIC and the double peaks in coccolithophore abundance agrees well with studies that have demonstrated the decrease in DIC during coccolithophore blooms, particularly in the autumn (Sep/Oct) months where we see the 2:1 ratio of TA:DIC (figure 5.21) (Robertson *et al.*, 1994; Dumousseaud *et al.*, 2010).

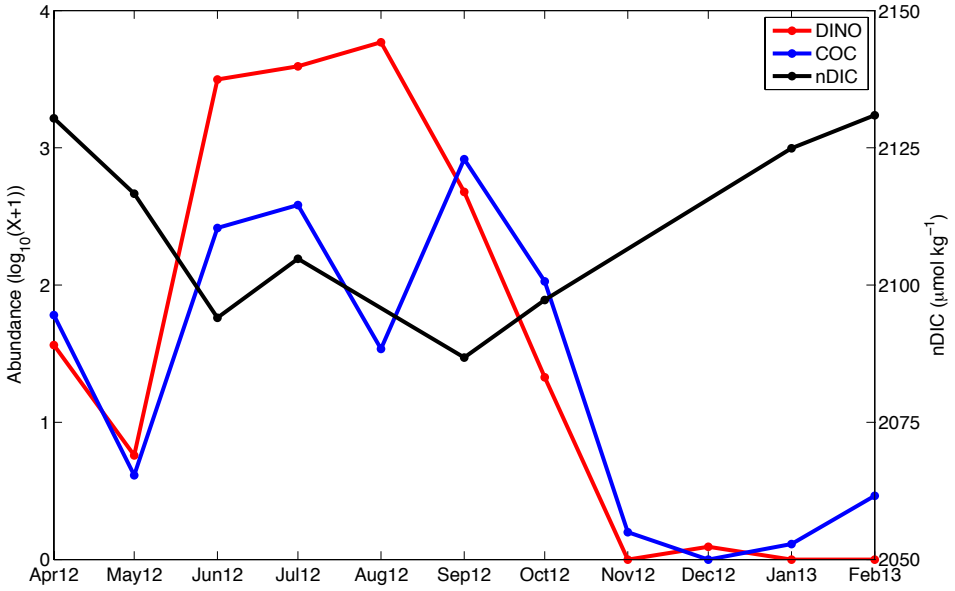

Figure 5.35: Monthly dinoflagellate (DINO = red), and coccolithophore (COC = blue) abundance ($\log_{10}$(x+1)) on the left y-axis, and monthly nDIC (black) on the right y-axis in μmol kg^{-1}, from April 2012 to February 2013 within region 1.

Comparing figures 5.7 and 5.27 a number of biological influences on the carbonate system can be inferred. The apparent breakdown in the relationship between TA and salinity occurs between 10°W and 35°W during the summer and autumn (figure 5.7b and d). The high salinity during the autumn is likely to be due to evaporation as this is the period when SST is at its highest. This signal would also be expected to be seen in increased TA. This decoupling of the relationship between TA and salinity during summer and autumn could also be due to calcification as this region and period corresponds to the highest abundance of coccolithophores (figure 5.27f and 5.35) which would cause a decrease in the TA without a concurrent change in salinity. Dumousseaud *et al.* (2010) reported a draw-down in TA in the northeast Atlantic during May and July of 2006 which corresponded to high abundances of *Emiliana huxleyi* which is the dominant coccolithophore in this region. Robertson *et al.* (1994) also report a decrease in the TA and DIC during a bloom of *Emiliana huxleyi* in the northeast Atlantic in June of 1991, which was estimated to have reduced the air-sea gradient of CO_2 by ~ 15 μatm and the TA:DIC ratio by about 2:1 due to changes in the carbonate system caused by calcification.

Figure 5.21 suggests that $CaCO_3$ formation occurred during Autumn in region 1 along with CO_2 release and photosynthesis, while CO_2 invasion occurred

in spring and winter. The carbonate data from Region 2 (figure 5.22) are harder to interpret, but there is an indication of $CaCO_3$ formation occurring in the autumn months as both nTA and nDIC have decreased along the 2:1 ratio line, and this is the region and period during which the TA:salinity relationship breaks down and coccolithophore abundance peaks (figures 5.7b and d, and 5.27f) . In region 3 the spring, summer, autumn and winter data all fall along the CO_2 release and invasion line, with possible $CaCO_3$ dissolution and formation occurring during parts of the June voyage (figure 5.23).

The range of Redfield ratios in regions 1, 2 and 3 demonstrates the regional variability (figures 5.24, 5.25 and 5.26). Region 1 had a C:N ratio of 6:1 $\pm$ 0.5 which was the closest to Redfield's ratio of 6.6:1 (Redfield *et al.*, 1963). Studies in the English Channel have found that the ratio of C:N was often higher than Redfield's, at around $\sim$ 8:1 (Kitidis *et al.*, 2012; Dumousseaud *et al.*, 2010). Although region 1 in this study includes the English Channel it also extends out into the northeast Atlantic over the shelf break where Dumousseaud *et al.* (2010) recorded a C:N ratio of 5.7:1 in 2006/2007. Region 2 had a high ratio of 11:1 $\pm$ 1.5 which agrees with Körtzinger *et al.* (2008) who recorded an average ratio of 11 at the PAP site. A high C:N ratio is indicative of carbon overconsumption, which is often observed towards the end of the productive season (Toggweiler, 1993; Kähler and Koeve, 2001). This can be seen during the autumn months in figure 5.24b as the nNO_x concentrations remain very low along with low concentrations of nDIC. Carbon overconsumption is when more carbon is fixed per unit of nutrient taken up, which often occurs during times of nutrient limitation (Toggweiler, 1993). The N:P ratios are closer to Redfields ratio of 16:1, with nutrient concentrations in region 1 having a ratio of 13:1 $\pm$ 1.7 and region 2 a ratio of 15:1 $\pm$ 0.9 (figure 5.26). The ratio of N:P in region 3 is much lower, at 3:1 $\pm$ 0.5. However it does not give a negative relationship unlike the other two ratios for region 3, but appears to be too low to be the result of species-specific N:P ratios which can give N:P ratios of between 7.1 to 43.3 (Quigg *et al.*, 2003; Klausmeier *et al.*, 2004), and is therefore likely due to the low concentrations in this region being below the limits of detection.

The ratios of C:N:P are much lower than the expected 106:16:1 Redfield ratio (figure 5.25) with region 1 having a C:N:P ratio of 75±14:13±1.7:1 and region 2 a ratio of 71±32:15±0.9:1. Martiny *et al.* (2013) examined the latitudinal variation in stoichiometric ratios and found that cold nutrient-rich high latitude regions had ratios close to 78:13:1, which is closest to our ratio measurements in regions 1 and 2. The latitudinal gradient of high ratios (195:28:1) in nutrient deplete warm low latitude regions, and low ratios in high latitude regions reported in Martiny *et al.* (2013), was suggested to be driven by varying plankton assemblages, with high abundances of diatoms with the low C:P and N:P ratios being associated with cold nutrient rich regions. Although the measurements used within Martiny *et al.* (2013) do not fall within regions 1 and 2 of this study, the high latitudinal trends described agreed with our measurements of ratios and plankton abundance, as diatoms had the greatest mean abundance throughout the sampling period in both regions.

5.6 Summary

This study demonstrates the seasonal and spatial variability in the carbonate system in the North Atlantic using a dataset collected from a VOS, which has been shown to be internally consistent, and coherent with previous data. Three regions are identified latitudinally, with the carbonate system being biologically driven in the higher latitudes and transitioning into the thermodynamically driven regions in the subtropics. This agrees with previous findings. The carbonate chemistry in the southernmost region, between 30°N and 14°N, is influenced by riverine input throughout the year, which decreases the TA, DIC and salinity. The northernmost region between 45°N and 50°N, which incorporates the English Channel and the shelf break is driven by the seasonal cycle of phytoplankton and the winter-mixing of carbon and nutrient rich waters and riverine inputs. Coccolithophore and dinoflagellate abundance were negatively correlated with DIC in this region, with peak coccolithophore abundance in September coinciding with the lowest concentration of DIC. The ratio of C:N:P was lower than the expected Redfield ratio, which the literature has suggested may be associated with higher latitudes and high abundances of diatoms. This agreed with our measurements of phytoplankton

indices, as diatoms had the greatest abundance. A decrease in the buffering capacity in the northeast Atlantic has been shown, which is likely due to the increased uptake of anthropogenic CO_2 within this region. This has global socio-economic implications as this negative feedback reduces the ability of this important sink region to take up anthropogenic CO_2, alongside a continued increase in anthropogenic emissions.

Chapter 6

Spatial and temporal variability in the influence of phytoplankton community structure on CO_2 flux in the North Atlantic

6.1 Abstract

This study combines two unique datasets that have been collected on-board a volunteer observing ship (VOS) across the North Atlantic to analyse the variability of the CO_2 sink in the North Atlantic at a range of different spatial and temporal scales. Phytoplankton indices collected from the continuous plankton recorder

(CPR) and the concentration of CO_2 within the surface waters are analysed to reveal that at seasonal time-scales phytoplankton play an important role in maintaining the air-sea flux of CO_2 within the northeast North Atlantic. Further southwestward towards the subtropical gyre sea surface temperatures are the main control on the seasonal flux of CO_2. At inter-annual time scales the North Atlantic Oscillation (NAO) drives the wind patterns and sea surface temperatures, which is the dominant driver of annual air-sea flux of CO_2. The abundance of several phytoplankton taxonomic groups, including coccolithophores, has increased in the North Atlantic between 1998 and 2011. Coccolithophores are calcifying phytoplankton that may be contributing to the increased concentration of pCO_2 within the surface waters, as CO_2 is a by-product of calcification. These complex interactions between the chemistry and plankton biology of the North Atlantic need to be considered for biogeochemical models of CO_2 variability, particularly as this important sink region has been shown to be highly variable.

6.2 Introduction

Understanding the changes in the carbonate cycle and the varying influences involved has become increasingly important with rising emissions and evidence of anthropogenic impacts on our environment (IPCC, 2013; Myhre *et al.*, 2013). With continued warming predicted from climate change, the solubility of DIC will decrease, therefore reducing the carbon flux from the atmosphere into the ocean. Model studies suggest that this has a particularly strong influence in the North Atlantic (Le Quéré *et al.*, 2010). The temperate and subtropical North Atlantic (14° N and 50° N) is an important sink region for carbon dioxide (CO_2), and is estimated to have a net air-sea flux of CO_2 of -0.22 Pg C y^{-1} (negative value representing marine uptake from the atmosphere), representing 13% of the global contemporary carbon sink and storing $\sim$ 23% of the global anthropogenic carbon inventory (Gruber *et al.*, 2009; Takahashi, 2009; Schuster *et al.*, 2009b, 2013). Although atmospheric concentrations of CO_2 remain fairly homogenous, regional variations in surface water CO_2 concentration are due to complex interactions between physical, chemical, and biological processes which drive the air-sea flux (Sarmiento and

Gruber, 2006). Watson *et al.* (2009) demonstrated significant inter-annual variability in the air-sea carbon flux in the northeast Atlantic between 2002 and 2007, which has been attributed to decadal scale climate variability (McKinley *et al.*, 2011; Schuster *et al.*, 2013).

Phytoplankton play an important role in the uptake of CO_2 due to photosynthesis, particularly in the North Atlantic where the spring bloom is a prominent feature (Takahashi *et al.*, 1993; Follows and Dutkiewicz, 2001; Shutler *et al.*, 2013). Carbon export is thought to be related to the size structure of the phytoplankton community with smaller phytoplankton such as some dinoflagellates and coccolithophorids expected to be responsible for less carbon export than larger cells such as diatoms (Bopp *et al.*, 2005; Ducklow and Doney, 2013). Continued global warming is predicted to increase stratification and therefore reduce the upward flux of nutrients, allowing smaller-sized phytoplankton to out-compete more nutrient dependant species such as diatoms. Bopp *et al.* (2005) used a global biogeochemical model to predict that this could reduce diatom abundance within the North Atlantic by up to 60%. Beaugrand *et al.* (2010) suggest that increasing numbers of smaller phytoplankton and zooplankton with increased stratification due to warming waters could have negative implications for fisheries, as food webs become more complex, as well as reducing the carbon export. By contrast, Henson *et al.* (2012) reported that during dinoflagellate blooms the total carbon flux was higher within a sediment trap at 3000 m at the PAP (Porcupine Abyssal Plain, 49°N 16.3°W) site than when diatoms were out-competing their smaller counter-parts. Palevsky *et al.* (2013) also found that during high levels of autotrophic production in the North Pacific, it was the smaller phytoplankton that were dominating the community structure. Some studies indicate a negative feedback between CO_2 flux and the activities of calcifying phytoplankton (Robertson *et al.*, 1993; Shutler *et al.*, 2013). This is because groups such as coccolithophores, of which *Emiliania huxleyi* are very common in the North Atlantic and form a large component of the phytoplankton blooms (Shutler *et al.*, 2013), produce CO_2 during calcification (equation 6.1) which can reduce the gradient of CO_2 between the atmosphere and surface waters, therefore reducing the flux.

$$Ca^{2+} + 2HCO_3^- \leftrightarrow CaCO_3 + H_2O + CO_2 \quad (6.1)$$

Other key variables that influence the CO_2 concentration within surface waters and the air-sea flux, include sea-surface temperature (SST) which influences the solubility of DIC, and mixing events which can bring nutrient and CO_2 rich waters from below the thermocline into surface waters. The seasonal cycle of sea surface pCO_2 is dependent on location within the North Atlantic as the subtropical regions tend to be driven more by SST, whereas in the subpolar and temperate regions there are higher nutrient concentrations and productivity which are thought to drive the spring/summer decrease in pCO_2 (Takahashi *et al.*, 1993; Takahashi and Sutherland, 2002; Körtzinger *et al.*, 2008).

Climate variables such as wind speed and SST which influence circulation and have a large impact on CO_2 flux (Le Quéré *et al.*, 2010) are often influenced in turn by different climate modes depending on their location. In the North Atlantic the North Atlantic Oscillation (NAO) is the predominant mode of variability, which is defined as the sea-level pressure difference between the Azores and Iceland (Hurrell, 1995). Significant correlations have been found between SST and the NAO in the North Atlantic and how this in turn impacts phytoplankton community structure (Harris *et al.*, 2013) and pCO_2 (Gruber *et al.*, 2002; Schuster *et al.*, 2009b, 2013). It is important to note that regionally these correlations have differing strengths due to the localisation of such modes, often with basin wide comparisons showing weak correlations (Henson *et al.*, 2012; Harris *et al.*, 2013).

The inter-play between these influences on the carbon cycle are difficult to quantify and likely to play an important role in the seasonal and inter-annual variability seen in the North Atlantic CO_2 flux. In order to understand and predict such processes, long term measurements are necessary on a global scale. One of the more cost-effective and productive ways to collect such data has been through the use of maintained measurements on board volunteer observing ships (VOS). Using data collected from a VOS route and modelled output data from Landschützer *et al.* (2014) this chapter aims to inter-relate CO_2 measurements, phytoplankton abundance indices and a range of climate variables to try to evaluate the drivers

of seasonal, inter-annual and decadal variability of CO_2 flux at a range of spatial scales within the North Atlantic.

6.3 Methods and results

6.3.1 Data

The underway measurements include barometric air pressure, salinity, sea surface temperature (SST), partial pressure of CO_2 in the surface waters (pCO_2), and nutrient concentrations that have been collected along the UK-Caribbean shipping route since 2002. For detailed methods see chapter 2 section 2.5 and chapter 5 section 5.3. The biological data is obtained from the Continuous Plankton Recorder (CPR) (for a detailed methodology see chapter 2 section 2.1), and satellite data were used as an indicator of Chl-a concentration (O'Reilly *et al.*, 1998; Werdell and Bailey, 2005), PIC (Particulate Inorganic Carbon) (Gordon *et al.*, 2001; Balch, 2005), and POC (Particulate Organic Carbon) (Stramski *et al.*, 2007). These data were obtained at a resolution of 9 km and frequency of 1 month from Aqua-MODIS (http://oceandata.sci.gsfc.nasa.gov). Mean monthly SST and wind speed data were obtained from the International Comprehensive Ocean-Atmosphere Data Set for the whole North Atlantic region (ICOADS, 1°enhanced data) (Woodruff, 1987). Monthly, annual and winter (DJFM) NAO indices were obtained from the Climate Data Guide: Hurrell North Atlantic Oscillation (NAO) Index (station-based) (Hurrell, 1995).

6.3.2 Calculation of air-sea CO_2 flux

Regional monthly-mean atmospheric xCO_2 data were obtained from the GLOBALVIEW marine boundary layer product (Dlugokency *et al.*, 2014). This was converted to atmospheric pCO_2 following (Dickson *et al.*, 2007):

$$pCO_{2,atm} = xCO_{2,atm} \times (P - P_{H_2O}) \tag{6.2}$$

Where P is the sea-level pressure, and P_{H_2O} is the water-vapour pressure.

The solubility of CO_2 (K_0, mol m^{-3} atm^{-1}) was calculated following Weiss

(1974) and Dickson *et al.* (2007), where S is salinity and SST is sea surface temperature:

$$\begin{aligned} K_0 &= (exp(90.5069 \times (100/SST) - 58.0931 \\ &\quad +22.2940 \times log(SST/100) + S \times (0.027766 - 0.025888 \times (SST/100) \\ &\quad +0.0050578 \times (SST/100)^2))) \times 1000 \end{aligned} \tag{6.3}$$

The Schmidt number (Sc) was calculated using Wanninkhof (1992) from measurements made by Jähne *et al.* (1987):

$$Sc = 2073.1 - (125.62 \times SST) + (3.6276 \times SST^2) - (0.043219 \times SST^3) \tag{6.4}$$

The gas transfer velocity (k_w, m yr^{-1}) was calculated using Wanninkhof (1992) and Sweeney *et al.* (2007):

$$k_w = (0.27 \times ((Sc/660)^{-0.5}) \times (u^2)) \times 87.6581277 \tag{6.5}$$

Where u is wind speed. Finally the air-sea flux of carbon dioxide (FCO_2, mol C m^{-2} yr^{-1}) was calculated using these formulations and the difference in the partial pressure of CO_2 between the atmosphere and the surface waters:

$$FCO_2 = -k_w \times K_0 \times ((pCO_{2,atm} - pCO_{2,sea})/1000000) \tag{6.6}$$

Where a negative FCO_2 value represents a sink of CO_2 from the atmosphere into the ocean, and a positive value represents a source from the ocean into the atmosphere.

6.3.3 Latitudinal bands

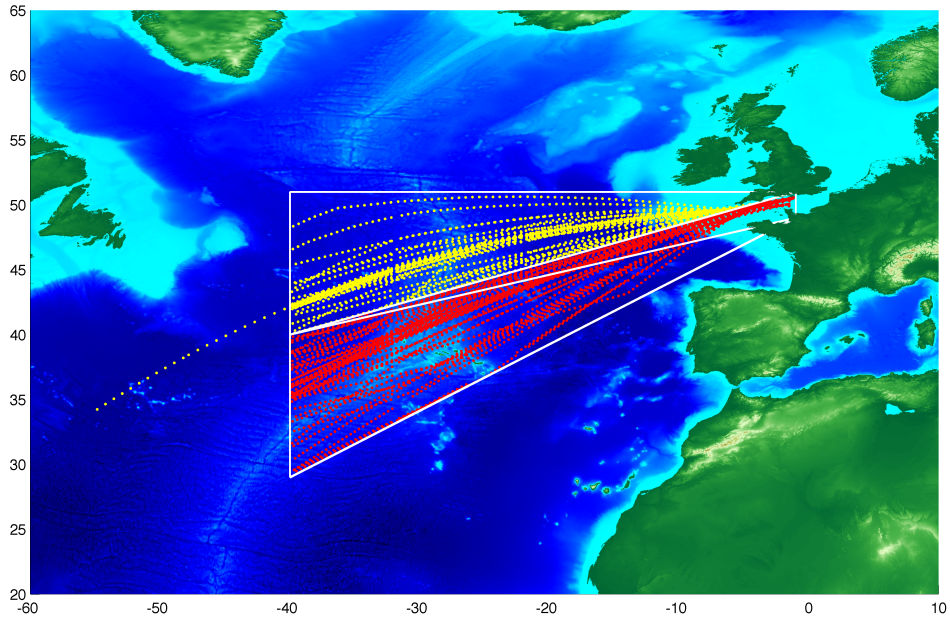

Figure 6.1: Map of the North Atlantic showing the location of each CPR sample. Two regions are shown outlined in white. Yellow samples = north Band. Red samples = south Band.

To avoid averaging across different water masses our first attempt to divide the data regionally was to split the dataset into two bands (north 40°- 50°N and south 30°- 40°N) and then average each month of data from 2002 to 2013 at each 1°longitude within each band (Schuster and Watson, 2007). Phytoplankton colour index (PCI) was used to represent total phytoplankton abundance as it has been shown to match chl-a estimates from satellite data relatively well (Raitsos *et al.*, 2014).

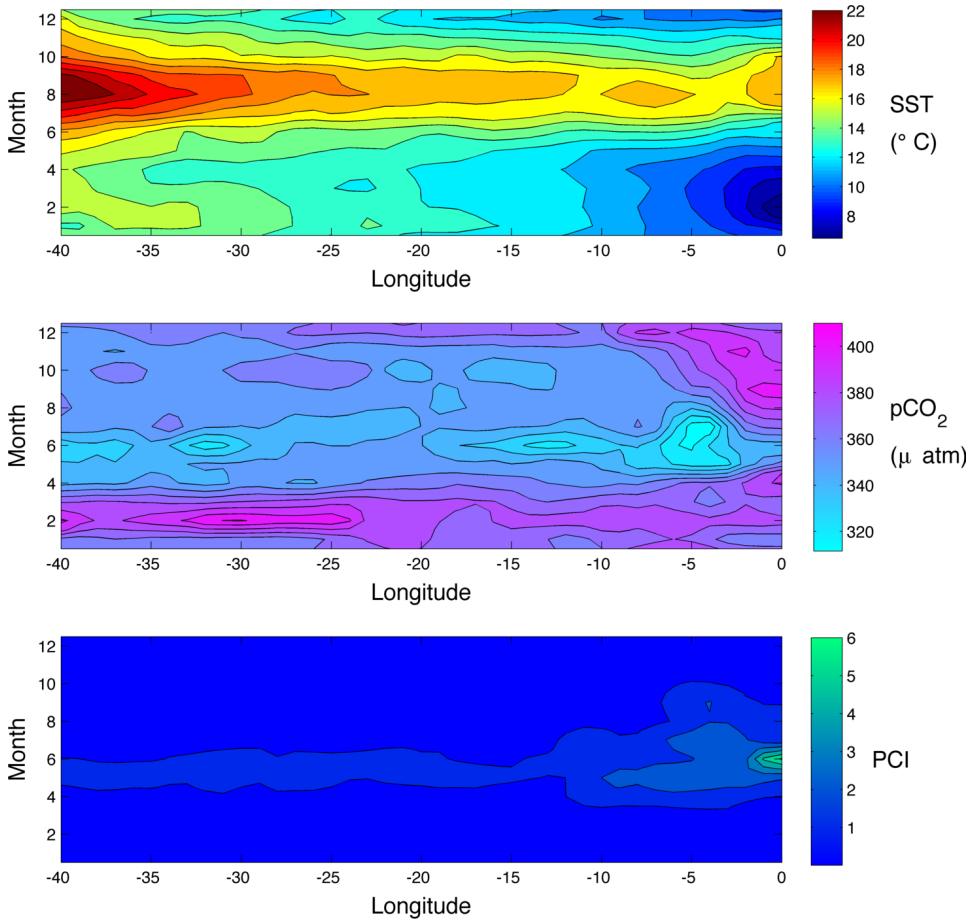

Figure 6.2: Monthly hovmoller plot against longitude for **a)** SST **b)** sea surface pCO_2 and **c)** PCI from 2002-2013 in the north band region of the North Atlantic (see figure 6.1).

In the north band of the sample area SST increases from east to west during June to October, but these higher SST waters do not contain higher concentrations of pCO_2. When temperature is the dominant influence on pCO_2, the pCO_2 in the surface waters remains high as it does not dissociate to form DIC as readily because the increased temperature decreases the solubility of DIC (Sarmiento and Gruber, 2006). The lack of correspondence between high SST and high pCO_2 suggest that SST is not the dominant driver of pCO_2 in this region. Phytoplankton (here represented by PCI) appear to drive the pCO_2 seasonal cycle between April and July, as the lowest pCO_2 concentrations coincide with the highest PCI across all longitudes (figure 6.2).

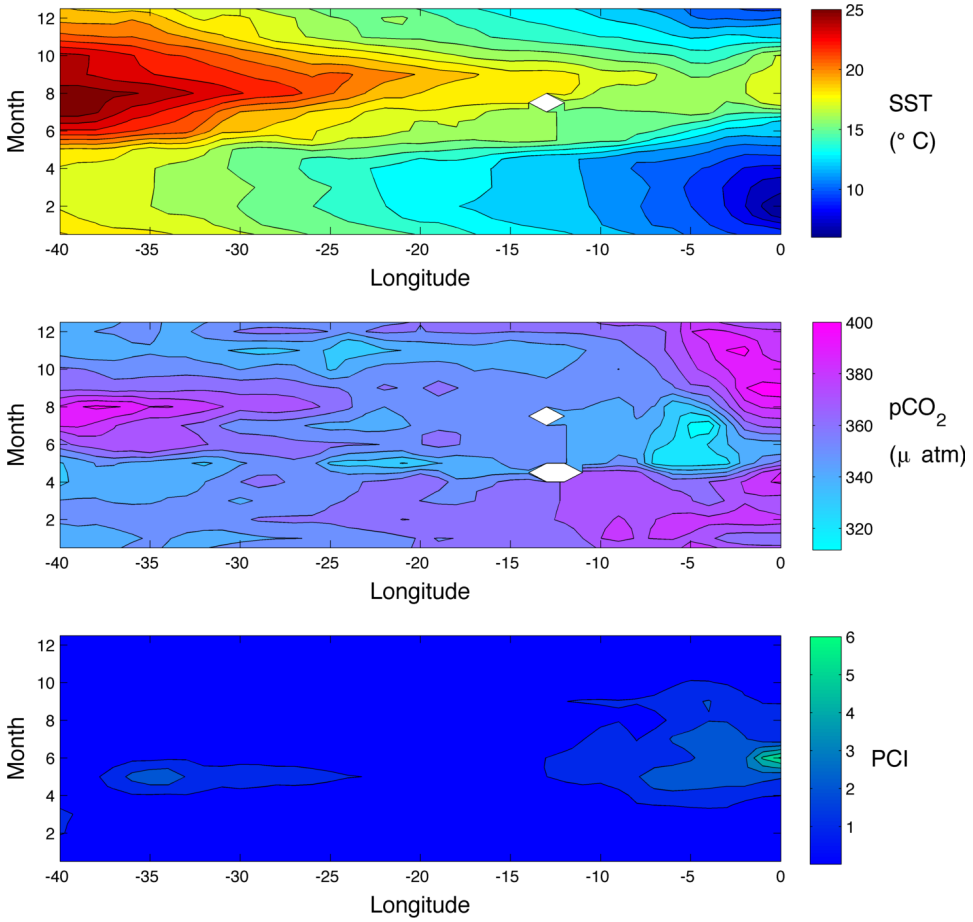

Figure 6.3: Monthly hovmoller plot against longitude for **a)** SST **b)** sea surface pCO_2 and **c)** PCI from 2002-2013 in the south band region of the North Atlantic (see figure 6.1).

In the south band phytoplankton drive the seasonal cycle of pCO_2 on the Eastern side of the Atlantic as high PCI is coincident with low pCO_2, but closer to the West Atlantic, SST is the dominant driver of pCO_2 as high pCO_2 waters at -40°W during August correspond with high SST (figure 6.3).

6.3.4 Provinces

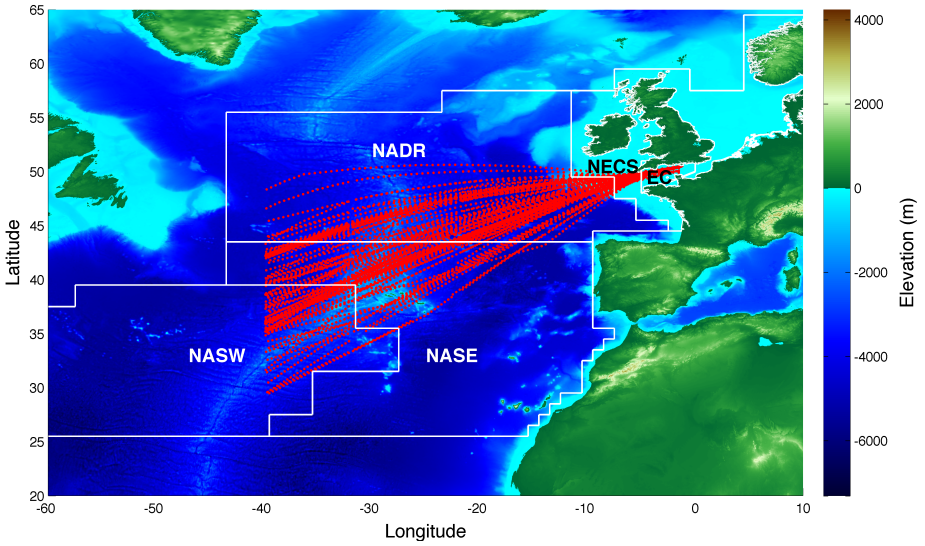

Figure 6.4: Map of the North Atlantic showing regions 1 to 5 outlined in white and labelled, and the elevation indicating the bathymetry. Red circles = CPR samples.

Longhurst provinces (Longhurst, 2006) were used to allocate the data to regions, providing a balance between avoiding the loss of spatial variation associated with phytoplankton abundance and adequately sampled months from the CPR dataset (Richardson *et al.*, 2006). An additional region within the Longhurst coastal province (NECS) was created to differentiate between the English Channel and the shelf seas, due to the high biogeochemical variability recorded within the English Channel (Kitidis *et al.*, 2012) (see table 6.1 and figure 6.4).

Table 6.1: Description of regions used (Longhurst, 2006)

No.	Acronym	Description
1	EC	Coastal - English Channel
2	NECS	Coastal - NE Atlantic Shelves Longhurst Province
3	NADR	Westerlies - N Atlantic Drift Longhurst Province
4	NASE	Westerlies - N Atlantic Subtropical Gyral Longhurst Province (East)
5	NASW	Westerlies - N Atlantic Subtropical Gyral Longhurst Province (West)

The English Channel is highly variable in its carbonate and nutrient conditions due to riverine input (Kitidis *et al.*, 2012). It is fully mixed throughout the year between 0°W and 3°W and transitional between stratified and fully mixed between 3°W and 5 °W (Pingree and Griffiths, 1978). The shelf-sea region (NECS, figure

6.4) is an important region for carbon export due to the spring and summer phytoplankton blooms, but quantifying the export and bio-physical interactions with the CO_2 cycle has proven difficult in this region due to the highly dynamic coastal interactions (Kitidis *et al.*, 2012; Laruelle *et al.*, 2014). The NADR region is within the northeast Atlantic Ocean and is characterised by the highly productive north Atlantic spring bloom and deep winter mixing with high inter-annual variability (200-800 m) (Körtzinger *et al.*, 2008). Both the NASE and NASW regions are seasonally stratified subtropical biomes (McKinley *et al.*, 2011) within part of the North Atlantic subtropical gyre which is influenced by the Portugal current. The NASE province contains the Azores and is further influenced by the Azores Current (Hooker *et al.*, 2000).

6.3.4.1 Seasonal variability

Monthly means of the dataset were calculated within each region as this is the smallest temporal resolution recommended by Richardson *et al.* (2006) to use with CPR data. The CPR data were divided into 6 key phytoplankton indices, namely phytoplankton colour index (PCI), spring-bloom forming diatoms (diatoms), *Rhizosolenia* (diatom genus often associated with a later blooming-time), dinoflagellates, silicoflagellates, and coccolithophores as described in chapter 5 section 5.3.13.

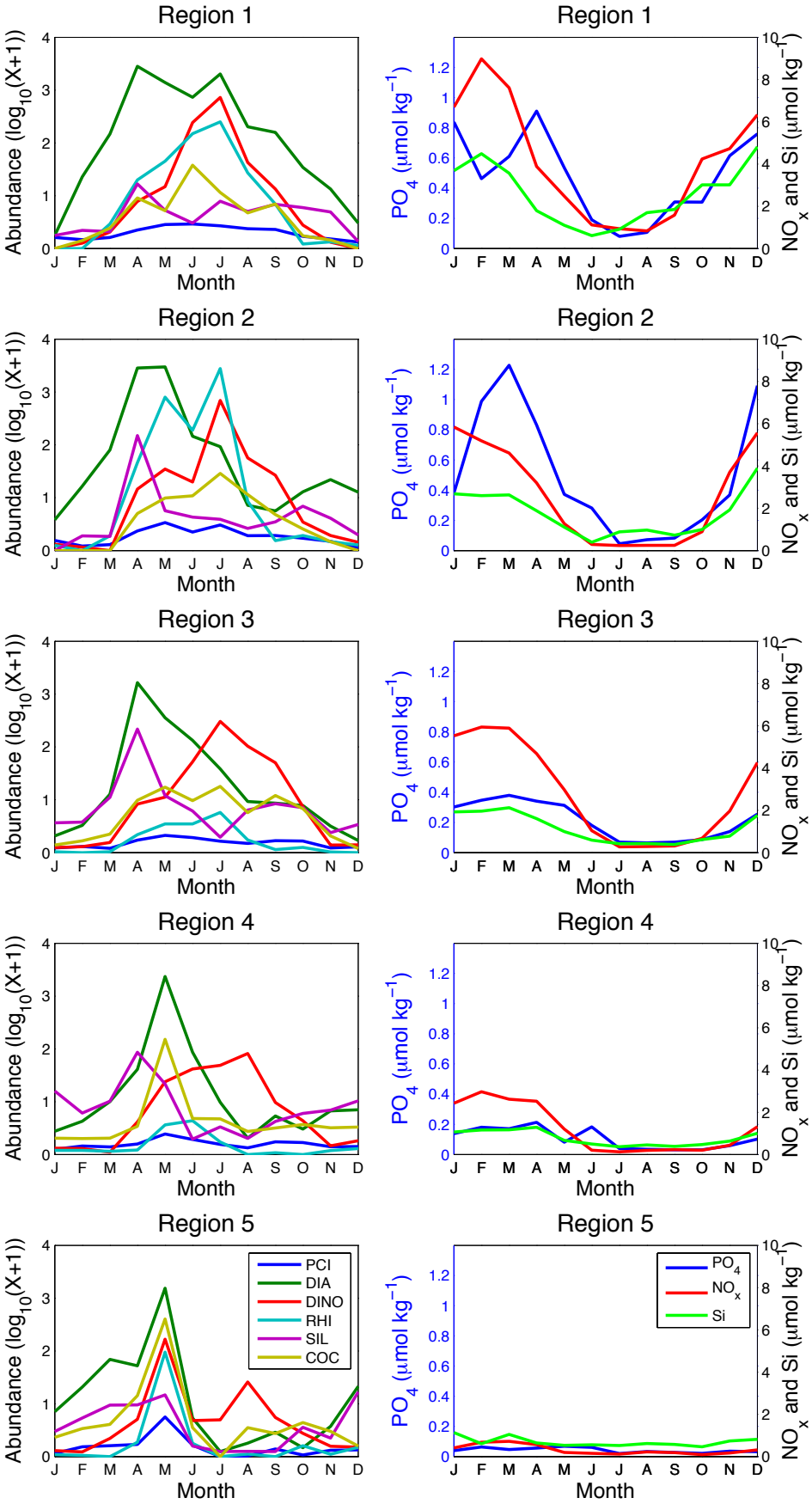

Figure 6.5: The left panel shows the monthly-mean phytoplankton index abundances (Blue = PCI, green = diatom, red = dinoflagellate, cyan = *Rhizosolenia*, purple = silicoflagellate, dark yellow = coccolithophore) and the right panel shows the monthly-mean nutrient concentrations (PO_4 = blue left axis, NO_x = red and Si = green, both right axis) in regions 1 to 5, averaged from 2002 to 2013.

Monthly-mean nutrient concentrations decrease from region 1 to 5, with seasonal maxima occurring in March/April and minima during June/July (right panel in figure 6.5). The left panel in figure 6.5 shows the monthly-mean phytoplankton abundance in regions 1 to 5, with diatoms having the largest peak in abundance in all five regions. The spring-blooming diatoms peak during April in regions 1 to 3 and May in regions 4 and 5. In region 1 there is a second peak in July. *Rhizosolenia* generally bloom slightly later than the spring-blooming diatoms because they can form algal mats that undergo vertical migrations to exploit nutrients at deeper depths. They do this through changes in buoyancy (Villareal *et al.*, 1993). This is evident in regions 1 to 3, but in regions 4 and 5 they reach a seasonal maxima in May which is during the same month as the spring-blooming diatoms. Dinoflagellates peak in July in regions 1 to 3, and in August in region 4 and May in region 5. Silicoflagellates peak in abundance in April and show a smaller Autumn peak in abundance in all five regions. Coccolithophore abundance in regions 1 to 3 has three peaks occurring in May, June/July, and September. In regions 4 and 5 there is a peak in abundance in May and another small peak in Autumn. In regions 1 to 4 apart from diatoms and silicoflagellates, the remaining phytoplankton indices bloom in the summer months, whereas in region 5 the peak phytoplankton abundance occurs in May for all indices apart from dinoflagellates. Generally the months where phytoplankton abundance is highest are when the nutrient concentrations are lowest due to the assimilation of nutrients by phytoplankton (figure 6.5). The annual seasonal cycle for each phytoplankton index and nutrient concentration from 2002 to 2013 within each region were investigated, with coccolithophore abundance and nutrient concentration plotted within appendix D (figures D.1 to D.4) to demonstrate the variance about the mean.

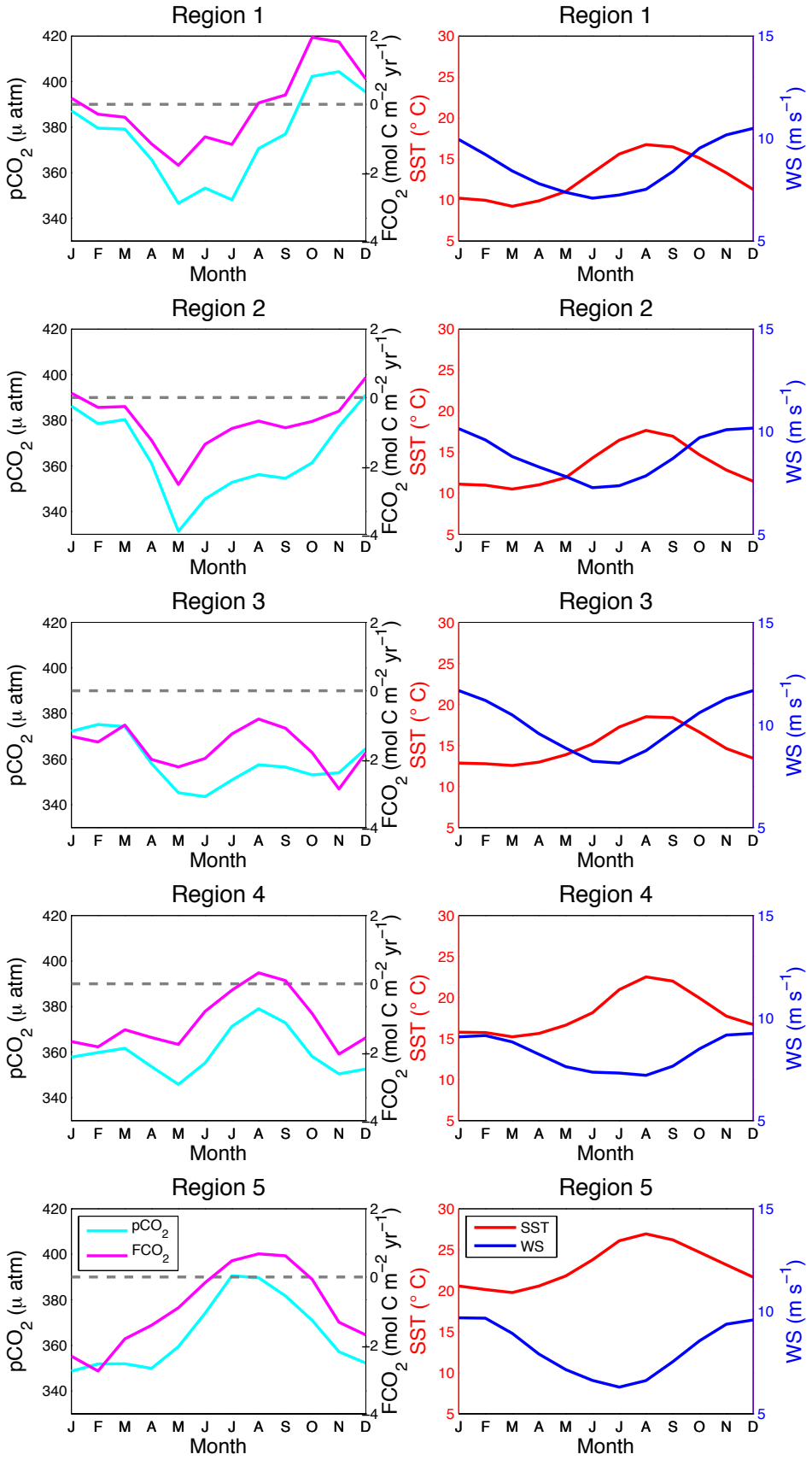

Figure 6.6: Left panel shows the monthly-mean sea-surface pCO_2 (left axis, cyan) and air-sea flux of CO_2 (right axis, pink) and the right panel shows the monthly-mean SST (red, left axis) and wind speed (blue, right axis) in regions 1 to 5, averaged from 2002 to 2013. The grey dashed line in the left panels indicates the zero flux line.

The mean seasonal cycle of the FCO_2 follows the oceanic pCO_2 cycle, and varies between regions 1 to 5 (left panel in figure 6.6). Region 1 has a seasonal minima in pCO_2 during May, June and July, and maxima during October and November, becoming a source of CO_2 during these winter months. Region 2 has the lowest pCO_2 concentrations occurring in May ($\sim$ 340 μatm), and another low pCO_2 signal in September, while the peak pCO_2 concentrations and fluxes occur in December, January and March.

Regions 3 and 4 have seasonal minima in both pCO_2 and FCO_2 during July and November, however the seasonal maxima are slightly different between regions with region 3 peaking in February/March and region 4 peaking in August when it becomes a source of CO_2. Region 5 has a peak in both FCO_2 and pCO_2 in August and the pCO_2 concentrations remain around 350 μatm during the rest of the season. This pattern is the same as the pattern of the SST record. Both regions 4 and 5 become sources of pCO_2 during August and September, which could be linked to the increasing SST during this period. The mean seasonal cycle of SST shows a peak in SST in all 5 regions during August and September. SST increases from regions 1 to 5 (ranging from $\sim$9°C to $\sim$25°C). The mean seasonal cycle of wind speed shows a peak in wind speed during December and January, and a seasonal low in wind speed during June and July in all 5 regions (ranging from $\sim$ 7 ms^{-1} to 12 ms^{-1}, right panel in figure 6.6).

The annual seasonal cycle for mixed layer depth (MLD) (Menemenlis *et al.*, 2008) was also investigated from 2002 to 2013 within each region. This is plotted within the appendix D figure D.5 for reference.

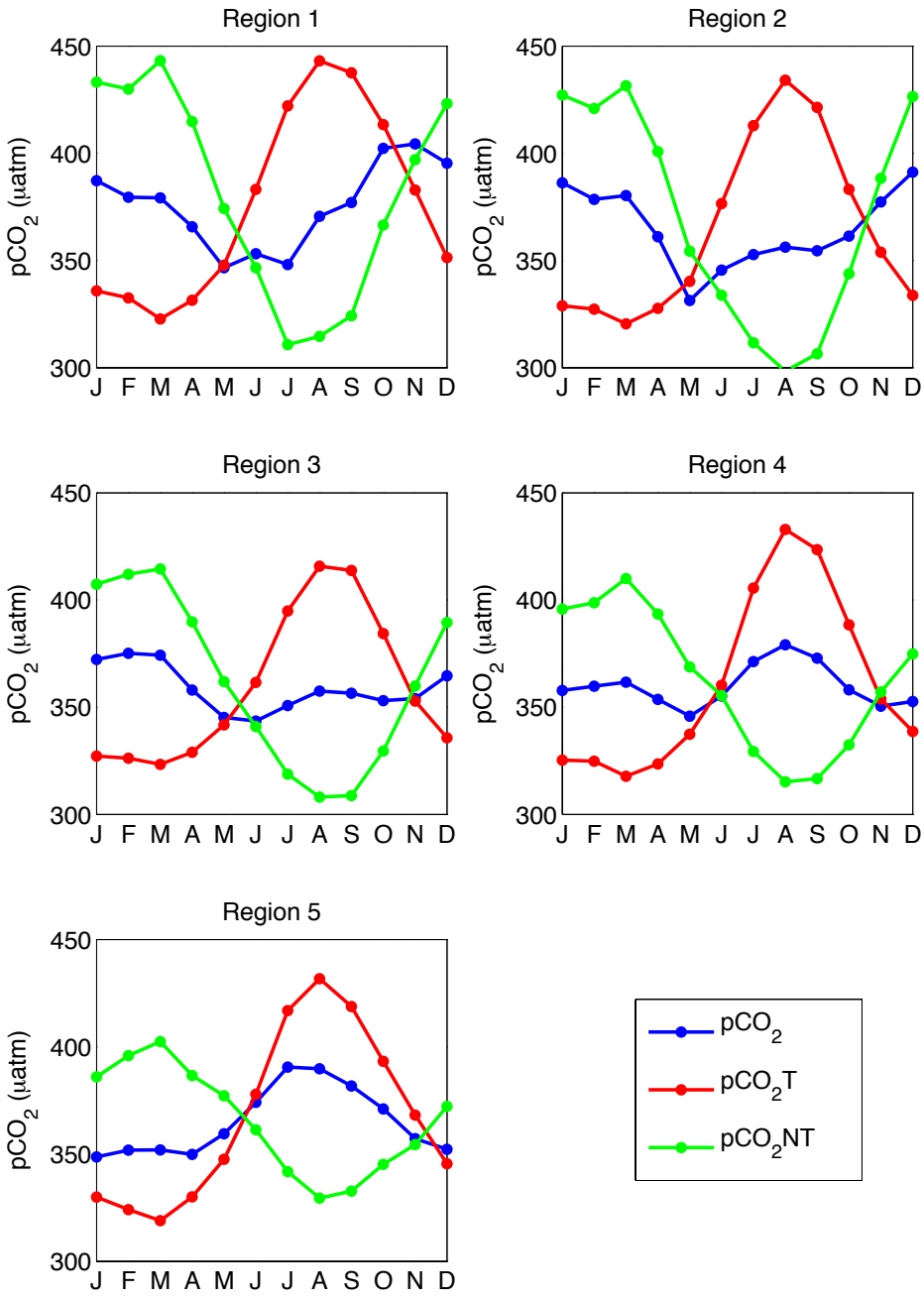

Figure 6.7: Monthly-mean sea-surface pCO_2 (blue), thermal pCO_2 (pCO_2T, red), and non-thermal pCO_2 (pCO_2NT, green) in regions 1 to 5, averaged from 2002 to 2013.

The mean seasonal cycle of thermal (pCO_2T) and non-thermal (pCO_2NT) driving components of pCO_2 were calculated using the monthly-mean SST and pCO_2 within each region (Takahashi and Sutherland, 2002; Körtzinger *et al.*, 2008) (see chapter 5 section 5.3.11). The $\sim$5°C seasonal range in SST seen in figure 6.6 equates to $\sim$100 μatm seasonal range in the pCO_2T in each region (figure 6.7). The seasonal cycle of pCO_2T is counteracted by the seasonal cycle of pCO_2NT, which has a decreasing seasonal range from region 1 to region 5, from $\sim$150 μatm

in region 1 to ∼75 μatm in region 5.

Principle component analysis (PCA) was carried out to analyse the monthly CO_2 flux, SST, and the different phytoplankton indices in each region from 2002 to 2013 (figure 6.8). A biplot of these results is included in appendix D figure D.7.

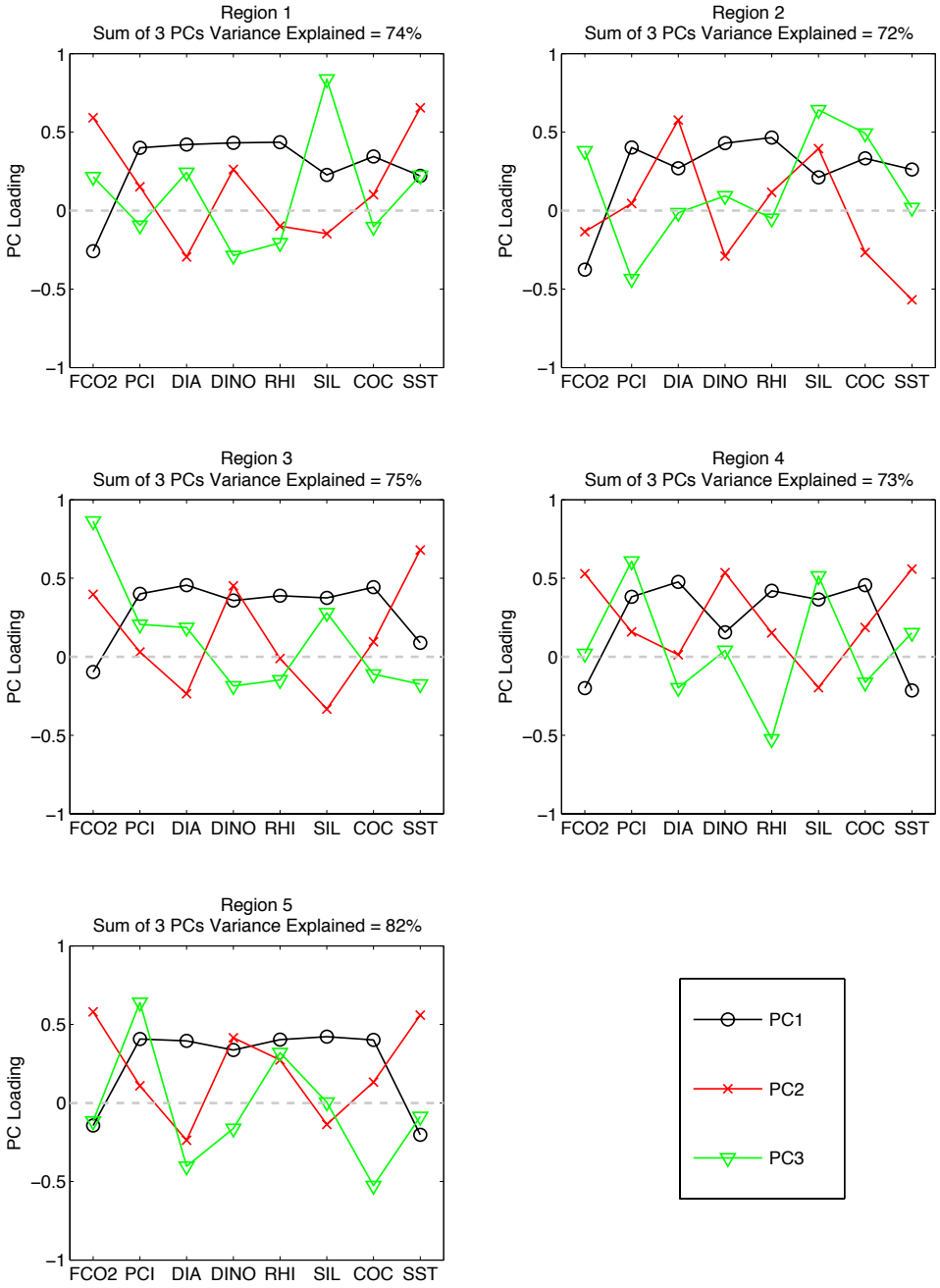

Figure 6.8: Line plot of the loadings of principal components 1, 2 and 3 when comparing monthly phytoplankton indices with sea surface temperature and air-sea flux of CO_2 from 2002 to 2013 in regions 1 to 5, with the variance explained by the sum of all three principal components displayed in the title.

Principal component 1 (PC1) in regions 1 to 3 shows that FCO_2 is negatively

associated with SST and the phytoplankton indices, whereas in region 4 and 5 SST and FCO_2 are positively associated and negatively associated with the phytoplankton indices. This suggests that phytoplankton abundance drives FCO_2 in regions 1 to 3, while SST drives FCO_2 in regions 4 and 5. PC2 shows that diatoms and silicoflagellates are negatively associated with FCO_2, while dinoflagellate abundance is positively associated with SST and FCO_2 in all regions except for region 2 (figure 6.8).

The correlation coefficients between all five phytoplankton indices and FCO_2, and pCO_2 were calculated, with a correction for temporal autocorrelation and significant correlations represented by an asterisk (figure 6.9, see chapter 3 section 3.3.6 for detailed methodology).

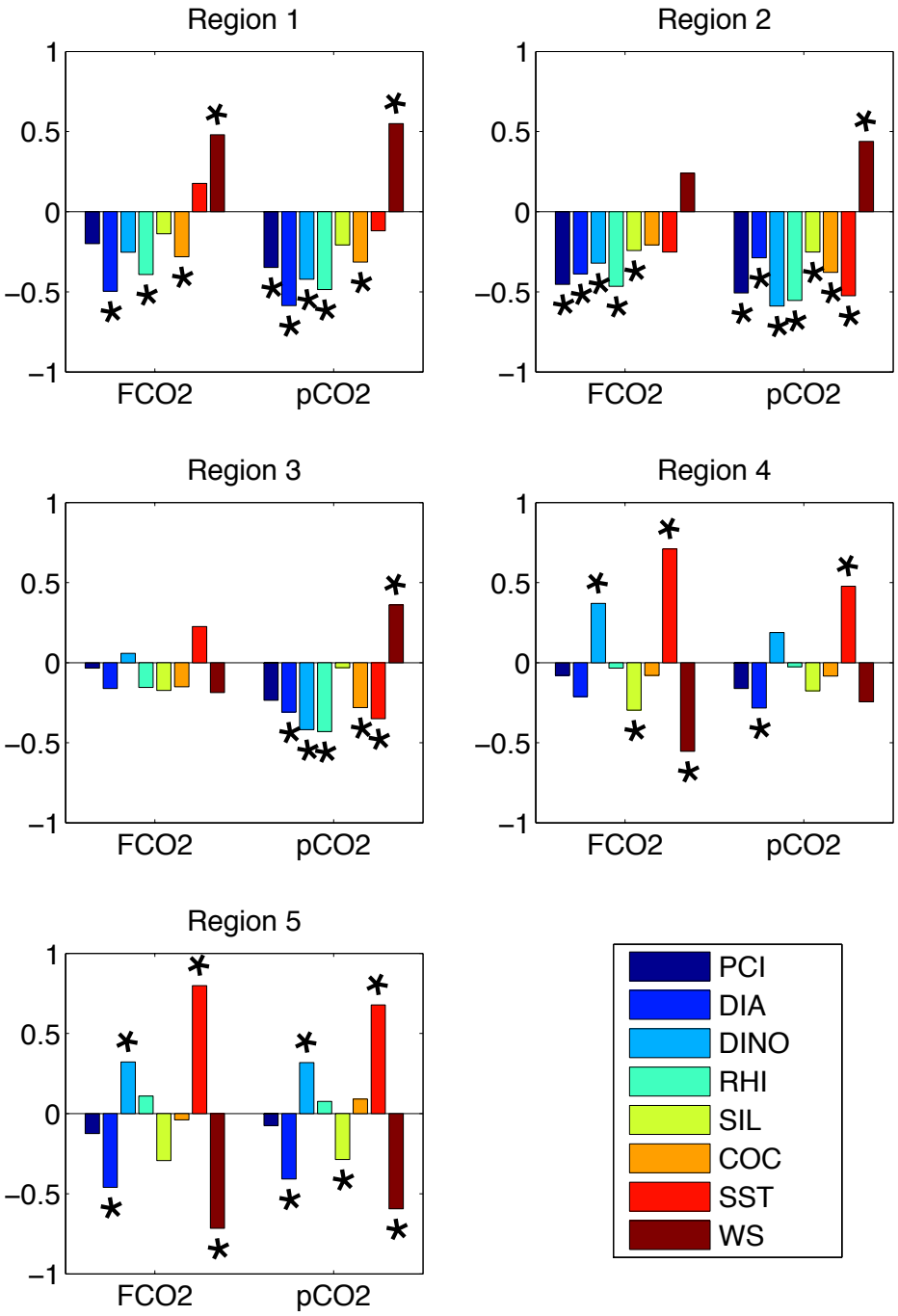

Figure 6.9: Pearson's correlation coefficients between the monthly air-sea flux of CO_2 (FCO_2), and sea surface pCO_2 and the phytoplankton indices, SST and wind speed (WS) in regions 1 to 5 from 2002 to 2013. After correcting for temporal autocorrelation, those coefficients with an asterisk were identified as significant (p-value<0.05) (Pyper and Peterman, 1998).

All phytoplankton indices are negatively correlated with pCO_2 and FCO_2 in regions 1, 2, and 3 (figure 6.9). Region 4 and 5 show a positive correlation with dinoflagellate abundance, which is likely due to the significant positive relationship between CO_2 and SST in these two regions, and the positive relationship between

SST and dinoflagellate abundance. Monthly wind speed and SST have opposing relationships with pCO_2 in all five regions, which corresponds to the seasonal cycles seen in figure 6.6. These results were further supported with cross-correlation analysis, which found that in regions 1 to 3 there was a lagged correlation between pCO_2 and SST, whereas in regions 4 and 5 there was a significant positive correlation with no lag. pCO_2 showed a significant negative correlation with PCI with no lag in regions 1 to 3, and a reduced negative correlation in region 4 and no correlation in region 5 (see appendix D figures D.8 to D.11 for details).

6.3.4.2 Inter-annual variability

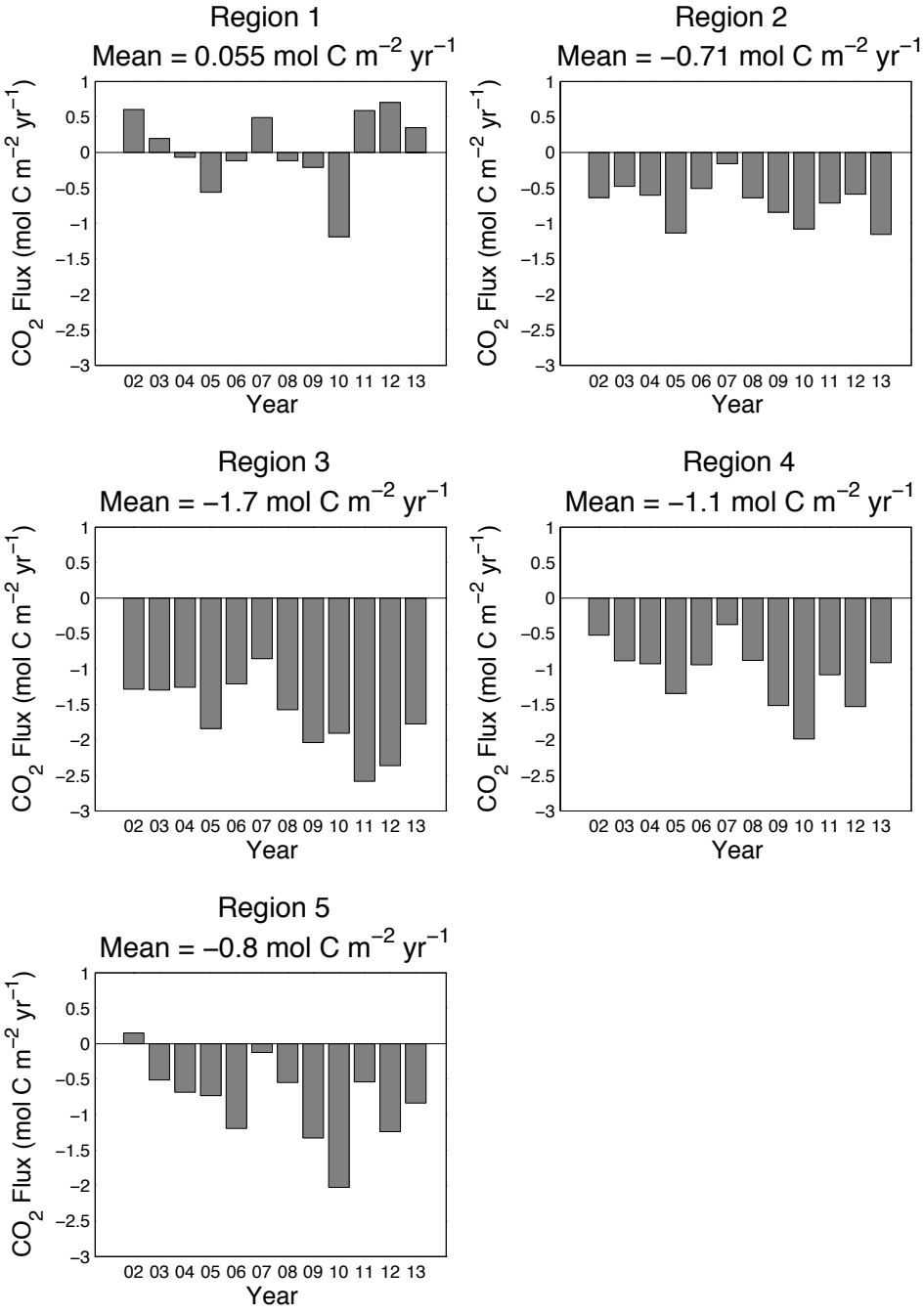

Figure 6.10: Annually averaged air-sea flux of CO_2 in regions 1 to 5, from 2002 to 2013, with the mean flux written above each plot. Negative values represent a sink of CO_2 from the atmosphere into the ocean, and positive values represent a source.

There is clear inter-annual variability in the air-sea CO_2 flux within each region (figure 6.10). Regions 2 to 5 are consistently net sinks, apart from the year 2002 in region 5 which was a small source, while region 1 is variable between a sink and a source of CO_2. The year 2007 was a low sink compared to other years in regions

2 to 5, while 2010 is a high sink year in regions 1, 4 and 5. Region 3 is the largest sink region with a mean sink of -1.7 mol C m^{-2} yr^{-1} throughout the study period, while region 1 is a mean source of 0.055 mol C m^{-2} yr^{-1}.

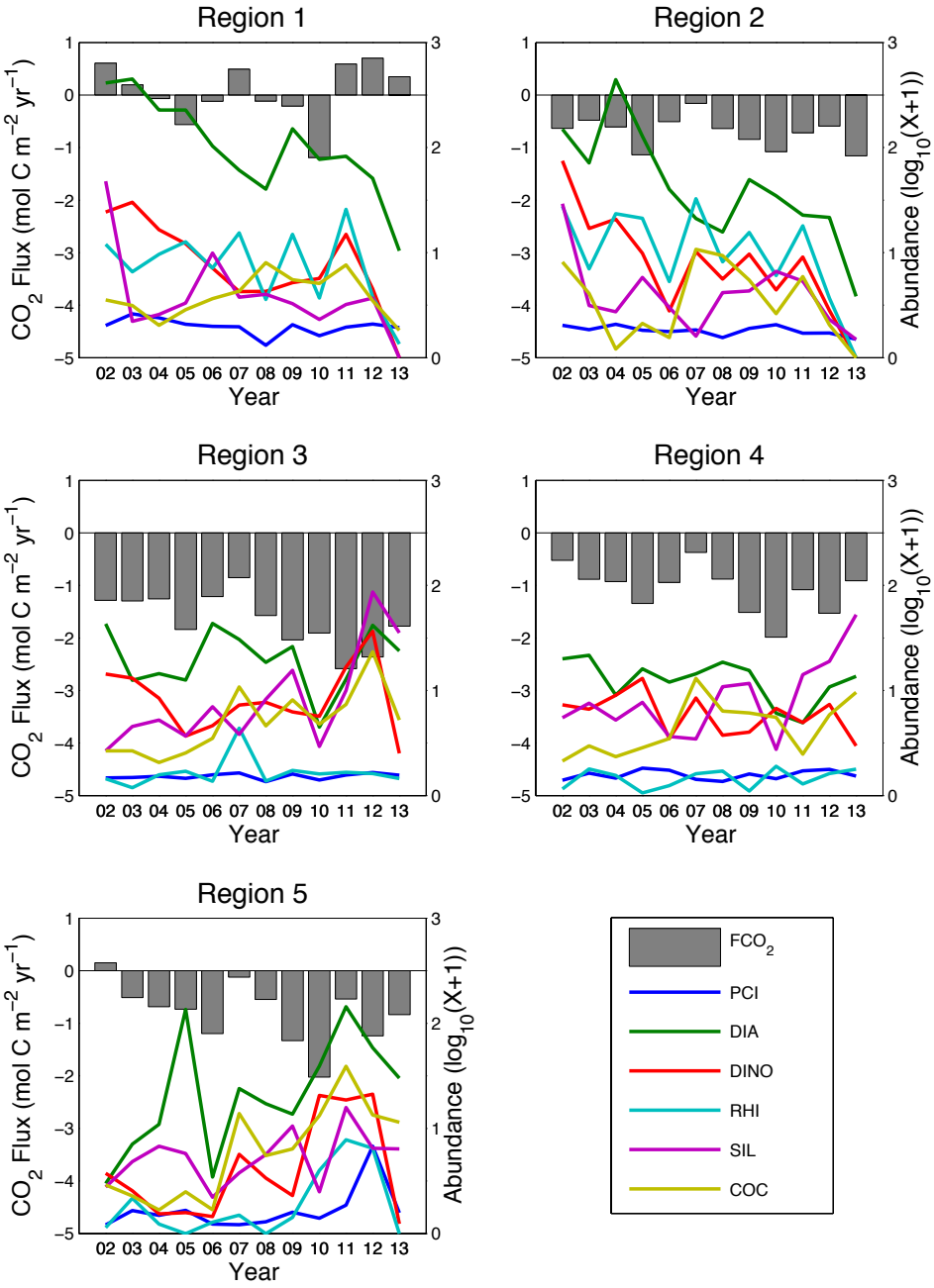

Figure 6.11: Annually averaged air-sea flux of CO_2 (grey bars = FCO_2, left axis) and phytoplankton index abundances (Blue = PCI, green = diatom, red = dinoflagellate, cyan = *Rhizosolenia*, purple = silicoflagellate, dark yellow = coccolithophore) in regions 1 to 5, from 2002 to 2013.

The average annual abundance shows that diatoms are generally the most abundant phytoplankton group from year-to-year. In regions 1 and 2 this annual diatom

abundance decreases with time from 2002 to 2013 (figure 6.11). Regions 3 and 5 show an increase in coccolithophore abundance, with high coccolithophore abundance corresponding to a decreased sink of CO_2 in 2007 in regions 2, 4 and 5.

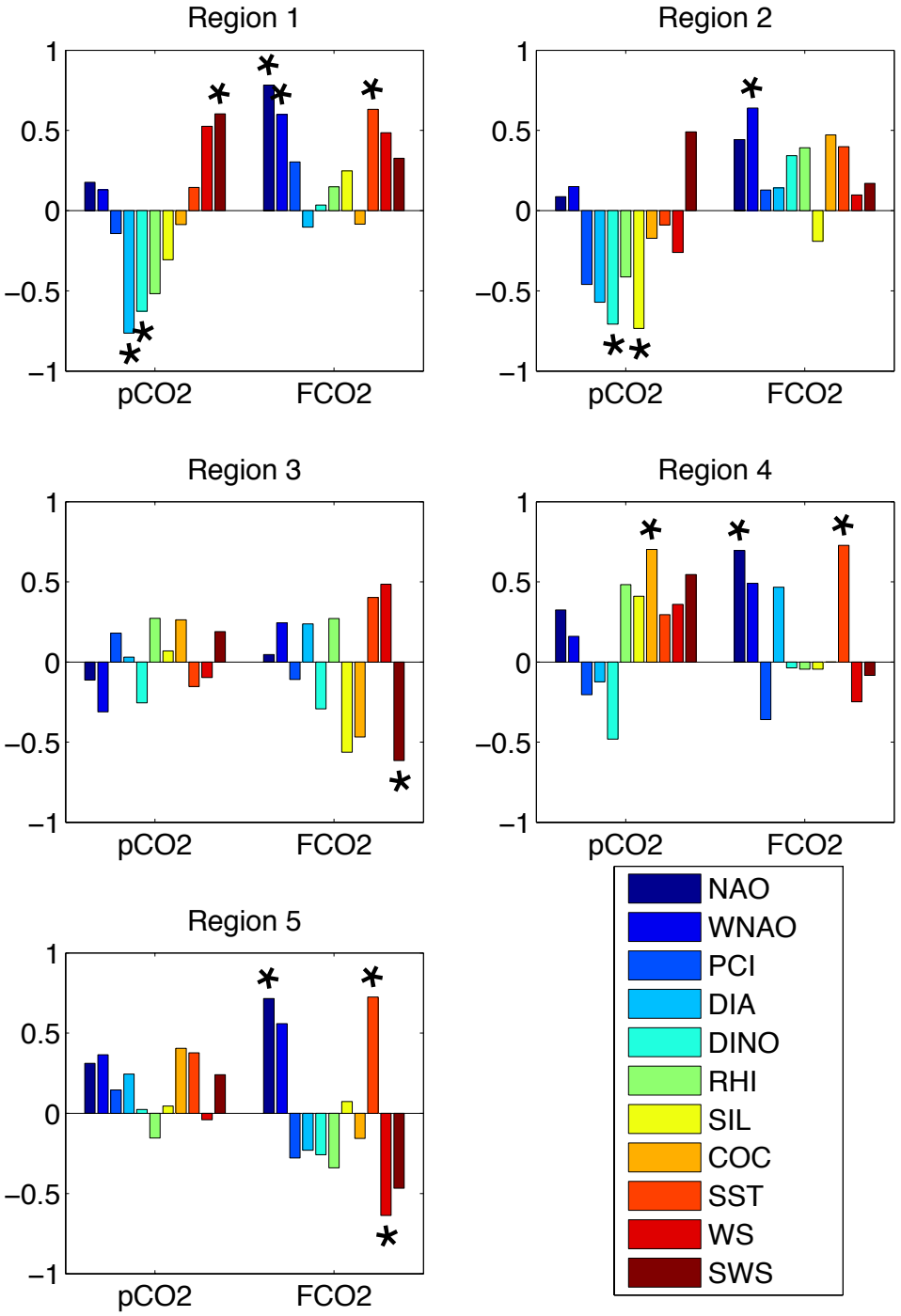

Figure 6.12: Pearson's correlation coefficients between the annual pCO_2 and the air-sea flux of CO_2, and the NAO, and winter NAO (WNAO) and phytoplankton indices, SST, wind speed (WS), and summer (May, June, July, August) wind speed (SWS) in regions 1 to 5 from 2002 to 2013. Those coefficients with an asterisk were identified as significant (p-value$<$0.05).

Annual pCO_2 is significantly negatively correlated with dinoflagellate abundance in both regions 1 and 2, and is negatively correlated with diatoms in region 1 and silicoflagellates in region 2 (figure 6.12). In region 4 there is a significant positive correlation between annual pCO_2 and coccolithophore abundance. The annual air-sea flux of CO_2 is positively correlated with the North Atlantic Oscillation (NAO) and winter NAO (WNAO) in regions 1, 2, 4 and 5, positively correlated with SST in regions 1, 4 and 5, and negatively correlated with SWS in region 3 and WS in region 5 (figure 6.12).

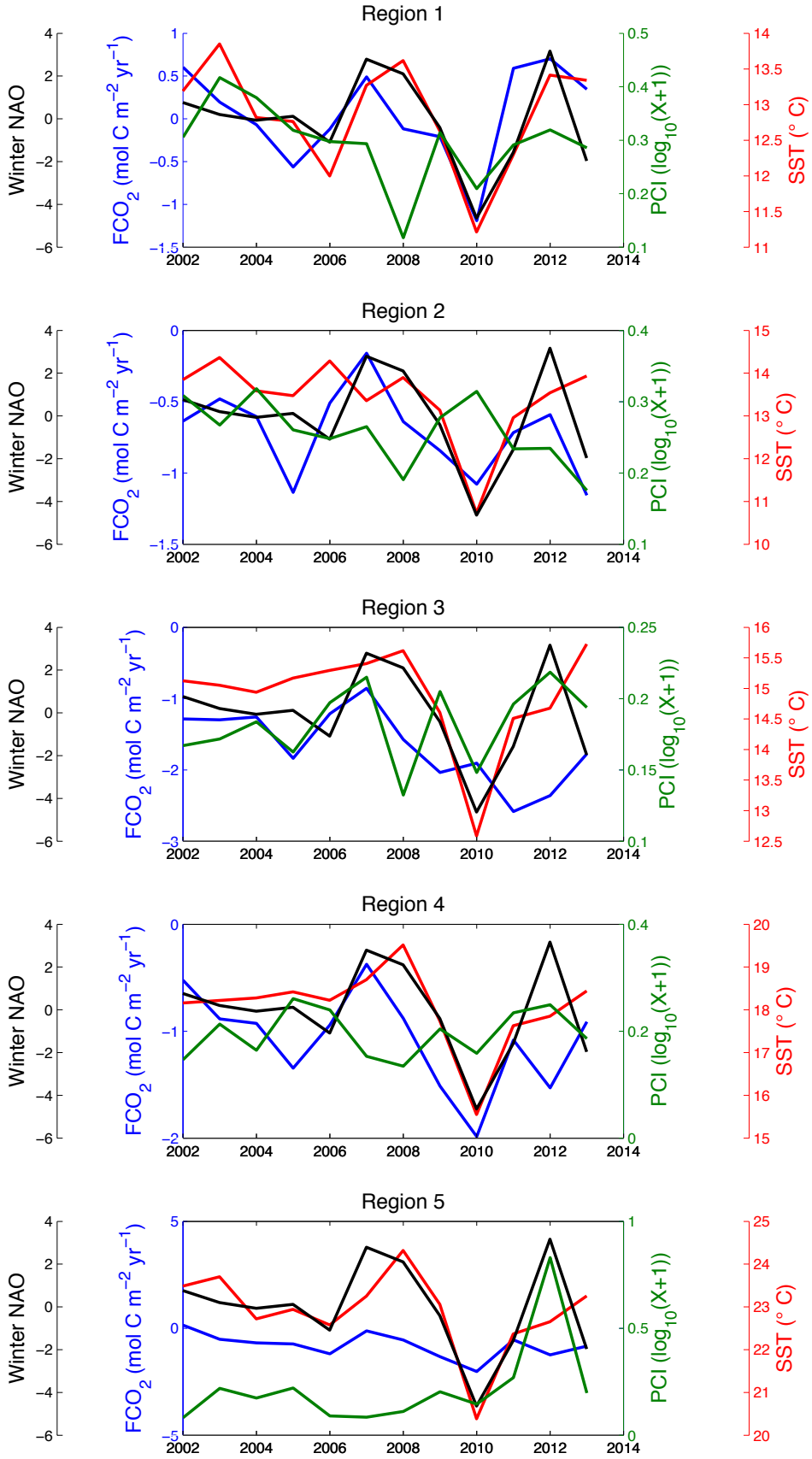

Figure 6.13: The annual winter North Atlantic Oscillation (Winter NAO = black, left axis), air-sea flux of CO_2 (FCO_2 = blue, left axis), Phytoplankton Colour Index (PCI = green, right axis), and sea-surface temperature (SST = red, right axis) in regions 1 to 5 from 2002 to 2013.

The winter NAO has a positive index in 2007 and 2012, and a negative index in 2010. The annual SST in all five regions has a similar trend to the winter NAO with low temperatures in 2010, and high temperatures in 2008 and 2013. In regions 1 to 4 the annual PCI drops below 0.2 $\log_{10}(x+1)$, and in region 5 there is a peak in PCI in 2012 up to $\sim$ 0.8 $\log_{10}(x+1)$. The annual air-sea flux of CO_2 is a sink in 2010 in regions 1, 2, 4 and 5 of $>$ -1 mol C m^{-2} yr^{-1}. In 2007 the sink decreases in all regions and becomes a source of CO_2 in region 1 (figure 6.13).

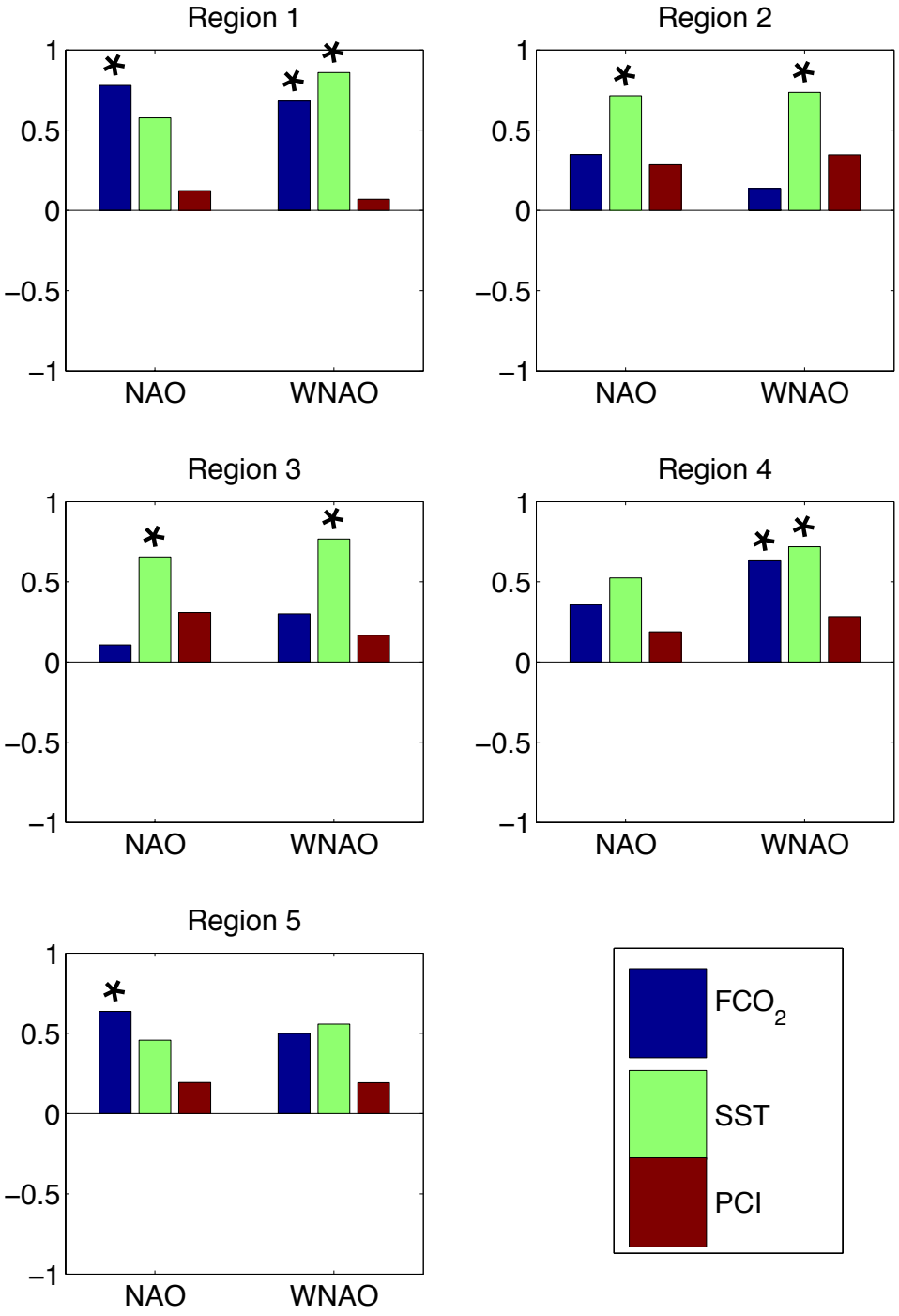

Figure 6.14: Pearson's correlation coefficients between the annual NAO and winter NAO and the air-sea flux of CO_2, SST and PCI in regions 1 to 5 from 2002 to 2013. Those coefficients with an asterisk were identified as significant (p-value$<$0.05).

In region 1 the air-sea flux of CO_2 is significantly positively correlated with both the NAO and the winter NAO, in region 4 it is correlated with the winter NAO and in region 5 it is correlated with the NAO. SST is significantly positively correlated with either one or both of the NAO indices in regions 1, 2, 3 and 4 (figure

6.14).

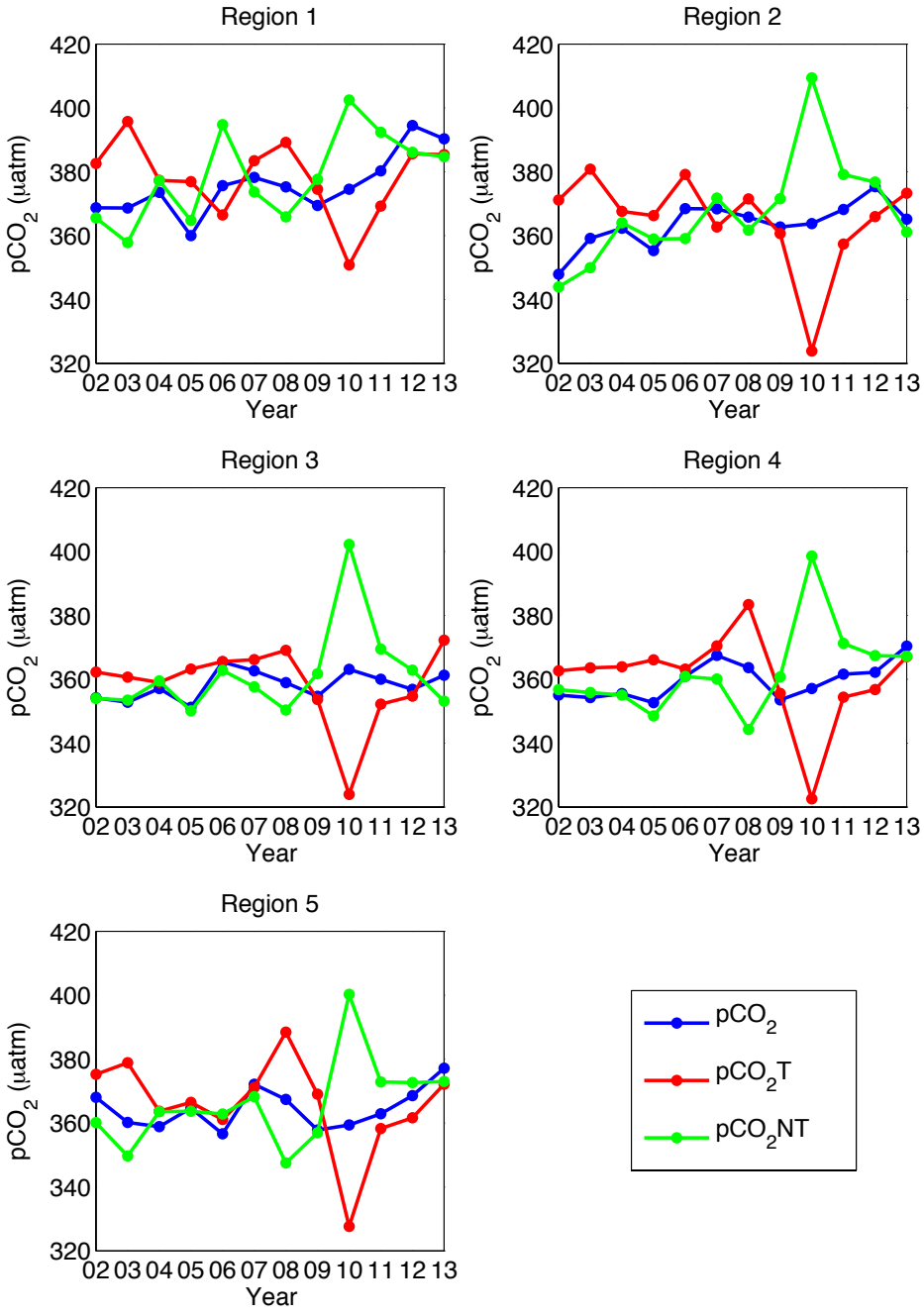

Figure 6.15: Annual sea-surface pCO_2 (blue), thermal pCO_2 (pCO_2T, red), and non-thermal pCO_2 (pCO_2NT, green) in regions 1 to 5, from 2002 to 2013.

Annual thermal (pCO_2T) and non-thermal (pCO_2NT) driving components of pCO_2 were calculated using annually averaged monthly pCO_2T and pCO_2NT within each region (Takahashi and Sutherland, 2002; Körtzinger *et al.*, 2008). In all five regions 2010 had a lower than normal annual SST (figure 6.13) which causes a decrease in the pCO_2T by ~ 40 μatm, which is counteracted by the pCO_2NT (figure

6.15). SST was high in all five regions in 2008, which caused an increased pCO_2T and decreased pCO_2NT. In regions 4 and 5 the annual SST in 2008 was higher than any year within the time-series (figure 6.13).

6.3.5 Basin-scale trends

Trends in the annual average FCO_2 and pCO_2 in the North Atlantic were calculated using the Landschützer *et al.* (2014) neural network-based estimates of CO_2 from 1998-2011. This time frame was chosen as these are the years that CO_2 measurements within the North Atlantic are adequately sampled and 2011 is the latest year available from the SOCAT (Surface Ocean CO_2 Atlas, http://www.socat.info) database (Bakker *et al.*, 2014). Trends were calculated by taking the linear slope of the twelve-month running mean for each 1°by 1°grid cell. Those trends that were outside of the 95% significance level are indicated with a cross-hatch.

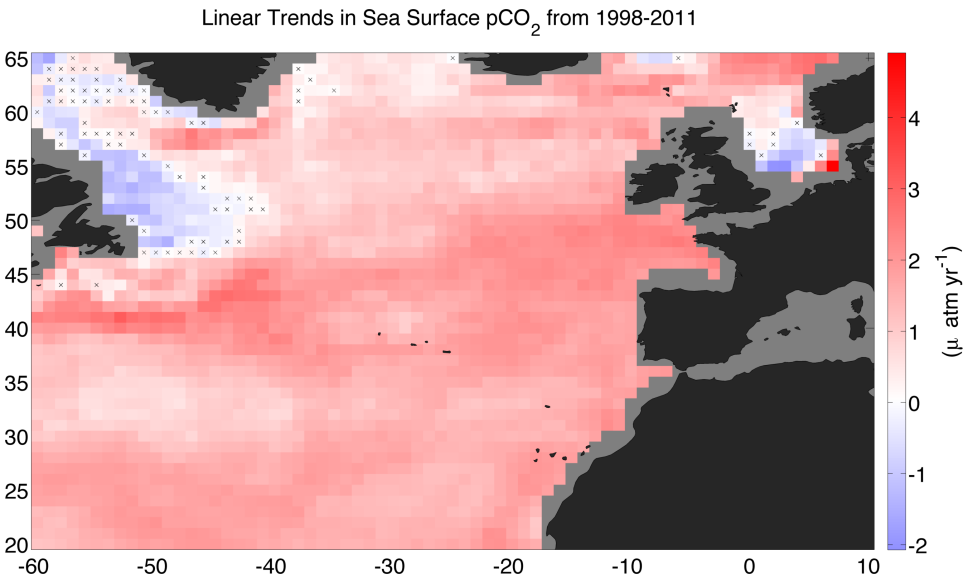

Figure 6.16: Linear trends in annual sea-surface pCO_2 in the North Atlantic from 1998 to 2011. Trends that are outside of the 95% significance level ($p \geq 0.05$) are indicated with a cross-hatch. Blue = decreasing pCO_2. Red = increasing pCO_2.

Annual average sea surface pCO_2 is increasing throughout most of the North Atlantic, with small decreasing regions within the Labrador Basin and the southern North Sea (figure 6.16).

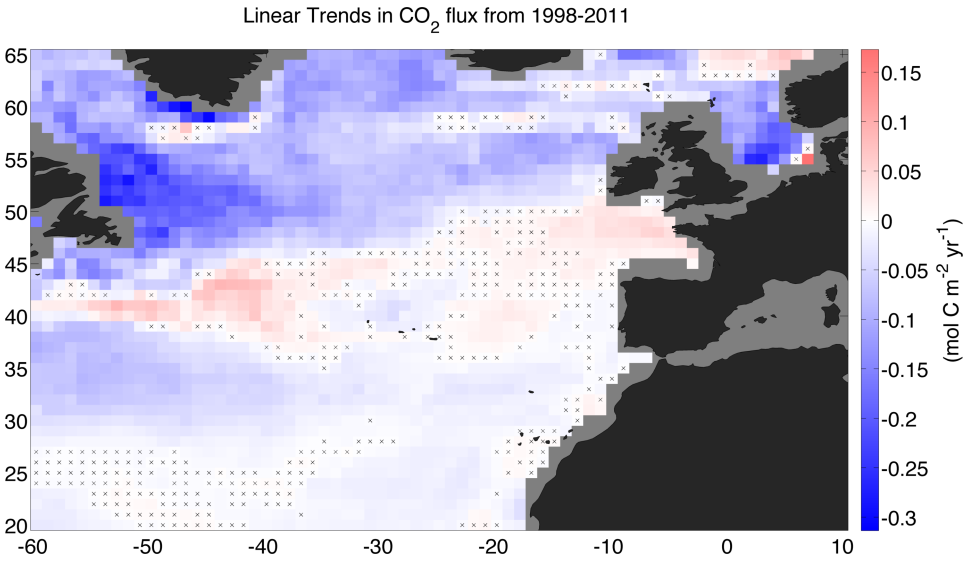

Figure 6.17: Linear trends in the annual air-sea flux of CO_2 (FCO_2) in the North Atlantic from 1998 to 2011. Trends that are outside of the 95% significance level ($p \geq 0.05$) are indicated with a cross-hatch. Blue = increasing sink. Red = decreasing sink.

The annual average FCO_2 shows an increasing sink (blue) in the northern North Atlantic, and a slight decreasing sink (mostly non-significant linear trends) in the southern North Atlantic (white-red) south of 40 to 50°N (figure 6.17). Areas with the strongest increasing sink are in the Labrador basin and the North Sea. The increasing sink in the northern North Atlantic suggests that the seawater pCO_2 concentration is increasing at a slower rate than the atmospheric pCO_2 concentration, and the difference between the two is therefore increasing.

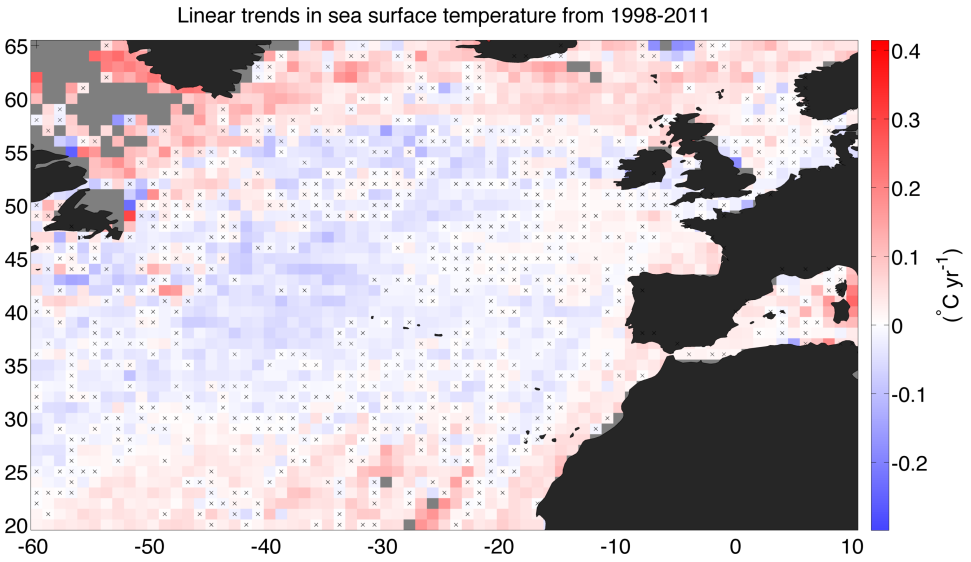

Figure 6.18: Linear trends in annual average SST in the North Atlantic from 1998 to 2011. Trends that are outside of the 95% significance level ($p \geq 0.05$) are indicated with a cross-hatch. Blue = decreasing SST. Red = increasing SST. Grey areas are where there were insufficient data.

SST has increased between 55 and 65°N, and has decreased or remained the same in waters between 25°N and 55 °N (figure 6.18).

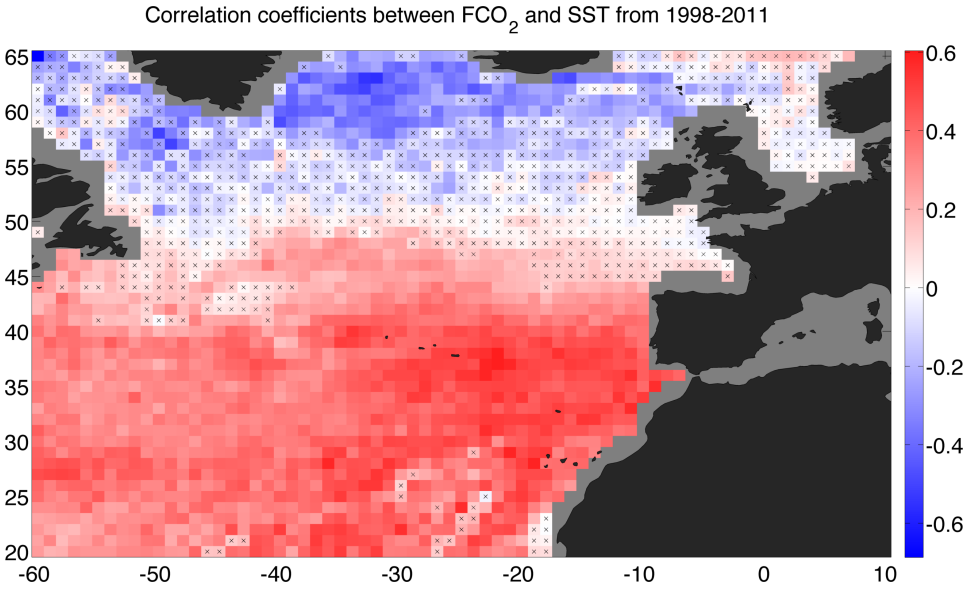

Figure 6.19: Correlation coefficients between the air-sea flux of CO_2 and SST in the North Atlantic from 1998 to 2011. Correlations that are outside of the 95% significance level ($p \geq 0.05$) are indicated with a cross-hatch. Blue = negative correlation. Red = positive correlation.

North of 55°N FCO_2 is negatively correlated with SST (figure 6.19). South of 50°N FCO_2 is positively correlated with SST due to the similar increasing trends in this region (mostly non-significant increasing linear trends).

Due to the irregular CPR sampling across the North Atlantic, objective mapping was used to interpolate the CPR data onto a regular grid in order to compare it with climate variables (see chapter 3 section 3.3.3 for detailed description of methods).

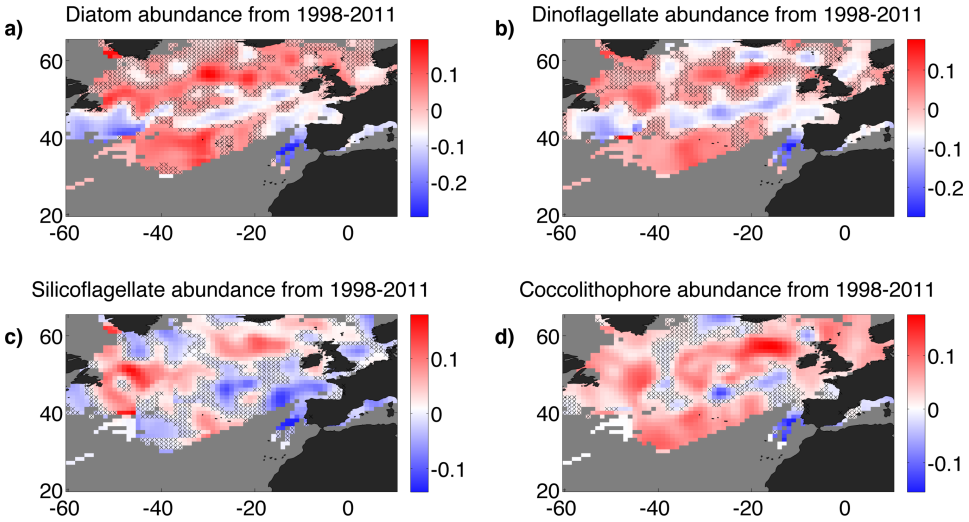

Figure 6.20: Annual linear trends in phytoplankton abundance in the North Atlantic from 1998 to 2011. a) diatoms, b) dinoflagellates, c) silicoflagellates, and d) coccolithophores. Trends that are outside of the 95% significance level ($p \geq 0.05$) are indicated with a cross-hatch. Blue = decreasing abundance. Red = increasing abundance. Grey areas are where there were insufficient data.

The linear trends of the average annual abundance of key phytoplankton indices show a patchy distribution. Diatom abundance has increased in a diagonal swathe across the North Atlantic from 50°N 50°W to 60°N 10°W, and decreased in the diagonal swathe from $\sim$ 40°N 60 °W to 51°N 10°W (south-west Ireland, figure 6.20a). Dinoflagellate abundance follows a similar though not as pronounced pattern as diatoms (figure 6.20b). The pattern of increasing silicoflagellate abundance (figure 6.20c) is similar to that of diatoms, but extends further south west, while coccolithophore abundance has increased throughout the N. Atlantic and into the North Sea (figure 6.20d). The linear trends of PCI and *Rhizosolenia* abundance showed similar regions of increase and decrease to those of the other phytoplankton indices and are included in appendix D figures D.12 to D.13 for reference.

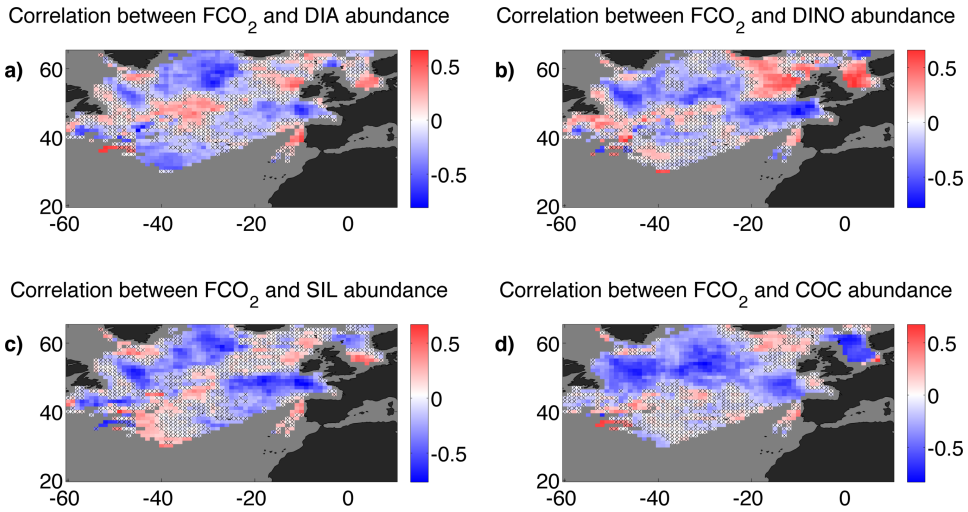

Figure 6.21: Correlation coefficients between the air-sea flux of CO_2 (FCO_2) and phytoplankton abundance in the North Atlantic from 1998 to 2011. a) diatoms (DIA), b) dinoflagellates (DINO, c) silicoflagellates (SIL), and d) coccolithophores (COC). Correlations that are outside of the 95% significance level ($p \geq 0.05$) are indicated with a cross-hatch. Blue = negative correlation. Red = positive correlation. Grey areas are where there were insufficient data. Note: Decreasing FCO_2 is an increasing sink.

Increasing diatom abundance correlated with the increasing sink of CO_2 (blue, figure 6.21a). The correlation coefficients between dinoflagellate abundance and FCO_2 are similar to those between FCO_2 and diatom abundance, again with a general trend of increasing abundance linked to an increasing sink (blue, figure 6.21b). Two distinct exceptions to this are centred on the North Sea and the region to the west of the UK (55°N 15°W) where dinoflagellate abundance has decreased (figures 6.20b and 6.21b).

The pattern of significant correlation between increasing silicoflagellate abundance and the increasing CO_2 sink (figure 6.21c) is similar to that of diatom abundance and the CO_2 sink. Most of the North Atlantic shows a significant correlation between increasing coccolithophore abundance and the increasing CO_2 sink, particularly in the North Sea where coccolithophore abundance has increased significantly (figure 6.20d and 6.21d). The correlation coefficients of PCI and *Rhizosolenia* abundance with FCO_2 are included in appendix D figures D.14 to D.15 for reference.

6.4 Discussion

6.4.1 Seasonal variability

Figures 6.2 and 6.3 clearly show the differing latitudinal seasonal cycle of pCO_2 and how this cycle is influenced by SST and phytoplankton abundance, with the SST seasonal cycle driving the pCO_2 cycle in the south region at western longitudes, and phytoplankton growth reducing the pCO_2 during spring/summer in the eastern longitudes. The opposing relationship between the biological and temperature driven influences on pCO_2 have been well described. For example, Takahashi and Sutherland (2002) describe the transition region between biologically dominated and temperature dominated effects on pCO_2 in the North Atlantic, and how subpolar waters show a biological dominance whereas within subtropical waters the temperature effects exceed those of biology. This is the first study that combines biological data from the CPR with observations of pCO_2 from the same platform, and the observations clearly support these previous findings.

At province-based spatial scales the seasonal maxima of the phytoplankton indices correspond to the seasonal minima in both the pCO_2 and air-sea flux of CO_2, with a larger integral of phytoplankton biomass throughout the summer in region 1, and a shorter bloom period in the spring in region 5 (figures 6.5 and 6.6). In region 5 although there appear to be low concentrations of nutrients (< 1 μmol kg^{-1}) there is still a relatively large bloom in phytoplankton during May. This indicates that the phytoplankton within this region are able to bloom under low-nutrient conditions, which could suggest that the nutrient concentration is enough to initiate the bloom but not maintain it, or it could be due to fast nutrient recycling and grazing, and the presence of nitrogen fixers such as *Trichodesmium sp.* (Capone *et al.*, 2005).

The ΔpCO_2 and air-sea flux of CO_2 were proportional to each other with short-term wind speeds having little effect on the flux of CO_2. This agrees with McKinley *et al.* (2011) and Le Quéré *et al.* (2010) who suggest that the main influence of winds are changes in circulation and the mixing of CO_2-rich waters from below the thermocline. Although the seasonal range in pCO_2T remains consistent in regions 1 to 5, the seasonal range in pCO_2NT reduces from region 1 to 5 (figure

6.7). This suggests that the biologically driven components of the seasonal pCO_2 cycle become less prominent from region 1 to region 5 and therefore the thermal driving component becomes more influential. Körtzinger *et al.* (2008) describe the seasonal pCO_2NT cycle at the PAP site as being driven by the biological drawdown of carbon during the winter to summer causing a decrease, and the increase during the summer to winter months being driven by mixing of deep waters. These mixing events bring up DIC and nutrient rich waters as well as a seasonal respiration element from below the thermocline (due to respiration occurring below the mixed layer) (Körtzinger *et al.*, 2008). This biogeochemical seasonal cycle is likely to be affecting all of our regions, as the same trend described in Körtzinger *et al.* (2008) can be seen in figure 6.7. This seasonal trend combined with the increasing SST during autumn increases the concentration of pCO_2 as the solubility of DIC is decreased (Sarmiento and Gruber, 2006). This supports the DIC measurements presented in chapter 5, and the results discussed within section 5.5.2 of significant trends between phytoplankton indices in the northeast Atlantic and normalised DIC, which were not present in the subtropical regions.

The transition from biologically driven to thermally driven CO_2 cycles described by Takahashi and Sutherland (2002) in the North Atlantic is evident between our regions. There was significant anti-correlation between both the FCO_2 and pCO_2 with phytoplankton abundance in regions 1 and 2, and the pCO_2 in region 3, and a significant positive correlation between SST and both the FCO_2 and pCO_2 in regions 4 and 5 (figure 6.9). This supports the latitudinal seasonal plots that show a transition between the north and south and from east to west (figures 6.2 and 6.3).

6.4.2 Inter-annual variability

The northeast Atlantic is a net sink for CO_2, but shows strong inter-annual variability (Schuster *et al.*, 2009b; McKinley *et al.*, 2011; Schuster *et al.*, 2013) (figure 6.10). 2007 stands out as a year with a particularly weak sink in regions 2 to 5, and a source year in region 1. In region 4 there was a significant positive correlation between average annual coccolithophore abundance and pCO_2 (figure 6.12),

and the highest average annual abundance of coccolithophores was recorded in 2007 (figure 6.11). In regions 2 and 5 a similar trend is seen between high annual coccolithophore abundance and a weaker annual FCO_2. The increased abundance of coccolithophores could increase the pCO_2 within the surface waters as it is produced during calcification, therefore reducing the flux of CO_2 from the atmosphere into the sea. During the summer of 1991, Robertson *et al.* (1994) report increased pCO_2 due to calcification from a bloom of *Emiliania huxleyi* in the northeast Atlantic (within the NECS and NADR Longhurst provinces (Longhurst, 2006)). Robertson *et al.* (1994) estimate a decrease in the air-sea gradient of CO_2 by 15 μatm due to the change in alkalinity from the bloom. Beaugrand *et al.* (2012) found a significant positive correlation between coccolithophore abundance and pCO_2 in the northeast Atlantic over 25 years. However, this was not corrected for temporal autocorrelation and could be the result of increasing SST increasing both the abundance of coccolithophores and pCO_2 simultaneously rather than coccolithophore abundance influencing the pCO_2 concentration directly (Beaugrand *et al.*, 2012).

2010 was a particularly strong sink year in regions 1, 4 and 5. This is likely to be due to the unusually low SST in 2010 in all five regions which would increase the solubility of DIC, reducing the concentration of pCO_2 as it dissociates more readily and therefore increasing the air-sea flux (figure 6.13). This can also be seen in figure 6.15 where the low SST in 2010 drives the pCO_2T concentration down, which is counteracted by the pCO_2NT, implying that there was a strong increase in pCO_2 concentrations due to non-thermal processes in 2010. This result highlights the risk of over-simplifying the processes that influence pCO_2, and demonstrates that caution should be taken when interpreting such results, especially at inter-annual time-scales.

The inter-annual variability in the FCO_2 in the North Atlantic has been linked to the NAO which is the major climate mode for the North Atlantic (Schuster and Watson, 2007). At the Bermuda Atlantic Time Series (BATS, 32°N 74°W) the NAO drives the inter-annual variability with no time-lag (Gruber *et al.*, 2002), while at the European Station for Time Series in the Ocean (ESTOC, 29.2°N

15.5°W) a three year time-lag was estimated between the NAO and FCO_2 (Santana-Casiano *et al.*, 2007; Schuster *et al.*, 2013). Our results agree with those from BATS, as we found that the NAO had significant correlations with no time-lag with both SST and the FCO_2 (figure 6.14). This agreement was to be expected as BATS is closer to the ship's route than ESTOC. Figure 6.13 shows that during strong positive (>1 (Henson *et al.*, 2012)) NAO periods annual SSTs are increased, while during strong negative (<-1 (Henson *et al.*, 2012)) NAO periods annual SSTs are decreased. This alteration in SST is likely to influence FCO_2, due to changes in the solubility, but also the changes in stratification which, if increased, may reduce the upwelling of carbon-rich waters and the availability of nutrients into the surface waters, therefore reducing productivity (Behrenfeld *et al.*, 2006; Körtzinger *et al.*, 2008; Hartman *et al.*, 2015). Past records of the NAO index show that it has been more positive than negative (figure 6.22). As our results suggest that positive NAO indices result in a reduced sink, we suggest that further negative indices, such as that seen in 2010 (figure 6.22), may result in an increased sink. There is still a lot of uncertainty surrounding the phase and variability of the NAO, but it is believed that anthropogenic warming is increasing the multidecadal variability of the NAO (Goodkin *et al.*, 2008). If this is the case, than it is likely that increased multidecadal variability of the NAO will also contribute to the multidecadal variability of the flux of CO_2 in the North Atlantic.

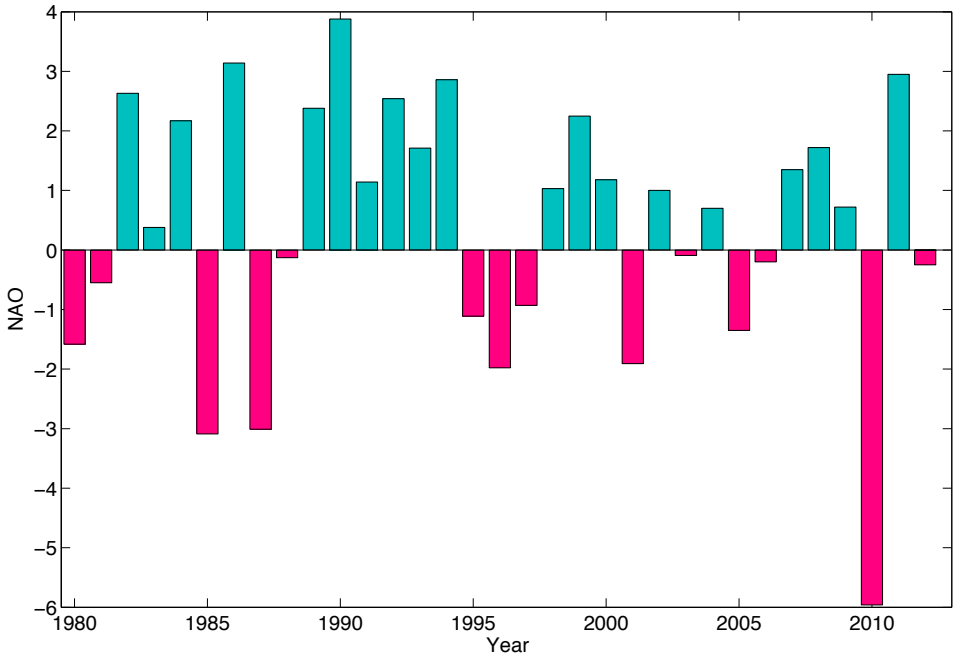

Figure 6.22: Annual NAO index from 1980 to 2012 (Hurrell, 1995). Cyan = positive NAO, pink = negative NAO.

The changes in wind patterns and circulation associated with the NAO are difficult to quantify but generally negative NAO phases are associated with decreased westerly winds and vice versa. Changes in circulation are thought to have a strong impact on the FCO_2 (Le Quéré *et al.*, 2010). Figure 6.12 suggests that changes in wind speed may have differing influences on the FCO_2 between regions as the correlation between FCO_2 and wind speed and summer wind speed is positive in regions 1 and 2 and negative in regions 4 and 5. This could be because increased mixing in regions 1 and 2 increases the pCO_2 due to upwelled carbon, whereas in regions 4 and 5 which contain lower nutrient conditions, mixing enhances productivity which increases the sink of carbon dioxide. These influences on the flux of CO_2 are very challenging to disentangle and quantify due to the complex interactions between them (Schuster *et al.*, 2013). Although influences can be inferred, it is advisable to be cautious when analysing data on inter-annual time scales as decadal climate variability is likely to have an over-arching impact on any trends (McKinley *et al.*, 2011).

6.4.3 Basin-scale trends

The concentration of surface water pCO_2 shows an increasing linear trend across most of the North Atlantic between 1998 and 2011 (figure 6.16). This is highly likely due to the increasing atmospheric concentration of CO_2 (Le Quéré *et al.*, 2010; Landschützer *et al.*, 2013; IPCC, 2013). Two regions stand out as showing a decreasing linear trend in pCO_2, the Labrador Sea and the southern North Sea. The Labrador Sea has been an interesting area in terms of phytoplankton abundance, with strong increases in abundance seen in this region (figure 6.20) (see chapter 3 sections 3.4.1 and 3.4.2). These areas show the strongest decrease in the FCO_2 (increasing sink regions) due to the decreasing pCO_2 (figure 6.17).

The linear trends in coccolithophore abundance from 1998-2011 show a striking increase in abundance across most of the North Atlantic and North Sea (figure 6.20d). This has also been shown by McQuatters-Gollop *et al.* (2010) since the mid 1990s to 2007 in the northeast Atlantic. The increasing SST in the northern latitudes ($> 55°$N) could be part-explanation for this increase, because as SST increases, stratification is likely to increase, therefore reducing the flux of nutrients from below the thermocline into the mixed layer and favouring smaller species, such as *Emiliania huxleyi*, to out-compete some of the larger (more nutrient dependent) phytoplankton species (Raitsos *et al.*, 2006). This trend of increasing coccolithophore abundance could therefore be linked to the longterm (from 1960 to 2012) trend of increasing SST in the North Atlantic (shown in chapter 3 figure 3.5). However, during the period used for this analysis (1998 to 2011) there was not a clear trend in SST and SSTs were not increasing throughout the whole North Atlantic (figure 6.18). The increase in coccolithophore abundance could also be contributing to the increased concentration of pCO_2 seen in figure 6.16 due to calcification (Robertson *et al.*, 1993; Shutler *et al.*, 2013). Shutler *et al.* (2013) used SeaWiFS data to estimate the abundance of coccolithophores within the North Atlantic from 1998 to 2007, and how this might be contributing to an increasing trend of pCO_2 concentration in this region. It was estimated that blooms could reduce the air-sea sink of CO_2 by 3 to 28%. We have analysed the relationships

between PIC from satellite data (Gordon *et al.*, 2001; Balch, 2005) and coccolithophore abundance for each region but found no significant correlations between high abundance years and PIC (see figure D.6 in appendix D). Feng *et al.* (2009) used shipboard culture experiments to demonstrate that during increased SST and pCO_2 concentrations, coccolithophore abundance increased but calcification decreased, suggesting that continued increases in SST and pCO_2 could reduce the calcium carbonate export relative to particulate organic carbon (POC). It is evident that the influences of calcifying plankton should be included in regional models to evaluate CO_2 variability, such as the inclusion of coccolithophores as a phytoplankton functional type in the PlankTOM10 ocean biogeochemistry model (Le Quéré *et al.*, 2005; Buitenhuis *et al.*, 2013). However these interactions are yet to be fully understood and therefore quantified, as many of these studies are still in their infancy (Riebesell *et al.*, 2009). It should also be noted that the export of carbon is likely to increase with this increasing trend of coccolithophore abundance, due to the "ballast effect", which is the link between fluxes of biominerals (opal and calcite) and POC (Armstrong *et al.*, 2002; Sanders *et al.*, 2010). This would mean that net sequestration of carbon is increased due to the increased calcite production. However, the increased dissolution of calcite with the continued (see Introduction chapter, figure 1.4) and predicted changes in pH, are likely to reduce the flux associated with ballast in the future (Riebesell *et al.*, 2009; Sanders *et al.*, 2010).

Although most of the North Atlantic shows a linearly increasing pCO_2 sink from 1998 to 2011, there is a band across the North Atlantic between 40°N and 50°N that suggests a decreasing/no significant change in the air-sea pCO_2 sink (figure 6.17). This trend agrees with the observations collected within this region as seen in figure 6.6. It is possible that the regional divide seen in figure 6.17 is caused by changes in circulation within this area, which could be linked to the NAO. Schuster *et al.* (2009b) describe the regional tripole in the NAO influence as a negative NAO phase causing increased SST in the northern latitudes, no-change or cooling in the mid-latitudes and warming in the lower latitudes. As discussed in sections 6.3.4.1 and 6.3.4.2 in the mid-latitudes, SST correlates with the NAO,

and therefore the NAO is influencing the inter-annual FCO_2. Whether the sink is ultimately driven by the NAO influencing the heat flux (Follows and Williams, 2004), which in turn could be influenced by alternative climate indices such as the ENSO and AMO (Shutler *et al.*, 2013; Sun *et al.*, 2015), these complex interactions are difficult to quantify and these relationships remain difficult to define.

6.5 Summary

Seasonally in regions 1 to 3, phytoplankton abundance plays an important role in air-sea CO_2 flux, but further south-westward across the North Atlantic in region 5, SST drives the seasonal air-sea CO_2 flux. On inter-annual time scales NAO influences SST which in turn influences the air-sea CO_2 flux. It is also possible that increasing coccolithophore abundance across the North Atlantic is increasing the concentration of pCO_2 due to calcification, which could have a negative feedback on the North Atlantic CO_2 sink. With global biogeochemical models predicting that continued warming will reduce the solubility and therefore carbon flux, particularly in the North Atlantic (Le Quéré *et al.*, 2010), the added implications of increasing coccolithophore abundance in these regions needs to be fully understood and included in such models. The use of VOS provides an ideal platform for combined observations of phytoplankton abundance and carbon flux. With continued development of sensors and financial support to maintain routes, it is likely that some of the long-term trends and key drivers of this variability will become apparent.

Chapter 7

Synthesis

7.1 Summary of key results

This study is the first to combine biological abundance indices from the CPR with pCO_2 measurements collected on-board the same VOS. Combining these datasets with measurements of DIC and oxygen concentration revealed that there are strong biological controls on the marine carbonate system in the North Atlantic on seasonal time scales. A simple and cost-effective method of estimating net community production from underway measurements of O_2 has been validated, and used to demonstrate that autotrophy dominates the North Atlantic, indicating that biological drawdown of carbon is important throughout the region. The suggestions of a decreased buffering capacity due to increased CO_2 concentrations made by Sabine *et al.* (2004), have been supported using discrete measurements of DIC and pCO_2 along a $\sim$7,400 km east-to-west transect. The inter-annual variability and decadal trends in the datasets are linked with the NAO, suggesting that the

environmental changes due to alterations in the NAO in turn influence CO_2 concentrations and phytoplankton abundance and distribution. This work confirms that climate modes drive inter-annual variability, and caution should be exercised when attributing any long-term trends to datasets of less than 10 years (McKinley *et al.*, 2011). It also agrees with estimates of regional biological and temperature control on pCO_2 suggested by Takahashi and Sutherland (2002). Results presented in this thesis demonstrate that phytoplankton photosynthetic activity plays an important role in the seasonal cycle of pCO_2 in temperate northeast Atlantic regions, and that SST drives the pCO_2 seasonal cycle in subtropical regions. The key findings of this research are listed below in bold under the headings of the initial objectives outlined in section 1.6:

1. Evaluate the regional and temporal variability in phytoplankton taxonomic group abundance and distribution within the North Atlantic over the past $\sim$50 years.

    - **SST increased from 1960 to 2012, linked to AMO and NAO**

      SST from 1960 to 2012 showed an increasing linear trend across the North Atlantic. The first and second principal components of SST in the North Atlantic were significantly correlated with the AMO and NAO respectively (figure 3.14), with the second principal component eigenvectors displaying a regional dipole that is characteristic of the NAO influence (figure 3.12). This supports findings from Harris *et al.* (2013) and Edwards *et al.* (2013) who found that the AMO is the underlying mechanism behind a number of biological trends in the North Atlantic, with correlations with the first and second principal component of SST respectively. The regional variation in climate mode influences on SST and wind speed likely drive the variability seen in phytoplankton distribution and abundance.

    - **Increase in PCI in the northeast Atlantic but no increase in individual phytoplankton indices**

      PCI showed an increasing linear trend across the North Atlantic from 1960-2012 (figure 3.6). However in the northeast Atlantic there was

not an evident increase in any of the other phytoplankton indices, suggesting that smaller phytoplankton species (that are represented in the PCI but not counted in the other phytoplankton indices) are increasingly dominating this region. The increasing PCI in the northeast Atlantic was significantly positively correlated with SST. This supports modelled predictions of increased stratification from global warming reducing the upward flux of nutrients, and therefore allowing smaller phytoplankton to out-compete some of the larger (more nutrient dependent) species such as diatoms (Bopp *et al.*, 2005). This may have negative implications for both the flux of carbon due to reduced export efficiencies, and the complexity of food webs which can impact on fisheries (Beaugrand *et al.*, 2010).

- **Increased abundance of phytoplankton at the Grand Banks of Newfoundland driven by increased wind speeds**

  All four phytoplankton indices showed a significant increase in abundance after the 1980's at the Grand Banks of Newfoundland (figure 3.36). This increase was significantly correlated with wind speed, indicating that nutrient transport into the photic zone by increased surface winds may have lead to the increased phytoplankton abundance.

- **Diatom abundance has increased relative to dinoflagellate abundance in the northeast Atlantic. This trend follows the SST trend**

  SST preceded and had a significant positive correlation with the ratio of diatom to dinoflagellate abundance from 1960 to 2012 in the northeast Atlantic (figure 3.41). The increasing SST trend in this region was correlated with both the AMO and NAO, confirming that climate modes play an important role in driving the phytoplankton trends.

2. Quantify the plankton net community production (NCP) of temperate to subtropical regions within the North Atlantic.

   - **A simple and cost-effective method to derive NCP was developed**

     Using calibrated *in situ* measurements of oxygen concentration from

the underway system of a VOS, monthly NCP was derived from December 2011 to March 2013 (figure 4.4). These calculations were based on mass balance equations (Emerson, 1987) in which the abiotic influences on oxygen concentration are subtracted from the mass balance change in oxygen concentration between time-steps. The method was validated by comparison with NCP estimates from discrete DIC measurements (figure 4.5), and previous studies which have estimated NCP using oxygen mass balance in the North Atlantic (figure 4.7). No significant difference in NCP estimates between Longhurst provinces (Longhurst, 2006) was found.

- **Autotrophy dominates the North Atlantic**

  All five biogeochemical regions were net autotrophic, with no significant difference in annual NCP across a range of 35°of latitude (figure 4.7).

- **The number of provinces where NCP estimates are derived from *in situ* observations was doubled**

  In previous studies, NCP had been derived using oxygen budgets within 3 Longhurst (2006) provinces of the North Atlantic. Our estimates overlapped 5 different Longhurst (2006) provinces (figure 4.7). The differing results in the latitudinal variation of NCP derived from global circulation models and some satellite derived models (Emerson, 2014) compared to the reduced latitudinal variation in NCP derived from *in situ* measurements, highlight the need for improved global coverage of data and an improved mechanistic understanding of why the approaches differ (Williams *et al.*, 2013). The method developed here is ideally suited to provide the required global coverage of *in situ* NCP estimates.

3. Determine the total alkalinity to salinity relationship in the North Atlantic.

   - **Relationship between total alkalinity and salinity was derived and used to estimate DIC over a >10 year time period**

Using discrete measurements of TA collected across the North Atlantic during four seasons between 2011 and 2013, the relationship between TA and salinity was determined (figure 5.17). The linear regression between these two measurements agreed well with published studies, and confirmed that alkalinity is conservative with salinity in the North Atlantic (figure 5.33). This allowed for the calculation of DIC (with a RMSE of ± 30.3 μmol kg^{-1}) using calculated TA and measured pCO_2 from 2002 to 2013 (figure 5.34).

4. Examine seasonal carbonate measurements to investigate biogeochemical processes that may be occurring in the North Atlantic.

   - **Dinoflagellate and coccolithophore abundance were significantly negatively correlated to the seasonal decrease in nDIC in the northeast Atlantic**

     All six phytoplankton indices were negatively correlated with salinity normalised DIC (nDIC) concentration in the northeast Atlantic. However only the correlations with dinoflagellate and coccolithophore abundance were significant ($p < 0.05$, figure 5.35). Significant trends between phytoplankton abundance and nDIC were only present in region 1 (northeast Atlantic), suggesting that the carbonate system is driven primarily by biology in this region, whereas the other regions are primarily driven by abiotic influences (mostly SST). This is consistent with the study of Takahashi *et al.* (1993) who suggested that the carbon cycle is driven by biology during the productive months in the subpolar/temperate regions of the North Atlantic, and that within lower latitudes the carbon cycle is primarily driven by temperature.

   - **The Revelle factor within the North Atlantic has increased, indicating that the buffering capacity has declined due to increased CO_2**

     Regions 1 and 2 had a Revelle factor of 15 ± 0.8 and 11 ± 0.9 respectively (figure 5.16). These values are higher than those derived in Takahashi *et al.* (1993) and Sabine *et al.* (2004) for the years 1993

and 1994, with region 1 presenting the larger increase. This suggests that the buffering capacity of regions 1 and 2 has decreased in the last 20 years, which is likely due to the increased uptake of CO_2, and therefore changes in speciation of the carbonate system within these regions (Riebesell *et al.*, 2009).

5. Investigate the flux of carbon dioxide in the northeast Atlantic in relation to phytoplankton distribution and abundance on seasonal, inter-annual and decadal time scales.

   - **At seasonal time scales phytoplankton play an important role in the drawdown of CO_2 in the northeast Atlantic**

     At province-sized spatial scales the seasonal maxima of the phytoplankton indices correspond to the seasonal minima in pCO_2 and DIC and increased air-sea uptake of CO_2 (figures 6.5 and 6.6). This corroborates the suggestion that photosynthesis drives the seasonal drawdown of sea surface CO_2 in this region (Takahashi *et al.*, 1993; Takahashi and Sutherland, 2002).

   - **At inter-annual time scales the NAO drives the environmental conditions which drives the CO_2 year-to-year variability**

     Significant correlations with no time-lag were found between the NAO and both SST and the FCO_2 (figure 6.14). This agrees with measurements taken at the BATS station (Gruber *et al.*, 2002). The correlations between positive NAO indices and a decreased CO_2 sink suggests that more negative NAO periods will increase the CO_2 sink in the northeast Atlantic.

   - **Increasing coccolithophore abundance could be adding to the CO_2 concentrations in the surface waters of the northeast Atlantic**

     In the NASE province there was a significant positive correlation between average annual coccolithophore abundance and pCO_2. This could be linked to the production of calcite which also produces CO_2. This region also had its highest average annual abundance of coccolithophores

in 2007 when the annual CO_2 sink was -0.37 mol C m^{-2} yr^{-1}, which was the smallest sink recorded for this region between 2002 and 2013. In the NECS and NASW province a similar trend is seen between high annual coccolithophore abundance and a weaker annual CO_2 sink (figure 6.11).

7.2 Limitations

Whilst this work has demonstrated a number of important relationships between biological indices and carbonate data, as with any study, there are limitations and uncertainties that must be recognised.

There are a number of limitations associated with using CPR data, mainly that it under-represents many of the smaller phytoplankton species and therefore must be considered a semi-quantitative sampling method. There are also implications associated with only sampling surface waters. This has been highlighted by Kemp *et al.* (2006) who suggest that using satellite observations to derive productivity estimates is inadequate, due to the inability to detect plankton biomass at depth. Kemp *et al.* (2006) suggest that the large algal mats formed at depth by some *Rhizosolenia* spp. may have important implications for carbon export and ocean biogeochemical models. These algal mats are often associated with oceanic frontal zones, such as the Azores Front (Kemp *et al.*, 2006). The Deep Chlorophyll Maximum (DCM) is not represented using satellite imagery, and may not be adequately represented in the CPR dataset, depending on the depth of the mixing created by the VOS wash (Hunt, 1968). The use of surface measurements from the underway pumped seawater system lacks measurements at depths greater than $\sim$ 5 to 7 m. This limitation represents the trade-off between data coverage and efficiency and the cost of obtaining such measurements. There is therefore a need to combine scientific datasets into comprehensible formats in which depth profiles along with surface measurements can be utilised. The importance of well-maintained time-series stations, and profiling floats, alongside the continued effort to enhance and increase VOS coverage and capabilities is evident, and will help to resolve and quantify the role the DCM plays in carbon export.

McKinley *et al.* (2011) call attention to the importance of time scale when investigating trends. McKinley *et al.* (2011) found that when surface water trends in CO_2 in the North Atlantic were analysed over a 25 year period, there was no significant difference from the atmospheric trend in CO_2. However, when analysing data from a 10 year period and with differing start and end years, significant trends were found, reflecting the inter-annual and decadal variability which are likely influenced by climate modes (McKinley *et al.*, 2011). This is evident when comparing results from chapters within this thesis. For example chapter 3 uses CPR data over a $\sim$50 year period to investigate changes in phytoplankton abundance and distribution in the North Atlantic, while chapter 6 compares the last $\sim$10 years of this data with CO_2 measurements. Between 1998 and 2011 both diatom and dinoflagellates showed a general increase in abundance across the North Atlantic, while between 1960 and 2012 both diatom and dinoflagellate abundance had increased around the Grand Banks of Newfoundland, but had decreased across most other regions within the North Atlantic. These two analyses of different time frames demonstrate the different regional shifts in phytoplankton abundance between the two periods, and the importance of caution when attributing any long-term trends. Using pCO_2 measurements from the North Atlantic McKinley *et al.* (2011) suggest that > 25 years of data are needed in order to determine any long-term trends. Because of the large interannual and decadal variability associated with phytoplankton productivity (Barton *et al.*, 2015), Henson *et al.* (2010) suggest a time series of ~ 40 years is required in order to attribute a long-term trend to global warming. In order to be confident of trends in the carbon variability of the North Atlantic long-term datasets are clearly needed, and therefore the continued effort to measure pCO_2 and other associated variables is vital.

7.3 Wider implications

Under different future climate scenarios, global mean surface temperatures are likely to rise by between 0.3°C (min. RCP2.6 (RCP = Representative Concentration Pathway)) and 4.8°C (max. RCP8.5) for 2081-2100 relative to 1986-2005 (IPCC, 2013). How the marine carbon cycle will respond to such changes, and the

processes involved in these changes, needs to be understood to enhance climate models and estimates of the future of the oceanic carbon sink.

It has been suggested that increased SST will lead to a decrease in phytoplankton biomass due to increased stratification, which would likely cause a decrease in carbon export in the North Atlantic (Bopp *et al.*, 2005; Beaugrand *et al.*, 2010). Chapter 3 presented data from the northeast Atlantic that showed PCI has increased with increasing SST, while diatoms and dinoflagellates have decreased in abundance from 1960 to 2012. This implies that smaller phytoplankton (picophytoplankton) could be increasing in abundance, as they would cause an increase in "greenness" (= PCI) due to clogging in the CPR samples. This supports the suggestion of a decreased nutrient supply to the surface waters due to increased stratification, enabling smaller phytoplankton to out-compete larger species which have a higher nutrient demand. This is likely to impact species such as diatoms, which generally bloom in turbulent high nutrient conditions. However it was demonstrated in section 3.5.2 that diatoms have increased relative to dinoflagellate abundance with the increasing SST trend in the northeast Atlantic. Kemp *et al.* (2006) demonstrate that there are diatom species that are well adapted to stratified conditions, and suggest that these species may play an important role in carbon export as they dominate the DCM. This could have wider implications for carbon export and biogeochemical models that describe these processes. However further investigation into quantifying the export of different phytoplankton groups and species, and their buoyancy-controlled migrations, is needed in order to determine these implications.

Beaugrand *et al.* (2010) demonstrate that increased temperatures are linked to an increase in biodiversity within the zooplankton and phytoplankton in the northeast Atlantic, which parallels a decrease in the mean size of copepods. This has increased the complexity of food webs, and could have implications for important fisheries within the region, such as the Atlantic cod. The biological carbon pump is expected to have a reduced export under these conditions as phytoplankton and copepod biomass is reduced, but also because more complex food webs would allow carbon to remain in the surface waters for longer periods as it is passed through

the food chain (Edwards and Richardson, 2004). The influence of the increase in PCI and decrease in the larger sized phytoplankton indices from 1960 to 2012 on the flux of CO_2 is not discernible because the CO_2 dataset used within chapter 6 only extends back to 1998. Since consistent measurements of pCO_2 were made on the UK to Caribbean VOS route (from 2002 to 2013), both the PCI and SST have shown no significant decrease or increase within our study region. It is likely that the combination of increased SST and decreased phytoplankton biomass has caused a reduction in carbon export in the northeast Atlantic, but a longer more consistent time-series of sea surface CO_2 measurements would be required to investigate this.

Many studies use a PQ value based on the Redfield ratio (Redfield *et al.*, 1963) or Laws (1991) for new and recycled production of 1.4 or 1.1 respectively, to convert moles of carbon to oxygen. Chapter 4 reported a range of PQ values from 0.78 to 1.4, suggesting that this simplistic conversion method is not sufficient for converting between carbon and oxygen and may introduce large errors. Caution should be taken when making such assumptions and where possible both carbon and oxygen should be measured if the conversion between the two is necessary. The persistent autotrophy demonstrated in the North Atlantic in chapter 4 highlights the need for further investigation into the lack of consistency between *in situ*, *in vitro* and satellite based NCP estimates.

Chapters 5 and 6 alluded to the increasing atmospheric concentration of CO_2 and consequent increase of CO_2 within surface waters, causing a reduction in the buffer capacity, particularly in the northeast Atlantic. This has global socio-economic implications as this negative feedback reduces the ability of this important sink region to take up anthropogenic CO_2 alongside a continued increase in anthropogenic emissions.

The feedback between calcification by coccolithophores in the North Atlantic and the concentration of CO_2 in the surface waters needs to be investigated further. Chapter 6 demonstrated an increasing abundance of coccolithophores across most regions of the North Atlantic which could add to increasing concentrations of CO_2, therefore reducing the air-sea flux. However, the carbon export may be increased

with increasing coccolithophore abundance, due to the "ballast effect", which is the link between fluxes of biominerals (opal and calcite) and POC (Armstrong *et al.*, 2002; Sanders *et al.*, 2010). This would mean that net sequestration of carbon is increased with increasing coccolithophore abundance due to increased calcite production. However, the increased dissolution of calcite with the continued (figure 1.4) and predicted changes in pH, are likely to reduce the flux associated with ballast in the future (Riebesell *et al.*, 2009; Sanders *et al.*, 2010).

The influence of the NAO on the environmental conditions in the North Atlantic is evident from this study, influencing both the flux of CO_2 and phytoplankton biomass. Although NAO indices have generally been more positive than negative since 1980, it is difficult to predict the alternations of the NAO, but our results suggest that more negative NAO periods may increase the sink of CO_2 in the northeast Atlantic.

7.4 Future research

The research presented in this thesis has led to several ideas for continuation of the work that unfortunately, due to time and economic constraints, were not possible. These suggestions are outlined below:

7.4.1 Further data analysis

Chapter 3 presented changes in the abundance and distribution of 4 key phytoplankton indices. With more time the species level and size class interactions within these indices would be investigated. For example there have been suggestions of decreases in individual species in regions of the North Atlantic, such as the dinoflagellate *Ceratium* spp, which may help to describe the decrease in dinoflagellate abundance relative to diatom abundance seen in the northeast Atlantic. The increase in PCI in the northeast Atlantic that was not evident in the other phytoplankton indices suggests an increase in smaller phytoplankton. This could be investigated by re-defining the plankton indices as size class groups rather than grouping by species. In turn the links between predators and their prey species

should be examined, such as the impact on phytoplankton distribution due to thermal range contraction and extension of copepod species, and the implications this may have for carbon export.

The NCP ode (ordinary differential equation solver) model developed in chapter 4 could be developed further and be utilised to investigate global NCP from oxygen observations from sources such as the World Ocean Circulation Experiment (WOCE) (Helm *et al.*, 2011). However, the error associated with measurement accuracies from these observations would need to be determined and may reduce the viability of such NCP estimates. Emerson and Bushinsky (2014) suggest that autonomous oxygen measurement accuracies need to be better than $\pm 3\%$, which is the current expected level of supersaturation due to NCP in the ocean mixed layer. Using levels of photosynthetically active radiation (PAR), plankton respiration (R) could be estimated using the oxygen change during the night time and used to determine net primary production (NPP = NCP + R). These estimates could then be compared with NPP estimates from satellite models such as the VGPM (Behrenfeld and Falkowski, 1997) or CbPM (Westberry *et al.*, 2008). It has been suggested that satellite data underestimate the spring Chl-a concentration and satellite-based models used to estimate productivity may overestimate photoacclimation, reducing the estimates of NPP (Emerson, 2014). Comparing these estimates may help to determine some of the key regions in which satellite productivity estimates differ from *in situ* measurements, and could be investigated further to aid our understanding as to which processes cause these discrepancies.

In chapter 5 a decrease in the buffer capacity of the northeast Atlantic was shown in comparison to Revelle factor estimates made from measurements 20 years prior (Takahashi *et al.*, 1993; Sabine *et al.*, 2004). In order to confirm that this decrease in the buffer capacity is due to climate change and not due to interannual variability or differences in the methodology used, data from sources such as GLODAP (**GL**obal **O**cean **D**ata **A**nalysis **P**roject (Key *et al.*, 2004)), of which an updated release is imminent) can be analysed. Using these datasets, process-models can be used to attribute the potential role of climate change, and to give a signal of how long the measurements need to be collected for in order to detect

long-term trends.

By defining the TA to salinity relationship in chapter 5, DIC could be estimated from calculated TA and measured pCO_2 using CO2SYS. This gave measurements of DIC dating back to 2002. Using a similar method of determining NCP from DIC measurements as in section 4.3.8 in chapter 4, the summertime NCP could be determined for the last 10 years of pCO_2 and salinity measurements. This NCP estimate would include a large error associated with the calculation of DIC ($\pm$30.3 μmol kg^{-1}) from calculated TA ($\pm$36.33 μmol kg^{-1}). However, it could be compared with summertime NCP estimates using the nutrient concentrations (which would have a smaller error associated with measurement uncertainty) that also date back from 2002 (calculated DIC and nutrient concentrations from 2002 to 2013 are displayed in figure C.1 in appendix C). These two independent estimates of summer NCP from calculated DIC and nutrient concentrations could be compared, and may provide useful insight into the inter-annual variability in the carbon flux due to biological drawdown.

Calculated DIC was compared with pCO_2 measurements from the *MV Benguela Stream* and satellite estimates of PIC (Particulate Inorganic Carbon) (Gordon *et al.*, 2001; Balch, 2005) and POC (Particulate Organic Carbon) (Stramski *et al.*, 2007) using the regions defined in chapter 5 section 5.2 (see appendix C for results). The regional variation between these correlations demonstrates the difficulty of using satellite estimates to derive carbonate parameters, and the biological influence on these parameters. Further investigation into the relationships between satellite estimates of carbonate parameters and *in situ* measurements is required to infer possible relationships and develop algorithms that can enhance satellite estimates further.

Further decomposition of the ΔpCO_2 from 2002 to 2013 may be possible using the calculated DIC and TA estimates from chapter 5. McKinley *et al.* (2011) calculated the annual linear trends of pCO_2 - nDIC (salinity normalised DIC) and pCO_2 - nTA (salinity normalised TA) between Iceland and Newfoundland from 1993 to 2005, to demonstrate that increasing salinity and decreasing nTA had contributed to an increase in pCO_2 in this region. Using a similar model to the NCP

ode model described in chapter 4 and calculated DIC and TA from chapter 5, the different components of ΔpCO_2 may be able to be inferred. These calculations would be similar to those described in Jiang *et al.* (2013) and Shadwick *et al.* (2015), whereby the difference between the observed pCO_2 concentrations and those modified by changes in DIC and temperature are calculated. This may help to disentangle the physical, biological, and chemical constituents of the carbon variability seen in the North Atlantic.

In chapter 6 the inter-annual variability of the air-sea flux of CO_2 (FCO_2) was found to be driven by inter-annual variability in SST which had significant correlations with the NAO. This relationship warrants further investigation into the regional influence of the NAO on air-sea heat flux in the North Atlantic (Marshall *et al.*, 2001), and how this influences the inter-annual variability of FCO_2 (Follows and Williams, 2004).

7.4.2 Improved measurements

An extension to the set-up measuring oxygen concentration on board the *MV Benguela Stream* would be to develop a method to correct the optode drift using atmospheric measurements of pO_2, as described in Emerson and Bushinsky (2014) and Bittig and Körtzinger (2015). Once validated, this set-up could be employed on all routes measuring underway O_2, allowing for a far greater coverage of accurate O_2 surface concentration measurements, which could be used to estimate NCP.

A flow cytometer could be added to the underway pumped seawater set-up described in section 2.5 on board the *MV Benguela Stream*. This would allow for determination of the fluorescence and size fraction of the plankton within the surface waters, which would validate the CPR results and provide further detail of the biological influence on pCO_2 variability. Palevsky *et al.* (2013) used a similar set-up to that on board the *MV Benguela Stream* and presented NCP estimates alongside CO_2 flux measurements and flow cytometry estimates of plankton groups, to indicate that the smaller size fractions of phytoplankton dominated the system when high levels of autotrophy were recorded in the Gulf of Alaska. However the viability of installing a flow cytometer on the *MV Benguela Stream* is dependent on its

autonomous capabilities. Currently this is limited, as the flow cytometer requires more frequent maintenance (every few days) than the monthly servicing that sustains the measurements of pCO_2 on board this VOS.

A valuable extension to the measurements on board the *MV Benguela Stream* would be the addition of a pH sensor. This would enable the calculation of the remaining carbonate components using pCO_2 and pH, and would aid the documentation of future changes in the carbonate chemistry. Takahashi and Sutherland (2013) describe the global deficit of reliable pH measurements due to calibration issues associated with pH sensors. If a viable automated pH sensor becomes available to the scientific community, this could also be housed within the CPR, which has the potential to provide a large network of *in situ* pH measurements globally.

7.4.3 Global extension of measurements

The areas of the world's oceans that are strong sinks for carbon dioxide, and the regions where sea surface CO_2 measurements have been made are given in figures 1.9 and 1.7. The North Atlantic and North Pacific are relatively well sampled, and represent strong sink areas. I would recommend continuing CO_2 measurements in these areas, and extending measurement networks into those areas that are undersampled (such as the Southern Ocean). This thesis demonstrates the importance of the combination of chemical measurements with biological parameters for understanding the biogeochemical processes that maintain these sink regions, and how they vary inter-annually. The North Pacific is an important carbon sink region that has regular measurements of CO_2 (figures 1.9 and 1.7). Figure 7.1 shows all the VOS routes that tow CPRs under the Global Alliance of CPR Surveys (GACS) initiative. The CPR route from Japan to Vancouver is important in understanding subpolar biological shifts, and it should be extended further south to incorporate this carbon sink region (seen in figure 1.9). As ocean warming continues, it is expected that there will be further poleward shifts of many marine species, such as the range contractions of the copepod *Calanus finmarchicus* (Hinder *et al.*, 2014), which is an important food source for fish. These biological shifts need to be consistently monitored, and enhancing and extending the CPR networks provides a

robust and cost-effective tool to do so.

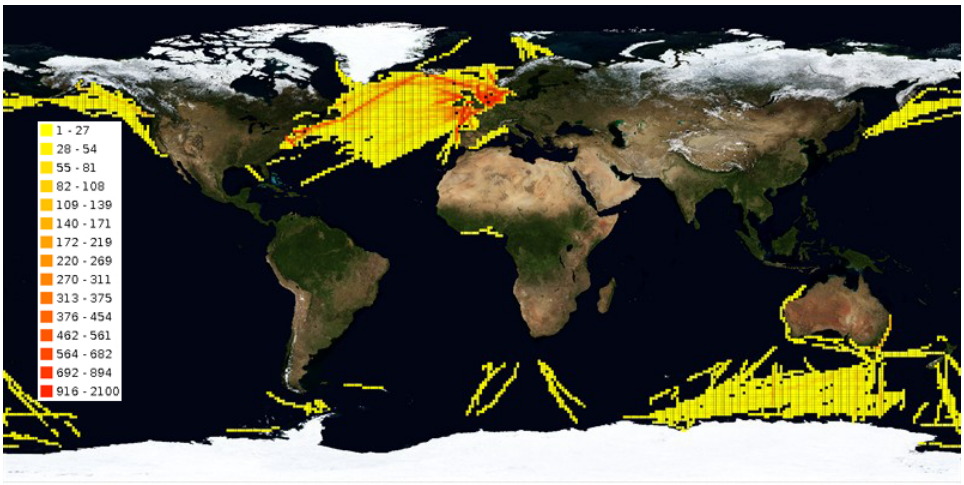

Figure 7.1: Global map of the density of CPR samples per 1 degree area. Adapted from http://www.globalcpr.org/maps/sample-density.aspx.

A recent scientific action plan has been implemented to increase measurements within the Southern Ocean (Southern Ocean Carbon and Climate Observations and Modelling (SOCCOM)) (Russell *et al.*, 2014). The action plan includes the release of nearly 200 Argo profiling floats, with many housing optodes to measure oxygen concentration. Using the method of calibrating these optodes to atmospheric oxygen concentration outlined by Emerson and Bushinsky (2014), would allow for the calculation of NCP. Presently, without correction these floats equipped with optodes are accurate to $\pm 3\%$ (Takeshita *et al.*, 2013), which is equivalent to the amount of supersaturation expected due to NCP (Emerson and Bushinsky, 2014). Correcting these optodes for drift would greatly enhance the understanding of biologically driven carbon drawdown and export in this region, and should be given special attention within this programme.

With continued warming tropical regions are likely to become more oxygen deplete (particularly within the thermocline) as solubility decreases and deep-water ventilation is reduced due to stratification (Doney, 2010). This could be the case for the Indian Ocean, where human impacts on the ecosystem are evident and are becoming of increasing concern (Ramanathan *et al.*, 2007). The second international Indian Ocean expedition (IIOE-2) aims to increase measurements within this region to evaluate such changes, and the impacts on the environment (Hood *et al.*, 2015). Using the model described in chapter 4 and a range of measurement

techniques such as gliders, profiling floats, and mooring sites (these have been suggested by the IIOE-2 science plan (Hood *et al.*, 2015)), the NCP could be estimated in the surface layer, together with the determination of any change in the volume of the oxygen minimum zones at depth. NCP and dissolved oxygen concentration could be monitored alongside phytoplankton indices, nutrient concentrations and other biological indices in order to monitor any changes in the health of the ecosystem, such as issues that arise from eutrophication (Naim, 1993). It is important that alongside individual measurement campaigns, long-term observational platforms are implemented and sustained to provide the long-term insight that is needed to infer any trends (McKinley *et al.*, 2011).

This thesis has demonstrated the importance of concurrent measurements of carbonate chemistry and plankton community structure, in order to infer interactions between the two. This would not be possible without the continued efforts to develop and maintain long term observations such as the VOS networks that tow CPRs and take underway measurements. Combining such measurements with depth profiles from profiling floats and sampling buoys, and global satellite observations, will help to reduce the discrepancies between *in situ* measurements and global scale models. One example is the difference between NCP derived from dissolved oxygen measurements, and NCP derived from satellite-based and global circulation models. The improved understanding and reduction in these discrepancies will enable the development of productivity algorithms and continue the enhancement of biogeochemical models that will aid prediction of future climate scenarios.

7.5 Conclusion

This study has successfully developed and implemented a simple and relatively inexpensive technique that enables *in situ* estimation of NCP in the surface ocean, with the potential to extend coverage of such measurements over wider regions at low cost. Through using VOSs as platforms for these sensors it is possible to monitor regions at ocean basin and gyre scale at relatively high temporal resolution without incurring the costs associated with conducting such studies using

dedicated research vessels. This study gives an excellent example of the potential of such systems for monitoring and improving our understanding of changes in biogeochemical processes and carbonate chemistry in the surface ocean. Once autonomous calibration and quality control protocols have been developed for the relevant optodes, such systems could help contribute to an enhanced global coverage of *in situ* NCP measurements and help us better understand the influence of climate change on the Worlds oceans. The current study has shown that the North Atlantic remained a significant sink of carbon dioxide between 2002 and 2013, despite strong inter-annual variability in CO_2 flux. The seasonal cycle in carbon drawdown was divided by region, with CO_2 flux in the northeast Atlantic being driven by the seasonal signal of phytoplankton production while SST drove the seasonal signal in CO_2 flux at lower latitudes in the subtropics. Meanwhile, the inter-annual variability in CO_2 flux was correlated to changes in the NAO and the influence that this had on SST.

Two key results were derived using data from the northeast Atlantic. Firstly, the increase in SST was significantly correlated with the increase in phytoplankton colour index measured by the CPR between 1960 and 2012, despite other phytoplankton indices decreasing over this time frame. This suggests that as the surface ocean warms and stratification is enhanced, smaller phytoplankton may be better equipped to dominate the system, compared with larger species that are more nutrient dependent. Secondly, the buffer capacity of the northeast Atlantic region has decreased compared to measurements from the 1990s. Combined, these two observations are likely to have significant effects on carbon flux, export efficiency and ecosystem dynamics. Whether or not these relatively localised trends will influence an ecosystem shift and affect the carbon sink at the North Atlantic basin scale, requires a longer and more consistent time series of measurements. Implementing the methods developed in this study to monitor the effects of climate change on the surface ocean would be a step towards this requirement.

Appendix A

APPENDIX: Variability in phytoplankton distribution and abundance in the North Atlantic from 1958 to 2012

A.1 Comparison of interpolation techniques

Figure A.1 shows the $\log_{10}$ of the total number of PCI samples collected using the CPR within each $1^{\circ} \times 1^{\circ}$grid cell from 1958 to 2012. The seas surrounding the United Kingdom (North Sea, Irish Sea and Bay of Biscay) have the greatest number of samples, with the western Atlantic showing fewer observations.

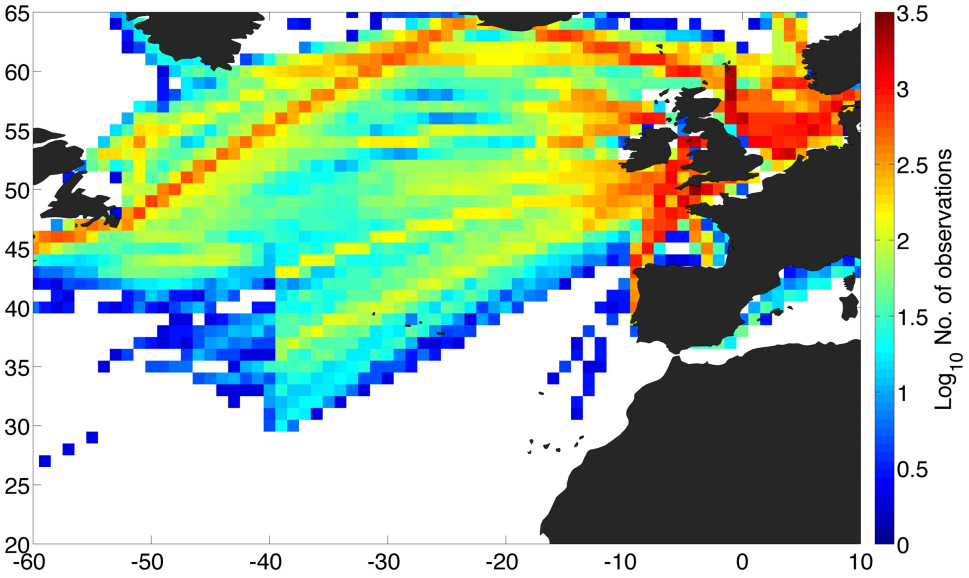

Figure A.1: Log_{10} total number of raw CPR samples taken within each $1° \times 1°$grid cell from 1958 to 2012.

Figure A.2 shows the CPR data after it has been gridded on to a $1° \times 1°$grid by taking the monthly mean for each grid point and then plotting the mean for each decade.

NOTE: Both silicoflagellate and coccolithophore abundance counts were started in 1993, before this only "presence" values were recorded.

Due to the reliance on voluntary sampling routes to collect CPR data there are often gaps in the dataset. There are a number of different interpolation techniques that can be used to fill these gaps, of which just a few are trialled in the following figures.

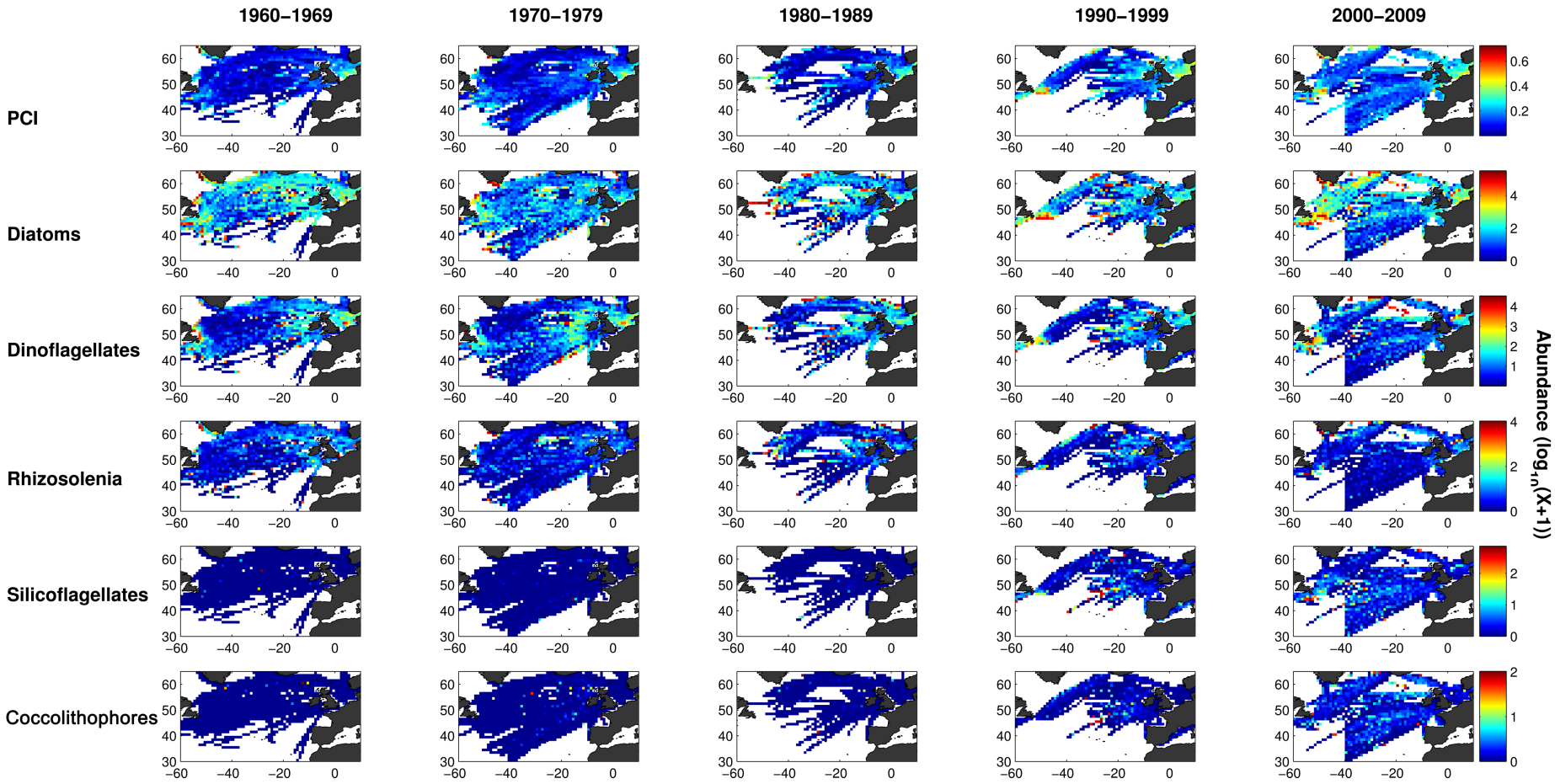

Figure A.2: Decadal abundance of phytoplankton groups in the North Atlantic, calculated using the mean monthly mean for each grid cell.

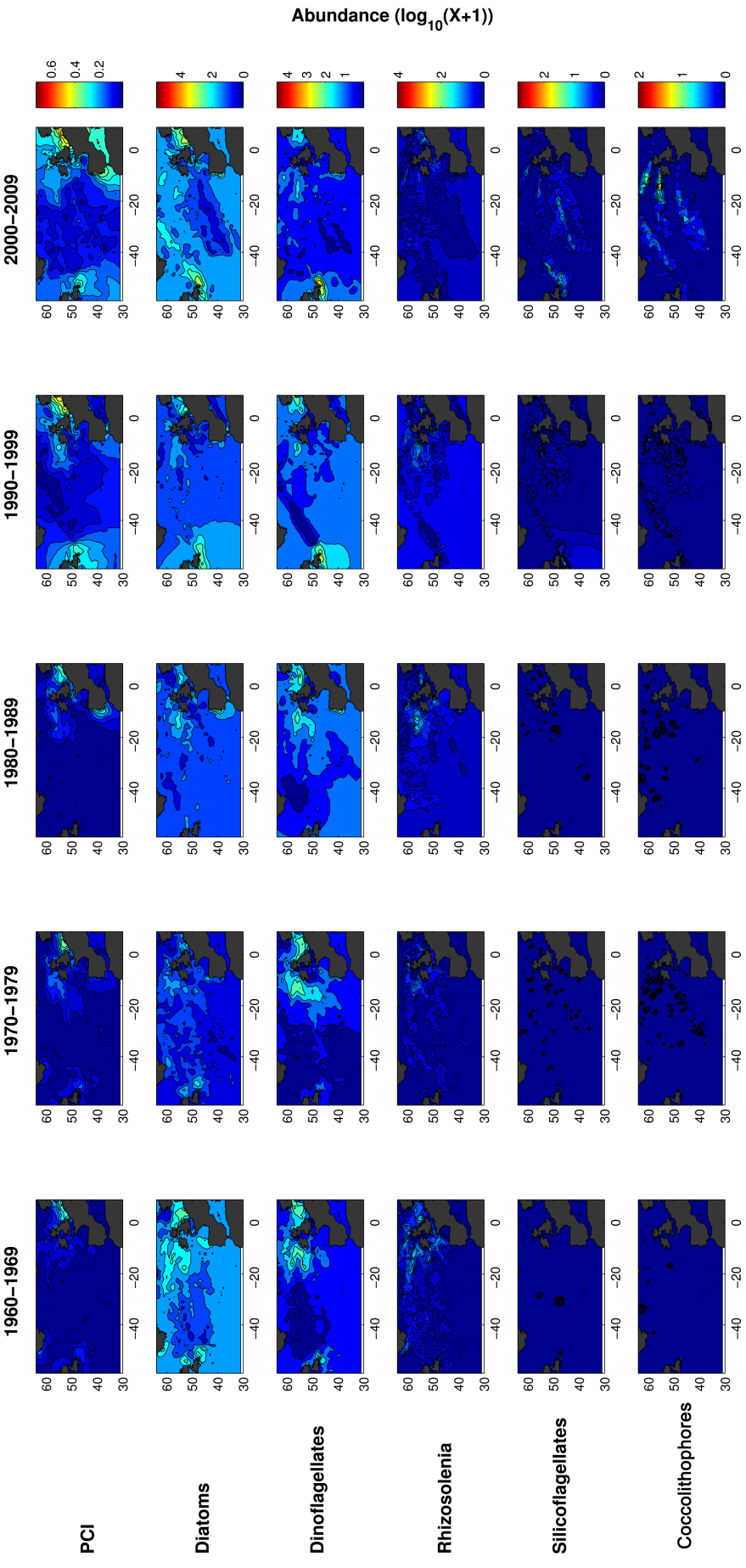

Figure A.3: Decadal abundance of phytoplankton groups in the North Atlantic, calculated using kriging interpolation.

The ordinary kriging methodology used in figure A.3 follows Chapter 2 in Edwards (2000). The following decadal maps (see figures A.4 and A.5) also used the same procedure for arranging the dataset but use different interpolation techniques. The interpolation techniques are employed to map the data onto a finer scale than the scale at which the samples were collected, the following decadal maps were interpolated on to a grid resolution of $0.5^\circ \times 0.5^\circ$.

To produce these decadal spatio-temporal maps the monthly data were separated into 5 year periods, and 12 monthly averaged maps were produced for each five year period using one of the interpolation techniques. 12 monthly decadal maps were produced by taking the same month from two of the five year periods within the decade, and applying the interpolation technique to each individual grid cell. These 12 monthly decadal maps were then combined to form one decadal map by averaging each grid cell.

The kriging procedure uses variograms to produce estimates of the spatial structure of the data. Firstly an experimental variogram is produced from the data, and then a theoretical variogram is produced by applying the appropriate model based on the experimental variogram. Throughout this analysis the experimental variograms were fitted with a spherical model, and the estimates of the theoretical variogram range, sill, and nugget were produced using the Matlab package variogramfit.m written by Schwanghart (2010).

Objective mapping is similar to kriging but it assumes that we know the mean drift of the trend and uses a covariance matrix where larger weights are assigned to points that are nearby and covary positively with the estimated values (Glover *et al.*, 2005). A weighted mean method is also applied in figure A.4 which uses inverse distance weighting to calculate the unknown values using the weighted average of the known values (Beaugrand *et al.*, 2001).

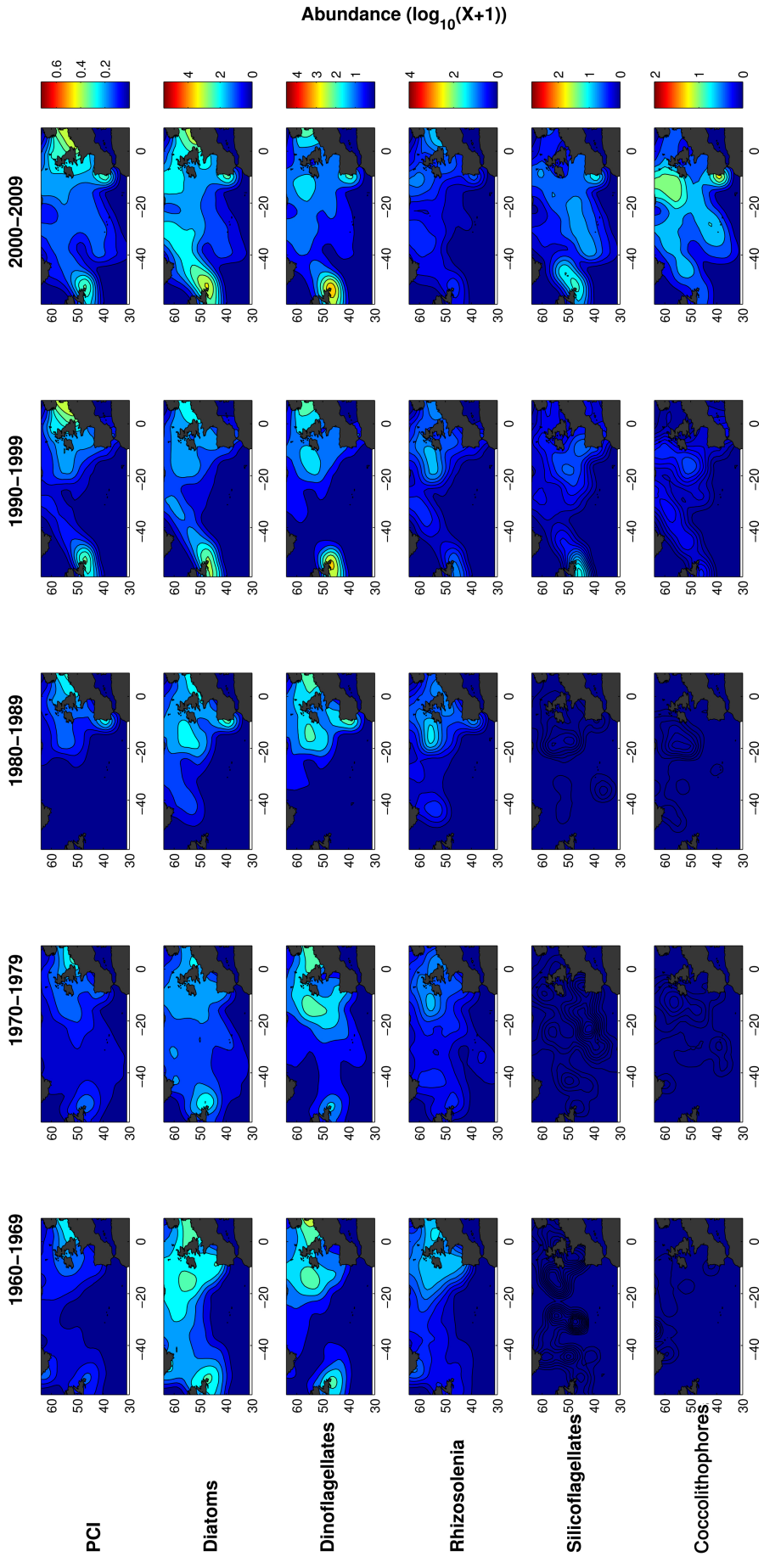

Figure A.4: Decadal abundance of phytoplankton groups in the North Atlantic, calculated using weighted mean interpolation.

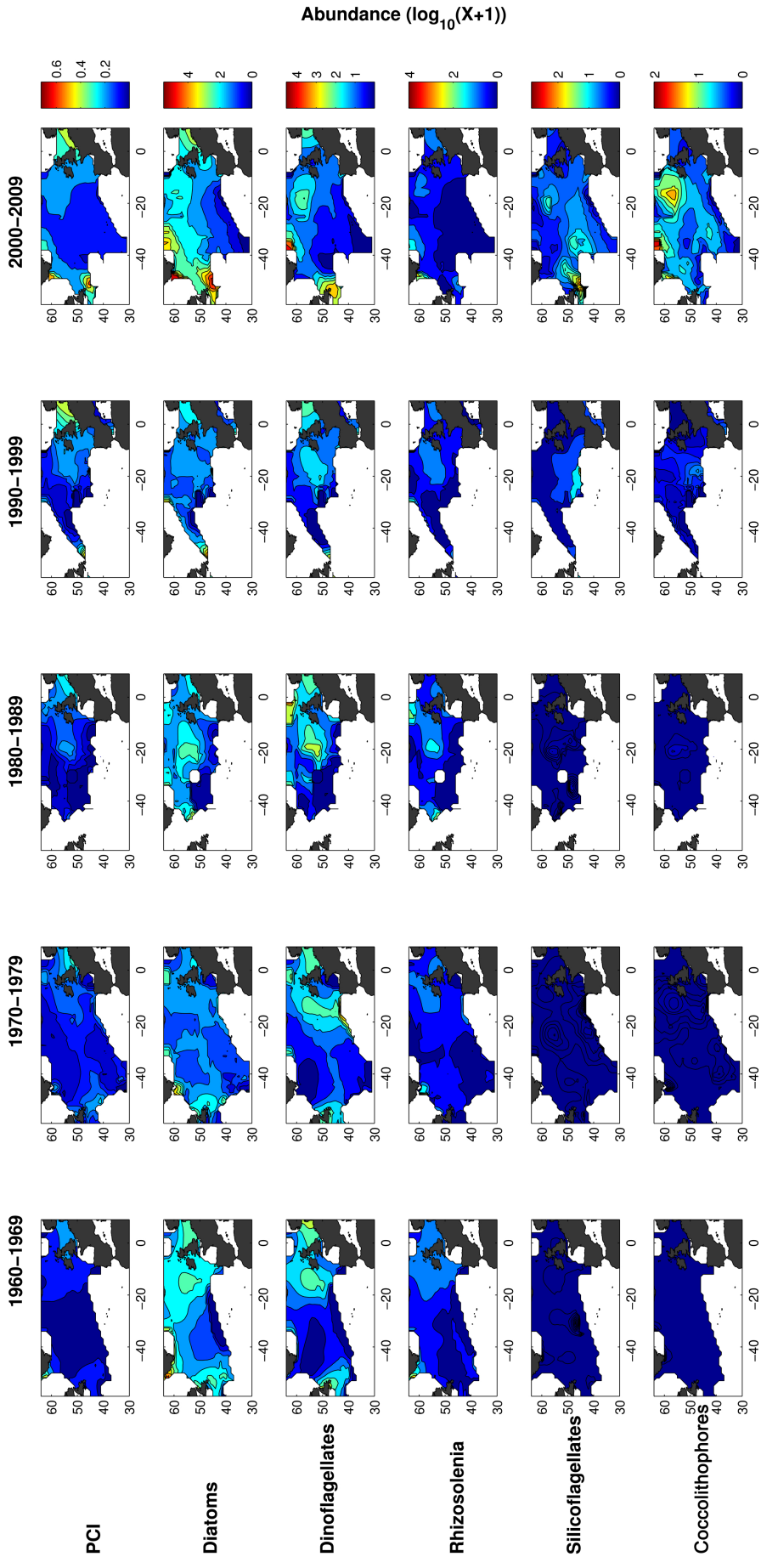

Figure A.5: Decadal abundance of phytoplankton groups in the North Atlantic, calculated using an objective mapping method.

The variance within the kriging method was high, which meant that the interpolation appeared very noisy. The weighted mean interpolation matches the gridded mean monthly data well, however it interpolates across a large area. The objective mapping method is similar to a weighted mean except that it takes into account the covariance matrix and how many points are near to the estimated value, and therefore gives better estimates and doesn't interpolate across regions where no samples have been recorded.

The model applied to the objective mapping and weighted mean method to construct figures A.5 and A.4 was spherical with an influence and cut off radius of 3.

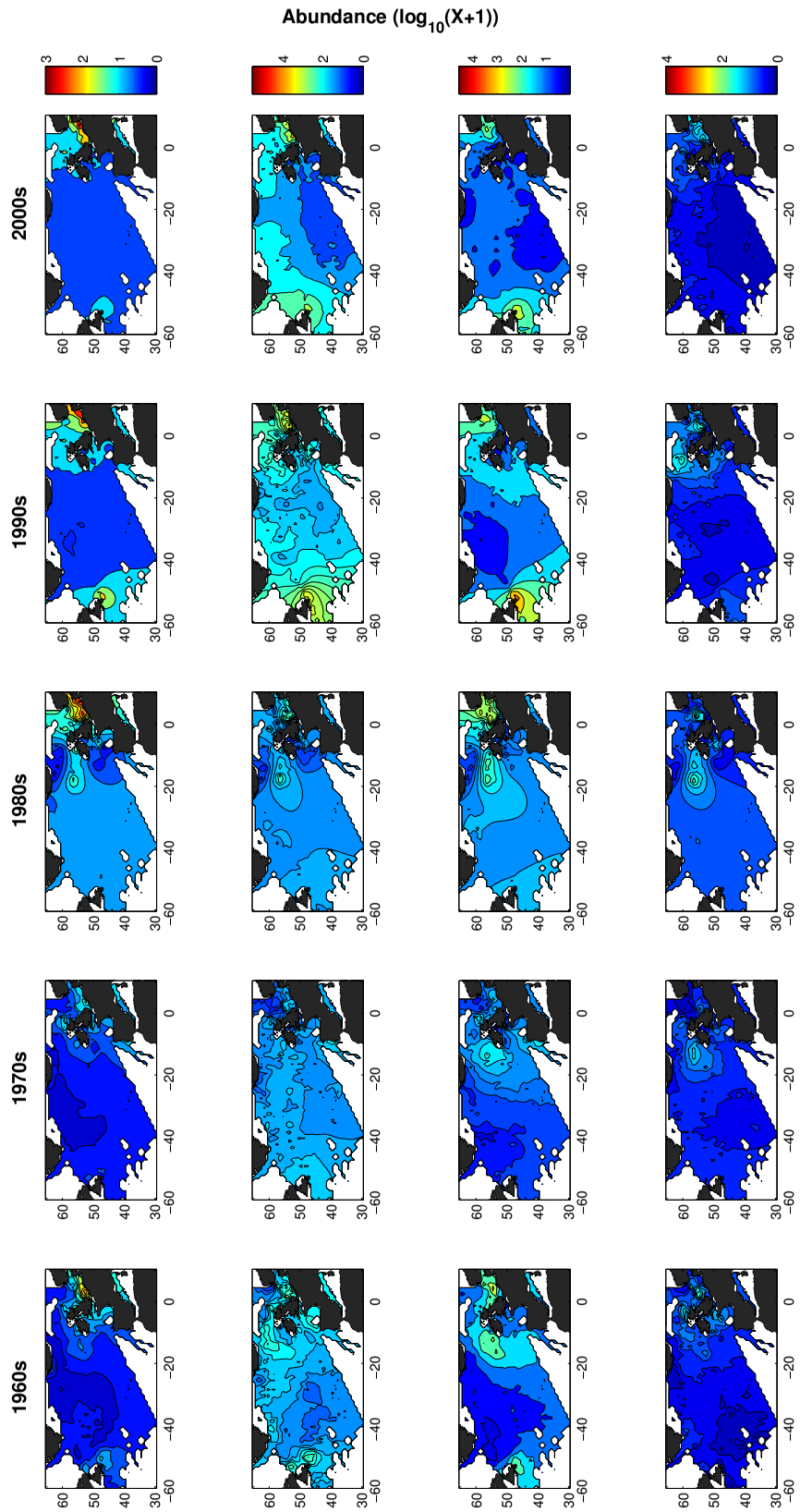

Figure A.6: Decadal abundance of phytoplankton groups in the North Atlantic, calculated using a spring metaphor nearest neighbour mapping method.

The interpolation method used in figure A.6 is based on a boundary value solver, whereby partially differential equations (PDE) are solved using finite difference, and formulated according to the nearest neighbours and the boundary parameters of the missing values. The method used here is based on a spring metaphor connecting each grid cell with every neighbour, extrapolating as a constant function. The boundary conditions for this method were set to spherical, treating the first and last set of values as the north and south poles of a sphere.

A.2 Decadal Anomalies

Decadal anomaly maps were produced by subtracting each grid cell value for the previous decade from the next decade to give a change in abundance between the two decades, where a positive value (red) represents an increase, and a negative value (blue) represents a decrease. This was carried out for both the weighted mean (see figure A.7) and the objective mapping (see figure A.8) interpolation method.

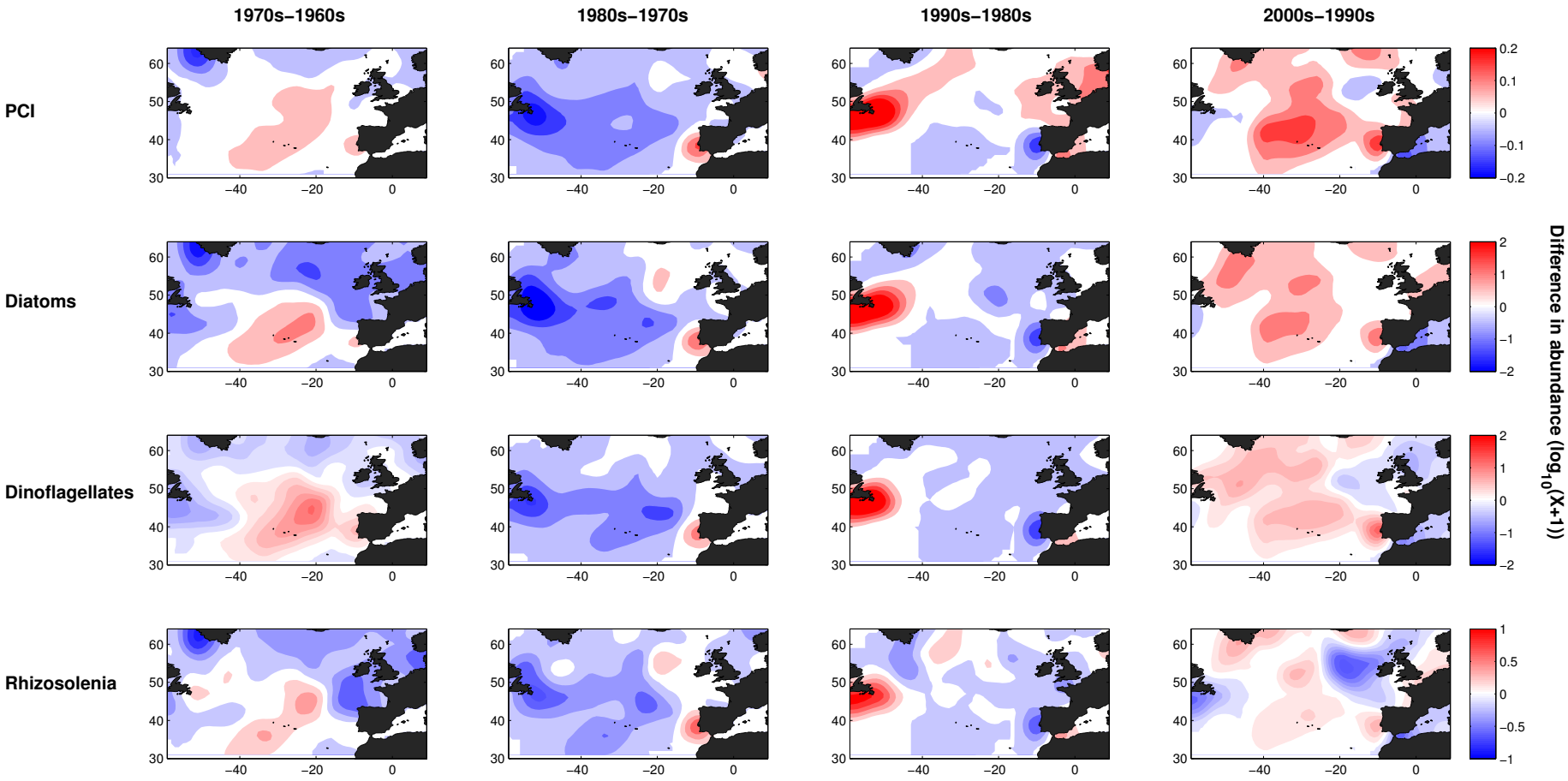

Figure A.7: Change in the decadal abundance of phytoplankton groups in the North Atlantic, calculated using weighted mean interpolation.

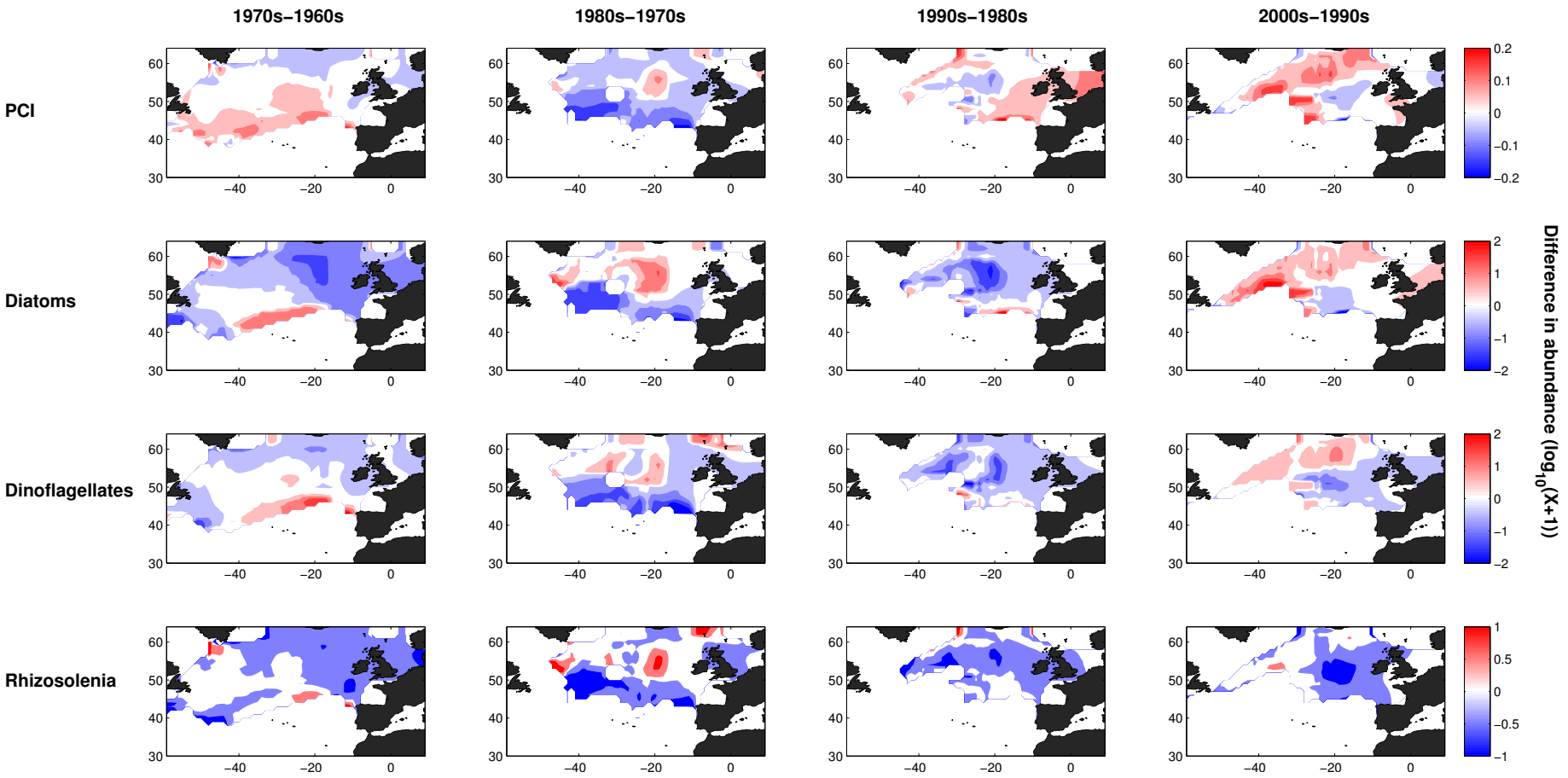

Figure A.8: Change in the decadal abundance of phytoplankton groups in the North Atlantic, calculated using an objective mapping method.

The decadal anomaly maps were then summed at each grid cell to create maps of the change in abundance across the 50 year time-series for each phytoplankton group, again where a positive value (red) represents an increase, and a negative value (blue) represents a decrease.

The weighted mean method produces similar anomaly maps to objective mapping however it covers a wider area of the North Atlantic (figures A.7 and A.8). From the 1990's to the 2000's phytoplankton abundance has increased across most of the North Atlantic, with a small region off the West of Ireland and in the North Sea showing decreases in abundance (figure A.7). The largest decrease in abundance occurred between the 1970's and the 1980's, however this was also a period where CPR sampling had reduced in the 1980's near the Grand Banks of Newfoundland (figure A.2).

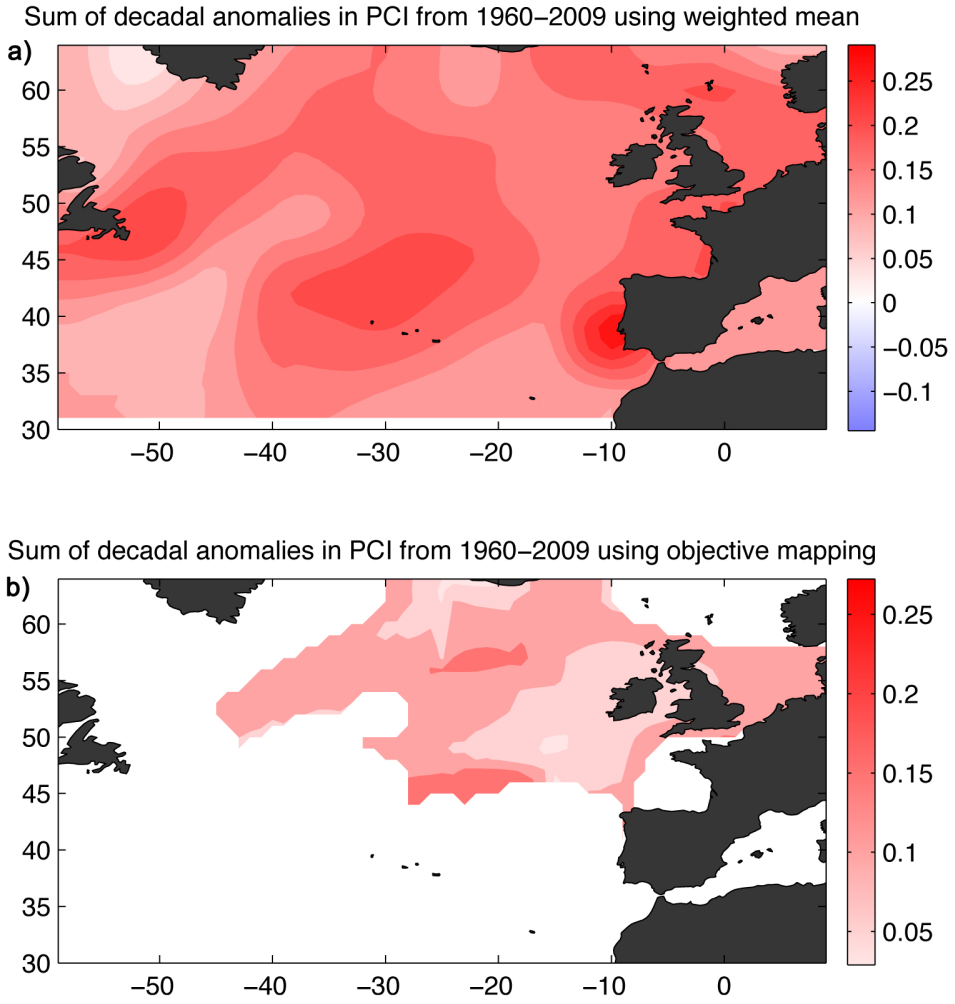

Figure A.9: Subplot showing the sum of decadal anomaly maps using a) weighted mean and b) objective mapping for PCI in the North Atlantic from 1960-2009.

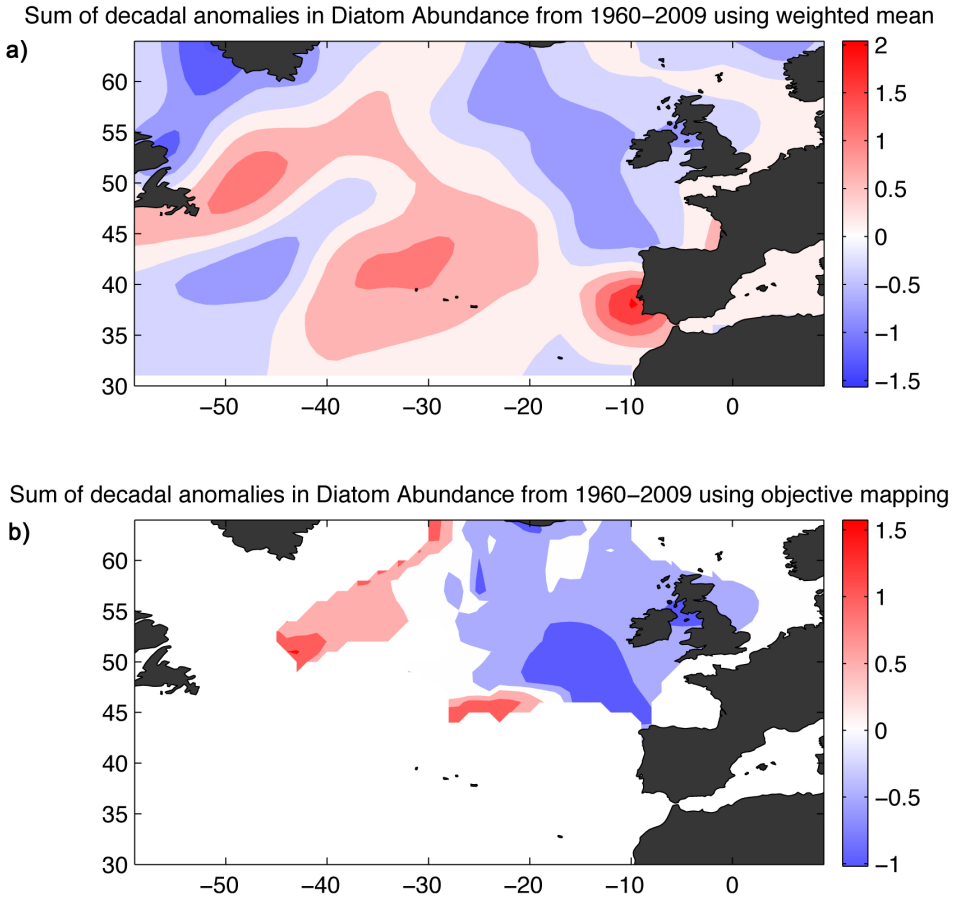

Figure A.10: Subplot showing the sum of decadal anomaly maps using a) weighted mean and b) objective mapping for diatom abundance in the North Atlantic from 1960-2009.

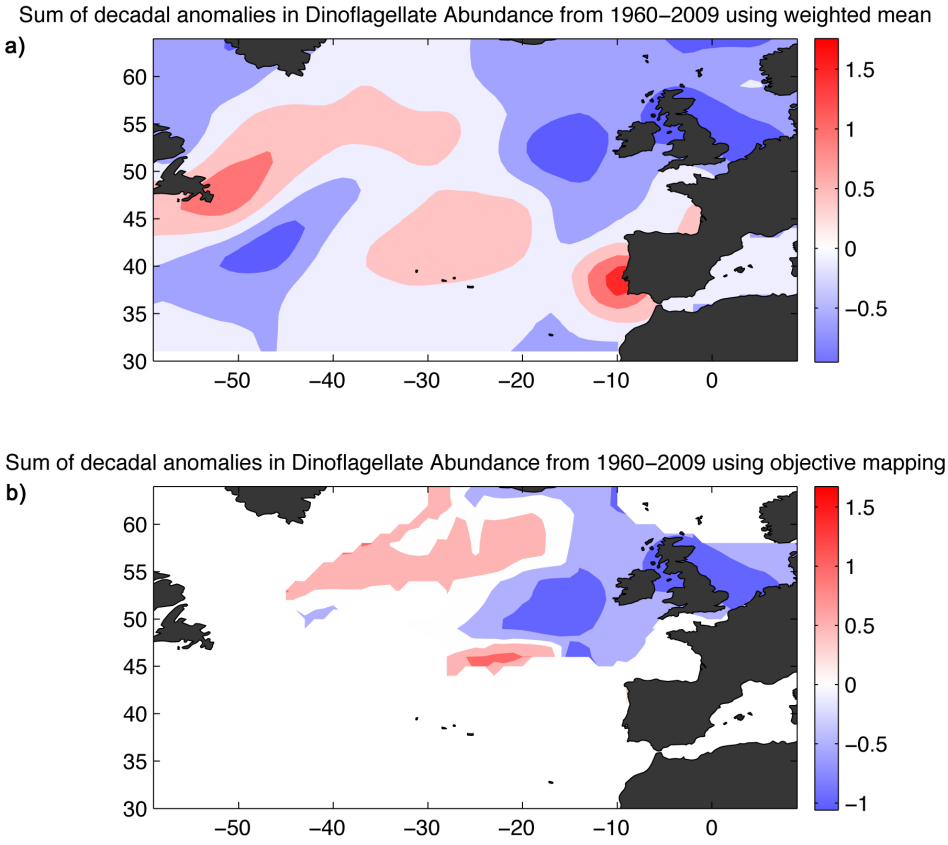

Figure A.11: Subplot showing the sum of decadal anomaly maps using a) weighted mean and b) objective mapping for dinoflagellate abundance in the North Atlantic from 1960-2009.

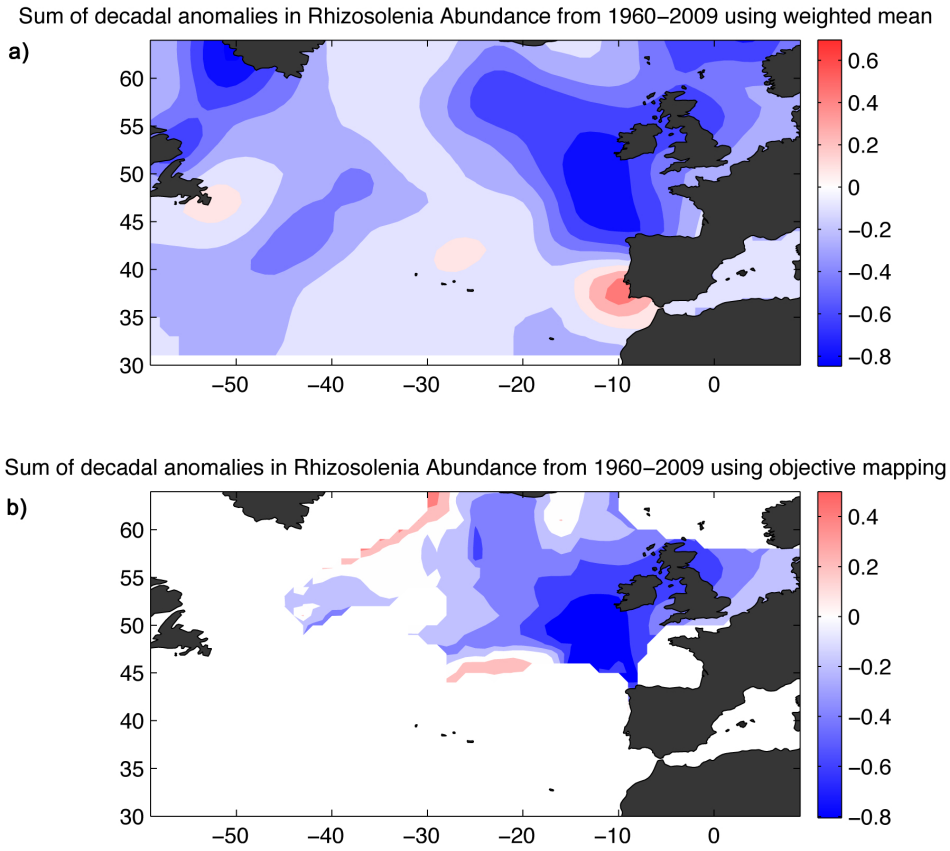

Figure A.12: Subplot showing the sum of decadal anomaly maps using a) weighted mean and b) objective mapping for *Rhizosolenia* abundance in the North Atlantic from 1960-2009.

The sum of the decadal anomaly maps show similar trends to the linear trend maps and the first principal component eigenvector maps (figures 3.6 to 3.19) , as they represent the change in the different phytoplankton indices from 1960-2009. For all phytoplankton indices the Grand Banks of Newfoundland, North of the Azores, and the region off the south-west of Portugal show an increase in abundance from 1960-2009 (figures A.9 to A.12). PCI is increasing across the whole of the North Atlantic (figure A.9), while *Rhizosolenia* are generally decreasing in abundance across most of the North Atlantic (figure A.12).

A.3 Regional temporal autocorrelation

Temporal autocorrelation was checked for in all four phytoplankton indices, SST, wind speed and summer wind speed in bio regions 1 to 9. Figure A.13 shows the

temporal autocorrelation in PCI in bio regions 1 to 9, as an example plot of temporal autocorrelation. If the sample autocorrelation lies within the 95% confidence interval boundaries then the samples can be assumed to be independent of each other, however if they lie outside of the boundary then autocorrelation is present within the dataset and the degrees of freedom for any significance test need to be adjusted accordingly (Glover *et al.*, 2005).

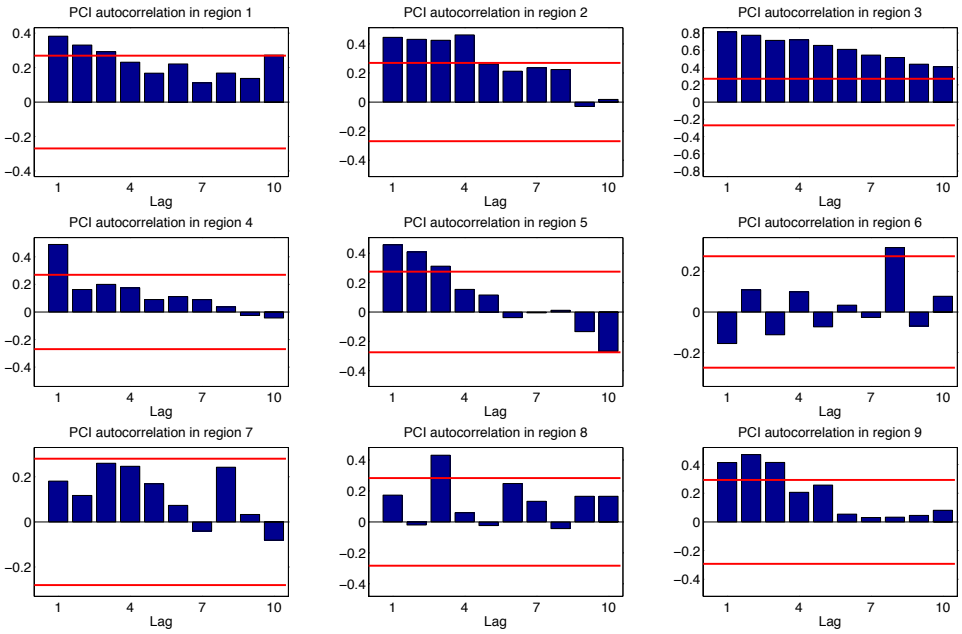

Figure A.13: Temporal autocorrelation (lag in years) in PCI in bio regions 1 to 9 from 1960 to 2012, with 95% confidence intervals (red lines).

Temporal autocorrelation was present in all of the variables. SST presented temporal autocorrelation in all 9 bio regions (data not shown), while diatom abundance showed relatively little temporal autocorrelation (data not shown). Out of the four phytoplankton indices PCI showed the most temporal autocorrelation (figure A.13). Region 6 showed the least temporal autocorrelation, while regions 1, 2, and 3 showed high temporal autocorrelation in most of the variables.

Table A.1 displays the significant correlations between annual phytoplankton indices, climate variables, and climate indices in regions 1 to 9 between 1960 and 2012 after correcting for temporal autocorrelation.

Table A.1: Significant ($p<0.05$, after correcting for temporal autocorrelation (Pyper and Peterman, 1998)) Pearson's linear correlation coefficients, p-values, and slopes between annual phytoplankton indices, climate variables, and climate indices in regions 1 to 9 between 1960 and 2012.

	Sig. Relationship	Pearson's correlation coefficient	Chelton's P-value	Slope
Region 1	PCI with SST	0.45	0.04	3.58
	RHI with DIA	0.52	0.00	0.62
	DIA with SST	0.50	0.05	0.64
	DIA with AMO	0.60	0.03	0.20
	DIN with SWS	-0.54	0.01	-0.40
	DIN with EAP	-0.50	0.03	-0.38
	SST with NAO	0.41	0.01	1.11
	SWS with NAO	0.33	0.03	1.48
Region 2	RHI with DIA	0.60	0.00	0.86
	RHI with DIN	0.60	0.00	1.04
	DIN with WS	-0.57	0.01	-0.50
	DIN with EAP	-0.55	0.01	-0.38
	DIN with NHT	-0.65	0.02	-0.27
	WS with EAP	0.54	0.03	0.43
	SWS with NAO	0.46	0.00	1.72
Region 3	PCI with DIN	0.51	0.03	3.26
	PCI with WS	0.64	0.02	3.30
	PCI with SWS	0.64	0.05	3.31
	RHI with DIA	0.50	0.00	0.70
	RHI with DIN	0.40	0.00	0.70
	DIA with AMO	0.58	0.01	0.22
	DIA with NHT	0.56	0.03	0.30
	SWS with NAO	0.58	0.00	2.30
Region 4	PCI with DIN	0.39	0.01	3.54
	RHI with DIA	0.56	0.00	0.82
	RHI with DIN	0.65	0.00	0.85
	DIA with DIN	0.39	0.01	0.35
	DIN with WS	-0.35	0.04	-0.37
	DIN with NHT	-0.40	0.03	-0.18
	SST with AMO	0.78	0.01	0.42
	SST with NHT	0.81	0.02	0.61
Region 5	PCI with RHI	0.44	0.01	4.43
	PCI with DIN	0.48	0.03	5.23
	RHI with DIA	0.43	0.00	0.40
	RHI with DIN	0.55	0.00	0.60
	DIA with DIN	0.39	0.01	0.47
	DIN with SST	-0.51	0.04	-0.18
	SST with AMO	0.65	0.01	0.36
	SST with NHT	0.64	0.04	0.50
	WS with EAP	0.47	0.03	0.31
	SWS with NAO	0.47	0.00	2.31
	SWS with EAP	0.50	0.01	0.56
Region 6	PCI with RHI	0.30	0.03	1.86
	PCI with DIA	0.80	0.00	9.58
	PCI with DIN	0.43	0.00	3.96
	PCI with SST	0.34	0.01	1.97
	PCI with WS	0.29	0.04	2.04
	PCI with EAP	0.31	0.03	1.62
	PCI with AMO	0.40	0.00	0.89
	RHI with DIA	0.57	0.00	1.12
	RHI with DIN	0.78	0.00	1.17
	DIA with DIN	0.64	0.00	0.49
	SST with NAO	-0.34	0.02	-1.35
	SST with AMO	0.70	0.01	0.27
	SWS with NAO	0.41	0.00	1.54
Region 7	PCI with RHI	0.63	0.00	4.68
	PCI with DIA	0.62	0.00	7.34
	PCI with DIN	0.57	0.00	4.92
	RHI with DIA	0.72	0.00	1.15
	RHI with DIN	0.51	0.00	0.59
	DIA with DIN	0.67	0.00	0.49
	DIA with AMO	0.42	0.04	0.09
	DIN with SST	0.34	0.04	0.28
	SST with NAO	-0.45	0.00	-1.52
	SST with AMO	0.61	0.03	0.20
Region 8	PCI with RHI	0.36	0.02	2.26
	PCI with DIA	0.76	0.00	8.49
	PCI with DIN	0.71	0.00	5.21
	PCI with EAP	0.43	0.02	2.16
	PCI with NHT	0.51	0.03	1.53
	RHI with DIA	0.48	0.00	0.84
	DIA with DIN	0.79	0.00	0.52
	DIA with AMO	0.45	0.01	0.09
	DIA with NHT	0.42	0.03	0.11
	DIN with WS	0.39	0.05	0.40
	SST with AMO	0.71	0.01	0.23
	SST with NHT	0.76	0.02	0.35
Region 9	PCI with RHI	0.63	0.00	1.99
	PCI with DIA	0.80	0.00	6.60
	PCI with DIN	0.69	0.00	3.98
	RHI with DIA	0.60	0.00	1.57
	RHI with DIN	0.33	0.02	0.61
	DIA with DIN	0.58	0.01	0.41
	DIN with WS	0.67	0.03	0.57
	SST with AMO	0.51	0.02	0.15
	WS with EAP	0.58	0.04	0.46
	WS with NHT	0.76	0.05	0.36

Abbreviations: PCI, Phytoplankton Colour Index; DIA, diatom abundance; DIN, dinoflagellate abundance; RHI, *Rhizosolenia* abundance; SWS, summer wind speed; WS, wind speed.

Appendix B

APPENDIX: Net community production in the North Atlantic

B.1 Comparison of NCP_{O_2} with plankton indices

The phytoplankton data from the CPR survey were divided into 6 key phytoplankton indices; phytoplankton colour index (PCI), spring-bloom forming diatoms (diatoms), *Rhizosolenia* (diatom genus often associated with a later blooming-time), dinoflagellates, silicoflagellates, and coccolithophores. The species included in these indices are presented in table 3.1 in chapter 3, with the addition of coccolithaceae and silicoflagellatae, as described in chapter 5 section 5.3.13. Monthly phytoplankton indices were averaged for each region defined in chapter 4 figure 4.3, and compared with monthly NCP_{O_2} (figure B.1). The CPR is only towed by the *MV Benguela Stream* from 40 °W to the UK, therefore there are no CPR samples in region 5, and few samples in region 4.

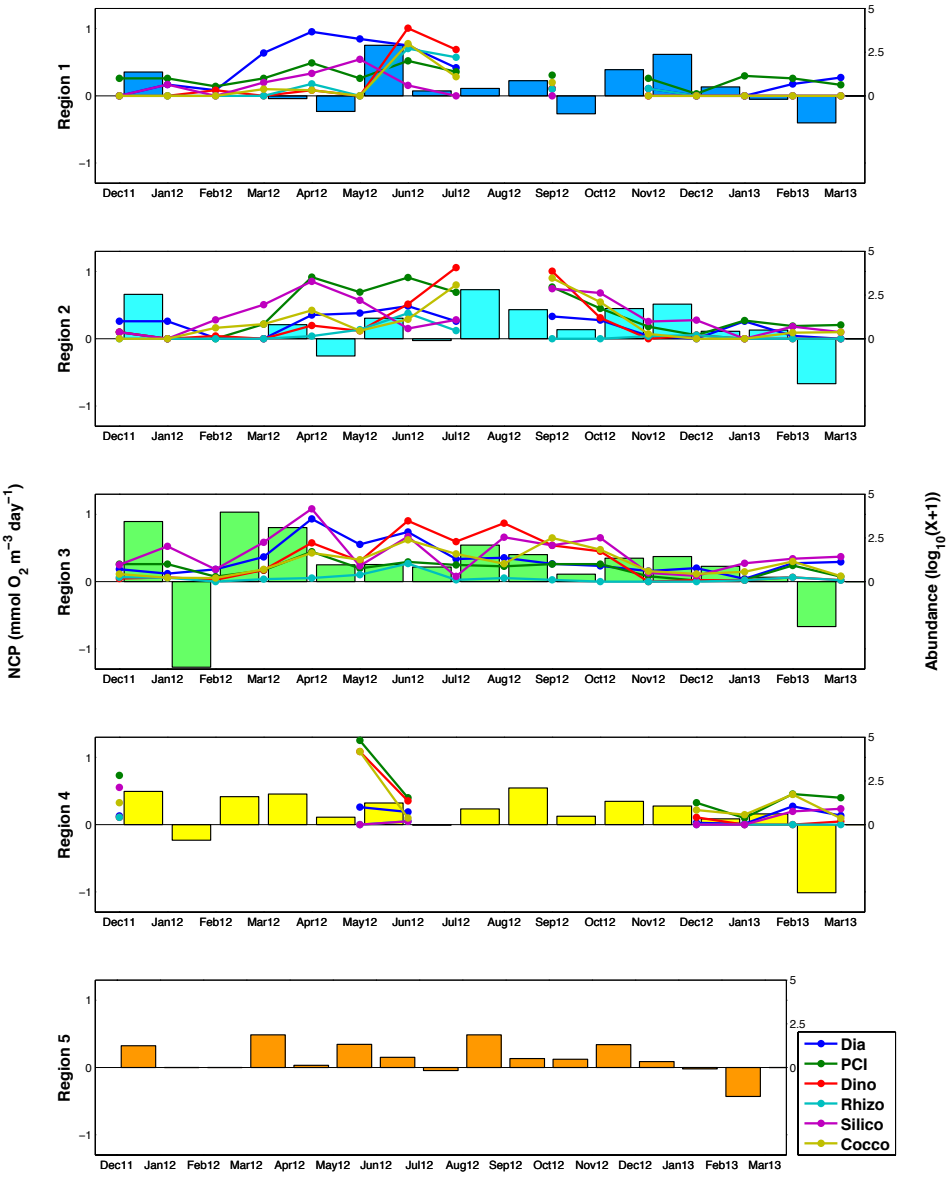

Figure B.1: Monthly mean NCP$_{O_2}$, and phytoplankton abundance over time in each of 5 biogeochemical regions (see Fig. 4.3). Monthly NCP$_{O_2}$ was calculated using equations 4.1 to 4.8 ([mmol O_2 m^{-3} d^{-1}], left axis), monthly phytoplankton indices are plotted as coloured circles and line (Diatoms = blue, PCI = green, Dinoflagellates = red, *Rhizosolenia* = cyan, Silicoflagellates = magenta, Coccolithophores = yellow, [$\log_{10}(x+1)$], right axis).

In region 1 peak dinoflagellate abundance corresponds to peak autotrophy between May and June 2012, this is also the case between August and September 2012 in region 2, however there are gaps in the CPR data in these regions. In region 3 peak diatom abundance corresponds to high autotrophy between March and April 2012, while dinoflagellate abundance corresponds to maintained autotrophy throughout the summer. There were no significant correlations found between the phytoplankton indices and monthly NCP$_{O_2}$.

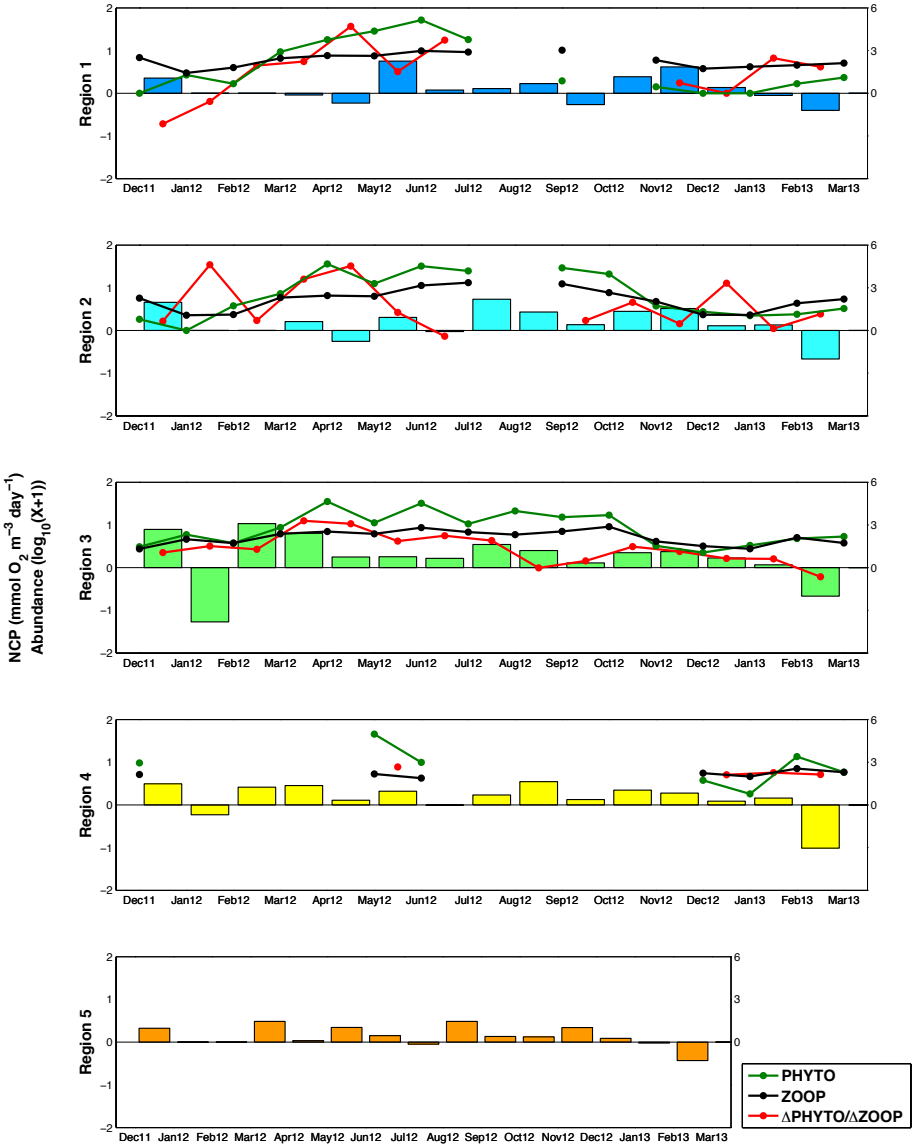

Figure B.2: Monthly mean NCP_{O_2}, total phytoplankton, total zooplankton, and the change in phytoplankton relative to zooplankton over time in each of 5 biogeochemical regions (see Fig. 4.3). Monthly NCP_{O_2} was calculated using equations 4.1 to 4.8 ([mmol O_2 m^{-3} d^{-1}], left axis), monthly plankton indices are plotted as coloured circles and line (total phytoplankton (PHYTO) = green, total zooplankton (ZOOP) = black, change in phytoplankton relative to zooplankton (ΔPHYTO/ΔZOOP) = red, [$\log_{10}(x+1)$], right axis).

The total phytoplankton and zooplankton abundance from the CPR survey are compared with monthly NCP_{O_2} in figure B.2. The change in phytoplankton relative to zooplankton abundance between months (ΔP/ΔZ) was calculated to investigate if the biological data corresponds to the estimated NCP_{O_2}. In region 1 and 2 there appears to be no correspondence between NCP_{O_2} and ΔP/ΔZ. In region 3, ΔP/ΔZ follows the NCP_{O_2} seasonal cycle reasonably well, however no significant correlations were found.

Appendix C

APPENDIX: The marine carbonate system in the North Atlantic

C.1 $>$ 10 years of calculated DIC with nutrient concentration

Figure C.1 shows the monthly nutrient concentrations collected on board the *MV Benguela Stream*, alongside DIC estimated using measurements of pCO_2 and equation 5.10 used to calculate TA from salinity. In regions 1 and 2 DIC is significantly correlated with nutrient concentrations, demonstrating the biological and mixing influences in these regions. In region 3 there are no significant correlations between DIC and nutrient concentration.

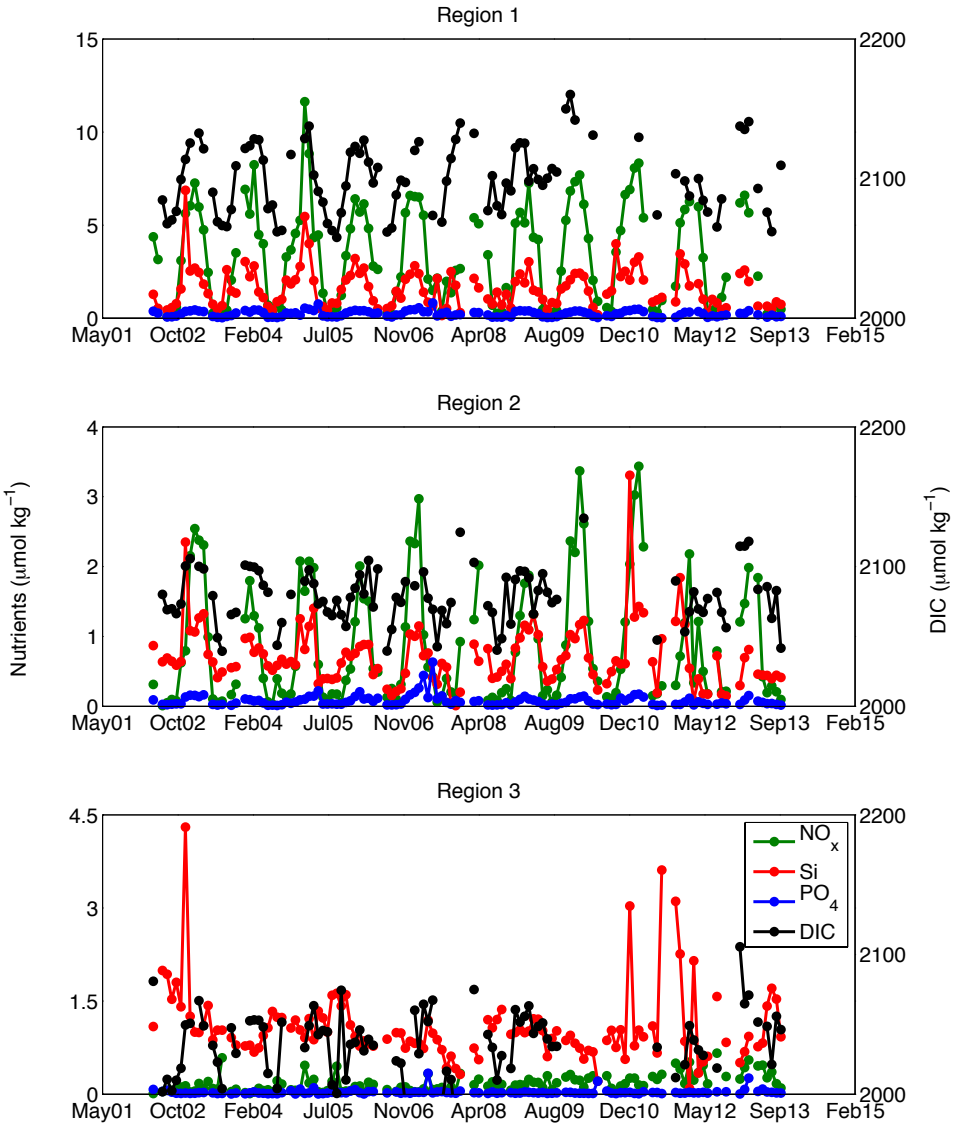

Figure C.1: Monthly NO_3 (green), Si (red), PO_4 (blue) on the left y-axis in μmol kg^{-1}, and monthly DIC (black) on the right y-axis in μmol kg^{-1}, from 2002 to 2013 for regions 1, 2, and 3. Note the different y axes scales for nutrients.

C.2 Comparison of satellite carbonate parameters with measurements

Satellite estimates of PIC (Particulate Inorganic Carbon) (Gordon *et al.*, 2001; Balch, 2005), and POC (Particulate Organic Carbon) (Stramski *et al.*, 2007) were obtained at a resolution of 9 km and frequency of 1 month from Aqua-MODIS (http://oceandata.sci.gsfc.nasa.gov). These were averaged for the regions defined in chapter 5 section 5.2, and compared with measurements of pCO_2 and calculated DIC to investigate whether relationships between these carbonate parameters and

satellite observations can be inferred.

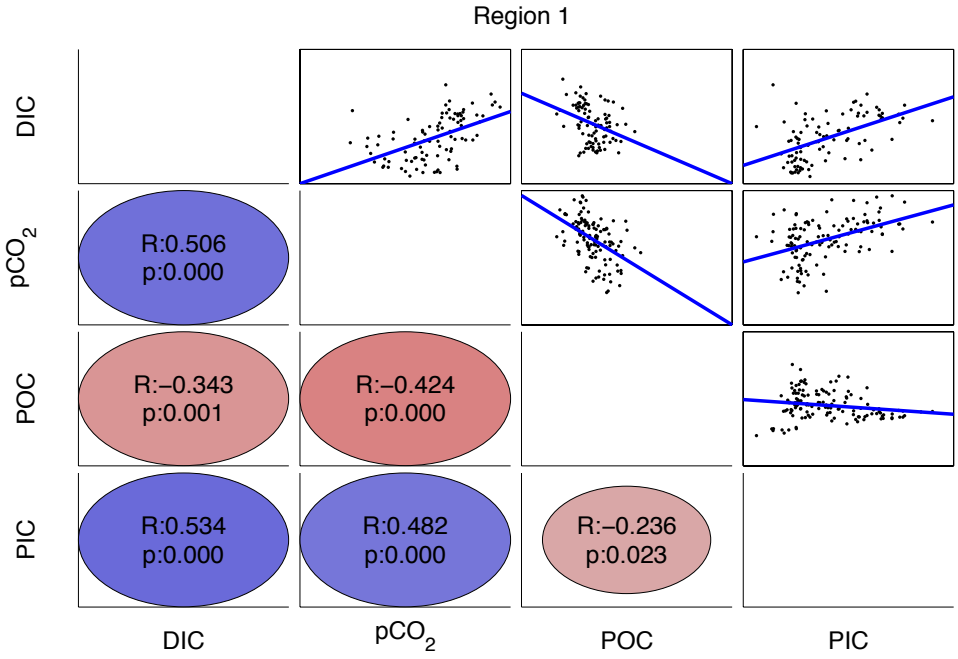

Figure C.2: Correlation matrix plot of monthly DIC, pCO_2, POC, PIC from 2002 to 2013 in region 1. Pearson's correlation coefficients and p-values are visualized as the colour and sizes of the circles, and values are displayed within (red = negative correlation, blue = positive correlation). Scatter plots with linear regression of each variable combination are also displayed.

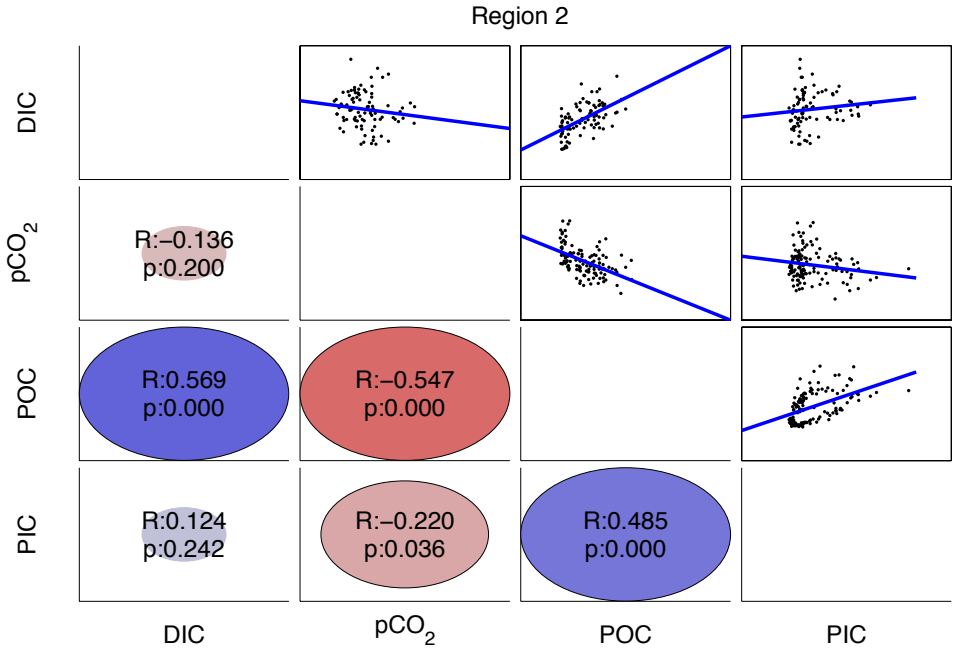

Figure C.3: Correlation matrix plot of monthly DIC, pCO_2, POC, PIC from 2002 to 2013 in region 2. Pearson's correlation coefficients and p-values are visualized as the colour and sizes of the circles, and values are displayed within (red = negative correlation, blue = positive correlation). Scatter plots with linear regression of each variable combination are also displayed.

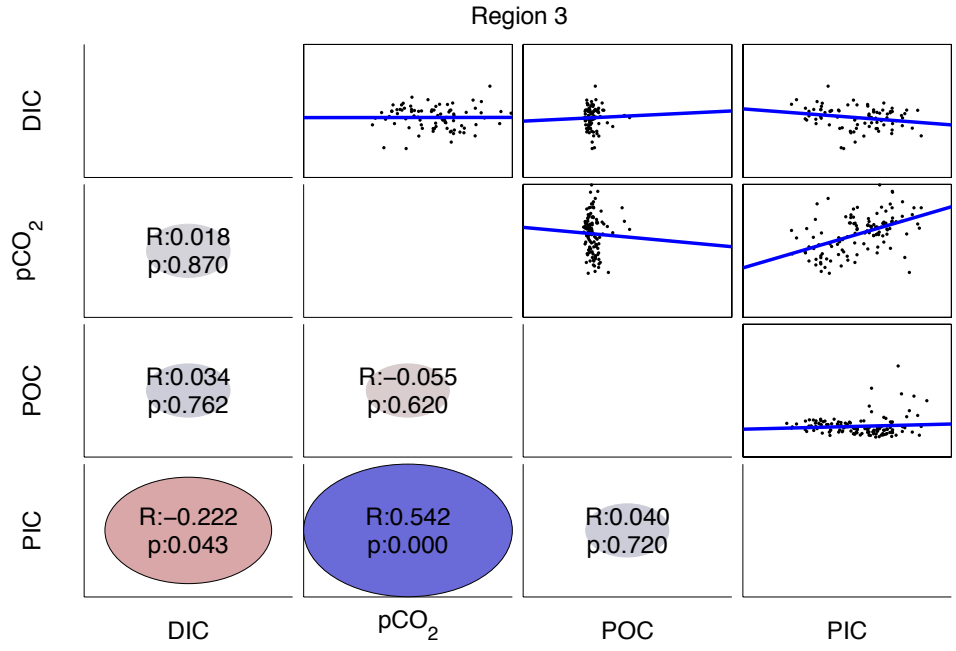

Figure C.4: Correlation matrix plot of monthly DIC, pCO_2, POC, PIC from 2002 to 2013 in region 3. Pearson's correlation coefficients and p-values are visualized as the colour and sizes of the circles, and values are displayed within (red = negative correlation, blue = positive correlation). Scatter plots with linear regression of each variable combination are also displayed.

Region 1 showed significant correlations between all four variables. Region 2 had significant correlations between POC and DIC, pCO_2, and PIC. Region 3 had a significant correlation between pCO_2 and PIC, and a weak significant correlation between PIC and DIC. The regional variation between these correlations demonstrates the difficulty of using satellite estimates to derive carbonate parameters, and inferring any relationships.

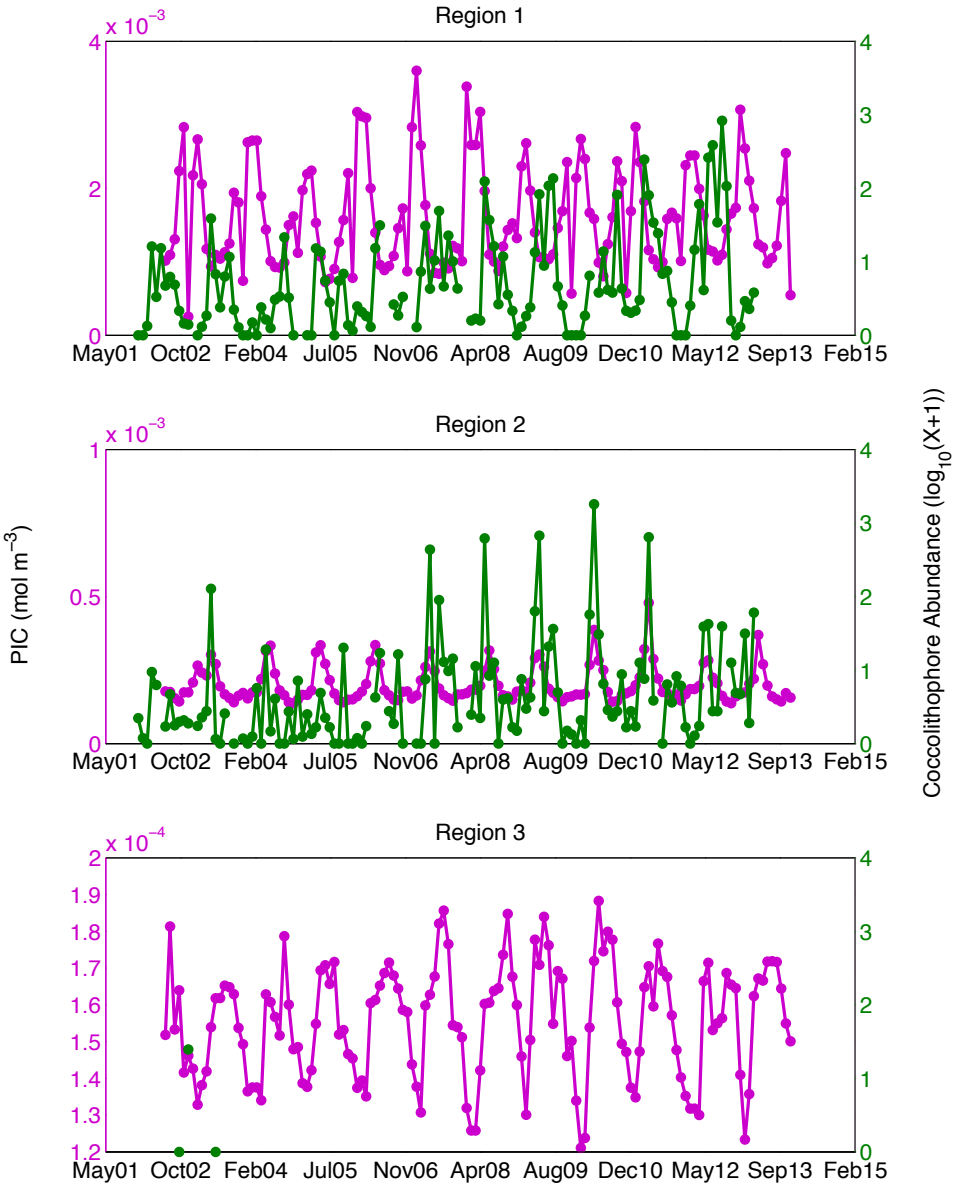

Figure C.5: Monthly PIC (Particulate Inorganic Carbon, pink) on the left y-axis in mol m^{-3}, and monthly coccolithophore abundance (green, $\log_{10}(x+1)$) on the right y-axis, from 2002 to 2013 for regions 1, 2, and 3. Note the different y axes scales for PIC.

PIC can be used to estimate coccolithophore abundance (Hopkins *et al.*, 2015).

Figure C.5 shows the comparison between satellite PIC (Gordon *et al.*, 2001; Balch, 2005) and coccolithophore abundance from the CPR. Region 1 shows a negative correlation, while region 2 has a positive correlation. This is likely due to the influence of abiogenic particulate matter and re-suspended material found in coastal waters, which can influence measurements of ocean colour (Morel and Prieur, 1977; Daniels *et al.*, 2012; Hopkins *et al.*, 2015). Therefore when using satellite PIC measurements to estimate coccolithophores abundance, caution should be taken when interpreting such results depending on the location and timing of mixing events.

Appendix D

APPENDIX: Spatial and temporal variability in the influence of phytoplankton community structure on CO_2 flux in the North Atlantic

D.1 Annual seasonal cycles

Figures D.1 to D.4 show the mean seasonal cycle and the inter-annual seasonal cycle from 2002 to 2013 within each region for coccolithophore abundance, and nutrient concentration.

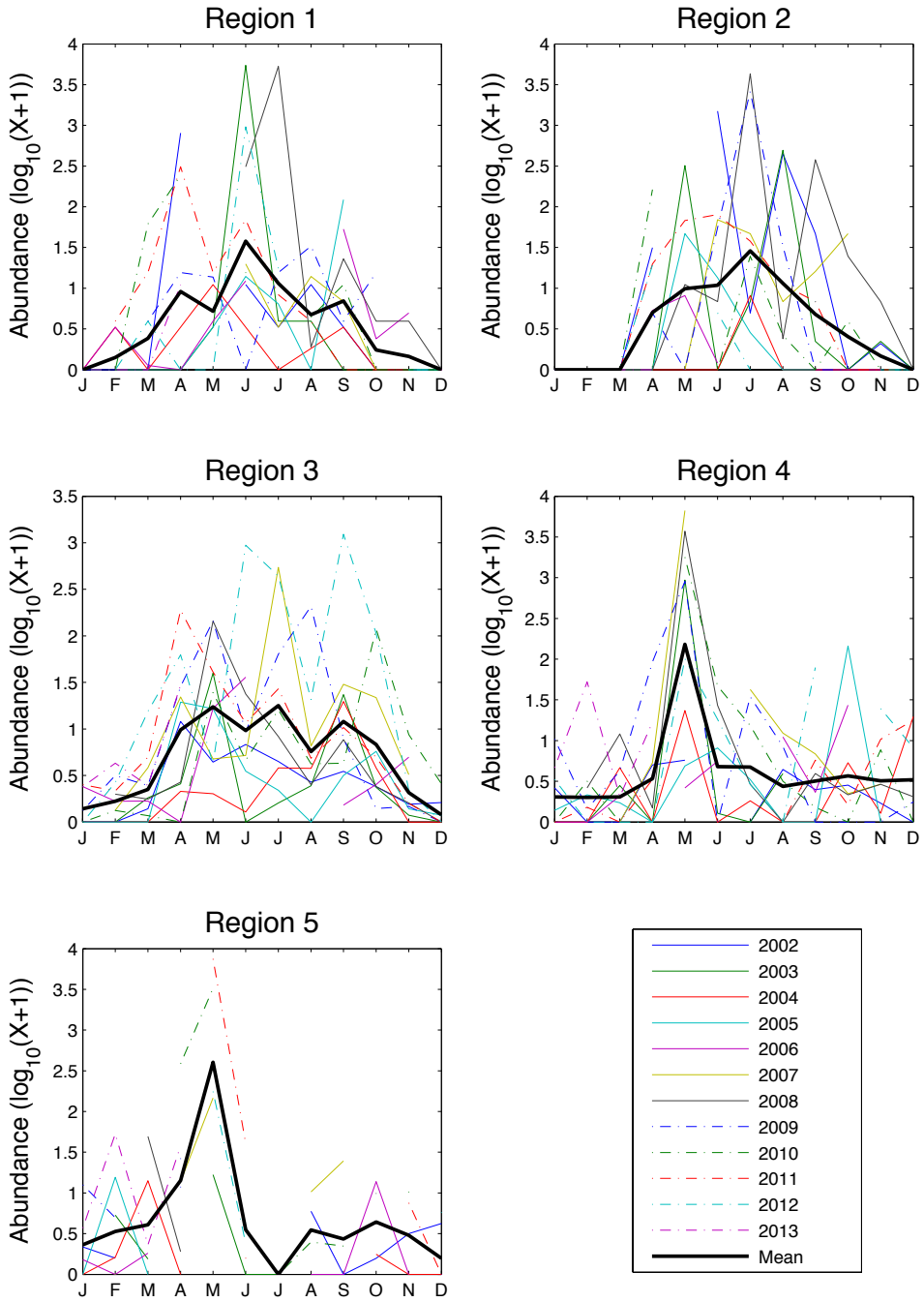

Figure D.1: Monthly mean coccolithophore abundance from 2002 to 2013 and the monthly mean of all years (black thick line) in regions 1 to 5.

There was high variance about the mean in all phytoplankton abundance indices (data not shown), coccolithophore abundance is plotted as an example (figure D.1). The mean seasonal cycle of coccolithophores is less prominent in regions 1 to 3, with 3 peaks occurring during May, July, and September. While in regions 4 and 5 there is a defined peak that occurs in May. High abundances of coccolithophores were recorded in regions 3 and 4 in 2012, and in 2007 in regions 2, 3

and 4. Nutrient concentrations are plotted in figures D.2 to D.4.

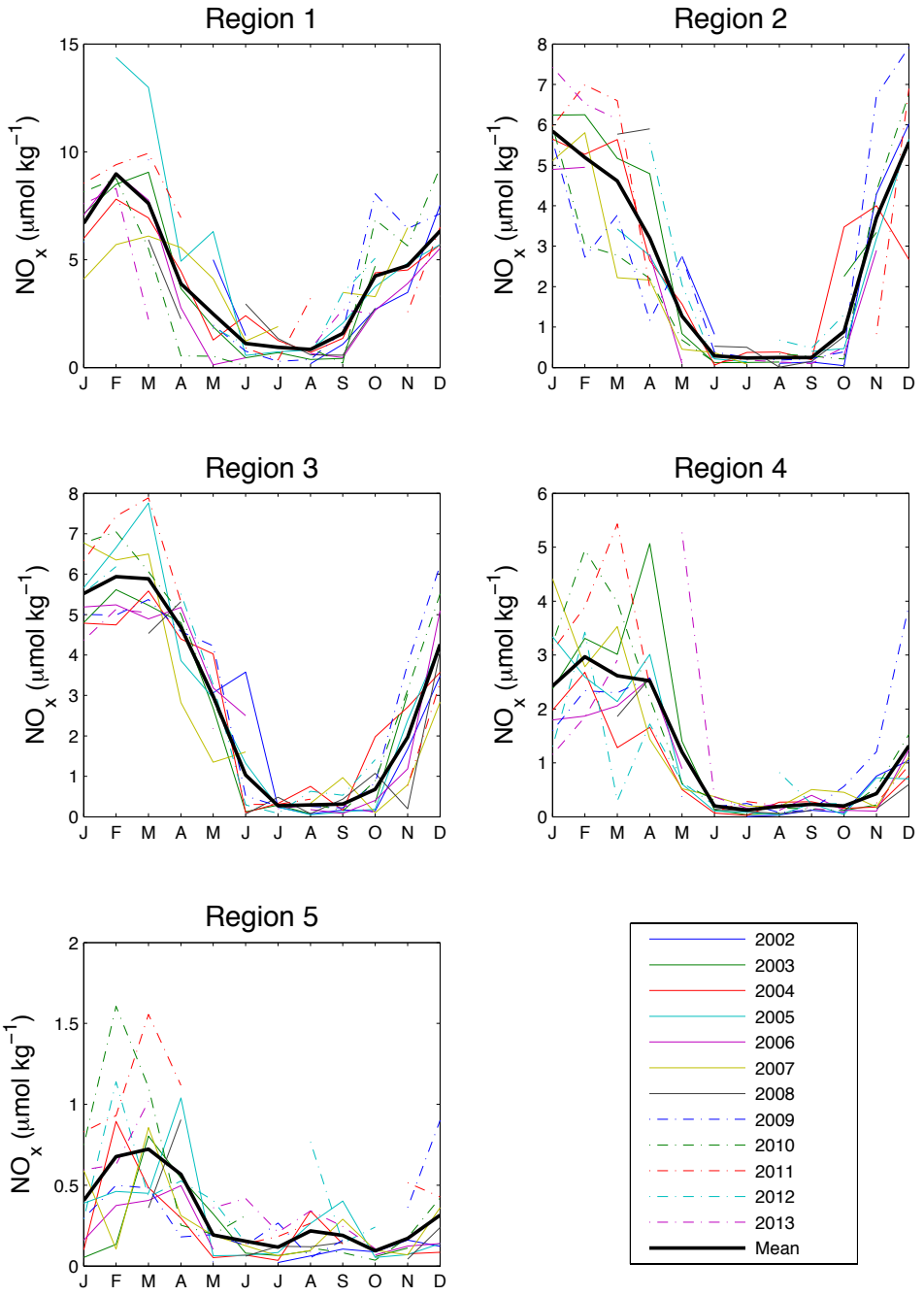

Figure D.2: Monthly mean nitrate and nitrite (NO_x) concentration from 2002 to 2013 and the monthly mean of all years (black thick line) in regions 1 to 5.

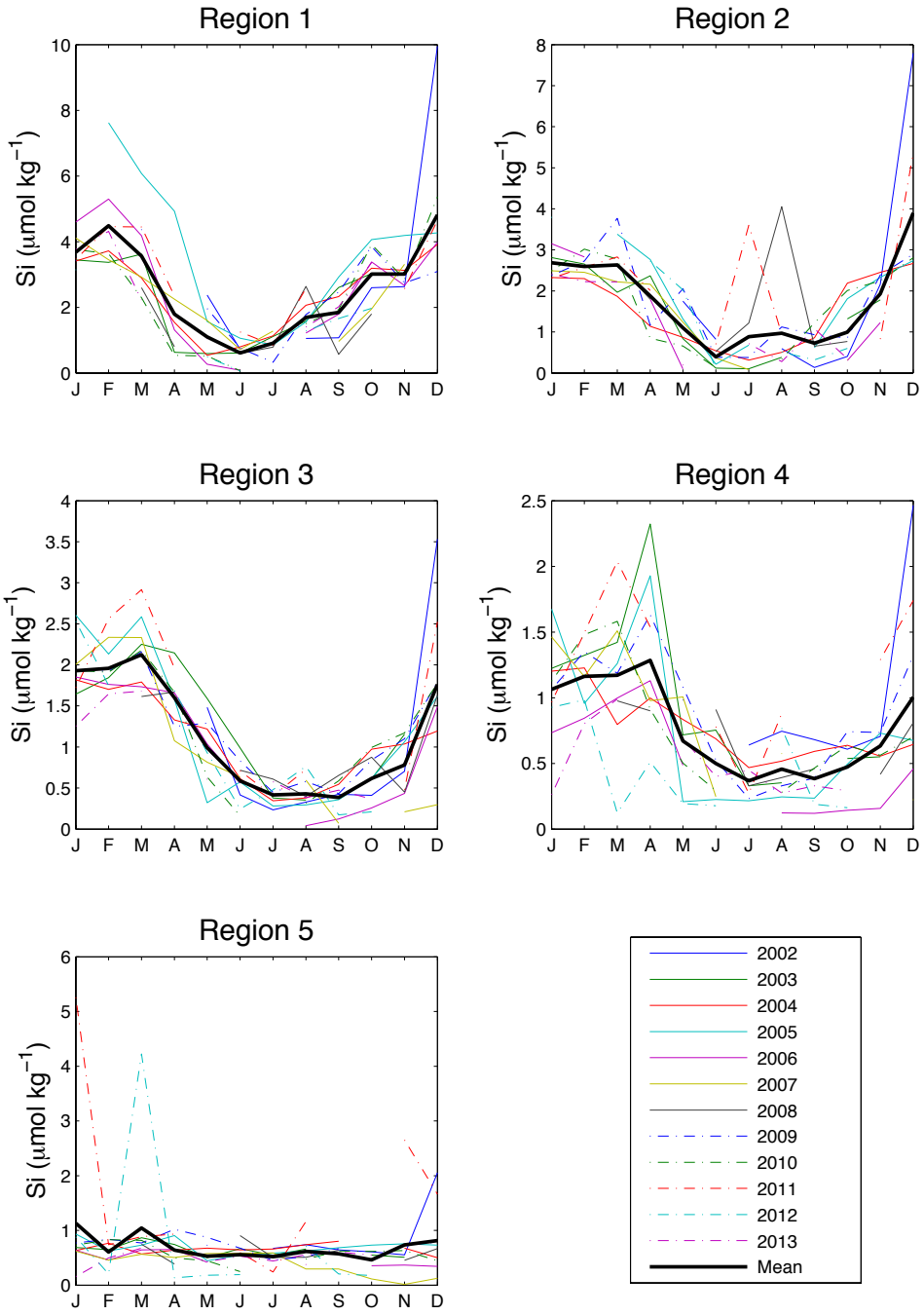

Figure D.3: Monthly mean silicate (Si) concentration from 2002 to 2013 and the monthly mean of all years (black thick line) in regions 1 to 5.

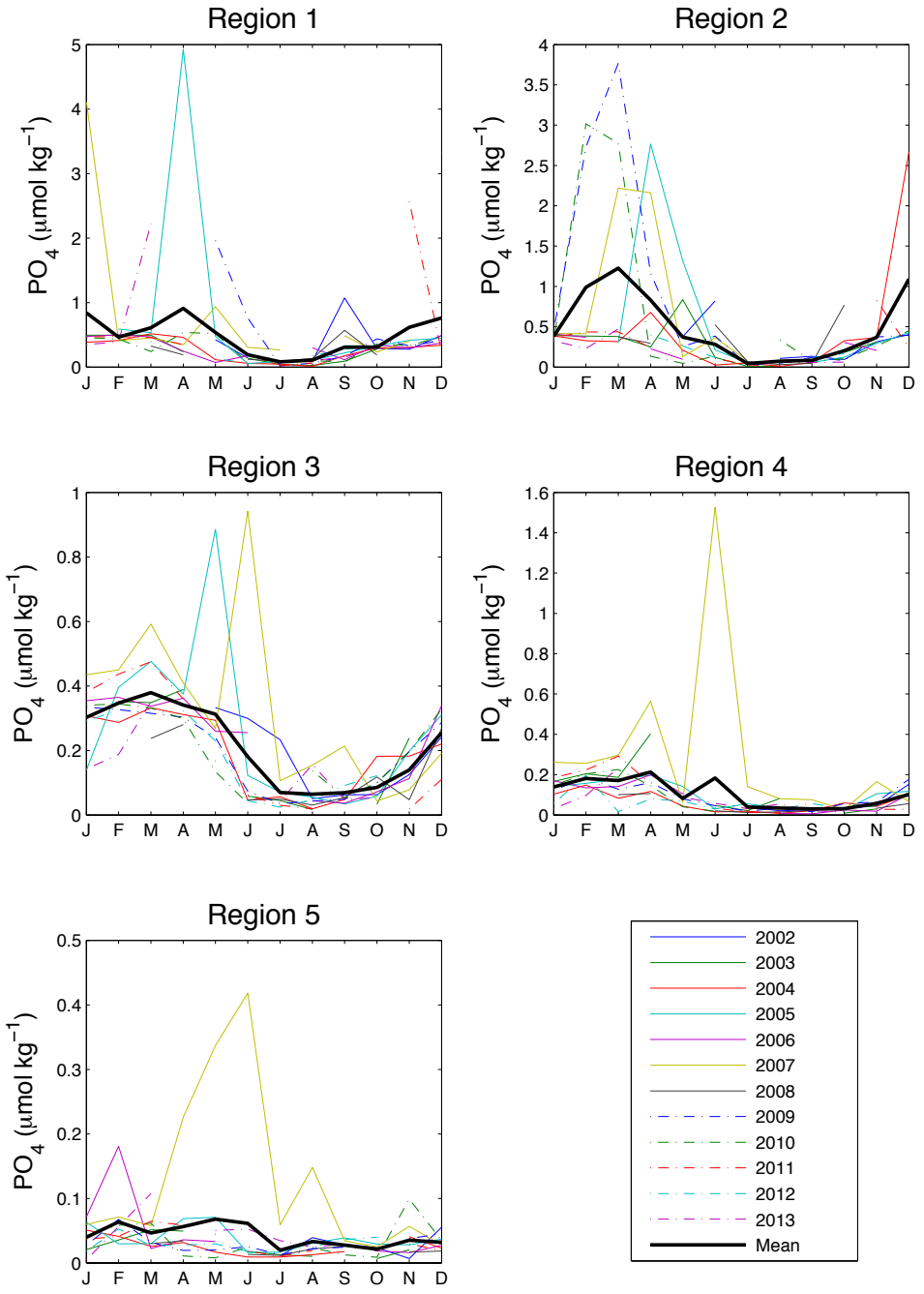

Figure D.4: Monthly mean phosphate (PO_4) concentration from 2002 to 2013 and the monthly mean of all years (black thick line) in regions 1 to 5.

In June 2007 phosphate concentrations were higher than other years in regions 3, 4 and 5. April of 2005 also had unusually high concentrations of phosphate in regions 1, 2 and 3. These high values were not apparent in either Si or NO_x concentrations, therefore they could be due to analytical error, sample preservation issues or biogeochemical processes such as the preferential remineralisation of particulate organic matter (Davis *et al.*, 2014). However further investigation is needed to determine the cause of these anomalous phosphorus years.

Monthly mean MLD was calculated for each region using ECCO2 daily 0.25° MLD (Menemenlis *et al.*, 2008), the seasonal cycle from 2002 to 2013 and the mean seasonal cycle is shown in figure D.5.

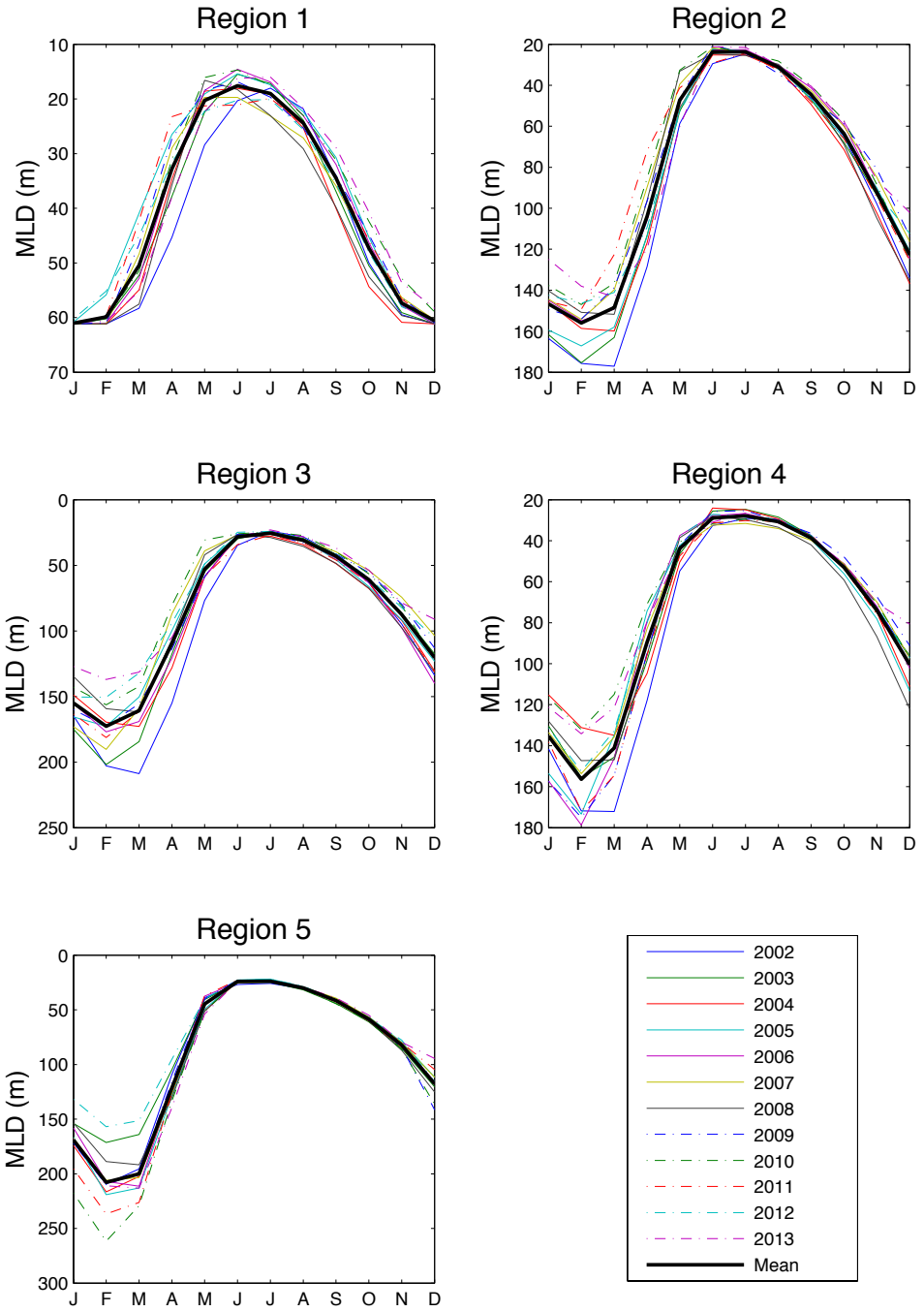

Figure D.5: Monthly mean mixed layer depth (MLD) from 2002 to 2013 and the monthly mean of all years (black thick line) in regions 1 to 5.

MLD shows a similar seasonal cycle in all five regions, with maxima occurring in the winter months. This is likely driven by both wind speed and SST. Region 5 has the deepest MLD reaching up to ∼250 m, while region 1 has the shallowest MLD with a maximum mean reaching ∼60 m.

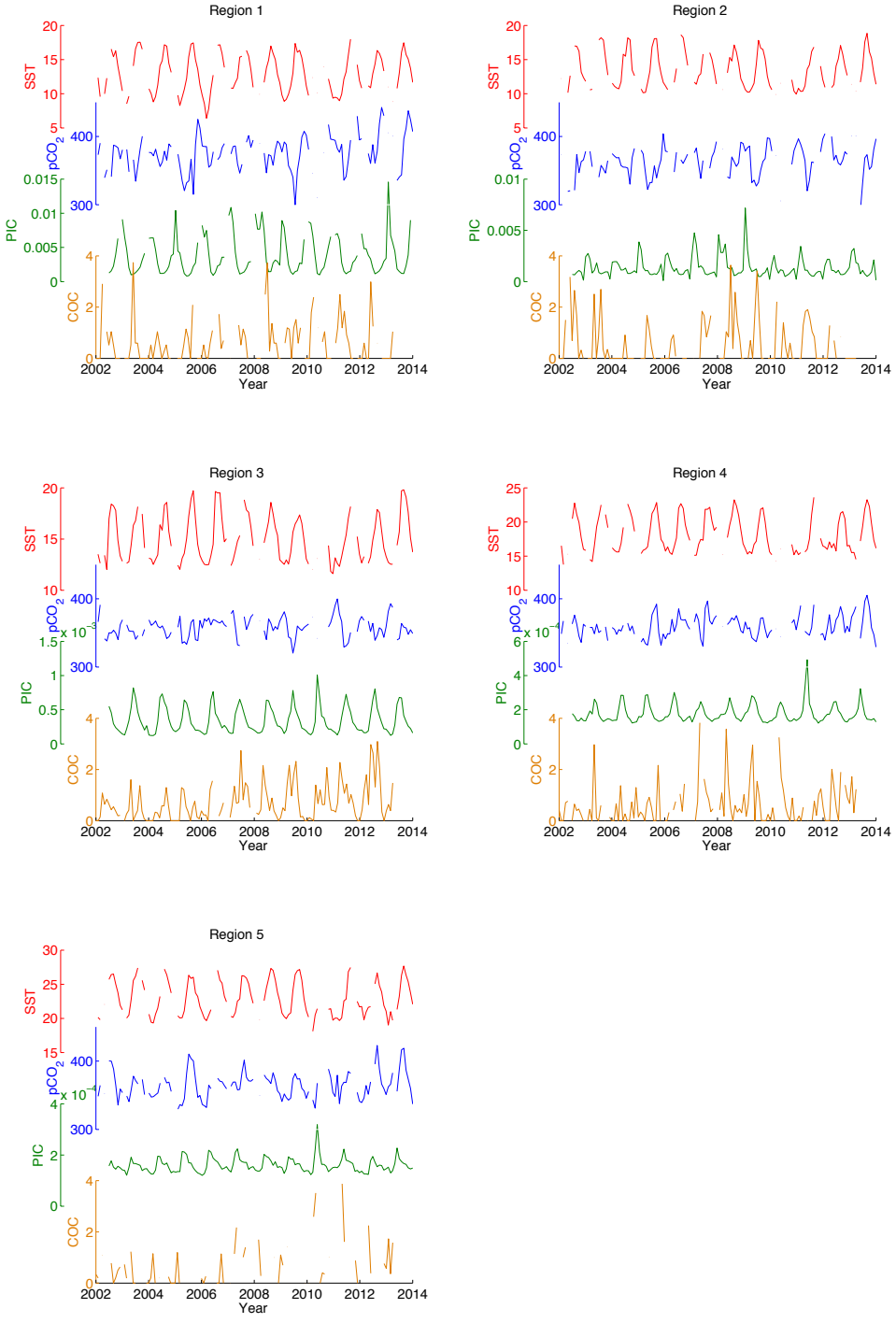

Figure D.6: Monthly mean SST (°C, red), pCO_2 (μatm, blue), PIC (mol m^{-3}, green), and coccolithophore abundance ($\log_{10}$(x+1), COC = orange) from 2002 to 2013 in regions 1 to 5.

Figure D.6 shows the monthly mean SST, pCO_2, PIC (Gordon *et al.*, 2001; Balch, 2005), and coccolithophore abundance from 2002 to 2013 in regions 1 to 5. No significant correlations between high abundance years of coccolithophores and PIC were found.

Biplot (figure D.7) shows the variance explained by principal component 1. In regions 1 to 3 FCO_2 is negatively associated with SST and the phytoplankton indices, whereas in region 4 and 5 SST and FCO_2 are positively associated and negatively associated with the phytoplankton indices, suggesting that SST drives FCO_2 in regions 4 and 5.

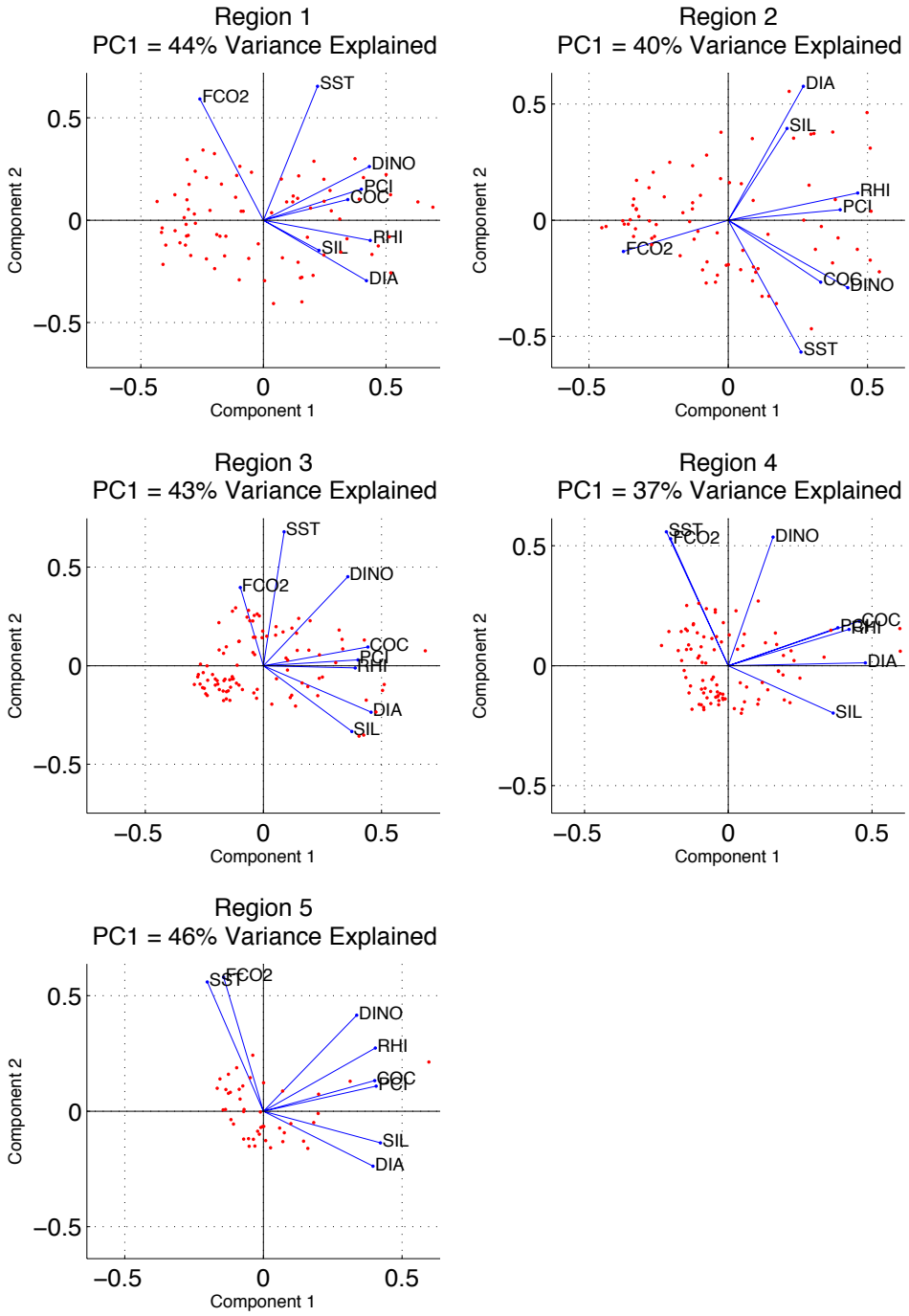

Figure D.7: Biplot of the loadings of principal components 1 and 2 when comparing monthly phytoplankton indices with sea surface temperature and air-sea flux of CO_2 (FCO_2) from 2002 to 2013 in regions 1 to 5, with the variance explained by principle component 1 displayed in the title.

D.2 Cross-correlation analyses

Cross-correlation analysis was carried out between variables. The red dashed line shows the 95% confidence interval, and the lag is monthly (figures D.8 to D.11). Cross-correlation between monthly pCO_2 and SST shows a lag in regions 1, 2 and

3; in regions 4 and 5 there was no lag. Cross-correlation between pCO_2 and the different phytoplankton indices was not significant and showed increased lag in regions 4 and 5, whereas significant negative correlations in regions 1, 2 and 3 were found. Figures D.8 to D.11 show the correlations between SST and PCI with pCO_2 for regions 1 and 5 for comparison.

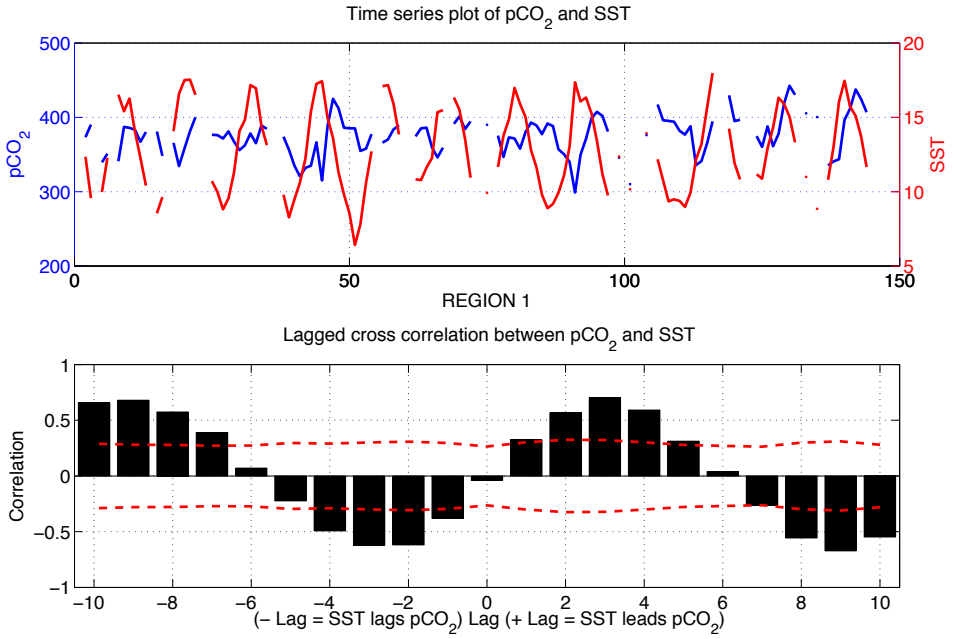

Figure D.8: Cross-correlation between monthly mean pCO_2 (μatm, blue line) and SST (°C, red line) from 2002 to 2013 in region 1. The bars above the red-dashed line denote significant correlations with $p < 0.05$.

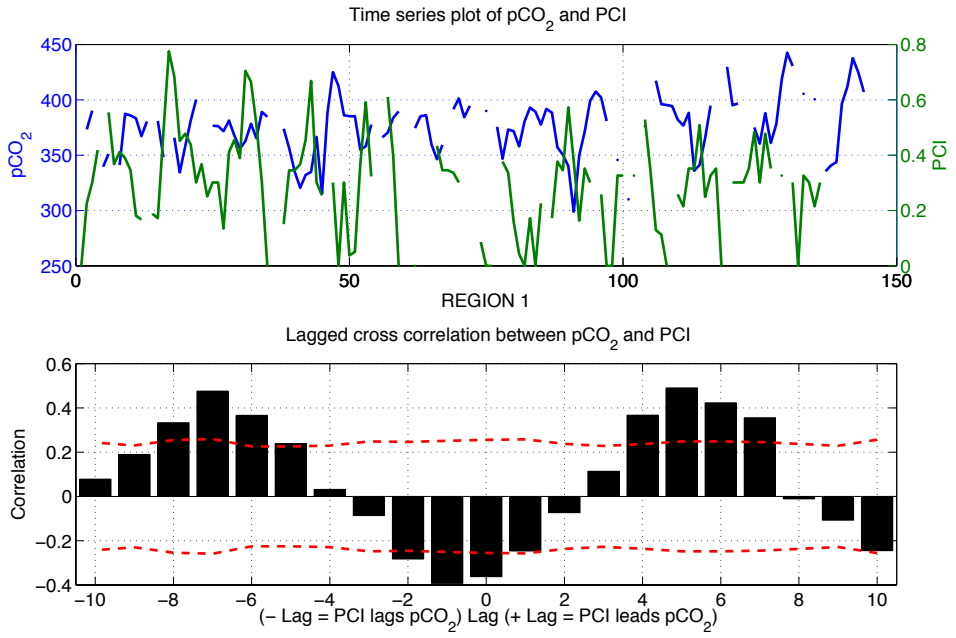

Figure D.9: Cross-correlation between monthly mean pCO_2 (μatm, blue line) and PCI ($\log_{10}$(x+1), green line) from 2002 to 2013 in region 1. The bars above the red-dashed line denote significant correlations with $p < 0.05$.

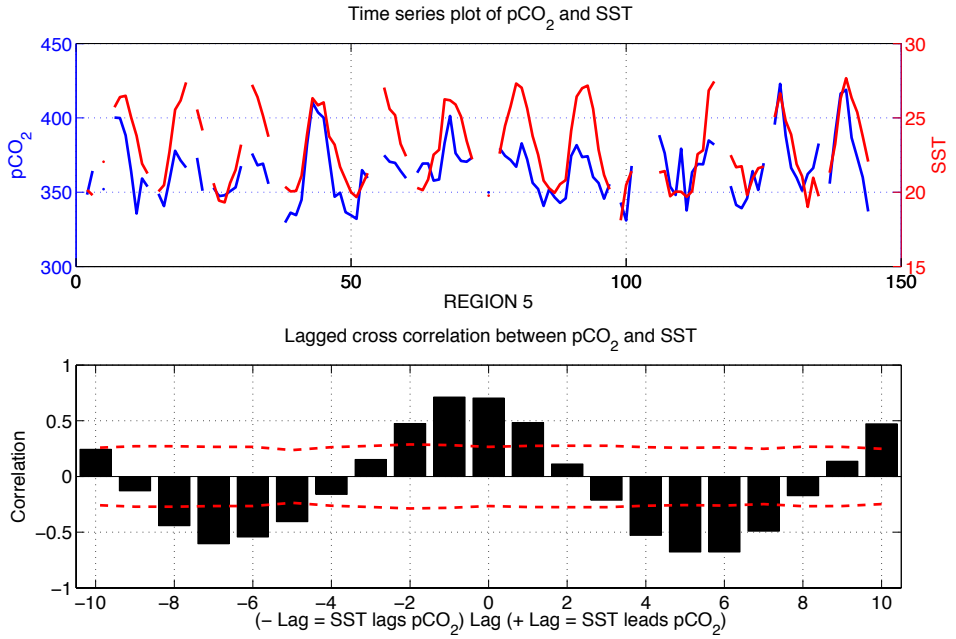

Figure D.10: Cross-correlation between monthly mean pCO_2 (μatm, blue line) and SST (°C, red line) from 2002 to 2013 in region 5. The bars above the red-dashed line denote significant correlations with $p < 0.05$.

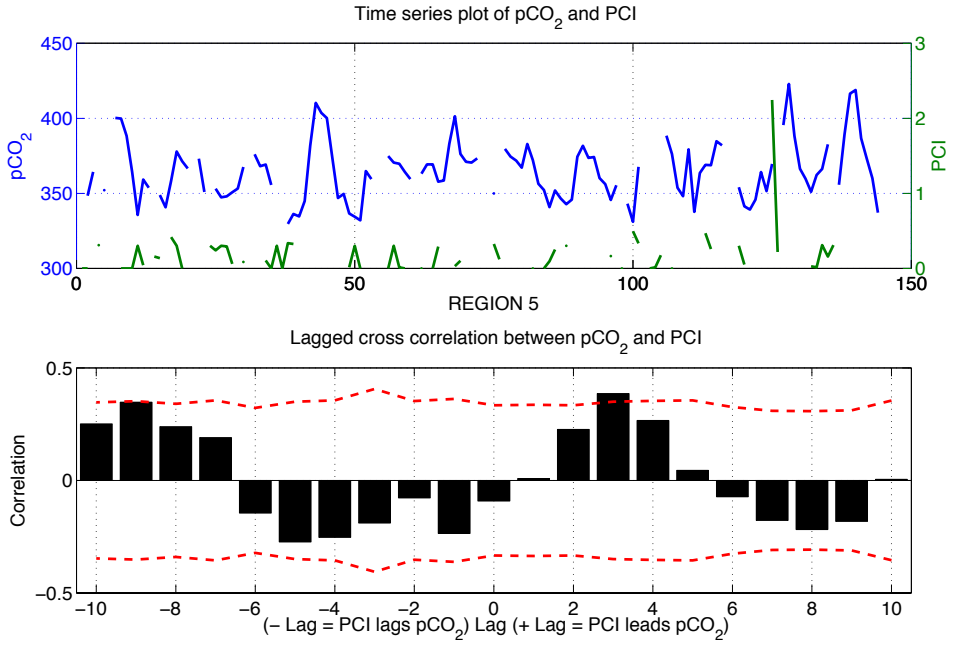

Figure D.11: Cross-correlation between monthly mean pCO_2 (μatm, blue line) and PCI ($\log_{10}$(x+1), green line) from 2002 to 2013 in region 5. The bars above the red-dashed line denote significant correlations with $p < 0.05$.

D.3 Basin-scale trends

The annual linear trends in PCI and *Rhizosolenia* abundance and the correlation coefficients with the air-sea flux of CO_2 (FCO_2) are shown in figures D.12 to D.15.

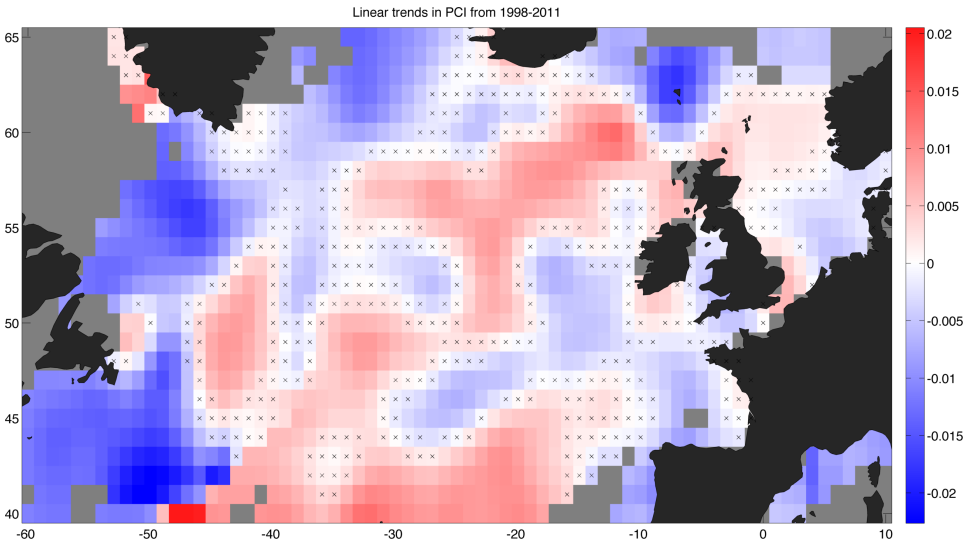

Figure D.12: Annual linear trends in Phytoplankton Colour Index (PCI) in the North Atlantic from 1998 to 2011. Trends that are outside of the 95% significance level ($p \geq 0.05$) are indicated with a cross-hatch. Blue = decreasing. Red = increasing. Grey areas are where there were insufficient data.

The linear trends of both PCI and *Rhizosolenia* abundance are patchy in distribution and similar to that of figure 6.20, with less significant trends ($p \geq 0.05$) seen in *Rhizosolenia* distribution (figure D.13).

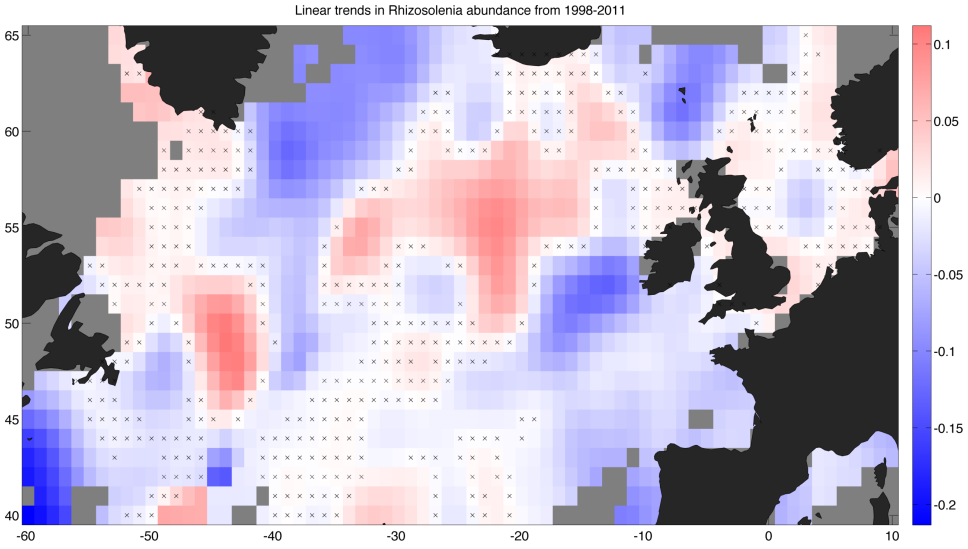

Figure D.13: Annual linear trends in *Rhizosolenia* abundance in the North Atlantic from 1998 to 2011. Trends that are outside of the 95% significance level ($p \geq 0.05$) are indicated with a cross-hatch. Blue = decreasing abundance. Red = increasing abundance. Grey areas are where there were insufficient data.

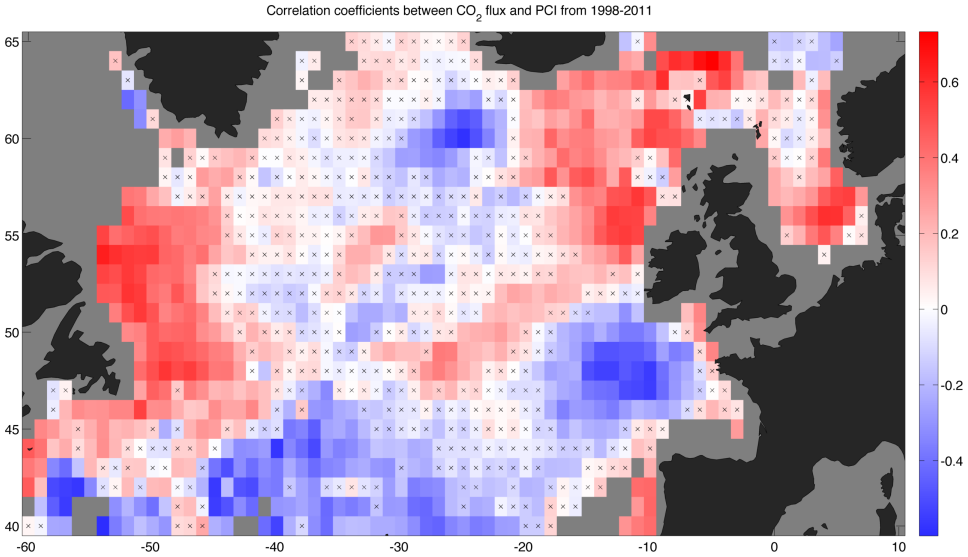

Figure D.14: Correlation coefficients between the air-sea flux of CO_2 (FCO_2) and Phytoplankton Colour Index (PCI). Correlations that are outside of the 95% significance level ($p \geq 0.05$) are indicated with a cross-hatch. Blue = negative correlation. Red = positive correlation. Grey areas are where there were insufficient data. Note: Decreasing FCO_2 is an increasing sink.

The correlation coefficients between PCI and *Rhizosolenia* abundance with FCO_2 are similar to each other, with the decreasing sink of CO_2 in the Bay of

Biscay correlating with the decreasing linear trends in PCI and *Rhizosolenia* abundance (figures D.14 and D.15). The decreasing linear trends in PCI towards the Labrador Sea, is correlated with the increasing sink in CO_2 in this region (figure D.14).

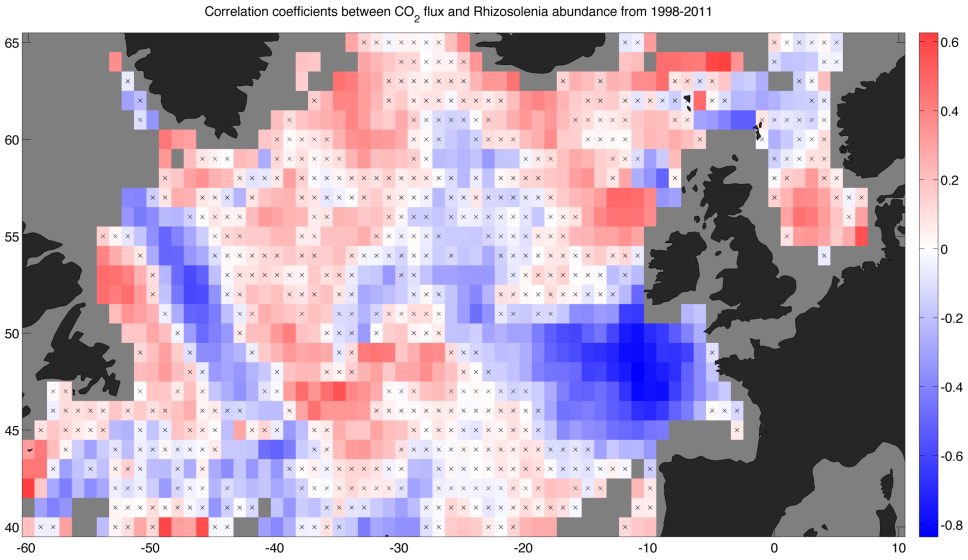

Figure D.15: Correlation coefficients between the air-sea flux of CO_2 (FCO_2) and *Rhizosolenia* abundance. Correlations that are outside of the 95% significance level ($p \geq 0.05$) are indicated with a cross-hatch. Blue = negative correlation. Red = positive correlation. Grey areas are where there were insufficient data. Note: Decreasing FCO_2 is an increasing sink.

References

Aanderaa Data Instruments (2007), Operating Manual Oxygen Optode.

Alvarez-Fernandez, S., H. Lindeboom, and E. Meesters (2012), Temporal changes in plankton of the North Sea: community shifts and environmental drivers, *Marine Ecology Progress Series*, *462*(2), 21–38.

Anderson, L., and J. Sarmiento (1994), Redfield ratios of remineralization determined by nutrient data analysis, *Global biogeochemical cycles*, *8*, 65–80.

Armstrong, R. a., C. Lee, J. I. Hedges, S. Honjo, and S. G. Wakeham (2002), A new, mechanistic model for organic carbon fluxes in the ocean based on the quantitative association of POC with ballast minerals, *Deep-Sea Research Part II: Topical Studies in Oceanography*, *49*(1-3), 219–236.

Bakker, D. C. E., B. Pfeil, K. Smith, S. Hankin, A. Olsen, S. R. Alin, C. Cosca, S. Harasawa, A. Kozyr, Y. Nojiri, K. M. O'Brien, U. Schuster, M. Telszewski, B. Tilbrook, C. Wada, J. Akl, L. Barbero, N. R. Bates, J. Boutin, Y. Bozec, W. J. Cai, R. D. Castle, F. P. Chavez, L. Chen, M. Chierici, K. Currie, H. J. W. De Baar, W. Evans, R. A. Feely, A. Fransson, Z. Gao, B. Hales, N. J. Hardman-Mountford, M. Hoppema, W. J. Huang, C. W. Hunt, B. Huss, T. Ichikawa, T. Johannessen, E. M. Jones, S. D. Jones, S. Jutterström, V. Kitidis, A. Körtzinger, P. Landschützer, S. K. Lauvset, N. Lefèvre, A. B. Manke, J. T. Mathis, L. Merlivat, N. Metzl, A. Murata, T. Newberger, A. M. Omar, T. Ono, G. H. Park, K. Paterson, D. Pierrot, A. F. Ríos, C. L. Sabine, S. Saito, J. Salisbury, V. V. S. S. Sarma, R. Schlitzer, R. Sieger, I. Skjelvan, T. Steinhoff, K. F. Sullivan, H. Sun, A. J. Sutton, T. Suzuki, C. Sweeney, T. Takahashi, J. Tjiputra, N. Tsurushima, S. M. A. C. Van Heuven, D. Vandemark, P. Vlahos, D. W. R. Wallace, R. Wanninkhof, and A. J. Watson (2014), An update to the surface ocean CO2 atlas (SOCAT version 2), *Earth System Science Data*, *6*(1), 69–90.

Balch, W. M. (2005), Calcium carbonate measurements in the surface global ocean based on Moderate-Resolution Imaging Spectroradiometer data, *Journal of Geophysical Research*, *110*.

Barnston, A., and R. Livezey (1987), Classification, seasonality and persistence of low- frequency atmospheric circulation patterns, *Monthly weather review*.

Bartlett, M. (1935), Some Aspects of the Time-Correlation Problem in Regard to Tests of Significance, *Journal of the Royal Statistical Society*, *98*(3), 536–543.

Barton, A. D., M. S. Lozier, and R. G. Williams (2015), Physical controls of variability in North Atlantic phytoplankton communities, *Limnology and Oceanography*, *60*(1), 181–197.

Bates, N., M. Best, and D. Hansell (2005), Spatio-temporal distribution of dissolved inorganic carbon and net community production in the Chukchi and Beaufort Seas, *Deep Sea Research Part II: Topical Studies in Oceanography*, *52*(24-26), 3303–3323.

Beaugrand, G. (2003), An overview of statistical methods applied to CPR data, *Progress In Oceanography*, *58*(2-4), 235–262.

Beaugrand, G. (2009), Decadal changes in climate and ecosystems in the North Atlantic Ocean and adjacent seas, *Deep Sea Research Part II: Topical Studies in Oceanography*, *56*(8-10), 656–673.

Beaugrand, G., M. Edwards, and L. Legendre (2010), Marine biodiversity, ecosystem functioning, and carbon cycles, *Proceedings of the National Academy of Sciences*, *107*(22), 10,120.

Beaugrand, G., F. Ibañez, and J. A. Lindley (2001), Geographical distribution and seasonal and diel changes in the diversity of calanoid copepods in the North Atlantic and North Sea, *Marine Ecology Progress Series*, *219*, 189–203.

Beaugrand, G., A. McQuatters-Gollop, M. Edwards, and E. Goberville (2012), Long-term responses of North Atlantic calcifying plankton to climate change, *Nature Climate Change*, *2*(12), 1–5.

Beaugrand, G., P. C. Reid, F. Ibañez, J. A. Lindley, and M. Edwards (2002), Reorganization of North Atlantic marine copepod biodiversity and climate., *Science (New York, N.Y.)*, *296*(5573), 1692–4.

Behrenfeld, M., and P. G. Falkowski (1997), A consumer's guide to phytoplankton primary productivity models, *Limnology and Oceanography*, *42*(7), 1479–1491.

Behrenfeld, M. J., R. T. O'Malley, D. a. Siegel, C. R. McClain, J. L. Sarmiento, G. C. Feldman, A. J. Milligan, P. G. Falkowski, R. M. Letelier, and E. S. Boss (2006), Climate-driven trends in contemporary ocean productivity., *Nature*, *444*(7120), 752–5.

Bell, S., and R. Johnson (1997), BATS methodology - Chapter 6: Determination of Dissolved Oxygen by the Winkler Procedure.

Benson, B. B., and D. Krause (1984), The concentration and isotopic fractionation of oxygen dissolved in freshwater and seawater in equilibrium with the atmosphere, *Limnology and Oceanography*, *29*(3), 620–632.

Bittig, H. C., and A. Körtzinger (2015), Tackling oxygen optode drift: Near-surface and in-air oxygen optode measurements on a float provide an accurate in-situ reference, *Journal of Atmospheric and Oceanic Technology*.

Bopp, L., O. Aumont, P. Cadule, S. Alvain, and M. Gehlen (2005), Response of diatoms distribution to global warming and potential implications: A global model study, *Geophysical Research Letters*, *32*.

Box, G. E. P., G. M. Jenkins, and G. C. Reinsel (1994), *Time series analysis: forecasting and control*, 3rd edn., Englewood Cliffs, NJ: Prentice Hall.

Boyer, T., M. Conkright, and S. Levitus (1999), Seasonal variability of dissolved oxygen, percent oxygen saturation, and apparent oxygen utilization in the Atlantic and Pacific Oceans, *Deep Sea Research Part I*, *46*, 1593–1613.

Bretherton, C., and M. Widmann (1999), The effective number of spatial degrees of freedom of a time-varying field, *Journal of Climate*, *12*, 1990–2009.

Brewer, P., and J. Goldman (1976), Alkalinity changes generated by phytoplankton growth, *Limnology and Oceanography*, *21*, 108–117.

Broecker, W., and E. Clark (2009), Ratio of coccolith CaCO3 to foraminifera CaCO3 in late Holocene deep sea sediments, *Paleoceanography*, *24*(3), 1–11.

Buitenhuis, E. T., T. Hashioka, and C. L. Quéré (2013), Combined constraints on global ocean primary production using observations and models, *Global Biogeochemical Cycles*, *27*(3), 847–858.

Cannaby, H., and Y. Hüsrevolu (2009), The influence of low-frequency variability and long-term trends in North Atlantic sea surface temperature on Irish waters, *ICES Journal of Marine Science*, pp. 1480–1489.

Capone, D. G., J. a. Burns, J. P. Montoya, A. Subramaniam, C. Mahaffey, T. Gunderson, A. F. Michaels, and E. J. Carpenter (2005), Nitrogen fixation by Trichodesmium spp.: An important source of new nitrogen to the tropical and subtropical North Atlantic Ocean, *Global Biogeochemical Cycles*, *19*.

Carter, B. R., J. R. Toggweiler, R. M. Key, and J. L. Sarmiento (2014), Processes determining the marine alkalinity and carbonate saturation distributions, *Biogeosciences*, *11*(7), 7349–7362.

Cianca, A., R. Santana, S. Hartman, J. Martin-Gonzalez, M. Gonzalez-Davila, M. Rueda, O. Linas, and S. Neuer (2013), Oxygen dynamics in the North Atlantic subtropical gyre, *Deep Sea Research II*, *93*, 135–147.

Colebrook, J. (1975), The Continuous Plankton Recorder survey: automatic data processing methods., *Bulletin of Marine Ecology, 8: 123- 142*.

Cooley, S. R., V. J. Coles, A. Subramaniam, and P. L. Yager (2007), Seasonal variations in the Amazon plume-related atmospheric carbon sink, *Global Biogeochemical Cycles*, *21*(3).

Cooper, D., A. Watson, and R. Ling (1998), Variation of pCO2 along a North Atlantic shipping route (UK to the Caribbean): A year of automated observations, *Marine chemistry*, *60*(1-2), 147–164.

Curry, R., B. Dickson, and I. Yashayaev (2003), A change in the freshwater balance of the Atlantic Ocean over the past four decades., *Nature*, *426*(6968), 826–9.

da Cunha, L. C., and E. T. Buitenhuis (2013), Riverine influence on the tropical Atlantic Ocean biogeochemistry, *Biogeosciences*, *10*(10), 6357–6373.

Dai, A., and K. Trenberth (2002), Estimates of freshwater discharge from continents: Latitudinal and seasonal variations, *Journal of hydrometeorology*, pp. 660–687.

Daniels, C. J., T. Tyrrell, A. J. Poulton, and L. Pettit (2012), The influence of lithogenic material on particulate inorganic carbon measurements of coccolithophores in the Bay of Biscay, *Limnology and Oceanography*, *57*(1), 145–153.

Davis, C. E., C. Mahaffey, G. A. Wolff, and J. Sharples (2014), A storm in a shelf sea: Variation in phosphorus distribution and organic matter stoichiometry, *Geophysical Research Letters*, *41*.

del Giorgio, P. A., and P. J. l. B. Williams (2005), *Respiration in aquatic ecosystems*, Oxford University Press.

Dickson, A. (1981), An exact definition of total alkalinity and a procedure for the estimation of alkalinity and total inorganic carbon from titration data, *Deep Sea Research Part A. Oceanographic Research Papers*, *28*(6), 609–623.

Dickson, A., and F. Millero (1987), A comparison of the equilibrium constants for the dissociation of carbonic acid in seawater media, *Deep Sea Research*, *34*(111), 1733–1743.

Dickson, A., C. Sabine, and J. Christian (2007), Guide to best practices for ocean CO2 measurements, *PICES special publication*, *3*(8).

Dickson, A. G. (1990), Standard potential of the reaction: AgCl(s) + 12H2(g) = Ag(s) + HCl(aq), and and the standard acidity constant of the ion HSO4 in synthetic sea water from 273.15 to 318.15 K, *The Journal of Chemical Thermodynamics*, *22*(2), 113–127.

Dlugokency, E., K. Masarie, P. Lang, and P. Tans (2014), NOAA Greenhouse Gas Reference from Atmospheric Carbon Dioxide Dry Air Mole Fractions from the NOAA ESRL Carbon Cycle Cooperative Global Air Sampling Network.

Doney, S. C. (2010), The growing human footprint on coastal and open-ocean biogeochemistry., *Science*, *328*(5985), 1512–1516.

Ducklow, H., C. Carlson, and N. Bates (1995), Dissolved organic carbon as a component of the biological pump in the North Atlantic Ocean, *Phil. Trans. R. Soc. Lond. B*, *348*, 161–167.

Ducklow, H. W., and S. C. Doney (2013), What is the metabolic state of the oligotrophic ocean? A debate., *Annual review of marine science*, *5*, 525–33.

Dumousseaud, C., E. P. Achterberg, T. Tyrrell, a. Charalampopoulou, U. Schuster, M. Hartman, and D. J. Hydes (2010), Contrasting effects of temperature and winter mixing on the seasonal and inter-annual variability of the carbonate system in the Northeast Atlantic Ocean, *Biogeosciences*, *7*(5), 1481–1492.

Edwards, M. (2000), *Large-scale temporal and spatial patterns of marine phytoplankton in the north-east Atlantic*, Ph.D. thesis, University of Plymouth.

Edwards, M., G. Beaugrand, P. Helaouët, J. Alheit, and S. Coombs (2013), Marine Ecosystem Response to the Atlantic Multidecadal Oscillation, *PLoS ONE*, *8*(2), e57,212.

Edwards, M., and A. A. J. Richardson (2004), Impact of climate change on marine pelagic phenology and trophic mismatch, *Nature*, *430*, 881–884.

Emerson, S. (1987), Seasonal oxygen cycles and biological new production in surface waters of the subarctic Pacific Ocean, *Journal of Geophysical Research*, *92*, 6535–6544.

Emerson, S. (2014), Annual net community production and the biological carbon flux in the ocean, *Global Biogeochemical Cycles*, *28*, 1–12.

Emerson, S., P. Quay, D. Karl, C. Winn, L. Tupas, and M. Landry (1997), Experimental determination of the organic carbon flux from open-ocean surface waters, *Nature*, *389*(October), 951–954.

Emerson, S., and C. Stump (2010), Net biological oxygen production in the oceanII: Remote in situ measurements of O2 and N2 in subarctic pacific surface waters, *Deep Sea Research Part I: Oceanographic Research Papers*, *57*(10), 1255–1265.

Emerson, S., C. Stump, and D. Nicholson (2008), Net biological oxygen production in the ocean: Remote in situ measurements of O2 and N2 in surface waters, *Global Biogeochemical Cycles*, *22*(3).

Emerson, S. R., and S. Bushinsky (2014), Oxygen concentrations and biological fluxes in the open ocean, *Oceanography*, *27*(1), 168–171.

Enfield, D. (2001), The Atlantic multidecadal oscillation and its relation to rainfall and river flows in the continental US, *Geophysical Research Letters*.

Falkowski, P. G. (1998), Biogeochemical Controls and Feedbacks on Ocean Primary Production, *Science*, *281*(5374), 200–206.

Feng, Y., C. E. Hare, K. Leblanc, J. M. Rose, Y. Zhang, G. R. DiTullio, P. a. Lee, S. W. Wilhelm, J. M. Rowe, J. Sun, N. Nemcek, C. Gueguen, U. Passow, I. Benner, C. Brown, and D. a. Hutchins (2009), Effects of increased pCO2 and temperature on the north atlantic spring bloom. I. The phytoplankton community and biogeochemical response, *Marine Ecology Progress Series*, *388*, 13–25.

Follows, M., and S. Dutkiewicz (2001), Meteorological modulation of the North Atlantic spring bloom, *Deep Sea Research Part II: Topical Studies in Oceanography*.

Follows, M., and R. G. Williams (2004), Mechanisms Controlling the Air-Sea Flux of CO2 in the North Atlantic, *The Ocean Carbon Cycle and Climate*, (1), 217–249.

Friis, K., A. Kortzinger, and J. M. Wallace (2003), The salinity normalization of marine inorganic carbon chemistry data, *Geophysical Research Letters*, *30*(2), 1085.

García, H., and L. Gordon (1992), Oxygen solubility in seawater: Better fitting equations., *Limnology and Oceanography*, *37*(6), 1307–1312.

Garcia, H., and R. Keeling (2001), On the global oxygen anomaly and air-sea flux, *Journal of Geophysical Research*, *106*, 31,155–31,166.

Garcia, H. E., R. A. Locarnini, T. P. Boyer, J. I. Antonov, O. K. Baranova, M. M. Zweng, and D. R. Johnson (2010), World Ocean Atlas 2009, Volume 3: Dissolved Oxygen, Apparent Oxygen Utilization, and Oxygen Saturation., *S. Levitus, Ed. NOAA Atlas NESDIS 70, U.S. Government Printing Office, Washington, D.C., 344 pp.*, *3*.

Gloël, J. (2012), *Triple oxygen isotopes and oxygen / argon ratio measurements to enhance coastal and open ocean production / respiration comparisons*, Ph.D. thesis, University of East Anglia, Norwich, UK.

Glover, D., W. Jenkins, and S. Doney (2005), *Modeling methods for marine science*, May, Cambridge University Press.

Goodkin, N. F., K. a. Hughen, S. C. Doney, and W. B. Curry (2008), Increased multidecadal variability of the North Atlantic Oscillation since 1781, *Nature Geoscience*, *1*(12), 844–848.

Gordon, R., G. C. Boynton, W. M. Balch, D. S. Harbour, T. J. Smyth, and W. B. Bay (2001), Retrieval of Coccolithophore from SeaWiFS Imagery Calcite Concentration radiance, *28*(8), 1587–1590.

Grasshoff, K., K. Kremling, and M. Ehrhardt (1999), *Methods of seawater analysis*, vol. 3rd editio, Wiley.

Gruber, N. (2009), Carbon cycle: Fickle trends in the ocean.

Gruber, N., M. Gloor, S. E. Mikaloff Fletcher, S. C. Doney, S. Dutkiewicz, M. J. Follows, M. Gerber, A. R. Jacobson, F. Joos, K. Lindsay, D. Menemenlis, A. Mouchet, S. A. Müller, J. L. Sarmiento, and T. Takahashi (2009), Oceanic sources, sinks, and transport of atmospheric CO2, *Global Biogeochemical Cycles*, *23*(1).

Gruber, N., C. D. Keeling, and N. R. Bates (2002), Interannual variability in the North Atlantic Ocean carbon sink., *Science (New York, N.Y.)*, *298*(5602), 2374–8.

Hallegraeff, G. M. (2010), Ocean Climate Change, Phytoplankton Community Responses, and Harmful Algal Blooms: a Formidable Predictive Challenge, *Journal of Phycology*, *46*(2), 220–235.

Hansen, H. P., and F. Koroleff (2007), Determination of nutrients, in Methods of Seawater Analysis, in: *Methods of Seawater Analysis* (Grasshoff, K., M. Ehrhardt, and K. Kremling, eds.), pp. 159–228, Wiley-VCH Verlag GmbH Weinheim, Germany.

Harris, V., M. Edwards, and S. C. Olhede (2013), Multidecadal Atlantic climate variability and its impact on marine pelagic communities, *Journal of Marine Systems*, pp. 1–15.

Hartman, S. E., Z.-P. Jiang, D. Turk, R. S. Lampitt, H. Frigstad, C. Ostle, and U. Schuster (2015), Biogeochemical variations at the Porcupine Abyssal Plain sustained Observatory in the northeast Atlantic Ocean, from weekly to interannual timescales, *Biogeosciences*, *12*, 845–853.

Hartmann, D. L., a. M. G. Klein Tank, M. Rusticucci, L. V. Alexander, S. Brönnimann, Y. Charabi, F. J. Dentener, E. J. Dlugokencky, D. R. Easterling, A. Kaplan, B. J. Soden, P. W. Thorne, M. Wild, and P. M. Zhai (2013), *Observations: Atmosphere and Surface. In: Climate Change 2013: The Physical Science Basis. Contribution of Working Group I to the Fifth Assessment Report of the Intergovernmental Panel on Climate Change*, Cambridge University Press, Cambridge, UK and New York, NY, USA, 2013.

Hays, G., A. Richardson, and C. Robinson (2005), Climate change and marine plankton, *Trends in Ecology & Evolution*, *20*(6), 337–344.

Hays, G. C. (1994), Mesh selection and filtration efficiency of the Continuous Plankton Recorder, *Journal of Plankton Research*, *16*(4), 403–412.

Hays, G. G. C. (2003), A review of the adaptive significance and ecosystem consequences of zooplankton diel vertical migrations, *Hydrobiologia*, *503*(1), 163–170.

Helaouët, P., G. Beaugrand, and M. Edwards (2013), Understanding Long-Term Changes in Species Abundance Using a Niche-Based Approach, *PLoS ONE*, *8*(11).

Helm, K. P., N. L. Bindoff, and J. a. Church (2011), Observed decreases in oxygen content of the global ocean, *Geophysical Research Letters*, *38*(23), 1–6.

Henson, S., R. Lampitt, and D. Johns (2012), Variability in phytoplankton community structure in response to the North Atlantic Oscillation and implications for organic carbon flux, *Limnology and Oceanography*, *57*(6), 1591–1601.

Henson, S., J. Sarmiento, J. Dunne, L. Bopp, I. Lima, S. Doney, J. John, and C. Beaulieu (2010), Detection of anthropogenic climate change in satellite records of ocean chlorophyll and productivity, *Biogeosciences*, pp. 621–640.

Henson, S. a., J. P. Dunne, and J. L. Sarmiento (2009), Decadal variability in North Atlantic phytoplankton blooms, *Journal of Geophysical Research*, *114*.

Hinder, S., G. Hays, and M. Edwards (2012), Changes in marine dinoflagellate and diatom abundance under climate change, *Nature Climate Change*, (2), 271–275.

Hinder, S. L., M. B. Gravenor, M. Edwards, C. Ostle, O. G. Bodger, P. L. M. Lee, A. W. Walne, and G. C. Hays (2014), Multi-decadal range changes vs. thermal adaptation for north east Atlantic oceanic copepods in the face of climate change, *Global Change Biology*, *20*(1), 140–146.

Holligan, P. M., E. Fcrmindcz, W. M. Balch, P. Boyd, H. Peter, M. Finch, B. Groom, K. Muller, D. A. Putdie, C. C. Trees, S. M. Turner, U. Kingdom, and S. Diego (1993), Abstract . The biogeochemical properties of an 28oW and lasted approximately West Hoe , beam attenuation coefficient , levels of particulate inorganic carbon , and coccolith Rates of both photosynthesis and calcification were typically relatively low with, *7*(4), 879–900.

Hood, R. R., H. W. Bange, L. Beal, L. E. Beckley, P. Burkill, L. Cowie, N. D. Adamo, G. Ganssen, H. Hendon, J. Hermes, M. Mcphaden, M. Roberts, S. Singh, E. Urban, and W. Yu (2015), The Second International Indian Ocean Expedition (IIOE-2) Draft Science Plan.

Hooker, S. B., N. W. Rees, and J. Aiken (2000), An objective methodology for identifying oceanic provinces, *Progress in Oceanography*, *45*, 313–338.

Hopkins, J., S. A. Henson, S. C. Painter, T. Tyrrell, and A. J. Poulton (2015), Phenological characteristics of global coccolithophore blooms, *Global Biogeochemical Cycles*.

House, J. I., I. C. Prentice, and C. C. Le Quéré (2002), Maximum impacts of future reforestation or deforestation on atmospheric CO2, *Global Change Biology*, *8*(11), 1047–1052.

Hunt, H. (1968), Continuous Plankton Records: contribution towards a plankton atlas of the north Atlantic and the North Sea. Part XI: The seasonal and annual distributions of Thaliacea., *Bulletin of Marine Ecology*, *6*, 225–249.

Hurrell, J. W. (1995), Decadal Trends in the North Atlantic Oscillation: Regional Temperatures and Precipitation, *Science*, *269*(5224), 676–679.

Hurrell, J. W., Y. Kushnir, G. Ottersen, and M. Visbeck (2003), An overview of the North Atlantic Oscillation. In The North Atlantic Oscillation: Climate Significance and Environmental Impact, *Geophysical Monograph Series*, pp. 1–35.

IPCC (2013), *Summary for Policymakers. In: Climate Change 2013: The Physical Science Basis. Contribution of Working Group I to the Fifth Assessment Report of the Intergovernmental Panel on Climate Change [Stocker, T.F., D. Qin, G.-K. Plattner, M. Tignor, S.K. Allen, J*, Cambridge University Press, Cambridge, United Kingdom and New York, NY, USA.

Jähne, B., G. Heinz, and W. Dietrich (1987), Measurement of the diffusion coefficients of sparingly soluble gases in water, *Journal of Geophysical Research*, *92*, 10,767.

Jiang, Z.-p., D. J. Hydes, T. Tyrrell, S. E. Hartman, M. C. Hartman, C. Dumousseaud, X. A. Padin, and I. Skjelvan (2013), Key controls on the seasonal and interannual variations of the carbonate system and air-sea CO2 flux in the Northeast Atlantic (Bay of Biscay), *Journal of Geophysical Research: Oceans*, *118*, 1–16.

Jiang, Z.-P., T. Tyrrell, D. J. Hydes, M. Dai, and S. Hartman (2014), Variability of alkalinity and the alkalinity-salinity relationship in the tropical and subtropical surface ocean, *Global Biogeochemical Cycles*.

Johnson, K. (2010a), Simultaneous measurements of nitrate, oxygen, and carbon dioxide on oceanographic moorings: Observing the Redfield ratio in real time, *Limnology and Oceanography*, *55*(2), 615–627.

Johnson, K., K. Wills, D. Butler, W. Johnson, and C. Wong (1993), Coulometric total carbon dioxide analysis for marine studies: maximizing the performance of an automated gas extraction system and coulometric detector, *Marine Chemistry*, *44*(2-4), 167–187.

Johnson, M. (2010b), A numerical scheme to calculate temperature and salinity dependent air-water transfer velocities for any gas, *Ocean Science*, *6*, 913–932.

Jones, P. D., D. H. Lister, T. J. Osborn, C. Harpham, M. Salmon, and C. P. Morice (2012), Hemispheric and large-scale land-surface air temperature variations: An extensive revision and an update to 2010, *Journal of Geophysical Research*, *117*.

Jönsson, B. F., J. E. Salisbury, and a. Mahadevan (2011), Large variability in continental shelf production of phytoplankton carbon revealed by satellite, *Biogeosciences*, *8*(5), 1213–1223.

Kähler, P., and W. Koeve (2001), Marine dissolved organic matter : can its C : N ratio explain carbon overconsumption?, *Deep Sea Research Part I: Oceanographic Research Papers*, *48*, 49–62.

Kaiser, M., M. Attrill, S. Jennings, D. Thomas, D. Barnes, A. Brierley, N. Polunin, D. Raffaelli, and P. l. B. Williams (2005), *Marine Ecology: Processes, Systems, and Impacts*, Oxford University Press.

Keeling, R., and B. Stephens (1998), Seasonal variations in the atmospheric O2/N2 ratio in relation to the kinetics of air-sea gas exchange, *Global Biogeochemical Cycles*, *12*(1), 141–163.

Kemp, a. E. S., R. B. Pearce, I. Grigorov, J. Rance, C. B. Lange, P. Quilty, and I. Salter (2006), Production of giant marine diatoms and their export at oceanic frontal zones: Implications for Si and C flux from stratified oceans, *Global Biogeochemical Cycles*, *20*, 1–13.

Key, R. M., A. Kozyr, C. L. Sabine, K. Lee, R. Wanninkhof, J. L. Bullister, R. a. Feely, F. J. Millero, C. Mordy, and T.-H. Peng (2004), A global ocean carbon climatology: Results from Global Data Analysis Project (GLODAP), *Global Biogeochemical Cycles*, *18*(4).

Kitidis, V., N. J. Hardman-Mountford, E. Litt, I. Brown, D. Cummings, S. Hartman, D. Hydes, J. R. Fishwick, C. Harris, V. Martinez-Vicente, E. M. S. Woodward, and T. J. Smyth (2012), Seasonal dynamics of the carbonate system in the Western English Channel, *Continental Shelf Research*, *42*, 30–40.

Klausmeier, C., E. Litchman, T. Daufresne, and S. Levin (2004), Optimal nitrogen-to-phosphorus stoichiometry of phytoplankton, *Nature*, *429*(May), 171–174.

Knap, A., A. Michaels, and A. Close (1996), Protocols for the Joint Global Ocean Flux Study (JGOFS) Core Measurements, *IOC Manuals and Guides*, *29*.

Körtzinger, A., J. Schimanski, and U. Send (2005), High quality oxygen measurements from profiling floats: A promising new technique, *Journal of Atmospheric and Oceanic Technology*, *22*, 302–308.

Körtzinger, A., U. Send, R. S. Lampitt, S. Hartman, D. W. R. Wallace, J. Karstensen, M. G. Villagarcia, O. Llinás, and M. D. DeGrandpre (2008), The seasonal pCO2 cycle at 49N/16.5W in the northeastern Atlantic Ocean and what it tells us about biological productivity, *Journal of Geophysical Research*, *113*.

Landschützer, P. (2014), *Variability of the Global Ocean Carbon Sink (1998 through 2011)*, Ph.D. thesis, The University of East Anglia.

Landschützer, P., N. Gruber, D. Bakker, and U. Schuster (2014), Recent variability of the global ocean carbon sink, *Global Biogeochemical Cycles*.

Landschützer, P., N. Gruber, D. C. E. Bakker, U. Schuster, S. Nakaoka, M. R. Payne, T. P. Sasse, and J. Zeng (2013), A neural network-based estimate of the seasonal to inter-annual variability of the Atlantic Ocean carbon sink, *Biogeosciences*, *10*, 7793–7815.

Landschützer, P., J. F. Tjiputra, K. Assmann, and C. Heinze (2011), A model study on the sensitivity of surface ocean CO2 pressure with respect to the CO2 gas exchange rate, *Biogeosciences Discussions*, *8*(6), 10,797–10,821.

Laruelle, G. G., R. Lauerwald, B. Pfeil, and P. Regnier (2014), Regionalized global budget of the CO2 exchange at the air-water interface in continental shelf seas, *Global Biogeochemical Cycles*, pp. 1199–1214.

Laws, E. (1991), Photosynthetic quotients, new production and net community production in the open ocean, *Deep Sea Research Part A*, *38*(1), 143–167.

Le Quéré, C., S. P. Harrison, I. Colin Prentice, E. T. Buitenhuis, O. Aumont, L. Bopp, H. Claustre, L. Cotrim Da Cunha, R. Geider, X. Giraud, C. Klaas, K. E. Kohfeld, L. Legendre, M. Manizza, T. Platt, R. B. Rivkin, S. Sathyendranath, J. Uitz, A. J. Watson, and D. Wolf-Gladrow (2005), Ecosystem dynamics based on plankton functional types for global ocean biogeochemistry models\rdoi:10.1111/j.1365-2486.2005.1004.x, *Global Change Biology*, *11*(11), 2016–2040.

Le Quéré, C., M. R. Raupach, J. G. Canadell, G. Marland, L. Bopp, P. Ciais, T. J. Conway, S. C. Doney, R. a. Feely, P. Foster, P. Friedlingstein, K. Gurney, R. a. Houghton, J. I. House, C. Huntingford, P. E. Levy, M. R. Lomas, J. Majkut, N. Metzl, J. P. Ometto, G. P. Peters, I. C. Prentice, J. T. Randerson, S. W. Running, J. L. Sarmiento, U. Schuster, S. Sitch, T. Takahashi, N. Viovy, V. D. Werf, R. Guido, and F. I. Woodward (2009), Trends in the sources and sinks of carbon dioxide, *Nature Geoscience*, *2*(12), 831–836.

Le Quéré, C., T. Takahashi, E. T. Buitenhuis, C. Rödenbeck, and S. C. Sutherland (2010), Impact of climate change and variability on the global oceanic sink of CO2, *Global Biogeochemical Cycles*, *24*, 1–10.

Leckebusch, G. C., and U. Ulbrich (2004), On the relationship between cyclones and extreme windstorm events over Europe under climate change, *Global and Planetary Change*, *44*(1-4), 181–193.

Lee, K. (2001), Global net community production estimated from the annual cycle of surface water total dissolved inorganic carbon, *Limnology and Oceanography*, *46*(6), 1287–1297.

Lee, K., L. T. Tong, F. J. Millero, C. L. Sabine, A. G. Dickson, C. Goyet, G.-H. Park, R. Wanninkhof, R. a. Feely, and R. M. Key (2006), Global relationships of total alkalinity with salinity and temperature in surface waters of the world's oceans, *Geophysical Research Letters*, *33*.

Lefèvre, D., C. Guigue, and I. Obernosterer (2008), The metabolic balance at two contrasting sites in the Southern Ocean: The iron-fertilized Kerguelen area and HNLC waters, *Deep Sea Research Part II*, *55*, 766–776.

Lefèvre, N. (2004), A decrease in the sink for atmospheric CO 2 in the North Atlantic, *Geophysical Research Letters*, *31*(7), 2–5.

Lefèvre, N., and L. Merlivat (2012), Carbon and oxygen net community production in the eastern tropical Atlantic estimated from a moored buoy, *Global Biogeochemical Cycles*, *26*(1).

Levitus, S., J. I. Antonov, T. P. Boyer, R. A. Locarnini, H. E. Garcia, and A. V. Mishonov (2009), Global ocean heat content 1955 2008 in light of recently revealed instrumentation problems, *Geophysical Research Letters*.

Lewis, E., D. Wallace, and L. Allison (1998), *Program developed for CO2 system calculations*, Carbon Dioxide Information Analysis Center, managed by Lockheed Martin Energy Research Corporation for the US Department of Energy.

LI-COR, I. (2007), *LI-7000 CO2/H2O Analyzer Instruction Manual*.

Liang, J.-H., C. Deutsch, J. C. McWilliams, B. Baschek, P. P. Sullivan, and D. Chiba (2013), Parameterizing bubble-mediated air-sea gas exchange and its effect on ocean ventilation, *Global Biogeochemical Cycles*, *27*(3), 894–905.

Longhurst, A. (2006), *Ecological geography of the sea*, Ecological Geography of the Sea Series, 2nd edn., Academic Press, San Diego.

Lovenduski, N. S., N. Gruber, and S. C. Doney (2008), Toward a mechanistic understanding of the decadal trends in the Southern Ocean carbon sink, *Global Biogeochemical Cycles*, *22*(3).

Lozier, M. S., A. C. Dave, J. B. Palter, L. M. Gerber, and R. T. Barber (2011), On the relationship between stratification and primary productivity in the North Atlantic, *Geophysical Research Letters*, *38*(18), 1–6.

Lueker, T. J., A. G. Dickson, and C. D. Keeling (2000), Ocean pCO2 calculated from dissolved inorganic carbon, alkalinity, and equations for K1 and K2: validation based on laboratory measurements of CO2 in gas and seawater at equilibrium, *Marine Chemistry*, *70*(1-3), 105–119.

Lüger, H., R. Wanninkhof, D. W. R. Wallace, and A. Körtzinger (2006), CO2 fluxes in the subtropical and subarctic North Atlantic based on measurements from a volunteer observing ship, *Journal of Geophysical Research: Oceans*, *111*(6).

Lüthi, D., M. Le Floch, B. Bereiter, T. Blunier, J.-M. Barnola, U. Siegenthaler, D. Raynaud, J. Jouzel, H. Fischer, K. Kawamura, and T. F. Stocker (2008), High-resolution carbon dioxide concentration record 650,000-800,000 years before present., *Nature*, *453*(7193), 379–382.

Luz, B., and E. Barkan (2009), Net and gross oxygen production from O2/Ar, 17O/16O and 18O/16O ratios, *Aquatic Microbial Ecology*, *56*, 133–145.

Margalef, R. (1978), Life-forms of phytoplankton as survival alternatives in an unstable environment, *Oceanologica Acta*, *1*, 493–509.

Marshall, J., Y. Kushnir, D. Battisti, P. Chang, A. Czaja, R. Dickson, J. Hurrell, M. McCartney, R. Saravanan, and M. Visbeck (2001), North Atlantic climate variability: phenomena, impacts and mechanisms, *International Journal of Climatology*, *21*(15), 1863–1898.

Martin-jézéquel, V., P. N. Copernic, F. Plouzane, and M. A. Brzezinski (2000), Silicon metabolism in diatoms : implications for growth, *Journal of Phycology*, *36*, 821–840.

Martinez, E., D. Antoine, F. D'Ortenzio, and C. de Boyer Montégut (2011), Phytoplankton spring and fall blooms in the North Atlantic in the 1980s and 2000s, *Journal of Geophysical Research*, *116*.

Martiny, A. C., C. T. a. Pham, F. W. Primeau, J. a. Vrugt, J. K. Moore, S. a. Levin, and M. W. Lomas (2013), Strong latitudinal patterns in the elemental ratios of marine plankton and organic matter, *Nature Geoscience*, *6*(4), 279–283.

Mathis, J. T., J. N. Cross, N. R. Bates, S. Bradley Moran, M. W. Lomas, C. W. Mordy, and P. J. Stabeno (2010), Seasonal distribution of dissolved inorganic carbon and net community production on the Bering Sea shelf, *Biogeosciences*, *7*(5), 1769–1787.

McKinley, G. (2000), Interannual variability of the air-sea flux of oxygen in the North Atlantic, *Geophysical Research Letters*, *27*(18), 2933–2936.

McKinley, G. a., A. R. Fay, T. Takahashi, and N. Metzl (2011), Convergence of atmospheric and North Atlantic carbon dioxide trends on multidecadal timescales, *Nature Geoscience*, *4*(9), 606–610.

McQuatters-Gollop, A., P. H. Burkill, G. Beaugrand, D. G. Johns, J.-P. Gattuso, and M. Edwards (2010), *Atlas of Calcifying Plankton: Results from the North Atlantic Continuous Plankton Recorder survey*, Tech. rep.

McQuatters-Gollop, A., A. J. Gilbert, L. D. Mee, J. E. Vermaat, Y. Artioli, C. Humborg, and F. Wulff (2009), How well do ecosystem indicators communicate the effects of anthropogenic eutrophication?, *Estuarine, Coastal and Shelf Science*, *82*(4), 583–596.

McQuatters-Gollop, A., P. Reid, M. Edwards, P. Burkill, C. Castellani, S. Batten, W. Gieskes, D. Beare, R. Bidigare, E. Head, and Others (2011), Is there a decline in marine phytoplankton?, *Nature*, *472*(7342).

Mehrbach, C., C. H. Culberson, J. E. Hawley, and R. M. Pytkowics (1973), Measurement of the apparent dissociation constants of carbonic acid in seawater at atmospheric pressure, *Limnology and Oceanography*, *18*.

Menemenlis, D., J. Campin, P. Heimbach, C. Hill, T. Lee, A. Nguyen, M. Schodlok, and H. Zhang (2008), ECCO2: High resolution global ocean and sea ice data synthesis.

Michaels, A. F., and M. W. Silver (1988), Primary production, sinking fluxes and the microbial food web, *Deep Sea Research Part A. Oceanographic Research Papers*, *35*(4), 473–490.

Millero, F. J., K. Lee, and M. Roche (1998), Distribution of alkalinity in the surface waters of the major oceans, *Marine Chemistry*, *60*(1-2), 111–130.

Mintrop, L. (2011), VINDTA Manual for Versions 3S and 3C.

Mintrop, L., F. Pérez, M. González Dávila, J. Santana-Casiano, and A. Körtzinger (2000), Alkalinity Determination by Potentiometry: Intercalibration using three Different Methods, *Ciencias Marinas*, *26*, 23–27.

Morel, A., and L. Prieur (1977), Analysis of variations in ocean color, *Limnology and Oceanography*, *22*(4), 709–722.

Myhre, G., D. Shindell, F.-M. Bréon, W. Collins, J. Fuglestvedt, J. Huang, D. Koch, J.-F. Lamarque, D. Lee, B. Mendoza, T. Nakajima, A. Robock, G. Stephens, T. Takemura, and H. Zhan (2013), 2013: Anthropogenic and Natural Radiative Forcing, in: *Climate Change 2013: The Physical Science Basis. Contribution of Working Group I to the Fifth Assessment Report of the Intergovernmental Panel on Climate Change*, pp. 659–740.

Naim, O. (1993), Seasonal response of a fringing reef community to eutrophication (Reunion Island, Western Indian Ocean), *Marine Ecology Progress Series*, *99*(137-151).

Najjar, R. G., X. Jin, F. Louanchi, O. Aumont, K. Caldeira, S. C. Doney, J.-C. Dutay, M. Follows, N. Gruber, F. Joos, K. Lindsay, E. Maier-Reimer, R. J. Matear, K. Matsumoto, P. Monfray, A. Mouchet, J. C. Orr, G.-K. Plattner, J. L. Sarmiento, R. Schlitzer, R. D. Slater, M.-F. Weirig, Y. Yamanaka, and A. Yool (2007), Impact of circulation on export production, dissolved organic matter, and dissolved oxygen in the ocean: Results from Phase II of the Ocean Carbon-cycle Model Intercomparison Project (OCMIP-2), *Global Biogeochemical Cycles*, *21*(3).

Najjar, R. G., and R. Keeling (2000), Mean annual cycle of the air-sea oxygen flux: A global view, *Global biogeochemical cycles*, *14*(2), 573–584.

Neuer, S., A. Cianca, P. Helmke, T. Freudenthal, R. Davenport, H. Meggers, M. Knoll, J. M. Santana-Casiano, M. González-Davila, M.-J. Rueda, and O. Llinás (2007), Biogeochemistry and hydrography in the eastern subtropical North Atlantic gyre. Results from the European time-series station ESTOC, *Progress In Oceanography*, *72*(1), 1–29.

Nondal, G., R. G. J. Bellerby, A. Olsen, and T. Johannessen (2009), Optimal evaluation of the surface ocean CO2 system in the northern North Atlantic using data from voluntary observing ships, *Limnology and Oceanography: Methods*, pp. 109–118.

Olsen, A., A. M. Omar, R. G. J. Bellerby, T. Johannessen, U. Ninnemann, K. R. Brown, K. A. Olsson, J. Olafsson, G. Nondal, C. Kivimäe, S. Kringstad, C. Neill, and S. Olafsdottir (2006), Magnitude and origin of the anthropogenic CO2 increase and 13C Suess effect in the Nordic seas since 1981, *Global Biogeochemical Cycles*, *20*(3).

O'Reilly, J. E., S. Maritorena, B. G. Mitchell, D. a. Siegel, K. L. Carder, S. a. Garver, M. Kahru, and C. McClain (1998), Ocean color chlorophyll algorithms for SeaWiFS, *Journal of Geophysical Research*, *103*.

Palevsky, H. I., F. Ribalet, J. E. Swalwell, C. E. Cosca, E. D. Cokelet, R. a. Feely, E. Virginia Armbrust, P. D. Quay, E. V. Armbrust, and P. D. Quay (2013), The influence of net community production and phytoplankton community structure on CO 2 uptake in the Gulf of Alaska, *Global Biogeochemical Cycles*, *27*.

Peng, T., T. Takahashi, W. Broecker, and J. Olafsson (1987), Seasonal variability of carbon dioxide, nutrients and oxygen in the northern North Atlantic surface water: observations and a model*, *Tellus*, *39B*, 439–458.

Pepin, P., G. Han, and E. J. Head (2013), Modelling the dispersal of Calanus finmarchicus on the Newfoundland Shelf: implications for the analysis of population dynamics from a high frequency monitoring site, *Fisheries Oceanography*, *22*(5), 371–387.

Pierrot, D. (2009), Recommendations for autonomous underway pCO2 measuring systems and data-reduction routines, *Deep Sea Research Part II: Topical Studies in Oceanography*, *56*(8-10), 512–522.

Pingree, R., and D. Griffiths (1978), Tidal fronts on the shelf seas around the British Isles, *Journal of Geophysical Research*, *83*(8), 4615–4622.

Planque, B., and J. J. Fromentin (1996), Calanus and environment in the eastern North Atlantic. I. Spatial and temporal patterns of C. finmarchicus and C. helgolandicus, *Marine Ecology Progress Series*, *134*, 111–118.

Pryor, S. C., R. J. Barthelmie, and E. Kjellström (2005), Potential climate change impact on wind energy resources in northern Europe: analyses using a regional climate model, *Climate Dynamics*, *25*(7-8), 815–835.

Pyper, B. J., and R. M. Peterman (1998), Comparison of methods to account for autocorrelation in correlation analyses of fish data, *Canadian Journal of Fisheries and Aquatic Sciences*, *55*(9), 2127–2140.

Quay, P., C. Peacock, K. Björkman, and D. Karl (2010), Measuring primary production rates in the ocean: Enigmatic results between incubation and nonincubation methods at Station ALOHA, *Global Biogeochemical Cycles*, *24*(3).

Quay, P., J. Stutsman, and T. Steinhoff (2012), Primary production and carbon export rates across the subpolar N. Atlantic Ocean basin based on triple oxygen isotope and dissolved O 2 and Ar gas measurements, *Global Biogeochemical Cycles*, *26*(2).

Quigg, A., Z. V. Finkel, A. J. Irwin, Y. Rosenthal, T.-Y. Ho, J. R. Reinfelder, O. Schofield, F. M. M. Morel, and P. G. Falkowski (2003), The evolutionary inheritance of elemental stoichiometry in marine phytoplankton., *Nature*, *425*(6955), 291–4.

Raitsos, D., S. Lavender, Y. Pradhan, T. Tyrrell, P. Reid, and M. Edwards (2006), Coccolithophore bloom size variation in response to the regional environment of the subarctic North Atlantic, *Limonology and Oceanography*, *51*(5), 2122–2130.

Raitsos, D. E., Y. Pradhan, S. J. Lavender, I. Hoteit, A. McQuatters-Gollop, P. C. Reid, and A. J. Richardson (2014), From silk to satellite: half a century of ocean colour anomalies in the Northeast Atlantic, *Global Change Biology*, *20*(2117-2123).

Ramanathan, V., M. V. Ramana, G. Roberts, D. Kim, C. Corrigan, C. Chung, and D. Winker (2007), Warming trends in Asia amplified by brown cloud solar absorption., *Nature*, *448*(7153), 575–578.

Raupach, M. R., M. Gloor, J. L. Sarmiento, J. G. Canadell, T. L. Frölicher, T. Gasser, R. a. Houghton, C. Le Quéré, and C. M. Trudinger (2014), The declining uptake rate of atmospheric CO2 by land and ocean sinks, *Biogeosciences*, *11*(13), 3453–3475.

Redfield, A., B. H. Ketchum, and F. A. Richards (1963), The influence of organisms on the composition of sea water, *The sea*, *2*, 26–77.

Reid, P., M. Edwards, and H. Hunt (1998), Phytoplankton change in the North Atlantic, *Nature*, *391*(February), 2103–2103.

Rhein, M., S. Rintoul, S. Aoki, E. Campos, D. Chambers, R. Feely, S. Gulev, G. Johnson, S. Josey, a. Kostianoy, C. Mauritzen, D. Roemmich, L. Talley, and

F. Wang (2013), 2013: Observations: Ocean, *Climate Change 2013: The Physical Science Basis. Contribution of Working Group I to the Fifth Assessment Report of the Intergovernmental Panel on Climate Change*, pp. 255–315.

Richardson, A., A. Walne, and A. John (2006), Using continuous plankton recorder data, *Progress in Oceanography*, *68*(1), 27–74.

Riebesell, U., V. Fabry, L. Hansson, and J. Gattuso (2011), *Guide to best practices for ocean acidification research and data reporting*, Luxembourg: Publications Office of the European Union.

Riebesell, U., A. Körtzinger, and A. Oschlies (2009), Sensitivities of marine carbon fluxes to ocean change., *Proceedings of the National Academy of Sciences of the United States of America*, *106*(49), 20,602–20,609.

Robertson, J., C. Robinson, D. Turner, P. Holligan, a.J. Watson, P. Boyd, E. Fernandez, and M. Finch (1994), The impact of a coccolithophore bloom on oceanic carbon uptake in the northeast Atlantic during summer 1991, *Deep Sea Research Part I: Oceanographic Research Papers*, *41*(2), 297–314.

Robertson, J., A. Watson, C. Langdon, R. Ling, and J. Wood (1993), Diurnal variation in surface pCO2 and O2 at 60 N , 20 W in the North Atlantic, *Deep Sea Research II*, *40*, 409–422.

Robinson, C., A. Poulton, P. Holligan, A. Baker, G. Forster, N. Gist, T. Jickells, G. Malin, R. Upstill-Goddard, R. Williams, and Others (2006), The Atlantic Meridional Transect (AMT) Programme: A contextual view 1995-2005, *Deep Sea Research Part II: Topical Studies in Oceanography*, *53*(14-16), 1485–1515.

Russell, J., J. L. Sarmiento, H. Cullen, R. Hotinski, K. Johnson, S. C. Riser, and L. Talley (2014), The Southern Ocean Carbon and Climate Observations and Modeling Program (SOCCOM), *Ocean Carbon and Biogeochemistry Article*, *7*, 1–28.

Rynearson, T., K. Richardson, R. Lampitt, M. Sieracki, a.J. Poulton, M. Lyngsgaard, and M. Perry (2013), Major contribution of diatom resting spores to vertical flux in the sub-polar North Atlantic, *Deep Sea Research Part I: Oceanographic Research Papers*, *82*, 60–71.

Sabine, C. L., R. a. Feely, N. Gruber, R. M. Key, K. Lee, J. L. Bullister, R. Wanninkhof, C. S. Wong, D. W. R. Wallace, B. Tilbrook, F. J. Millero, T.-H. Peng, A. Kozyr, T. Ono, and A. F. Rios (2004), The oceanic sink for anthropogenic CO2., *Science (New York, N.Y.)*, *305*(5682), 367–71.

SAHFOS (2006), *SAHFOS Annual Report 2006*.

SAHFOS (2014), Plankton data on the B Route (mid Atlantic to Portsmouth).

Sambrotto, R., G. Savidge, and C. Robinson (1993), Elevated consumption of carbon relative to nitrogen in the surface ocean, *Nature*, *363*, 248–250.

Sanders, R., P. J. Morris, A. J. Poulton, M. C. Stinchcombe, A. Charalampopoulou, M. I. Lucas, and S. J. Thomalla (2010), Does a ballast effect occur in the surface ocean?, *Geophysical Research Letters*, *37*(8), 1–5.

Santana-Casiano, J. M., M. González-Dávila, M. J. Rueda, O. Llinás, and E. F. González-Dávila (2007), The interannual variability of oceanic CO2 parameters in the northeast Atlantic subtropical gyre at the ESTOC site, *Global Biogeochemical Cycles*, *21*.

Santer, B. D., T. M. L. Wigley, J. S. Boyle, D. J. Gaffen, J. J. Hnilo, D. Nychka, D. E. Parker, and K. E. Taylor (2000), Statistical significance of trends and trend differences in layer-average atmospheric temperature time series, *105*, 7337–7356.

Sarmiento, J., and N. Gruber (2006), *Ocean biogeochemical dynamics*, Princeton.

Sarthou, G., K. Timmermans, S. Blain, and P. Treguer (2005), Growth physiology and fate of diatoms in the ocean: a review, *Journal of Sea Research*, *53*(1-2), 25–42.

Schlesinger, M., and N. Ramankutty (1994), An oscillation in the global climate system of period 65-70 years, *Nature*, *367*, 723–726.

Schuster, U., A. Hannides, L. Mintrop, and A. Kortzinger (2009a), Sensors and instruments for oceanic dissolved carbon measurements, *Ocean Science*, *5*(4), 547–558.

Schuster, U., G. A. McKinley, N. Bates, F. Chevallier, S. C. Doney, A. R. Fay, M. González-Dávila, N. Gruber, S. Jones, J. Krijnen, P. Landschützer, N. Lefèvre, M. Manizza, J. Mathis, N. Metzl, A. Olsen, A. F. Rios, C. Rödenbeck, J. M. Santana-Casiano, T. Takahashi, R. Wanninkhof, and A. J. Watson (2013), An assessment of the Atlantic and Arctic seaair CO2 fluxes, 19902009, *Biogeosciences*, *9*(8), 10,669–10,724.

Schuster, U., and A. Watson (2007), A variable and decreasing sink for atmospheric CO2 in the North Atlantic, *Journal of Geophysical Research*, *112*(10.1029), 1–10.

Schuster, U., A. Watson, and N. Bates (2009b), Trends in North Atlantic sea-surface fCO 2 from 1990 to 2006, *Deep Sea Research II*, *56*(8-10), 620–629.

Schwanghart, W. (2010), Variogramfit, *MATLAB Central File Exchange (http://www.mathworks.co.uk/matlabcentral/fileexchange/25948-variogramfit)*.

Serret, P., E. Fernández, C. Robinson, E. Woodward, and V. Pérez (2006), Local production does not control the balance between plankton photosynthesis and respiration in the open Atlantic Ocean, *Deep Sea Research Part II: Topical Studies in Oceanography*, *53*(14-16), 1611–1628.

Serret, P., C. Robinson, E. Fernández, E. Teira, G. Tilstone, and V. Pérez (2009), Predicting plankton net community production in the Atlantic Ocean, *Deep Sea Research Part II: Topical Studies in Oceanography*, *56*(15), 941–953.

Shadwick, E. H., T. W. Trull, B. Tilbrook, a. J. Sutton, E. Schulz, and C. L. Sabine (2015), Seasonality of biological and physical controls on surface ocean CO 2 from hourly observations at the Southern Ocean Time Series site south of Australia, *Global Biogeochemical Cycles*, *29*, 223–238.

Sharqawy, M. (2010), Thermophysical properties of seawater: A review of existing correlations and data, *Desalination and Water Treatment*, *16*(10), 354–380.

Shutler, J. D., P. E. Land, C. W. Brown, H. S. Findlay, C. J. Donlon, M. Medland, R. Snooke, and J. C. Blackford (2013), Coccolithophore surface distributions in the North Atlantic and their modulation of the air-sea flux of CO2 from 10 years of satellite Earth observation data, *Biogeosciences*, *10*, 2699–2709.

Shutler, J. D., T. J. Smyth, S. Saux-Picart, S. L. Wakelin, P. Hyder, P. Orekhov, M. G. Grant, G. H. Tilstone, and J. I. Allen (2011), Evaluating the ability of a hydrodynamic ecosystem model to capture inter- and intra-annual spatial characteristics of chlorophyll-a in the north east Atlantic, *Journal of Marine Systems*, *88*(2), 169–182.

Sokal, R., and F. Rohlf. (1995), *Biometry: The principles and practice of statistics in biological research.*, 3rd edn., W.H. Freeman, New York.

Spitzer, W. S., and W. J. Jenkins (1989), Rates of vertical mixing, gas exchange and new production: Estimates from seasonal gas cycles in the upper ocean near Bermuda, *Journal of Marine Research*, *47*(1), 169–196.

Stanley, R. H. R., W. J. Jenkins, D. E. Lott, and S. C. Doney (2009), Noble gas constraints on air-sea gas exchange and bubble fluxes, *Journal of Geophysical Research*, *114*.

Stoffelen, A. (1996), Error modelling of scatterometer, in-situ, and ECMWF model winds: A calibration refinement, *Tech. rep. 93R. Neth. Meteorol. Inst., de Bilt, Netherlands.*

Stramski, D., R. a. Reynolds, M. Babin, S. Kaczmarek, M. R. Lewis, R. Röttgers, a. Sciandra, M. Stramska, M. S. Twardowski, and H. Claustre (2007), Relationships between the surface concentration of particulate organic carbon and optical properties in the eastern South Pacific and eastern Atlantic Oceans, *Biogeosciences Discussions*, *4*, 3453–3530.

Sun, C., J. Li, and F.-F. Jin (2015), A delayed oscillator model for the quasi-periodic multidecadal variability of the NAO, *Climate Dynamics*.

Sverdrup, H. (1953), On conditions for the vernal blooming of phytoplankton, *Journal du Conseil*, *18*, 287–295.

Sweeney, C., E. Gloor, A. R. Jacobson, R. M. Key, G. McKinley, J. L. Sarmiento, and R. Wanninkhof (2007), Constraining global air-sea gas exchange for CO2 with recent bomb 14C measurements, *Global Biogeochemical Cycles*, *21*, 1–10.

Takahashi, T. (2009), Climatological mean and decadal change in surface ocean pCO2, and net seaair CO2 flux over the global oceans, *Deep Sea Research Part II*, *56*(8-10), 554–577.

Takahashi, T., J. Olafsson, J. G. Goddard, D. W. Chipman, and S. C. Sutherland (1993), Seasonal variation of CO2 and nutrients in the high-latitude surface oceans: A comparative study, *Global Biogeochemical Cycles*, *7*(4), 843–878.

Takahashi, T., and S. Sutherland (2002), Global seaair CO 2 flux based on climatological surface ocean p CO 2, and seasonal biological and temperature effects, *Deep Sea Research Part II*, *49*, 1601–1622.

Takahashi, T., and S. C. Sutherland (2013), *Climatological mean distribution of pH and carbonate ion concentration in global ocean surface waters in the unified pH scale and mean rate of their changes in selected areas*, Tech. rep., Lamont-Doherty Earth Observatory of Columbia University.

Takahashi, T., S. C. Sutherland, and A. Kozyr (2009), Global ocean surface water partial pressure of CO2 database: measurements performed during 19682008 (Version 2008), *ORNL/CDIAC-152, NDP-088r, Carbon Dioxide Information Analysis Center, Oak Ridge National Laboratory, US Department of Energy, Oak Ridge, Tennessee, doi*, *10*.

Takeshita, Y., T. R. Martz, K. S. Johnson, J. N. Plant, D. Gilbert, S. C. Riser, C. Neill, and B. Tilbrook (2013), A climatology-based quality control procedure for profiling float oxygen data, *Journal of Geophysical Research: Oceans*, *118*(10), 5640–5650.

Telszewski, M., A. Chazottes, U. Schuster, A. J. Watson, C. Moulin, D. C. E. Bakker, M. Gonzalez-Davila, T. Johannessen, A. Kortzinger, H. Luger, A. Olsen, A. Omar, X. A. Padin, A. F. Rios, T. Steinhoff, M. Santana-Casiano, D. W. R. Wallace, and R. Wanninkhof (2009), Estimating the monthly pCO(2) distribution in the North Atlantic using a self-organizing neural network, *Biogeosciences*, *6*(8), 1405–1421.

Thomas, H., A. E. F. Prowe, I. D. Lima, S. C. Doney, R. Wanninkhof, R. J. Greatbatch, U. Schuster, and A. Corbiere (2008), Changes in the North Atlantic Oscillation influence CO2 uptake in the North Atlantic over the past 2 decades, *Global Biogeochemical Cycles*, *22*(4).

Toggweiler, J. R. (1993), Carbon overconsumption, *Nature*, *363*, 210–211.

Ueyama, R., and B. Monger (2005), Wind-induced modulation of seasonal phytoplankton blooms in the North Atlantic derived from satellite observations, *Limnology and oceanography*, *50*(6), 1820–1829.

Ullman, D. J., G. a. McKinley, V. Bennington, and S. Dutkiewicz (2009), Trends in the North Atlantic carbon sink: 1992-2006, *Global Biogeochemical Cycles*, *23*.

Uppala, S., P. Kå llberg, A. Simmons, U. Andrae, V. da Costa Bechtold, M. Fiorino, J. Gibson, J. Haseler, A. Hernandez, G. Kelly, X. Li, K. Onogi, S. Saarinen, N. Sokka, R. Allan, E. Andersson, K. Arpe, M. Balmaseda, A. Beljaars, L. van de Berg, J. Bidlot, N. Bormann, S. Caires, F. Chevallier, A. Dethof, M. Dragosavac, M. Fisher, M. Fuentes, S. Hagemann, E. Hólm, I. L. Hoskins B.J., J. P.A.E.M., R. Jenne, A. McNally, J.-F. Mahfouf, J.-J. Morcrette, N. Rayner, R. Saunders, P. Simon, A. Sterl, K. Trenberth, A. Untch, D. Vasiljevic, P. Viterbo, and J. Woollen (2005), The ERA-40 re-analysis, *Quarterly Journal of the Royal Meteorological Society*.

Velo, A., F. F. Pérez, X. Lin, R. M. Key, T. Tanhua, M. de la Paz, A. Olsen, S. van Heuven, S. Jutterström, and a. F. Ríos (2010), CARINA data synthesis project: pH data scale unification and cruise adjustments, *Earth System Science Data*, *2*(1), 133–155.

Villareal, T., M. Altabet, and K. Culver-Rymsza (1993), Nitrogen transport by vertically migrating diatom mats in the North Pacific Ocean, *Nature*, *363*, 709–712.

Visbeck, M., E. P. Chassignet, R. G. Curry, T. L. Delworth, R. R. Dickson, and G. Krahmann (2003), The ocean's response to North Atlantic Oscillation variability, *Geophysical Monograph Series*, *134*, 113–145.

von Allmen, P., D. Menemenlis, G. Spiers, and D. Bogucki (2009), Remote Sensing of the Mixed Layer Depth, http://ecco2.jpl.nasa.gov/meetings/2009/Allmen_MLDlidar.pdf.

Wallace, J., and D. Gutzler (1981), Teleconnections in the geopotential height field during the Northern Hemisphere winter, in: *Monthly Weather Review*.

Wanninkhof, R. (1992), Relationship between wind speed and gas exchange over the ocean, *Journal of Geophysical Research*, *97*(92), 7373–7382.

Wanninkhof, R., W. E. Asher, D. T. Ho, C. Sweeney, and W. R. McGillis (2009), Advances in Quantifying Air-Sea Gas Exchange and Environmental Forcing*, *Annual Review of Marine Science*, *1*(1), 213–244.

Wanninkhof, R., G. H. Park, T. Takahashi, C. Sweeney, R. Feely, Y. Nojiri, N. Gruber, S. C. Doney, G. a. McKinley, a. Lenton, C. Le Quéré, C. Heinze, J. Schwinger, H. Graven, and S. Khatiwala (2013), Global ocean carbon uptake: magnitude, variability and trends, *Biogeosciences*, *10*(3), 1983–2000.

Warner, A., and G. Hays (1994), Sampling by the continuous plankton recorder survey, *Progress in Oceanography*, *34*(2-3), 237–256.

Watson, A. J., U. Schuster, D. C. E. Bakker, N. R. Bates, A. Corbière, M. González-Dávila, T. Friedrich, J. Hauck, C. Heinze, T. Johannessen, A. Körtzinger, N. Metzl, J. Olafsson, A. Olsen, A. Oschlies, X. A. Padin, B. Pfeil, J. M. Santana-Casiano, T. Steinhoff, M. Telszewski, A. F. Rios, D. W. R. Wallace, and R. Wanninkhof (2009), Tracking the variable North Atlantic sink for atmospheric CO2., *Science (New York, N.Y.)*, *326*(5958), 1391–3.

Weiss, R. (1974), Carbon dioxide in water and seawater: The solubility of a non-ideal gas, *Marine chemistry*, *2*, 203–215.

Werdell, P. J., and S. W. Bailey (2005), An improved in-situ bio-optical data set for ocean color algorithm development and satellite data product validation, *Remote Sensing of Environment*, *98*, 122–140.

Westberry, T., M. J. Behrenfeld, D. a. Siegel, and E. Boss (2008), Carbon-based primary productivity modeling with vertically resolved photoacclimation, *Global Biogeochemical Cycles*, *22*(2).

Williams, P. J. l. B. (1993), On the definition of plankton production terms., *ICES marine science symposia*.

Williams, P. J. l. B., and N. Jenkinson (1982), A transportable microprocessor-controlled precise Winkler titration suitable for field station and shipboard use, *Limnology and Oceanography*, *27*, 576–584.

Williams, P. J. l. B., P. D. Quay, T. K. Westberry, and M. J. Behrenfeld (2013), The oligotrophic ocean is autotrophic., *Annual review of marine science*, *5*, 535–49.

Williams, R., and M. Follows (2011), *Ocean dynamics and the carbon cycle: Principles and mechanisms*, Cambridge University Press.

Winkler, L. (1888), Die Bestimmung des im Wasser gelösten Sauerstoffes, *Berichte der deutschen chemischen Gesellschaft*, *21*, 2843–2846.

Wolf-Gladrow, D. a., R. E. Zeebe, C. Klaas, A. Körtzinger, and A. G. Dickson (2007), Total alkalinity: The explicit conservative expression and its application to biogeochemical processes, *Marine Chemistry*, *106*(1-2), 287–300.

Woodruff, S. D. (1987), A comprehensive ocean-atmos data set, *Bulletin of the American Meteorological Society*, *68*, 1239–1250.

Woods, S., and T. A. Villareal (2008), Intracellular ion concentrations and cell sap density in positively buoyant oceanic phytoplankton, *Nova Hedwigia Beihefte*, *133*, 131–145.

Woolf, D. K., and S. A. Thorpe (1991), Bubbles and the air-sea exchange of gases in near-saturation conditions, *Journal of Marine Research*, *49*(3), 435–466.

Zeebe, R., and D. Wolf-Gladrow (2001), *CO2 in Seawater: Equilibrium, Kinetics, Isotopes: Equilibrium, Kinetics, Isotopes*, Elsevier.

Zhang, J.-Z., G. Berberian, and R. Wanninkhof (2002), Long-term storage of natural water samples for dissolved oxygen determination., *Water research*, *36*(16), 4165–4168.